CHALLENGES IN THE FUNCTIONALIZATION OF NANOPARTICLES FOR PLASMON RULER-BASED SINGLE-PROTEIN STUDIES

Dissertation zur Erlangung des Grades

„Doktor der Naturwissenschaften“

im Promotionsfach Chemie

am Fachbereich Chemie, Pharmazie, Geographie und Geowissenschaften

der Johannes Gutenberg-Universität Mainz

Alena Kuzmina

geb. am 23.06.1993 in Novosibirsk

Mainz, 2026

D77 - Dissertation Johannes Gutenberg-Universität Mainz

Lizenz

Diese Dissertation ist lizenziert unter der **Creative Commons Namensnennung 4.0 International Lizenz (CC BY 4.0).**

1. Berichterstatter: [redacted]

2. Berichterstatter: [redacted]

Tag der mündlichen Prüfung: 27.08.2026

EIDESSTATTLICHE ERKLÄRUNG

Die vorliegende Arbeit wurde im Zeitraum von April 2021 bis April 2026 in der ‚Nanobiotechnology Group' von Prof. Dr. Carsten Sönnichsen am Institut für Physikalische Chemie der Johannes Gutenberg-Universität Mainz durchgeführt.

Ich versichere, dass ich die vorliegende Arbeit selbstständig und ohne fremde Hilfe verfasst, andere als die angegeben Quellen nicht benutzt und die den Quellen wörtlich und inhaltlich entnommenen Stellen als solche kenntlich gemacht habe.

Ich versichere, dass ich diese Dissertation bisher weder im In- noch im Ausland (einem Beurteiler oder einer Beurteilerin) schriftlich oder in elektronischer Form als Prüfungsarbeit vorgelegt habe.

(Alena Kuzmina)

This thesis is dedicated to the Nanobiotechnology Group.
Thank you for your kind support and encouragement.

ABSTRACT

Proteins are an important building block of life. In this context, single-molecule methods are a key tool for deeper understanding of their function. One such method is the plasmon ruler: It combines the advantages of multiplexing, long-time measurement and good signal-to-noise ratio. My work investigates the chemical challenges of plasmon ruler assembly with aim to increase the robustness and yield of the dimer constructs, and therefore enable broader future application. For this, I systematically explore the theoretical constraints of the assembly, predicting optimal assembly conditions, the requirements for particle stabilization and expected assembly time. With these constraints in mind, I evaluate the quality of the particles and improve the particle functionalization protocol. Additionally, I quantify the particle functionalization, uncovering discrepancies between reality and previous theoretical assumptions, leading to a deeper understanding of the assembly. To complete the understanding of key factors leading to assembly success or failure, I consider the role of individual components such as the protein, the particle chemistry and the assembly concept. I single out the particle reactivity as a key bottleneck, showing the necessary steps for assembly improvement. With this, I ensure future assembly success. With the knowledge from my investigations, I revisit a novel and previously not understood dynamic signal in the plasmon ruler experiment. Combining the insights gained on particle quality and particle-substrate interactions, I explain the origin of this signal as an artifact. With this I highlight the importance of particle quality control in the dimer experiment. The total sum of my work is a route for successful plasmon ruler assembly: I provide a recipe for optimal particle functionalization and assembly concept, ensuring reproducibility and robustness. This work serves as basis for future scientists, bringing the plasmon ruler method closer to a streamlined application in the single-molecule community. The improved robustness and reproducibility of the plasmon ruler will help uncover the remaining unknows of proteins such as Hsp90, closing the knowledge gaps in the areas such as e.g. protein memory effects and long-term behavior.[1]

ZUSAMMENFASSUNG

Proteine sind ein wichtiger Baustein des Lebens. In diesem Zusammenhang sind Einzelmolekülmethoden ein Schlüsselwerkzeug für ein tieferes Verständnis ihrer Funktion. Der Plasmon Ruler ist eine solche Methode; er vereint die Vorteile von Multiplexing, Langzeitmessung und einem guten Signal-Rausch-Verhältnis. Meine Arbeit untersucht die chemischen Herausforderungen des Aufbaus von Plasmon Rulern mit dem Ziel, die Robustheit und Ausbeute der Dimerkonstrukte zu erhöhen und so eine breitere zukünftige Anwendung zu ermöglichen. Dafür untersuche ich systematisch die theoretischen Rahmenbedingungen des Aufbaus, sage optimale Aufbaubedingungen, die Anforderungen an die Partikelstabilisierung und die erwartete Reaktionszeit voraus. Mit diesen Einschränkungen im Hinterkopf evaluiere ich die Qualität der Partikel und verbessere das Funktionalisierungsprotokoll. Zusätzlich quantifiziere ich die Partikelfunktionalisierung und decke Diskrepanzen zwischen Realität und früheren theoretischen Annahmen auf. Dies sichert ein tieferes Verständnis des Dimeraufbaus. Um das Verständnis der Schlüsselfaktoren beim Aufbau zu vervollständigen, betrachte ich die Rolle einzelner Komponenten wie das Protein, die Partikelchemie und das Aufbaukonzept. Dabei stelle ich die Partikelreaktivität als entscheidenden Faktor fest und zeige die notwendigen Schritte zur Verbesserung des Aufbaus. Damit sichere ich den zukünftigen Erfolg der Methode. Mit dem Gesamtwissen aus meiner Arbeit erkläre ich ein bisher nicht verstandenes dynamisches Signal im Plasmon Ruler Versuch. Indem ich die gewonnenen Erkenntnisse zur Partikelqualität und Teilchen-Substrat-Interaktionen kombiniere, erkläre ich den Ursprung dieses Signals als Artefakt. Damit unterstreiche ich die Bedeutung der Kontrolle von Partikelqualität und Rahmenbedingungen für die Plasmon Ruler Methode. Die Gesamtsumme meiner Arbeit ist ein Rezept für den erfolgreichen Aufbau von Plasmon Rulern: Ich liefere ein Rezept für optimale Partikelfunktionalisierung und Aufbaukonzepte, um Reproduzierbarkeit und Robustheit sicherzustellen. Diese Arbeit dient als Grundlage für zukünftige Wissenschaftler und bringt die Plasmon Ruler Methode näher an eine breitere Anwendung in der Einzelmolekül-Gemeinschaft. Die verbesserte Robustheit und Reproduzierbarkeit des Plasmon Rulers wird helfen, die verbleibenden Unbekannten von Proteinen wie Hsp90 aufzudecken und die Wissenslücken in Bereichen wie z. B. Proteingedächtniseffekten und Langzeitverhalten zu schließen.[1]

CONTENT

I. INTRODUCTION

Proteins can be regarded as machines that regulate life. The majority of proteins are involved in binding and transport processes, e.g. hemoglobin,[2] followed closely by catalytic processes, with the other functions divided among serving in signal transduction, enzyme regulation and more.[3] Understanding their working mechanism gives a glimpse into the complex structure of life, and in particular our own human organism.

One approach to comprehend how a machine works is to look at its structure. In a protein, the very basis of the structure is a sequence made up of a total of 20 canonical amino acids.[4] This structure undergoes complex folding, at last forming the final and functional (tertiary or quaternary) structure of a protein. Resolving the final structure remains subject of rigorous studies.[5] A milestone example on this topic is the advance in cryogenic electron microscopy (cryo-EM). This method first yielded atomic-resolution images, awarding its pioneers the 2017 Nobel Prize in chemistry.[6] This method drastically increased the solved protein structures. In the field of membrane proteins listed in the Protein Data Bank in 2024, over 80% of protein structures had been mapped using this method.[7] Another important method is the nuclear magnetic resonance (NMR) spectroscopy,[8] which can measure proteins in their natural environment and does not require the crystallization step needed for cryo-EM. The studies of protein structures were further enhanced with the introduction of AlphaFold and later AlphaFold2 in 2021,[9] which is a machine learning model for predicting the structure from sequence.

Therapeutical development and biomedical research are beneficiaries of these advancements: One such example is the cryo-EM based resolution of the fibril structure of amyloid-β, which is a contributor to the Alzheimer's disease.[10] Another example is the characterization of the interaction between potential inhibitors with the oncogenic protein K-Ras using NMR.[11]

The example of NMR brings us to the next point: Protein dynamics. As Henzler-Wildman and Kern summarize in their review article titled "Dynamic personalities of proteins",[12] the function of a protein is governed by its motion. As such, their article highlights the importance of the dimension of time to understanding protein function.

There exist several methods that enable insight into protein dynamics. One key method already mentioned in this field is the NMR, with examples of studies on folding pathways.[13–15] Another solution-based method is the Small-Angle X-Ray Scattering (SAXS).[16]

These methods are valuable tools for probing a protein population. However, they have the drawback of averaging, and thus obscuring information on heterogeneity and rarer phenomenons.[17] Without this information, the dynamic picture is incomplete. This challenge is addressed by single-molecule studies, completing the understanding of

protein function. Subsequently, better comprehension of protein function can lead to advances in important fields such as, for example, disease therapy.[18,19]

To illustrate the importance of single-molecule studies, I use the example of the Heat Shock Protein 90 (Hsp90), which is part of this work.

1. The Heat Shock Protein 90 (Hsp90)

The Hsp90 is a chaperone protein to a variety of client proteins. It is a homo-dimer, consisting of two identical monomeric units.[20] It can seen as a machine that plays a central part in proteostasis,[i] with its key functions being the folding or refolding as well as activation or deactivation of its clients. The protein fulfills these complex tasks by undergoing an ATP-driven cycle[22] between a "closed" and "open" state, during which it processes its clients. In a simplified way, this process is shown in Figure I-1.

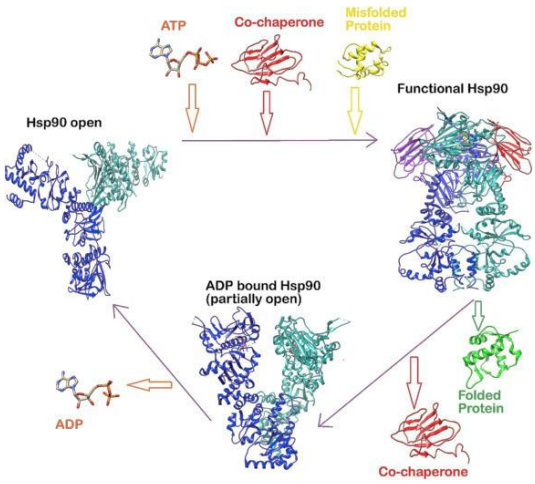

Figure I-1. The Hsp90 cycle. The working cycle includes the association of ATP, a co-chaperone, as well as a misfolded protein. During the cycle, the Hsp90 undergoes a conformational change from an open (client-free) and a closed conformation. With the cycle completed, the folded protein and the co-chaperone are released. At last ADP is released, and the protein returns to an open conformation. Reprinted with permission from Verma et al., *Biochimie* 2016, *127*, 227–240. DOI: 10.1016/j.biochi.2016.05.018.[23]

Hsp90 makes up 1-2% of the total protein mass in eucaryotic cells, with the percentage increasing when the organism experiences stress.[24] Hsp90's broad-band function in proteostasis has made it a subject of intense studies for over 40 years.[25] Despite extensive research, a lot of unknowns remain subject of debate.[25] In particular, questions remain about mechanisms of its function. These questions arise from the fact that Hsp90 is responsive to a large variety of clients in a client-specific way,[26] with no single mechanism that can be applied to all cases. Thus, Hsp90 remains an attractive target for research.

[i] Proteostasis: This term refers to the process of maintaining the balance between the synthesis, folding and degradation of proteins in a biological system, among other tasks.[21]

Over the years, many efforts were made to explore this protein's nature, starting with crystallographic studies,[27] as well as ensemble measurements in solution (e.g. via NMR, small-angle X-ray scattering, SAXS),[28–30] revealing populations of its closed and open states, as well as ensemble interactions with inhibitors. These ensemble measurements provided valuable information on the protein population. However, to further probe the behavior on fundamental, single-molecule level, other techniques had to be invented, as highlighted below.

2. Single-molecule protein dynamics in the picture

To probe single-molecule behavior, a variety of techniques have been developed,[31,32] each with its strengths and limitations. The following section gives a brief overview over the most common methods, giving preference to those that have been previously used to probe the Hsp90 protein.

2.1. Förster Resonance Energy Transfer (FRET)

FRET is a method that uses two or more dyes to track distance changes between the dyes, and therefore monitor protein motion. The donor dye is excited, and the energy is transferred radiation-free to the acceptor dye.[33] This happens under the conditions that the molecules are not more than around 10 nm apart (depending on the dye),[34] and the donor and acceptor transition dipole orientations approximately parallel. There must also be an overlap between the donor fluorescence and acceptor absorption spectrum. In a typical single-molecule FRET experiment, the protein labeled with the dyes is fixed onto a substrate, as shown in Figure I-2.

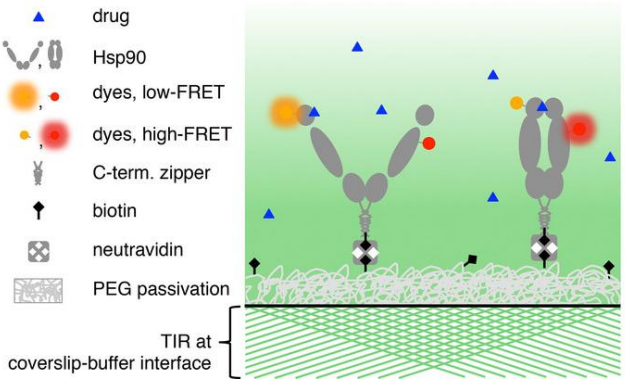

Figure I-2. Sketch of a Hsp90 FRET experiment with two dyes. The protein is functionalized with two dyes (orange and red circles) and fixed onto a polyethylene glycol (PEG) passivated glass surface via a biotin-neutravidin coupling. The measurement is performed in a total internal reflection microscope setup (TIR). This narrows the excitation to the area where the protein is fixed, and therefore reduces fluorescence and scattering from other nonrelated sources. Adapted with permission from Schmid et al., *ChemPhysChem* 2018, *19* (14), 1716–1721. DOI: 10.1002/cphc.201800342. © Wiley-VCH GmbH.[3535]

The measurement is limited by the lifetime of the dyes, which are prone to photo-bleaching, depending on experimental conditions. Typically, a single-molecule FRET experiment lasts up to several minutes until the dyes bleach.[36,37] This is one of the major

challenges in single-molecule FRET. As such, rare events and long dwell-times are difficult to probe with this method.

2.2. Force-spectroscopy

The force-spectroscopy field offers a variety of techniques, such as atomic force spectroscopy (AFM), optical and magnetic tweezers.[38] In the case of the Hsp90 protein studies, optical tweezers have been previously employed to successfully measure protein Hsp90 folding, assembly and domain interactions.[39,40] In the optical tweezers experiment, the protein is attached to dielectric silica beads held in a laser beam. One bead is held in place, and the other is moved, thus applying force to the protein and coercing it to unfold. The force necessary to unfold (and refold) its different structure elements varies (Figure I-3). Such unfolding and refolding patterns are studied to further gain information on protein behavior under different conditions relevant for its biological function.

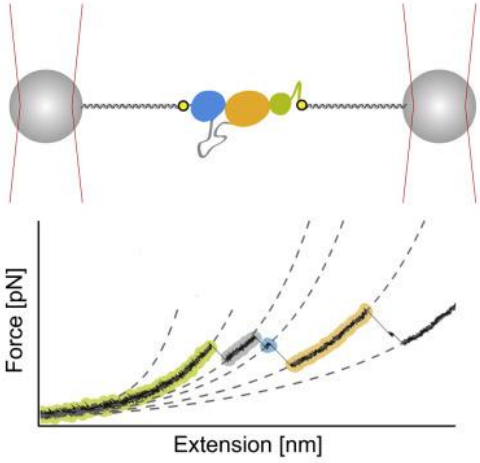

Figure I-3. Sketch showcasing the principle behind the optical tweezes measurement. The protein is trapped between two dielectric beads and is forced to unfold. The force necessary to unfold the protein is then recorded against the displacement of the second bead (called extension in the figure). An abrupt change in the force ("snapping down") is observed when a particular structural element unfolds upon sufficiently high force. This pattern in unique to a specific protein and protein state. Reprinted with permission from Jahn et al., *Structure* 2018, *26* (1), 96-105.e4. DOI: 10.1016/j.str.2017.11.023. © Elsevier.[39]

Despite being a well-established method, there is ongoing work on expanding its measurement possibilities. For example, a recent study from 2025[41] has combined the optical tweezers with FRET, allowing simultaneous multi-dimensional detection of protein motion. As such, this measurement method's strength is observation of domain-specific single-molecule behavior. This method, however, is not force-free, and the limitations of the FRET measurement principle apply to the combined method as well.

2.3. Nanopores

Several other methods aim to expand the single molecule technique portfolio. One such measurement principle is the so-called use of a nanopore. This is a substrate-based method, with possible variations regarding the substrate where the pore is located. One such example is the solid-state, lipid-bilayer passivated NEOtrap.[42] During the

measurement, a voltage is applied across the membrane, leading to an ionic current that flows through the pore. When a molecule e.g. a protein passes or is trapped within this pore, the current changes. This change in ion mobility is proportional to the volume and shape of the molecule, allowing to detect a specific protein passing the pore,[43] or potentially determine its conformation.[44]

A key challenge of the nanopore is the limited dwell time of the molecular species in the pore. If the pore measurement is to be label-free, then other tricks need to be employed to keep the species trapped as long as possible. The challenge of label-free fixation has been addressed by placing a DNA origami "plug",[42] as shown in Figure I-4. A more recent study by the same group has shown an increased trapping time for the protein avidin of 100 ms.[45] However, authors report that challenges remain, with the general aim to improve the method for trapping times in the range of hours.[42]

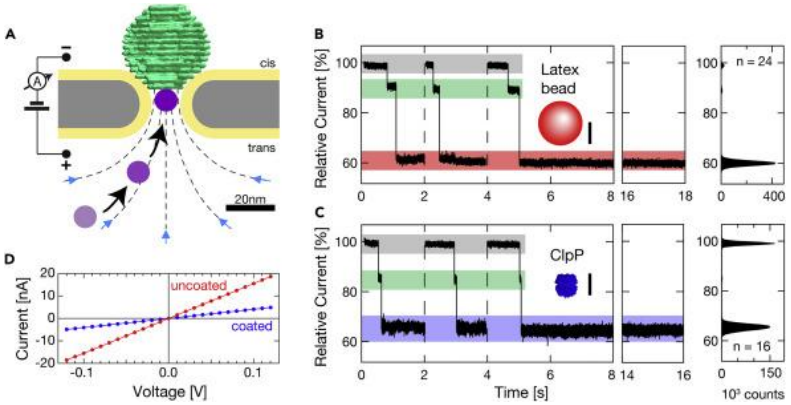

Figure I-4. NEOtrap: the measurement principle. (a) Sketch of the measurement principle, with a solid-state SiN pore (grey) coated in a lipid bilayer (yellow), with a DNA origami bead blocking the pore. Violet sphere illustrates the trapping of the analyte. Pores are indicated as 24-30 nm in size.[42] The (b-c) Single-pore relative current time traces. The grey shaded part indicates the free current, the green shaded part the docking of the DNA origami plug and the red/violet part the trapping of the analyte (a latex bead or a ClpP protein). (d) Current changes of a coated and uncoated pore. Schmid et al., *iScience* 2021, *24* (10), 103007. DOI: 10.1016/j.isci.2021.103007, licensed under CC BY 4.0.[42] DNA-origami image used with permission of RSC, from Kopatz et al.,[46] permission conveyed through Copyright Clearance Center, Inc.

The portfolio of single-molecule techniques does not end here. Efforts are made to use sophisticated measurement techniques, for example on the bases of quantum tunneling[47] or plasmon based methods[48] to probe single-protein dynamics. In the following section, I introduce the plasmon ruler method,[49] which has been developed in our group.

2.4. The Plasmon Ruler

The method of the plasmon ruler aims to improve on the time limit of single-molecule studies by replacing dyes with non-bleaching gold particles. The basis of the measurement is the effect of plasmon coupling, which occurs when two gold particles come into close proximity. The principle of the plasmon coupling is discussed in greater depth in the theoretical essentials (chapter 2).

Previously, our group has shown a successful proof-of-concept of this method, whereby the Hsp90 protein dynamics could be tracked over a period of over 24 h.[49] Most importantly, the measurements have shown novel and rare long-lived states in the

conformation dynamics, thus expanding the knowledge of protein behavior. The plasmon ruler method was shown to be a useful tool to expand the portfolio of single-molecule measurements, with potential for easy measurement of hundreds of single proteins at the same time, for time periods that cannot yet be easily accessed by the FRET and similar methods.

However, for wide-spread application of this method, several optimizations must yet be performed. One such key challenge is the low yield of successful dimer constructs that hinders the application of this method to its full potential.

The following section introduces the state-of-the-art plasmon ruler assembly, summarizing the challenges and previous efforts of my predecessors, which served as a basis for my work.

3. Hsp90 Plasmon Ruler Assembly—A recap of previous works and current state

To retrieve reliable information about protein motion, the plasmon ruler must be assembled at defined chemical sites. In a FRET experiment, the dyes are chemically attached to the protein in solution, before the construct is deposited onto a pre-passivated glass substrate for measurement. The same concept is applied to the plasmon ruler assembly—with certain key differences that I highlight as I explain the protocol in the following.

3.1. The state-of-the-art plasmon ruler protocol

The plasmon ruler protocol is made of two major components: the protein and the two particles that replace the dyes.

To attach the protein to the particles at specific sites, the protein is modified by our collaborators from the group of Thorsten Hugel at the University Freiburg. The modification switches a 285 tyrosine residue to a cysteine. This introduces a thiol group, which can later be used for protein attachment in maleimide-mediated reactions (Figure I-5a).

The second component are the two particles. Contrary to a dye molecule, a gold particle is—on average—equally reactive across the many square nanometers of its surface. To give the particles more defined and controllable reactive sites, they are covered by a polymer mixture. This serves simultaneously as protection against non-specific aggregation, as I will show in the theoretical essentials (chapter 2). The protocol uses linear polyethylene glycols (PEGs) with a thiol on one end for the attachment to gold and another group on the other end. The second group is either neutral (methoxy) for passivation purposes or reactive (amine) for linking to the protein.

The protocol uses two polymer types: a 2000 g/mol neutral methoxy-PEG (ca. 45 repeating units) for passivation and a 3000 g/mol amino-PEG (ca. 67 repeating units) for protein attachment. In addition, a small amount of 3000 g/mol biotin-PEG is mixed in

to attach one particle covalently to a passivated glass slide.[ii] The entire construct is shown in Figure I-5b.

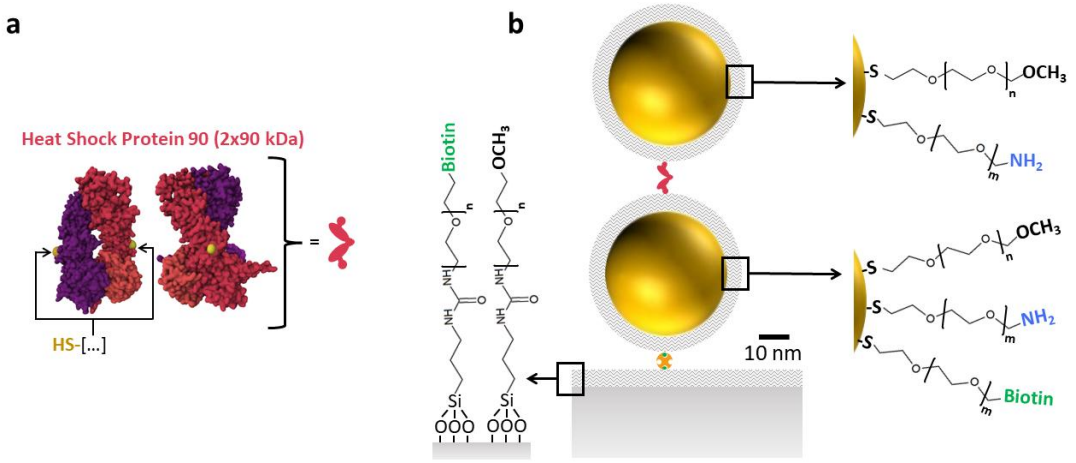

Figure I-5. State-of-the-art Hsp90 plasmon ruler assembly. (a) Hsp90 dimer structure [PDB: 2CG9][50], with modified T285C sites marked yellow. The representation of the introduced thiols is exaggerated for better view. (b) Sketch of the assembled plasmon ruler, approximately to scale. The example shows two 40 nm sized particles, covered by a mixture of polymers and attached to a passivated glass slide by biotin-streptavidin-chemistry. The protein is attached via reactive thiols to the amino groups in the polymer shell by activation with the linker molecule SMCC (Succinimidyl-4-(N-maleimidomethyl)cyclohexan-1-carboxylate). The linker is not shown in the sketch. The glass slide is passivated using silane-PEGs with a mixture of biotin and methoxy end groups. Detailed protocols are listed in the Appendix.

The reactivity of this polymer shell is tuned by mixing different ratios of the abovementioned polymers. Following challenges are kept in mind:

(1) The protein must attach with one site per particle only.

(2) There must only be one protein present between two particles.

(3) The particles must be sufficiently reactive, so assembly ideally happens upon first hit.

The state-of-the-art protocol addresses these points by tuning the polymer ratios. The particle where the protein is first attached is modified by PEGs carrying 3% amino, 10% biotin and 87% neutral methoxy groups. This heightens the likelihood that only one protein will be present between two assembled particles, and lowers the probably of the second reactive protein site encountering an anchor on the same particle. The second particle is modified with an increased amount of 15% amino groups, filling the rest with 85% methoxy groups. This ensures a higher reactivity of the particle towards the first.

[ii] The topic of passivation of glass surfaces for single-molecule experiment is broad and not the focus of this work. The state-of-the-art passivation protocol is referenced in the Appendix. This work sometimes uses other types of passivation techniques or none at all. When this is the case, the method is indicated in the respective section.

This protocol sufficed to successfully show that recording of protein motion using a plasmon ruler is possible.[49] However, challenges arose, as I show in the following part.

3.2. The problem of low yield and other challenges

First attempts with the plasmon ruler showed the expected signal corresponding to protein motion. However, the yield of plasmon rulers showing fluctuating motion was low. Roughly, the yield lay below 4%, and fluctuations were shown in only about one third of experiments.[49,51,52] Additionally, the study was complicated by the insufficiently robust glass substrate passivation.[52] Thus, the method could not yet reliably deliver the necessary statistics for meaningful protein motion studies.

To address this problem, my predecessor Bastian Flietel further studied the plasmon ruler assembly.[52] His approach to the challenge of the low yield and the substrate passivation issue was a change of assembly strategy, with initial success.

In Figure I-6 I show both methods to illustrate the two concepts. [49,51] In the initial protocol (a), the dimer is assembled sequentially. The first particle is deposited onto a pre-passivated glass substrate. The protein is added in a second step, and in a third step, the second particle is flushed in to form the dimer. This method relies on substrate passivation to control the density of the deposited particles. It also requires several hours to complete due to its sequential nature.[52]

In the new method shown by Bastian Flietel (b), called the batch assembly, all components are mixed together in solution. After a certain reaction time, the mixture of all constructs is deposited onto a glass substrate. No passivation is used, because the density of the constructs is adjusted by the particle concentration as they are flushed in.

As Bastial Flietel proved, the second method saves effort and time.[52] An additional positive aspect is that the substrate no longer needs passivation for particle density control. In his thesis, Bastial Flietel reports that the batch synthesis yielded fluctuating time traces in 90% of cases, as compared to only one third in the original protocol.

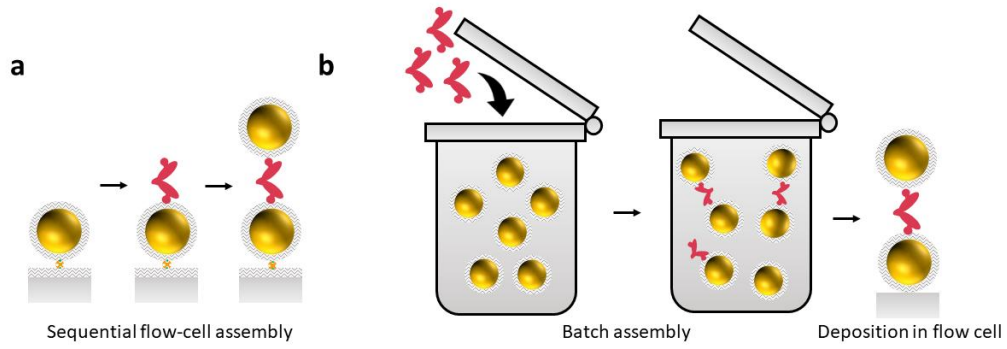

Figure I-6. Plasmon ruler assembly strategies. (a) Sequential assembly in flow cell: The first particle is anchored with streptavidin-biotin chemistry onto a pre-passivated, PEGylated glass slide. The protein is added, and then the second particle is flushed in excess. The passivation prevents a non-specific oversaturation of the surface with the second particle. (b) Assembly in batch (typically done in a plastic tube): The protein is added to a dispersion of particles and left to react. The ratio of protein to particles is optimized to statistically deliver the highest yield of 18%.[52] The resulting mixture of monomers, dimers and multimers is flushed into a flow chamber. The surface coverage by particle constructs is controlled by dilution of the mixture.

However, after initial success, this assembly strategy also stopped yielding results, with more than ten measurements performed by three independent persons not yielding fluctuating traces typical of protein motion. Additionally, the batch method showed a novel type of dynamic signal that was not yet understood.[52] It was unclear whether the signal could be attributed to the protein motion, which is problematic for a method that aims to expand on the current state-of-the-art of single-molecule studies.

Therefore, the central challenges remained: The plasmon ruler assembly protocol was not yet robust and required further investigation.

4. A more thorough study of challenges is needed

To summarize previous results, the different assembly methods did not yield a sufficient and reproducible number of dynamic protein traces. This means that the current protocol is not robust, and the reliability of the data not ensured. At the same time, the interest in long-term measurements of protein motion persists—also outside the Hsp90 community.

Addressing these challenges is the basis of my work. My main goal was a sustainable improvement of the plasmon ruler assembly. My aim was to find key factors playing a role in assembly success and failure for smart and targeted improvement effort. To achieve this, I split the challenge into separate questions:

(1) Does the state-of-the-art protocol fulfill the theoretical criteria necessary for a successful assembly and measurement? And if not, what needs to be changed?

In this context, one factor is the signal strength, which is based on the particle size and interparticle distance. Additionally, it is important to know if the assembly is colloidally stable and force-free, which ensures that the dynamic signal can be measured without interference of additional forces. Lastly, a critical part of the assembly is its kinetics. Important factors are diffusion and reactivity of the partners, and their relation to the expected assembly time. Revision of these key factors for assembly is necessary to ensure its success or explain its failure.

(2) How does reality relate to the theoretical criteria in (1)?

The central part of this question is the particle and its functionalization. Here, the quality of the polymer layer is the prerequisite for colloidal stability. The polymer layer thickness, on the other hand, is what determines the final interparticle distance and signal strength.[iii] Previous works[51,52] have made theoretical assumptions about the polymer thickness and the resulting interparticle distance. For a complete picture, these assumptions now require revision and proof. In addition, particle reactivity is of importance. Were the particles already sufficiently reactive? Is there room for

[iii] The interparticle distance is made up of the protein and the polymer layer. However, the protein size is fixed, so the only variable is the polymer layer thickness.

improvement, and if so, which steps are necessary to improve the functionalization and make it more stable?

(3) Which part of the assembly process has the biggest influence on its success or failure?

This question arises when considering the complexity of the assembly. The assembly is made of particles, but also the protein itself. For instance, the protein could be wrongly oriented or its binding sites unavailable, thus hindering the assembly. On the other hand, the chemistry chosen for assembly could be a source of failure due to its inefficiency. The assembly concept itself could also pose a problem. For targeted protocol improvement, it is important to differentiate between these factors.

(4) What is the novel signal,[52] and is it related to the protein motion?

This question is important to answer to increase the robustness and reliability of the plasmon ruler method itself. Because the signal looks similar to a protein trace but has a novel multi-level pattern, it is critical to understand its nature. If it is an artifact, then knowing the cause can prevent it from occurring and getting confused with protein-related data. If it does belong to the protein, then it is sensible to investigate it further. For these reasons, the study of the novel signal is paramount for the future application of the plasmon ruler method.

Finding answers to these questions is the basis for a broader application and reliability of the plasmon ruler method. In the following, I present a summary of my work and explain how I addressed these questions.

4.1. Summaries of chapters

In **chapter 2**, I study the **theoretical criteria** necessary for assembly. With the boundary element method (BEM) simulation, I observe signal trends in relation to particle size and distance. I show that the state-of-the-art protocol lies within a reasonable range to for signal measurement. Further, I explore the particle dimer stability criteria with the DLVO (Derjaguin-Landau-Verwey-Overbeek) model, which is suitable to predict colloidal interactions. I calculate the minimal interparticle distance where the dimer construct experiences no excessive attractive or repulsive forces. This ensures two things: The possibility of the construct to readily assemble, and the force-free measurement of protein movement. Lastly, I predict the assembly time frame, and the importance of particle reactivity in this process.

Chapter 3 moves to the second question, exploring the relation between particle functionalization and the predicted ideal state in chapter 2. Here I explore the polymer layer on the particle, which is important for colloidal stability. I test its robustness under different conditions, in particular in the protein buffer, and show how to improve it. Additionally, I quantify the polymer thickness and relate it to the interparticle distance and coupling strength, revealing discrepancies between previous assumptions and the

new knowledge. Lastly, I show how polymer modification has a non-neglectable influence on particle stability, and offer solutions to improve it.

In **chapter 4**, I address the remaining unknows regarding dimer assembly and single out the key factor responsible for success and failure. For this I apply a screening scheme that differentiates between influence factors such as the protein, the assembly tactic and the chemistry in use. For the chemistry, I use a selection of common strategies known in biochemistry. With this I single out the chosen chemistry as the main responsible factor for assembly success.

In **chapter 5**, I summarize my findings. I give an overview of the answers to the key questions related to the plasmon ruler dimer assembly and what they mean for the future of the plasmon ruler method.

II. THEORETICAL ESSENTIALS

This chapter lies the groundwork for the investigation of the dimer assembly. It serves two goals: Firstly, to provide a guide for the dimer assembly in terms of key aspects such as suitable particle size and maximally tolerable interparticle distance. And secondly, to examine whether the state-of-the-art dimer assembly—with its specific modification and chosen particle sizes—fits the criteria established by this guide.

To do this, I address the theory behind plasmon coupling, which is the basis for transducing the protein motion into a spectroscopic signal. This gives an overview over the general trends, as well as an approximation of a minimal suitable particle size and the respective interparticle distance. Afterwards, I focus on the assembly basics. For this, I inspect interparticle interactions and kinetics involved. The interactions help determine the balance between colloidal stability and readiness to assemble. The kinetics predict the time scales during which assembly is expected to happen. Together, they provide the necessary information about the constraints of the dimer assembly.

1. The plasmon coupling theory

To evaluate the quality of the signal transduction of a plasmon ruler, it is first necessary to understand how it works. In the plasmon ruler experiment, the protein is labeled with two nanosized gold particles, which serve as trackers of the protein dynamics. The principle behind this measurement is similar to the method based on Förster Resonance Energy Transfer (FRET).[34,37] This method employs the distance-dependent energy transfer between two dyes to track the labeled protein motion. As previously mentioned in the introduction, FRET has limitations such a dye bleaching, which significantly reduces measurement time to the range of minutes. In the plasmon ruler, the dyes are replaced by non-bleaching gold particles, and the measured effect is the plasmon coupling strength of the two particles. For better understanding of the results presented in this chapter, I explain in the following how the plasmon effect and plasmon coupling work.

1.1. The plasmon effect

When an electromagnetic wave passes a nano-sized particle, the electrons in the conductive band are displaced with the electric field (Figure II-1a). At the same time, the positive nuclei remain in place, producing a restoring force. The result is a collective oscillation of electrons that can be described as a quasiparticle called plasmon.[53,54] The plasmon can be approximated with the model of a damped harmonic oscillator, which is driven by the incident light at the resonance frequency. In practice, this leads to the observed phenomenon of absorption and scattering, with the strongest effect appearing at the resonance frequency. For a spherically shaped gold particle, this is seen as a peak

in the spectrum at the resonance wavelength λ_{res}, where the intensity is the highest (Figure II-1b).

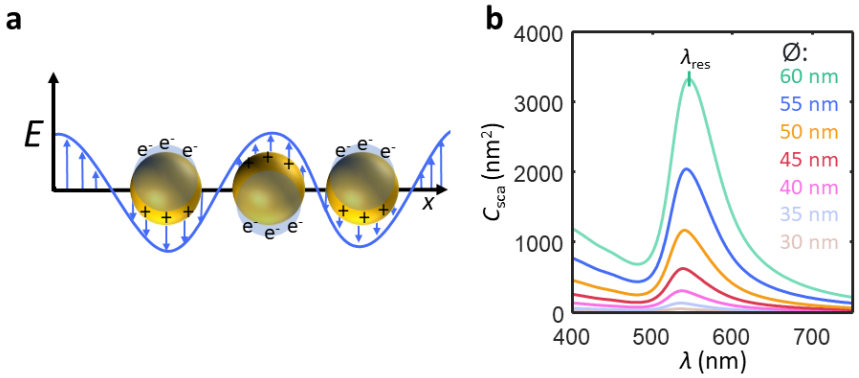

Figure II-1. The plasmon effect. (a) When an electromagnetic wave hits a nano-sized gold particle, the conduction band electrons are periodically displaced against the positive nuclei. (b) Simulated scattering cross section of 30-60 nm particles. As an example, the resonance frequency λ_{res} is marked for the 60 nm particle. Details on the simulation are presented in the Appendix A.

Further, the scattering depends on material, shape and volume (as demonstrated in Figure II-1b) and environment of a particle.[iv] The latter is the reason why plasmonic gold particles are employed in sensing applications.[56] Another effect is seen when two plasmonic particles are brought into close proximity, leading to plasmon coupling.

1.2. The plasmon coupling

As soon as the distance between two particles is small enough, the plasmon coupling occurs. One way to describe it is to see it as a coupling of two harmonic oscillators, which together form a new system with a red shifted resonant wavelength and stronger scattering intensity (Figure II-2a-b).[57–59] Jain et al.[60] have shown that the resulting red shift decays approximately exponentially with the growing interparticle distance, as illustrated in Figure II-2c. The decay can be described with the following equation:

II.1

$$\Delta\lambda_{res} \approx a \cdot \exp\left(-\frac{D}{b}\right)$$

In this equation, $\Delta\lambda_{res}$ is the resonant wavelength shift. a is the prefactor and b is the decay constant. The decay constant is in the range of 0.2x the particle diameter, and significant coupling occurs approximately at an interparticle distance of 2x the particle radius.[60]

The exact form of this decay depends on several factors such as particle size and the refractive index of the medium. A similar correlation is expected for the difference in scattering intensity caused by the interparticle distance change.[61]

[iv] This relationship is described by the Clausius Mossotti equation, for further reading see e.g. Nolting, 2013, p.163,[55] and Bohren and Huffman, 1998.[54]

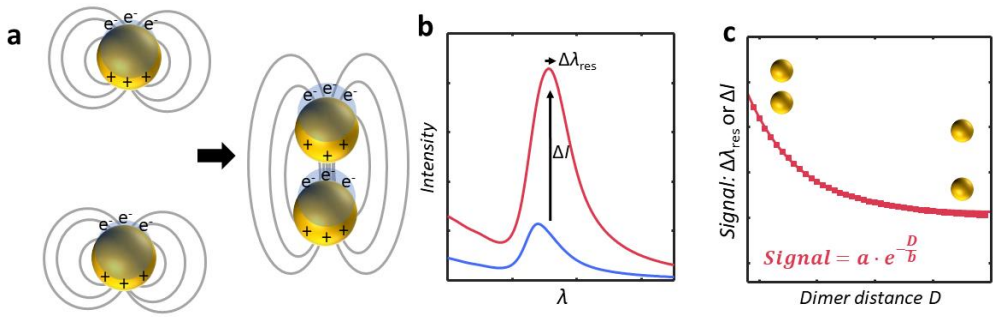

Figure II-2. Plasmon coupling. (a) Plasmon coupling occurs when two particles are placed within a sufficiently close distance of approximately 2x the particle radius or less.[60] (b) Figure shows a simulated spectrum of a 50 nm particle and the resulting spectrum when it forms a dimer with another 50 nm particle. The specific interparticle distance is 18 nm, corresponding to the presumed interparticle distance of the state-of-the-art Hsp90 dimer. Details on the simulation are presented in the Appendix A. The plasmon coupling results in an increased scattering intensity ΔI, as well as a small red shift of the resonance wavelength $\Delta\lambda_{res}$. (c) Representation of the exponential decay of the signal (either $\Delta\lambda_{res}$ or ΔI) with the growing distance between the particles. Simulated data is used for this illustration, with red squares representing the signal at a specific distance and the red line the fit, as described by the inset function.

1.3. Tracking the Hsp90 protein motion with plasmon coupling

The presented correlation between interparticle distance and plasmonic coupling strength permits to estimate the distance between two coupled particles. Consequently, the motion of a protein between two such plasmonic particles can be translated into a (quantifiable) signal.

In the case of the Hsp90 protein, the motion of interest is the change between its "closed" and "open" conformation. Both conformations correspond to two specific interparticle distances. The interparticle distance consists of the protein itself (8-13 nm[62,63] for the closed-open state, measured between the T285C-T285C modified cystein positions where the protein is attached to the particles), and the two polymer layers on the respective particles. As a default value, I assume a 5 nm polymer layer thickness for a 3000 g/mol PEG polymer.[v] This results in a total interparticle distance of 18-23 nm for the state-of-the-art protein dimer, which I use as a point of reference in this chapter.

The example in Figure II-3a shows the expected particle spectra for the Hsp90 coupled dimer in its "closed" and "open" conformation. The protein motion can be followed in two ways: By tracking the distance-dependent shift of the resonance position $\Delta\lambda_{res}$ or the intensity of the spectrum at a given wavelength. Using the example of intensity change, Figure II-3b shows how the tracking of this motion over time produces a

[v] In the following chapter, I discuss in more detail why this value is not necessarily realistic, and compare it with experimentally measured values. However, for the sake of consistency with previous publications[49,51,52] and for simplicity, I use this assumption of 5 nm for the examples in this chapter.

recorded series of "open" and "closed" states of the protein that can be further analyzed to extract biological information.

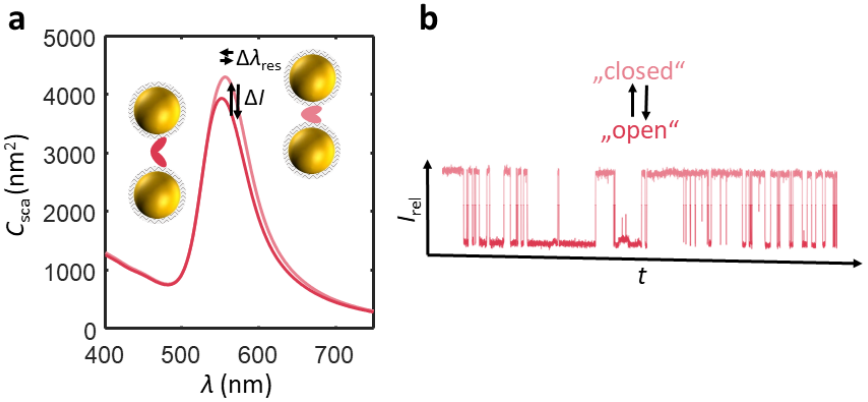

Figure II-3. Protein dynamics revealed by the plasmon coupling effect. (a) A simulated example spectrum of a Hsp90 dimer construct made with two 50 nm particles. The protein displays two conformations: an "open" and "closed" one. The "closed" conformation shrinks the interparticle distance, and the "open" conformation enlarges the distance. The effect is seen in form of a slight red shift of the resonance wavelength and in the change of the scattering intensity at a fixed wavelength. For this figure, I used 50 nm particles, with an interparticle distance of 18-23 nm, corresponding to the assumed state-of-the-art interparticle distances. The details on the simulation are provided in the Appendix A. (b) The switch from one conformation to the other is recorded over time, producing a "time trace" for a single protein, which can be as long as many hours.

The opening and closing occurs randomly in a given number of assembled plasmon rulers, which is why a single-particle visualization technique is necessary to follow and record individual proteins. Experimentally, this is done with the use of a dark field microscope setup, the details for which are provided in the Appendix B. Figure II-4a shows a schematic sketch of the setup. With a small enough interparticle distance and big enough particle size, it is possible to differentiate between single particle and dimer constructs, even with the human eye. An example of this is shown in Figure II-4b for reference, with blue arrows showing the monomer particles and the red arrows pointing at the brighter and bigger dimers.

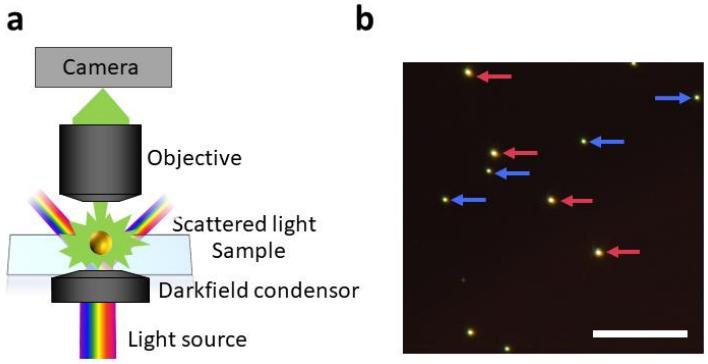

Figure II-4. Single particle measurement. (a) A dark-field microscope is used to excite and collect scattered light of single particles. The setup is made of a light source, a condenser that redirects the light so it hits the sample and bypasses the objective, the sample in a flow chamber and the objective that collects light and transmits it to a camera. More details in the Appendix B. (b) A real color photo of single particles (blue arrows) and dimers (red arrows). Scalebar: 50 µm.

Compared to the difference between a monomer and a dimer, the difference between an "open" and "closed" dimer is much smaller (compare Figure II-2b and Figure II-3a).

Therefore, whether or not the protein's motion can be reliably measured depends on the interparticle distance and the particle size. One way to gain a measure of this is to predict the plasmon coupling strength by simulating the particle dimer spectra. This gives an idea about the general trends related to the ideal distance and size. In the following section, I present the simulation results and use them to evaluate the current Hsp90 plasmon ruler, as well as give recommendations for future iterations of the assembly strategy.

1.4. Prediction and evaluation of plasmon coupling strength with BEM simulations

This part presents the simulations done to predict trends in plasmon coupling between different pairs of particles at specific interparticle distances. For better understanding, I first introduce the simulation toolbox, which is necessary to comprehend the strengths and limits of this method. Further, to compare the particle sizes and signal trends, I explain the quality parameter called "sensitivity". Based on this parameter, I evaluate the state-of-the-art plasmon ruler and I recommend a suitable range for the particle size.

1.4.1. A brief introduction to the MNPBEM tool

The simulations of coupled dimer pairs were done with the MNPBEM (metal nanoparticle boundary element method) toolbox. For the simulations, I give credit to Karl Wander and Dr. Şirin Çeliksoy, who provided invaluable support.

MNPBEM is a toolbox that predicts the scattering cross section C_{sca} (nm^2) of a particle. It is important to note that this is not the experimentally measured spectrum intensity. C_{sca} represents the frequency-dependent scattering strength of a given particle, and it is independent of the light source and exposure time. Subsequently, the frequency dependent scattering intensity, $I_{sca}(\omega)$, is proportional to the scattering cross section and the incident light per area, $\frac{I_0(\omega)}{A}$, according to:

II.2
$$I_{sca}(\omega) = \frac{I_0(\omega)}{A} \cdot C_{sca}(\omega)$$

For this reason, I use the terms cross section and intensity interchangeably, even if strictly speaking I operate with the cross section and not with measured intensity values.

The toolbox calculates the cross section by splitting a particle into elements and solving the Maxwell equations for each element. Specifically, this approach solves the equations only for the boundaries between different dielectric materials, rather than the entire volume.[64] Inputs and details on the assumptions made for the simulation are listed in the Appendix A. The simulation was performed for an experimentally reasonable range of particles between 30 and 60 nm. This is because smaller particles produce a weaker signal that is more difficult to measure experimentally. On the other hand, particles above 60 nm experience attractive forces that are increasingly difficult to balance out with suitable functionalization, while keeping the interparticle distance within a suitable range for a measurable plasmonic coupling.

1.4.2. Sensitivity as a measure of quality

A measure of quality is necessary to discuss trends and compare the suitability of one particle size over another for the measurement of protein motion. One such measure is the sensitivity of a dimer pair at a given interparticle distance. The sensitivity, in this context, is a measure for the signal shift depending on the interparticle distance change. In this work, the sensitivity is given as a numeric derivative of the distance-dependent signal ($\Delta\lambda_{\mathrm{res}}$ or ΔI). This is illustrated in Figure II-5 using the example of a 30 nm particle pair. The stronger the signal at a given distance change, the more sensitive is the assembly towards interparticle distance changes.

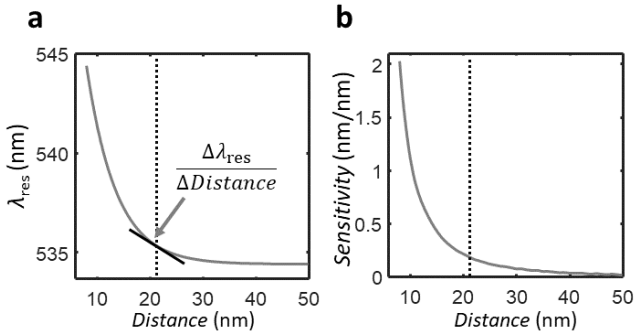

Figure II-5. Sensitivity illustrated with the example of a 30 nm particle pair. (a) Grey line represents the trend of the resonance position dropping with the interparticle distance. The sensitivity is represented by the slope of the signal. As an example, this is drawn in for the marked average interparticle distance of the state-of-the-art dimer (dotted black line). For simplification, individual data points are omitted. (b) Sensitivity plot of (a), determined by numerical derivation. The black dotted line shows the average interparticle distance of the state-of-the-art dimer.

In the following sections, I use the sensitivity to discuss the trends for the two possible detection methods: The resonance wavelength detection and the intensity change detection.

1.4.3. Tracking protein motion via: Resonance wavelength position

As previously mentioned, one way to read out the protein motion from the plasmon coupling of two particles is to track the shift of the coupled dimer's resonance position. Figure II-6 shows the resonance position extracted form the simulated data for particle pairs between 30-60 nm. All particle sizes display a similar exponentially decay. However, the sensitivity (b) shows nuances in the trend.

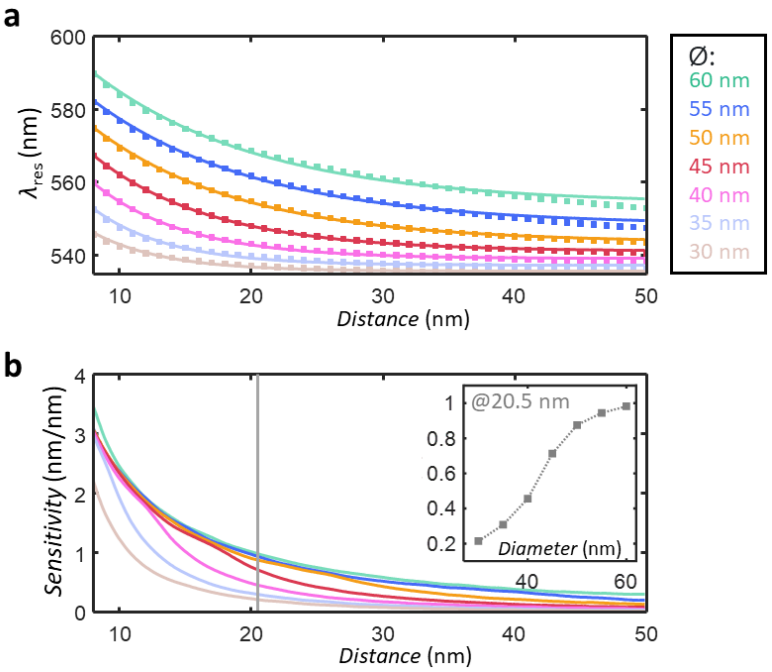

Figure II-6. Predicted resonance wavelength shift. (a) Resonance position is plotted against the interparticle distance for dimer pairs varying from 30 to 60 nm in particle diameter. Individual squares show simulated data, connected by a guide to the eye. Grey lines mark the interparticle distance resulting from the "open" and "closed" protein conformation in the state-of-the-art Hsp90 dimer. (b) Sensitivity determined from data in (a), derived mathematically as a derivative of the λ_{res}. Grey line at 20.5 nm marks the average interparticle distance between the "closed" and "open" conformation of the Hsp90 protein in the state-of-the-art assembly. Inset: Sensitivity value trend at the interparticle distance of 20.5 nm, for particle diameters between 30-60 nm.

Thereby the general trend overserved is that the resonance wavelength shift is higher for bigger particles, but the exact difference depends strongly on the specific interparticle distance. In general, the resulting sensitivity is higher at shorter distances and drops towards larger distances. At the same time, 40-60 nm particles display a comparable sensitivity until a distance of approximately 14 nm. From a distance of about 18 nm, 50-60 nm particles retain a constant, highest sensitivity, and the lower particle diameters drop. For the state-of-the-art dimer, the resulting resonance position shift for particles between 30 nm and 60 nm range between 1.1-4.9 nm, corresponding to the interparticle distance change of 5 nm caused by the protein motion.

In terms of the limit of detection, a difference of 1.1 nm is still sufficiently high for a reliable measurement. However, the tracking of the resonance position requires a recording of the spectrum. If only one dimer were measured, then this would be a viable detection method. However, for multiple simultaneously measured dimers, the time resolution would be too low.

An alternative to this is the tracking of the intensity change at a single wavelength, which will be discussed in the following section.

1.4.4. Tracking protein motion via: Intensity change

The measurement of intensity change at a single wavelength is a fast method, requiring no recording of a spectrum. However, it has certain constraints that need to be minded, such as the choice of detection wavelength. In the following, I will briefly explain the relevance of the detection wavelength choice, before discussing the simulated data results.

To measure the motion at a single wavelength, it is first necessary to find the best position for measurement. This position is called the detection wavelength. Ideally, this is the place where the difference in intensity is the strongest when the interparticle distance changes between the "closed" and "open" protein state. The position of strongest change is where the spectrum displays the highest slope, which is at its full width half maximum (FHWM), to its right side.[65] This position is marked in Figure II-7a with a black line.

In reality, it is not always possible to measure exactly at the FWHM. This is because nanoparticles are polydisperse, and because the choice of light sources is limited by what is currently available on the market. Figure II-7b shows how these two factors can impact the resulting measurement by tracking the resulting sensitivity. This is done for particles between 30-60 nm at the FWHM (the ideal case) and two fixed LEDs of choice. Notably, the LED with the wavelength closest to the resonance position leads to a drop in sensitivity for bigger particles. This is because the spectrum shifts to higher wavelengths relative to the detection wavelength. Ideally, it is best to avoid LEDs that are too close to the resonance peak position to avoid this case.

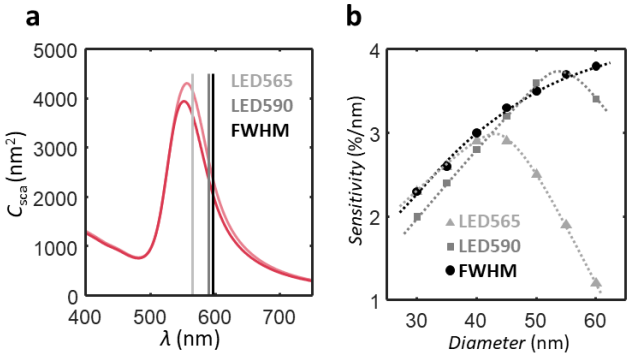

Figure II-7. Sensitivity depends on the detection wavelength. (a) Scattering spectrum of a 50 nm particle for the state-of-the-art Hsp90 dimer, with a distance of 18 nm (red) and 23 nm (pale red). The lines mark potential detection wavelengths. Examples include the detection at the FWHM (full width half maximum), which is purely theoretical, and two experimentally available LEDs. (b) Sensitivity determined at 20.5 nm for particle pairs between 30-60 nm. 20.5 nm is the mean distance of the open and closed state-of-the-art Hsp90 dimer. The sensitivity value drops when the LED position relative to the spectrum is not ideal, e.g. when the LED crosses the resonance position or lies to the left of it. Note that the values for the FWHM are unique for each particle pair. The FWHM is therefore not a fixed value, unlike the LEDs.

To keep the results in this chapter independent of a specific light source, I will use the FWHM as a standard for the display of results.

Figure II-8 shows the simulated scattering cross section for pairs of particles between 30-60 nm.

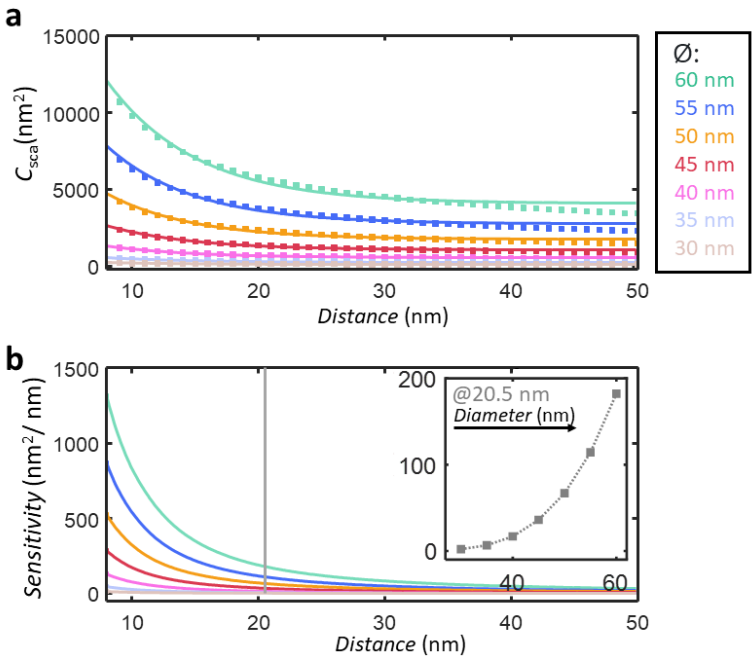

Figure II-8. Predicted intensity change at the FWHM. (a) Scattering cross section plotted against the interparticle distance for dimer pairs varying from 30 to 60 nm in particle diameter. Individual squares show simulated data, connected by a guide to the eye. (b) Sensitivity determined by numerical differentiation from data in (a). Grey line marks the average interparticle distance resulting from the "open" and "closed" protein conformation in the state-of-the-art Hsp90 dimer (20.5 nm). Inset: Sensitivity value trend at the interparticle distance of 20.5 nm, for particle diameters between 30-60 nm.

An alternative way of estimating the signal is to compare the relative intensity change in %, compared to a reference value. This is more practical for estimates, because the scattering cross section values themselves are disconnected from experimental values that include additional input of the light source, exposure etc.

For the display, the interparticle distance of 20 nm was chosen as a point of reference. The respective sensitivity grows with the particle diameter. For the state of-the-art dimer, the expected relative intensity change for particles between 30-60 nm lies in the range between 12-20%.

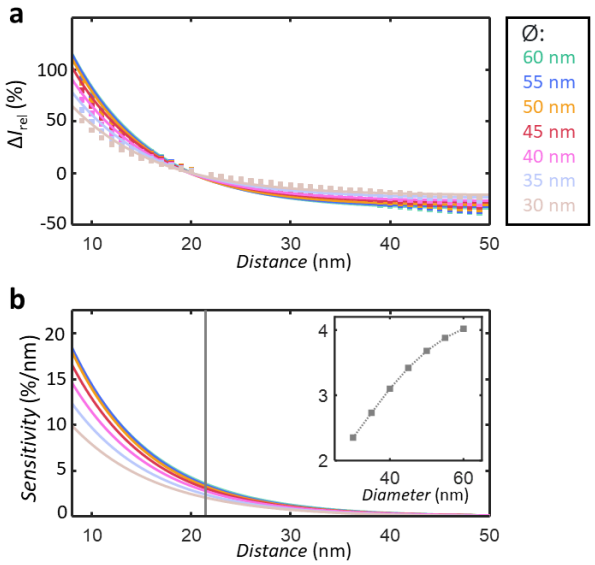

Figure II-9. Relative intensity change. (a) Scattering cross section plotted against the interparticle distance for dimer pairs varying from 30 to 60 nm in particle diameter. Individual squares show simulated data, connected by a guide to the eye. (b) Sensitivity determined by numerical differentiation from data in (a). Grey line marks the average interparticle distance resulting from the "open" and "closed" protein conformation in the state-of-the-art Hsp90 dimer (20.5 nm). Inset: Sensitivity value trend at the interparticle distance of 20.5 nm, for particle diameters between 30-60 nm.

So far, the straightforward conclusion is that bigger particles experience stronger resonance position shifts and relative changes in intensity. Therefore, bigger particles are advantageous in terms of signal strength. Qualitatively, bigger particles are also easier to see by eye, as the scattering cross section scales with the square of the particle volume.[54,55] Typically, 40 nm particles can still be seen comfortably with the eye, with the distinction getting harder for smaller diameters. For this reason, I drop the particles smaller than 40 nm from further investigation in the following chapters.

Following this section's outcome, the biggest possible particles should be employed to assemble the dimer. However, larger particles also lead increasing attractive interparticle forces, which are unwanted in the case of the protein dimer. This issue will be highlighted in the following section.

2. Assembly

The dimer assembly is a critical step, requiring favorable thermodynamic and kinetic conditions. When ideal conditions are met, the assembly proceeds specifically at the designed sites, and as fast as theoretically possible. Key variables in this process are the particle size, their charge, concentration, the solution properties and the resulting interparticle distance of the final assembly.

The following sections will discuss these variables by separating the problem into two major topics: Firstly, by examining the total interaction potential and finding conditions under which the particles experience neither strong attractive nor repulsive forces. And secondly, determining on which time scales the assembly is expected to occur. Lastly, the findings are used to assess the state-of-the-art assembly. In addition, they provide a guide for future alterations of the assembly process, possibly with other chemistries and proteins.

2.1. When is the assembly stable and force-free?

Two criteria must be fulfilled for successful dimer assembly and the measurement of the protein motion. Firstly, the particle solution must be colloidally stable, and secondly, the assembled dimer must be in a "force-free" state. This means that whichever attractive and repulsive forces present between the two particles must balance out. Otherwise, the particles may experience either strong attraction and stick, or repulse each other. Both cases would prevent free protein motion, and must be avoided.

Colloidal stability—the minimum requirement. A dispersion of particles is considered colloidally stable when its potential energy barrier is larger than the kinetic energy of the system.[66] An estimate for this is the comparison of the energy barrier to the thermal energy of the system, $k_B T$.[vi] Colloidal stability is ensured when the repulsive energy barrier is in the orders of magnitude of several $k_B T$.[vii] When no sufficient barrier is present, the particles aggregate non-specifically (meaning: not at the designed chemical sites) after a given amount of time. Therefore, colloidal stability is a necessity for dimer assembly.

The "force-free" state. For this work, this state is defined as the distance between the two particles where the value of the potential equals or is less than the thermal energy $k_B T$ at the interparticle distance corresponding to the assembled dimer. At this distance, the protein motion can be measured undisturbed by excessive attractive or repulsive

[vi] k_B is the Boltzmann constant, and T the temperature of the system. $k_B T$ is defined as the Boltzmann factor, which characterizes the distribution of a system's mean kinetic energy at a given temperature.[67]

[vii] This depends on various factors such as particle size, concentration, the dispersion medium and, of course, the time. For example, Wijenayaka et al.[68] have shown that for a stable 1 week dispersion of 13 nm particles, a barrier of 16 $k_B T$ is required.

forces. This condition is stricter than the previous, because it excludes excessive repulsive interactions.

To find the conditions under which these criteria are met, it is necessary to account for all significant interactions between the two particles.

The DLVO theory. One way to approach this problem is to use the DLVO (Dejarguin-Landau-Vervey-Overbeek) theory.[69,70] This theory describes the interaction between two bodies, which is mainly governed by the attractive van-der-Walls potential and (in the case of same-charge particles) the repulsive electrostatic double-layer potential. For nano-sized particles, this theory gives good approximation up to a size of 1 µm,[71] and is therefore suitable for the plasmon ruler system under investigation in this work. Additionally, I account for the polymer shell around the particles by adding the so-called "entropic repulsion", which is sometimes also called "steric repulsion", in the total sum.

The total sum E_{total} is therefore made of the three components:

$$E_{\mathrm{total}} = E_{\mathrm{VdW}} + E_{\mathrm{Coulomb}} + E_{\mathrm{Entropic}} \tag{II.3}$$

E_{VdW}: Van der Walls potential

E_{Coulomb}: Electroctatic double-layer/Coulomb potential

E_{Entropic}: Entropic/steric repulsion

Below, I will first discuss each component individually, before summarizing the total sum and showing for which particle diameters and interparticle distances the force-free criterium is fulfilled.

2.1.1. Van der Waals interactions

Van der Walls (vdW) interactions are often the cause for aggregation of particles in solution. They are present between any two bodies, and result from charge fluctuations present in any atoms and molecules. For atoms and small molecules, the interaction E_{VdW} at a distance D is described by the following equation:[72]

$$E_{\mathrm{VdW}}(D) = -\frac{C_{\mathrm{VdW}}}{D^6} \tag{II.4}$$

C_{VdW} is a factor characterizing the two objects and the medium between. This interaction is a sum of Keesom (dipole-dipole) and Debye interactions (dipole-induced dipole) as well as London dispersion interactions between transient dipoles.[70,72]

For more complex and big objects such as nanoscale gold particles, the Hamaker integral approximation can be used to estimate the interaction energy. This method sums up vdW interactions between pairs of atoms across the volume of the two particles. The following formula results for a construct of two spherical gold particles:[72,73]

$$E_{\mathrm{VdW}}(D) = -\frac{A}{3}\left[\frac{r^2}{D(4r+D)} + \frac{r^2}{(2r+D)^2} + \frac{1}{2}ln\left(1 - \frac{4r^2}{(2r+D)^2}\right)\right] \tag{II.5}$$

This formula is derived for particles with equal radii r and the edge-to-edge (gold-to-gold) distance D. The Hamaker constant A[viii] for the gold/water/gold system is $2.5 \cdot 10^{-19}$ J.[74] The contribution of the grafted polymer is a complex problem. On one hand, the Hamaker constants of the gold/water/PEG and PEG/water/PEG are smaller ($6.19 \cdot 10^{-20}$ J and $3.7 \cdot 10^{-20}$ J respectively). Their contribution to the attraction is therefore expected to be smaller, too. Nonetheless, their vdW attraction contributes strongly at very small distances of a few nm (see Appendix A). This problem becomes more complex when considering that the polymer only makes up a small fraction compared to the bulk of water between the particles.[73(Sup)] The exact composition of the polymer shell is unknown, so any calculation using tabulated values is only a guess. Since deeper theoretical studies were not within the scope of this work, I rely on a simple model where the vdW potential of the polymer is neglected, while acknowledging the limits of this approximation.

Figure II-10 shows vdW potentials for 40-50-60 nm particles. Here and in all subsequent figures, the energy values are plotted as multiples of k_BT for visual comparison to the thermal energy.

As expected, the vdW interaction increases with bigger particle size. Accordingly, the tendency for undesired self-aggregation grows. Experiments with real particles support this finding: Above the approximate threshold of 60 nm, colloidal stabilization becomes more challenging. In the cases of weak stabilization (e.g. via additionally grafted polymers), particles often self-assemble in a golden layer, suggesting that many particles attach to each other nonspecifically (Figure II-10c). Often times, this self-assembly is reversible by sonication, which means that there is still enough polymer present to ensure a short-time dispersion. Nonetheless, it is undesired because it often occurs on the scale of about 24 hours, which is relevant for the protein measurement.

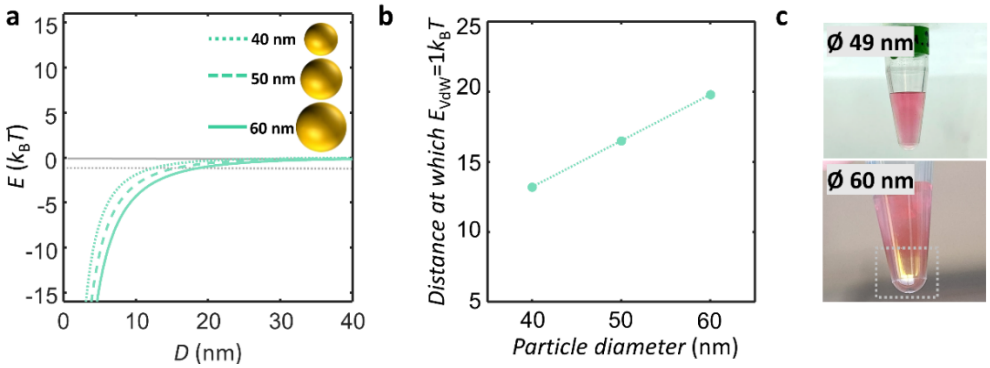

Figure II-10. Van der Waals attraction between particles. (a) VdW attraction calculated for 40-60 nm particles. Dashed grey line represents the thermal energy k_BT. (b) The vdW interaction grows with particle size, represented by distance at which the vdW interaction equals the thermal energy k_BT at 275 K. (c) Photos on the right show particle samples stabilized by 2000 g/mol methoxy-PEG polymer. Whereas smaller 49 nm particles remain well redispersed over days, particles above the approximate threshold of 60 nm often show self-aggregation over the course of 24 h, resulting in an optically discernible gold film.

[viii] The Hamaker constant is derived from the C_{vdW} by accounting for the number density of atoms of the two bodies involved.

As the findings show, the particles experience increasing vdW attraction with growing size, which needs to be compensated by sufficient repulsion.

2.1.2. Coulomb/Electrostatic double-layer interactions

One possible source of repulsion (or attraction in the case of opposite charges) is the electrostatic interaction. Below I will first describe the Coulomb's law, which is the basis for the estimation of the interaction strength. After that I will describe how this law can be applied to the gold particles, and the critical role which the particle charge and medium play in the interaction strength. Lastly, I show how the interaction potential affects the assembly under the specific experimental conditions.

The Coulomb's law. Electrostatic interactions are present between any charged objects. According to Coulomb's law, the potential E_{Coulomb} is proportional to object's charge q. It is also inversely proportional the product of the (constant) permittivity in the vacuum (ε_0) and the experimentally variable dielectric permittivity of medium around the objects (ε) as well as the distance *D* between them.[70]

$$E_{\text{Coulomb}} = \frac{q_1 q_2}{4\pi\varepsilon_0 \varepsilon D} \qquad \text{II.6}$$

Thereby, same-charged objects experience repulsion, and differently charged objects experience attraction. The more charges are present, the stronger is the interaction. Additionally, the medium between the objects can weaken this interaction. In practice, the buffer medium used in the assembly can be approximated as water. Therefore, the critical remaining variable is the particle charge.

The charge of gold particles in a buffer medium. To understand the charge of the gold particle and the medium's effect on it, it is necessary to first look at its source.

The surface of gold particles has been shown to be largely attractive for anions.[75] This is because surface gold atoms have a lower coordination number compared to atoms in bulk. Subsequently, this electrophilic character is stronger for atoms on the edges and corners compared to planar faces.[75,76] Additionally, the bare surface properties of gold are modified by polarization effects caused by the water molecules.[77]

When placed in an aqueous buffer, as is the case in the plasmon ruler assembly, a gold particle experiences the following effects: Its electrophilic surface attracts anions, and the anions attract cations. This is the result of electrostatic attraction, which at the same time is counteracted by entropy and the thermal motion, which drives the charges away. The end result is the formation of an electrostatic double layer around the particle, illustrated in Figure II-11.

The first layer of ions, called the Stern layer, is tightly bound to the gold surface. Beyond that is an ion cloud that is not as tightly bound, but that moves together with the particle. The boundary between the bound and free charges is called the slipping plane. Beyond it follows the diffuse layer of ions. A practical measure of the effective total particle charge is the ζ-potential (read as: Zeta). ζ-potential represents the potential at the slipping plane. It is experimentally measurable and, in the context of electrostatic interactions between particles, more relevant than the "true" surface potential of a particle.[70,78]

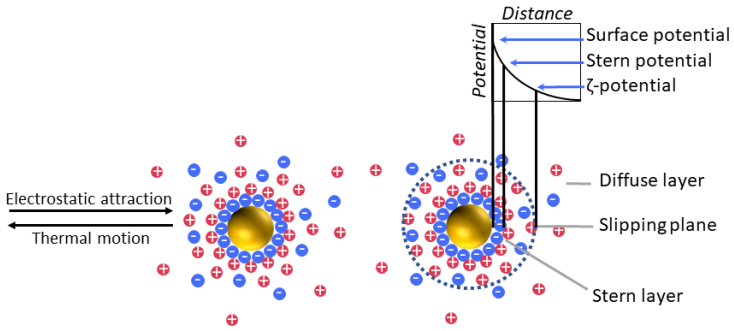

Figure II-11. Gold particles in an electrolyte solution. Left: The sketch shows how ions are attracted to the electrophilic gold surface, and the attraction counteracted by entropy and the thermal motion. Right: As a result, the particle's surface potential is shielded by the electric double layer (also called Stern layer, with its respective Stern potential) and the diffuse charges beyond. The ions become more diffuse with growing distance from the particle surface, but they are still attracted by the particle. The slipping plane marks the boundary where the ions begin to move freely in the diffuse layer. The ζ-potential is measured at this boundary. Inset: shows the location of the respective potentials at the respective distance.

To further complicate this picture, gold particles are not present in the "bare" state in colloidal solutions. Stabilizing molecules are added during the particle synthesis. Most commonly, the molecules are electrostatic agents themselves, such as sodium citrate or cetyltrimethylammonium chloride/bromide (CTAC, CTAB, respectively).[79–81] The aforementioned molecules are physisorbed onto gold, and provide additional charges to stabilize the particles against aggregation. Alternatively, physi- or chemisorbed neutral polymers such as PEG (polyethylene glycol)[82] can both stabilize the particles with steric repulsion, as well as contribute charges if the polymer has charged functional end groups (e.g. COO^-, NH_3^+). In total, the resulting charge of a particle is a sum of all physi- and chemisorbed species on its surface.

One last contributing factor to account for is the buffer's ionic strength. This is important because dissolved ions are attracted to the present charges, resulting in a shielding effect that masks the charges of one particle from those of another. The higher the content of salt, the higher the shielding, and the less effective is the stabilizing effect provided by charged molecules such as sodium citrate or CTAC.

The contribution of the ionic strength can be described using the Debye length, κ^{-1}.[70] The Debye length is defined as the length at which the original electric potential has decayed to 1/e. It is only dependent on the properties of the solution, and is shorter for higher ionic strengths. The Debye length can be calculated using the concentration of the ions, c. For 1:1 salts such as e.g. KCl, the Debye length can be described with the following, simplified formula for a temperature of 25°C:[70(p.312)]

II.7

$$\kappa^{-1} = \left(\frac{\varepsilon_0 \varepsilon_r k_B T}{2\rho_\infty e^2}\right)^{1/2} = 0.304 \cdot \frac{10^{-9}}{\sqrt{c}}\ [\mathrm{m}]$$

ρ_∞: bulk ion concentration

e: elemental charge

The electrostatic interaction between two particles can now be calculated by accounting for its effective potential in the form of ζ-potential, as well as the medium's ionic strength. For two spherical gold particles with a radius r at a distance D, the Coulomb's law is modified to the following expression:

$$E_{\text{Coulomb}}(D) = \left(\frac{r^2}{2r}\right) Ze^{\kappa D}$$

In this simplified expression, the interaction constant Z includes the dielectric properties of the medium as well as the effective particle charge. The detailed calculation, including values for the dielectric constants, is presented in the Appendix A.

II.8 To summarize, three experimentally variable inputs influence the electrostatic potential: the particle size, the ζ-potential and the ionic strength of the aquatic medium. In the following section, I will show how these variables affect the potential, and what it means for the plasmon ruler assembly.

The role of the ionic strength. As a first study, I show how the ionic strength of the buffer affects the electrostatic potential. The particles in a state-of-the-art dimer assembly are same-charge, and therefore experience repulsion. The magnitude of this repulsion however is influenced by the ionic strength of the buffer and the resulting charge shielding. Therefore, this estimation helps predict whether or not the resulting repulsion is strong enough to negatively affect assembly.

To illustrate the trend, I use a 50 nm particle for this example, which represents the average suitable size value. I also fix the ζ-potential to a realistic average value of 10 mV, [ix] while varying the remaining variable within an experimentally reasonable range. Figure II-12 shows how the variation of the ionic strength affects the total potential.

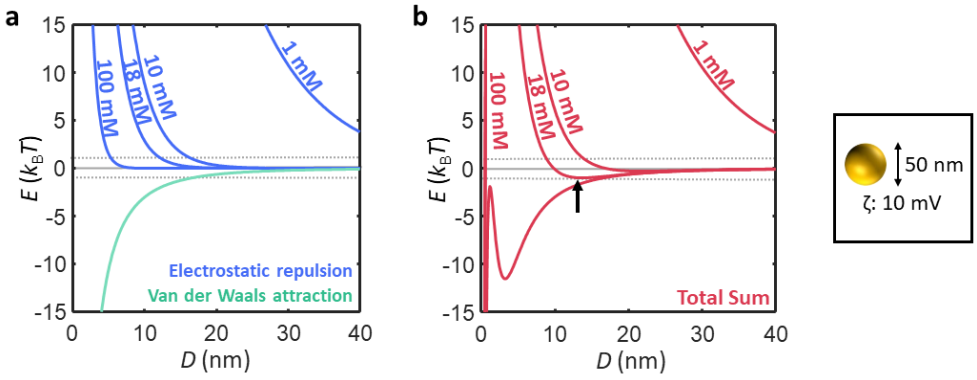

Figure II-12. Influence of the ionic strength on the electrostatic potential. (a) Van der Waals attractive potential (green) for a 50 nm sphere with a hypothetical ζ-potential of 10 mV, and respective electrostatic potentials (blue) resulting from variable ionic strengths. The ionic strengths correspond to solutions of a 1:1 salt NaCl. (b) The total sum of van der Waals attraction and electrostatic repulsion. Black arrow points to the threshold concentration of 18 mM where the potential well is only as deep as the thermal energy.

As seen in (a), the total electrostatic repulsion is gradually dampened with growing salt content in the solution. The total sum of both the vdW and the respective repulsive

[ix] For the end result, it does not matter if the potential has a positive or a negative sign, as either would result in the same repulsion. The value of 10 mV is derived as a good enough approximation for particles used in the typical state-of-the-art dimer assembly.[83]

potentials shows that, starting from a concentration 18 mM, the attractive minimum crosses the thermal energy threshold. This means that concentrations of salt higher than this threshold will increase the interparticle attraction, to a point where the particles aggregate irreversibly if they are able to approach each other closely enough.

In the Hsp90 plasmon ruler experiment, the protein buffer in use is made of 40 mM HEPES (2-[4-(2-Hydroxyethyl)piperazin-1-yl]ethane-1-sulfonic acid), containing 10 mM $MgCl_2$ and either 50 mM or 150 mM KCl, at pH 7.4.[49,51,52] The resulting ionic strength is therefore high enough to shield a particle with any ζ-potential below 10 mV. This means that particles are expected to aggregate, in absence of additional stabilizing agents.

The following section will show that this is equally the case for particles with higher (realistically possible) ζ-potentials as well.

The role of the ζ-potential. In accordance with the Coulomb's law, more charges lead to stronger electrostatic interaction. Therefore, it is reasonable to assume that with a high enough ζ-potential, the particles may experience enough repulsive force, even in a high ionic strength medium.

The ζ-potential can differ depending on the adsorbed and bound species on the gold surface. In particular, highly charged molecules such as DNA or carboxy/amino end groups on PEG can lead to an increase of several tenth of mV. For estimation of this trend, I selected a range of ζ-potentials between 0-100 mV, which covers most common functionalizations.[83]

Most importantly, whether or not the ζ-potential plays a role depends strongly on the ionic strength. For this demonstration, I use the experimentally relevant protein buffers: (1) a HEPES buffer with 50 mM KCl and (2) a HEPES buffer with 150 mM KCl. Both have been used interchangeably in previous work with the Hsp90 protein.[49,51,52]

The lower salt protein buffer (1) results in Figure II-13b show a relatively deep attractive minima (below -10 k_BT) for ζ-potentials between 10-100 mV. Interestingly, both potential wells have a similar depth for both 10 and 100 mV, but the energy barrier to cross over the minimum is higher for the 100 mV. Lower potentials show no repulsion at all.

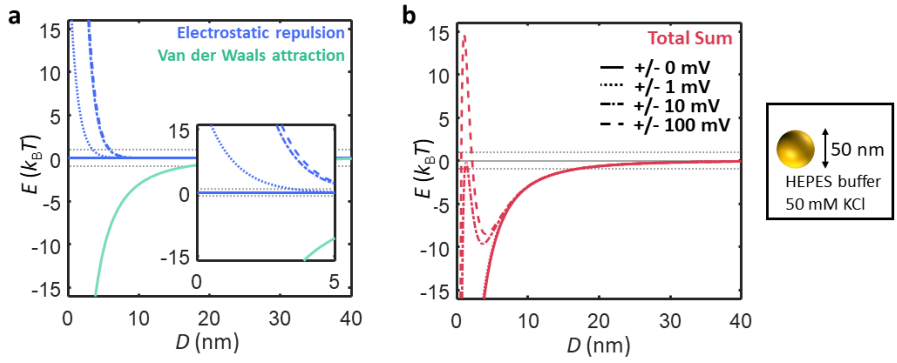

Figure II-13. Influence of the ζ-potential on the electrostatic potential for a buffer containing 50 mM KCl. (a) Electrostatic repulsion calculated for ζ-potentials between 0-100 mV for a 50 nm particle (blue lines). Respective vdW potential is shown in green. (b) The total sum of vdW and electrostatic potentials for each ζ-potential. Between 10-100 mV, the electrostatic repulsion is sufficient to produce a first minimum with a depth a little below -10 k_BT. Inset on the right shows the fixed variables (particle size, 50 nm, and buffer condition).

This situation looks expectedly more dramatic for the high salt buffer (2) (Figure II-14). The repulsion is so weak that the interaction is governed entirely by the vdW attraction for all ζ-potentials.

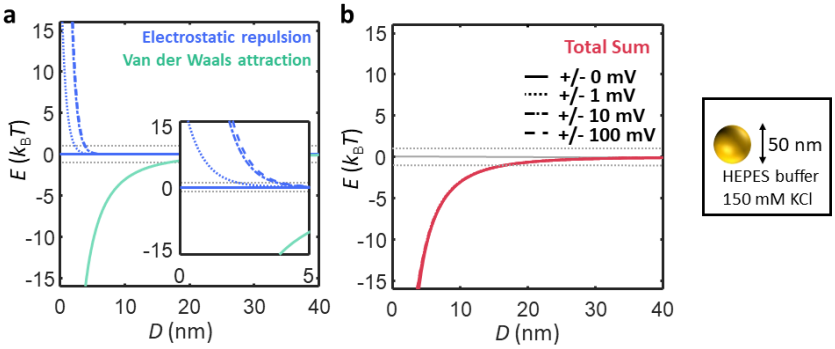

Figure II-14. Influence of the ζ-potential on the electrostatic potential for a buffer containing 150 mM KCl. (a) Electrostatic repulsion calculated for ζ-potentials between 0-100 mV for a 50 nm particle (blue lines). Respective vdW potential is shown in green. (b) The total sum of vdW and electrostatic potentials for each ζ-potential. Compared to the 50 mM KCl buffer, neither ζ-potential leads to a sufficiently high electrostatic repulsion. Inset on the right shows the fixed variables (particle size, 50 nm, and buffer condition).

In summary, the contribution of the ζ-potential is irrelevant to the particle stabilization under the given buffer conditions. Therefore, regardless of the chosen particle charge and functionalization, electrostatic interactions play no role in the particle stabilization.

One remaining variable that is not discussed in greater detail here is the particle size. In the Appendix A, I show that it has a comparatively small effect within the chosen particle range. Additional supplementary information related to the calculations done in this section is also documented in the Appendix.

This section has shown that particles cannot be stabilized against aggregation with electrostatic interactions under the given buffer conditions. This means that the relevant component responsible for colloidal stability is the repulsive steric interaction, which is discussed as follows.

2.1.3. Repulsive steric interaction

Since assembly experiments take place under high salt conditions where electrostatic repulsion is not sufficient to counteract vdW attraction, the particles must be stabilized by steric repulsion. This can be done by using hydrophilic polymers as spacers. A polymer shell still experiences van der Waals attraction, but this is counteracted by more dominant steric repulsion. In the case of the hydrophilic polymer PEG, the repulsion is generated by two factors: the unfavored, reduced entropy when the polymer chains overlap, and the unfavored displacement of water.[70(p.387)]

Zámbó et al.[73] have shown how the repulsion E_{entropic} can be described for two particles at a distance D. Thereby the particles are covered by a polymer layer with a thickness δ, and a respective grafting density in the form of average polymer chain distance s:[70]

$$\frac{E_{\text{Entropic}}}{k_B T} = \frac{16\pi r \delta^2}{35 s^2}\left\{28\left[\left(\frac{2\delta}{D}\right)^{1/4} - 1\right] + \frac{20}{11}\left[1 - \left(\frac{D}{2\delta}\right)^{11/4}\right] + 12\left(\frac{D}{2\delta} - 1\right)\right\} \quad \text{II.9}$$

The grafting density and the polymer length are connected: the denser the layer, the thicker the shell. Depending on density (and chain length), the polymer can take on different conformations when grafted onto a surface. Literature differentiates between two extreme cases: the mushroom conformation (polymer layer thickness is close to the diameter of its coil in solution) and the brush conformation (polymer layer thickness is bigger than the diameter of its coil in solution). Figure II-15 illustrates the two cases, comparing them to the unattached polymer.

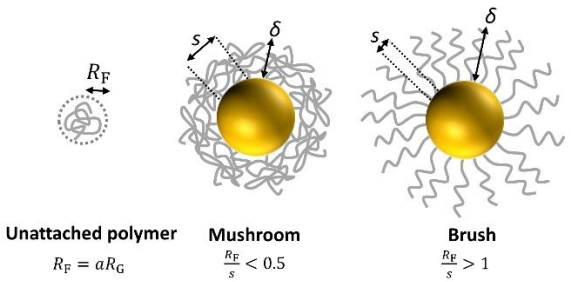

Figure II-15. PEG configurations. Grafted PEG can take on different configurations, with the two limiting cases called mushroom and brush. The cases are defined by comparing the Flory Radius $\boldsymbol{R_F}$ of the free polymer to the distance between the grafted polymer attachment points s, which roughly describes the lateral space that a single polymer occupies on the particle. $\boldsymbol{R_F}$ describes the radius of a polymer coil in a given solvent. It is related to the gyration radius $\boldsymbol{R_G}$ of a coil in equilibrium (experiencing neither attractive or repulsive forces) through a factor *a*, which accounts for interactions resulting from the respective solvent.[70] Mushroom configurations correspond to a grafted polymer size similar to that of the free polymer, and brush configurations take up much less lateral space, becoming elongated instead.[84]

Consequently, a polymer of *N* repeating units has a range of lengths it can take in a grafted state. For estimation, I illustrate this range for PEG polymers commonly used with gold particles, from 2000 to 5000 g/mol (corresponding to about 45-113 repeating units). Figure II-16 shows the smallest polymer thickness using the Flory estimation, corresponding to the mushroom conformation. This assumes that the polymer length equals approximately the diameter of the polymer in solution. Theoretically, the upper boundary is represented by the polymer in a fully stretched line. This would be an extreme

and unlikely case of a brush conformation. Many sources reference the work of Jeppesen et al.[85] when estimating brush conformation. Their fully stretched polymer length was determined by pulling apart polymer covered mica beads, and observing at which point the linking bond (biotin-streptavidin) was broken. This is, of course, also an overestimate of a realistic, unperturbed polymer on a particle. Nonetheless, it is a useful point of reference. I have therefore used their data as an estimate for the polymer conformation, as shown in Figure II-16.

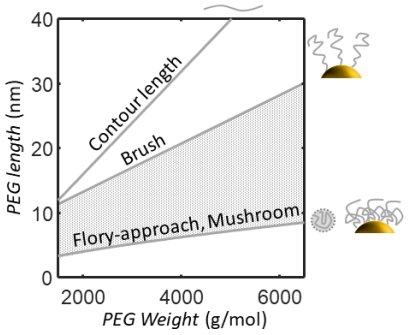

Figure II-16. Grafted polymer lengths. A polymer can take on different configurations when grafted onto a surface. For the lower boundary, the Flory approach can be used to estimate the grafted polymer thickness. The upper boundary corresponds to a more stretched and denser brush conformation. Both are smaller than the contour length of the polymer chain. Data used from Jeppesen et al.[85]

The grey shaded area in Figure II-16 marks the possible resulting polymer lengths between a mushroom and a brush conformation. For a 2000 g/mol PEG used in the state-of-the-art plasmon ruler protocol, this could mean that the polymer length is anywhere between 4-12 nm. This affects the interparticle distance, and the expected intensity change between the "open" and "closed" protein conformations.

To showcase the significance of this range, I use formula 0 for the example case of two 50 nm particles. For the polymer, I use experimental data for the grafting density and polymer length from the study of Li et al.[86] The study used a 2000 g/mol PEG polymer, with the polymer layer thickness ranging across 3.9-5.7-9.4 nm, with respective grafting densities: 0.18-0.54-2.47 chains/nm^2. (Note how the polymer length falls well into the grey shaded area of expected polymer thickness in Figure II-16.)

The resulting total interaction potential (Figure II-17) shows that only the thickest polymer layer (9.4 nm) produces an attractive potential well in the range of k_BT. Smaller grafting densities and subsequently less thick polymer layers lead to deeper potential wells, and therefore to stronger attraction and aggregation.

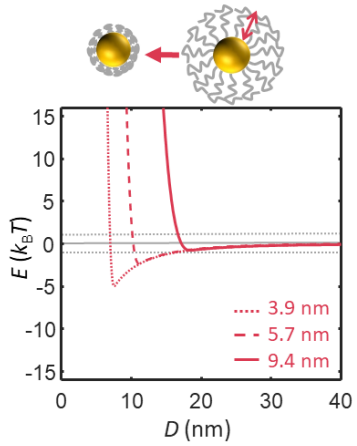

Figure II-17. Role of polymer length and grafting density. The total interaction potential is displayed for two gold spheres of 50 nm, in HEPES buffer (150 mM KCl), and presuming for simplicity that the particles are not charged (ζ= 0 mV). Polymer density and length data was taken from Li et al.; grafting density was converted to average PEG-to-PEG distance. Grey dotted lines indicate the thermal energy k_BT. A potential well deeper than k_BT appears when the polymer thickness shrinks due to lower grafting density.

For steric stabilization of a particle sample, this means that it is not enough to simply pick a polymer with a suitable weight. The final polymer layer thickness must be tested, e.g. using dynamic light scattering (DLS). This ensures that the polymer layer produces a sufficiently large interparticle distance, where the particle attraction drops below k_BT, as illustrated in the sketch in Figure II-18a.

The table in Figure II-18 summarizes the minimal polymer layer thickness necessary to stabilize particle sizes 40-50-60 nm. This minimal thickness provides the distance where the attractive interaction is at the threshold of the thermal energy. This thickness can be achieved either by choosing longer polymer chains or tuning the grafted polymer conformation. As seen for smaller PEG chains in the weight range of 2000 g/mol (Figure II-18c), the brush conformation is necessary for good stabilization. Bigger chains above ~5000 g/mol are expected to give a sufficiently thick layer even in mushroom conformation.

a

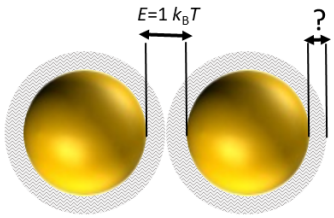

b

Ø (nm)	D (nm), E=1 k_BT	Polymer thickness (nm)
40	13.3	6.7
50	16.6	8.3
60	20.0	10.0

c

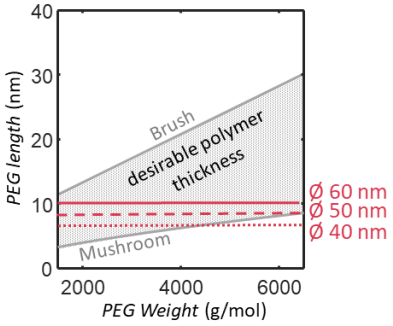

Figure II-18. Minimal polymer layer thickness. (a) Sketch of two particles covered by a polymer. The polymer layer must provide a sufficient minimal distance between the particles, so that the total interaction energy potential is equal to or less than the thermal energy, k_BT. (b) Table summarizing the minimal interparticle distance at at which the criterium in (a) is fulfilled, for the respective particle size. The interparticle distance corresponds to a certain polymer thickness, that can be achieved either by choosing a longer polymer or tuning the polymer conformation. (c) Graph from Figure II-16, showing polymer thickness depending on polymer weight of the linear PEG. The figure shows the possible lengths the grafted polymer can achieve through a tuning of conformation. The drawn in lines shows the minimal necessary polymer layer thickness for the stability criterium in (a) for different particle sizes. Shaded grey area above these lines shows the desirable achievable polymer layer thickness.

2.1.4. Conclusion: The polymer layer is a critical factor

The theoretical calculations have shown that attractive vdW interaction exceeds the thermal energy threshold starting from an interparticle distance between 13-20 nm. Under the experimental buffer conditions, this attraction cannot be balanced out by electrostatic repulsion. This leaves the steric stabilization as the main significant interaction that prevents unwanted aggregation and attractive forces.

In this context, the findings show that the 2000 g/mol and 3000 g/mol PEG mixtures used in the state-of-the-art assembly protocol can potentially ensure good particle stability. However, this depends on the polymer conformation. High fractions of the shorter PEG in a mushroom conformation are problematic, and are not expected to sufficiently stabilize particles above the threshold of 40 nm. Practically, this means that the polymer thickness needs to be controlled, and measures taken to ensure the preference of the brush conformation.

If the polymer layer is sufficiently thick, then the particles should be stable against aggregation, and the protein motion should not be hindered by attractive or repulsive interactions. This condition is also favorable for assembly speed: In the absence of repulsive interactions, the dimer construct assembly should be controlled by diffusion and reactivity only. The next section follows up on this topic.

2.2. Kinetics: Assembly under diffusion-controlled conditions

Knowledge of the expected assembly time is important when working with fragile molecules. Proteins in particular require careful handling in a temperature-controlled environment, which is not necessarily optimal for diffusion-controlled assembly. As such, assembly conditions influencing the reaction time have to strike a balance between the protein's needs and conditions for the fastest possible reaction.

The following subsections will introduce the theory behind diffusion-controlled assembly and summarize on which timescales the assembly is expected to happen.

2.2.1. Estimating diffusion-controlled assembly—the theory

If the particles are tailored to be force-free, the reaction between particles can be described as diffusion-controlled. This means that in order for assembly to happen, two reaction partners need to diffuse into each other's proximity, and that no repulsive barrier is present to hinder approach.

Diffusion time is a parameter that can be used to measure and predict assembly time. The Stokes-Einstein equation relates the diffusion coefficient D_H to the temperature T, the solution's viscosity η and the Boltzmann constant k_B as well as the particle radius R_H.

$$D_H = \frac{k_B T}{6\pi\eta R_H} \qquad \text{II.10}$$

The temperature is a fixed variable, as it cannot be varied to prevent protein damage. Thus, the only variable of interest is the particle radius. Figure II-19 shows how the diffusion coefficient drops when comparing a <1 nm molecule to a much bigger 60 nm particle. Table 1 summarizes the diffusion data used in this figure.

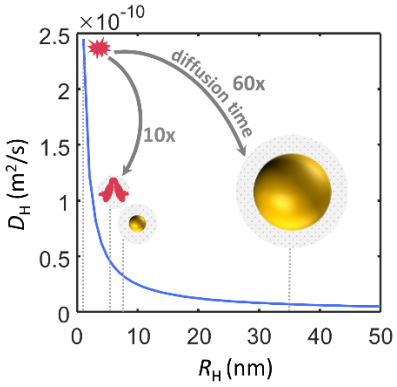

Figure II-19. Diffusion coefficient. Calculated diffusion coefficients for various nanoscale objects such as a small dye molecule (radius <1nm), the Hsp90 protein (marked in red), a small 5 nm gold particle and a bigger 60 nm gold particle covered by a 4.5 nm PEG layer (marked in grey shade).

Table 1. Diffusion coefficients of example molecules. Values for rhodamine 6G and Hsp90 are taken from literature, and those for the particles were estimated using the Stokes-Einstein equation.

Species	R_H (nm)	D_H (m²/s)
Rhodamine 6G (fluorescent dye)	0.6 [87]	$4.2 \cdot 10^{-10}$
Hsp90	5.2 [88]	$2.8 \cdot 10^{-11}$
5 nm particle + 3000 g/mol PEG	7.5	$3.3 \cdot 10^{-11}$
60 nm particle + 3000 g/mol PEG	35	$7.0 \cdot 10^{-12}$

Another variable necessary for estimation of the reaction time is the particle concentration, which determines the average distance from reaction partner A to partner B. Assuming, for simplicity, that reaction partner A is fixed and the other diffuses towards it on the shortest path possible, we can calculate the reaction time t_{direct} using the average interparticle distance and the diffusion coefficient.

$$t_{direct} \approx \frac{{r_0}^2}{6D_H} \qquad \text{II.11}$$

r_0 is the average interparticle edge-to-edge distance. For calculation of r_0 from a given concentration, I refer to the Appendix A. Figure II-20a shows how reaction time drops with growing concentration and shorter average distance between the reaction partners. In addition, graphic b shows an exemplary calculation of t_{direct} for a small diffusing molecule as well as for a large 60 nm particle, with a diffusion time of 14 ms and 860 s each.

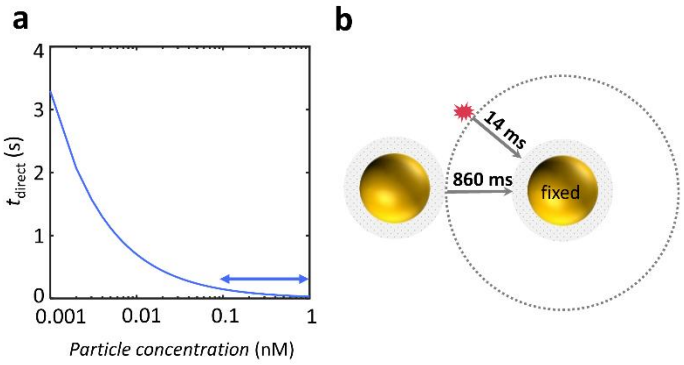

Figure II-20. Concentration and reaction time. (a) Relationship between the particle concentration and reaction time. Arrow marks experimentally relevant concentration range[x] for nanoscale particles. (b) An example calculation for diffusion time at a specific concentration for a small molecule (rhodamine, D_H=$4.2 \cdot 10^{-10}$ m²/s) and a big particle (60 nm+PEG layer, D_H=$7.1 \cdot 10^{-12}$ m²/s) at a concentration of 0.1 nM, with an average interparticle distance of 2480 nm.

[x] Higher concentrations are impractical because they are difficult to achieve, especially for bigger particles. The resulting dispersion is also viscous, so the Stokes-Einstein equation would have to be modified to account for that. On the other hand, smaller concentrations are also impractical due to longer average diffusion time to the next best partner.

This rough estimation suggests that even bigger particles should assemble within a time frame that barely makes a difference when compared to the total handling time within a laboratory experiment performed by human hand. Therefore, neither repulsive forces nor diffusion should prose a problem for the assembly. This leaves two significant parameters to consider, which is the fact that a particle realistically does not diffuse following a straight line, and also does not necessarily react upon first hit.

2.2.2. Reactivity is a critical and unknown factor

As already remarked by my predecessor Bastian Flietel[89], the abovementioned calculation is merely the ideal case. In reality, however, the reacting partners may have varying reactivity as well as not take the straightest path towards each other. Grebenkov et al.[90] have accounted for these factors in the derived equation 7 below, which I reproduce here to complete the theory.

$$t_{\mathrm{mean}} = \frac{(r_{\mathrm{center}} - r_{\mathrm{particle}})(2R^3 - r_{\mathrm{center}} r_{\mathrm{particle}}(r_{\mathrm{center}} + r_{\mathrm{particle}}))}{6 D_{\mathrm{H}} r_0 r_{\mathrm{particle}}} + \frac{R^3 - {r_{\mathrm{particle}}}^3}{3\kappa {r_{\mathrm{particle}}}^3}$$

II.12

r_{center} is the distance of the diffusing species to its target, and r_{particle} is the radius of the target. *R* represents the radius of volume around the target. Additionally, there is the reactivity factor κ, with $\kappa = \infty$ corresponding to perfect reactivity. Bastian Flietel[89] calculated that, depending on reactivity and for a particle concentration of 0.1 nM, the assembly could happen anywhere below 10 min.

However, the question remains why no significant assembly has been seen for the state-of-the-art system, suggesting that the realistic reactivity is far below the optimal value.

3. Theoretical essentials—the summary

The findings show that the choice of the ideal assembly parameters is complex. To start, the parameters (particle size, interparticle distance, respective attractive forces and diffusion coefficients) are interconnected. Plasmon theory says that bigger particles are better in terms of signal for the Hsp90 assembled dimer. The maximal particle size however is limited by the growing attractive vdW interactions, which have to be balanced by means of steric repulsion. The bigger the particle size, the thicker is the necessary polymer distance and the bigger the final interparticle distance. This lowers the plasmonic coupling and sensitivity of the dimer. Under the present conditions and with the state-of-the-art PEG polymers in use, a safe particle size is in the range of 50 nm, but not above 60 nm. Special attention should also be given to the polymer grafting process, so that the polymer thickness is sufficient to stabilize the particles.

In terms of assembly speed, theory suggests that the process of one reaction partner meeting the other is fast enough to happen on a scale of minutes. This is still the case even for bigger particles with a diffusion coefficient some orders of magnitude slower than that of small molecules.

While the overall model of straight diffusion to the reaction partner is admittedly simplified compared to reality, it nonetheless shows that the biggest challenge is the

reactivity of both partners. There should be enough linking groups in a close proximity over the particle's surface, so that one hit leads to a guaranteed reaction with one of these groups. In addition, the specific chemistry between the linkers can also facilitate reaction through its intrinsic reactivity, which is independent of the density of linkers on the particle's surface.

In total, theory says that the dimer assembly should happen and fluctuation signal is measurable under the given conditions. However, experiments show a low assembly yield and in many cases no fluctuation signal indicative of the protein motion, as explained in the introduction (chapter 1). This suggests a discrepancy between reality and assumptions made in the theory.

The following two chapters lean onto this discussion, exploring the experimental findings regarding interparticle distance, particle stability as well as reactivity in relation to the dimer assembly.

III. PARTICLE FUNCTIONALIZATION – QUANTITY AND QUALITY

The chemical functionalization of a particle is the basis for a successful assembly. It is a step that is essential for colloidal stability, sufficient reactivity and a force-free protein measurement. Further, the thickness of the functionalization layer determines the interparticle distance. Previous works in our group[51,52] have relied on theoretical assumptions to determine variables such as the polymer layer thickness, its state when grafted onto the particle and its quality. However, because there is a discrepancy between theoretically predicted assembly success and experimental failure, further investigation is necessary.

To fill in the gaps in the current knowledge, I investigated the particle functionalization and present the results in this chapter.

1. Functionalization is complex

To get an understanding of potential pitfalls and complications, I studied the state-of-the-art protocol and compared it to the current knowledge in literature.

The state-of-the-art dimer assembly relies on previously established functionalization protocols.[49,51,52] As explained in the introduction, the basis of the functionalization is a linear PEG polymer with a thiol group to attach to the gold surface and second reactive end group on the opposite end for further modification and assembly. This type of functionalization is common and well established in literature, especially in the context of drug delivery and nanocarriers.[86,91]

At the same time, there exist several hints that this reaction is not as straightforward as generally assumed. This is reflected in works that characterize and address certain challenges, such as improving the polymer grafting density for better stealth properties in vivo applications.[92] Such works involve tuning of the grafting density, most often to force the polymer into the preferred brush conformation for a thicker layer.[86,93] The general summary of these works is that a simple ligand exchange reaction does not necessarily yield a polymer layer that is sufficiently thick for colloidal stability and immune against adsorption of biological components, e.g. proteins. The latter in particular is a critical factor for the protein dimer assembly, since nonspecific adsorption of the Hsp90 protein would lead to a lack of correct assembly or improper assembly.

Another complication step is added when a second polymer end group is introduced. For example, Toro-Mendoza et al.[94] suspect a variation in grafting density depending on the end group, and observe differences in stealth properties between methoxy, amino and

carboxy-PEG. Additionally, Retout et al.[95] found a complication when functionalizing particles with PEG mixtures, in a similar way that is done in the Hsp90 dimer assembly. They discovered that the ratios of a PEG mixture in solution are not necessarily the same as on the grafted particle, a fact that has implications for particle reactivity in assembly.

As seen in this short overview, the seemingly straight-forward functionalization is complicated. This is a problem for the dimer assembly, where the interparticle distance and the particle quality must fulfill strict criteria to ensure sufficient plasmon coupling strength, colloidal stability and a force-free protein movement. Therefore, there is a need for deeper understanding of the particle functionalization in the plasmon ruler dimer assembly.

2. The "unknows" to be addressed in this chapter

Together with the abovementioned complications, it is clear that the quality and quantity of the particle functionalization should not be taken for granted. To systematically address this challenge, I single out two categories that I refer to as the "unknowns" and sketch in Figure III-1. The first category relates to the "bulk" properties of the polymer (a). Important keywords are the polymer layer thickness as well as the polymer conformation. This is critical for the interparticle distance, the colloidal stability and the minimization of nonspecific interactions, e.g. with other particles or the protein. The second topic is related to the second reactive end group (b), and how it affects stability and reactivity of a particle. This is a critical part, since reactivity of the dimer assembly is one of the areas in need of improvement.

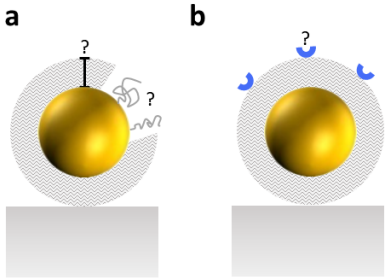

Figure III-1. "Unknowns" of the particle functionalization. (a) Sketch of a particle with a polymer layer. The unknown factors are the polymer conformation and the resulting layer thickness. (b) Sketch of a particle depicting reactive end groups (blue symbols). The exact location of end groups and their availability for reaction is not known.

I begin this chapter with part (a), quantifying the polymer shell and determining its quality as well as potential for improvement. After that, I investigate the complications related to part (b), and conclude this work package with a comparison to the theory presented in chapter 2, highlighting the importance of particle functionalization in the assembly process.

3. Quantifying the "bulk" properties of the polymer layer

The polymer layer on top of a particle is a critical component, serving to stabilize the particle against nonspecific aggregation, and determining the future interparticle dimer distance. As observed in the previous chapter, the polymer is a flexible construct, and straightforward grafting may or may not result in a shell with desirable thickness and density. Here, I investigate its bulk properties and compare them to theoretical predictions.

3.1. A recap of the functionalization strategy

In the state-of-the-art plasmon ruler experiment, particles are coated with a PEG polymer. This linear polymer carries a thiol group to covalently attach to the gold surface, and another group that is either non reactive (methoxy group) or reactive (e.g. amino group for maleimide chemistry). The polymer is grafted using a ligand exchange reaction, as illustrated in Figure III-2. This means that the polymer is added to a particle dispersion already covered by a stabilizer molecule, e.g. cetyltrimethylammonium chloride (CTAC, Figure III-2a). Since this molecule is not covalently attached, there is a constant exchange of molecules until all CTAC is replaced by covalently attached PEG (b).

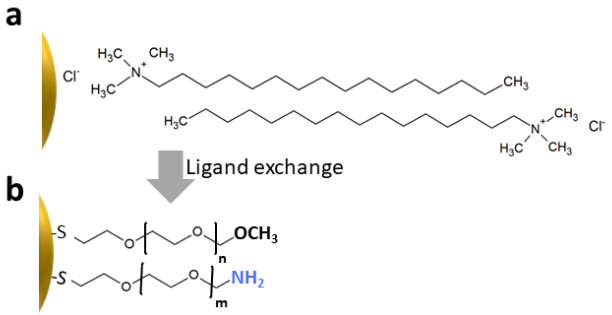

Figure III-2. PEGylation. (a) Sketch of a gold particle surface and the attached CTAC molecule. The particle is electrostatically stabilized CTAC. (b) Sketch of a gold particle surface with a thiol-attached PEG. The example shows two end groups in use in the state-of-the-art protocol: methoxy and amino. In a ligand-exchange reaction, the CTAC is gradually replaced by covalently attached PEG.

At first glance, this is a seemingly straightforward reaction. However, a complication arises from the polymer's flexible nature, which may yield any result between a mushroom and brush conformation. This leaves a lot of freedom between either a low or high density polymer shell.

As mentioned previously, this step cannot be left to uncertainty. This is because particles covered by a low density polymer tend to interact nonspecifically with each other and/or other molecules such as proteins.[86,93] This may lead to unwanted nonspecifically formed aggregates, or proteins that are not properly attached via the intended linking sites. Both would lower the potential protein dimer yield. Additionally, a lack of knowledge about the polymer thickness leads to uncertainty in the interparticle distance, which is critical for plasmon coupling strength and the measured signal.

To address the issues, I assessed the state-of-the-art functionalization protocol and modified it for better grafting density and polymer thickness. I quantified the improved

thickness with DLS measurements, and estimated its stability in protein buffer conditions. The improved protocol was later used for all subsequent assembly experiments.

3.2. The functionalization protocol can be further improved

To understand the current state of the functionalization protocol, I conducted a study to see if the polymer layer stability, thickness and grafting density can be further tuned.

3.2.1. How to tune the grafted polymer conformation: An overview

The problem of tuning the polymer conformation—and thus its thickness and density—on any given surface is known in literature. There are several ways, e.g. switching from the grafting-to process to the grafting-from,[96] which yield a higher density by avoiding the steric repulsion between the polymer chains. This particular process however requires a development of an entirely new protocol, where the polymerization happens on the particle itself. A simpler possibility is tuning the ratio between particle and polymer,[86] with a higher ratio yielding higher density. However, this only yields an improvement to a certain degree. This is because the most common solvent used in functionalization protocols is water, where the polymer coil is present in an expanded state (Figure III-3a). The amount of grafted polymer coils onto a particle is therefore limited by its size. This method is already in use in the state-of-the-art functionalization protocol.

An alternative method for improving the density and thickness is the grafting in the presence of a θ-solvent[97[p.384]] (refer also to the previous chapter). For this, literature often suggests the use of either sodium or potassium salts.[98,99] This method works by reducing the initial free polymer coil size by making solvent conditions less favorable.[xi] As a result, more polymer chains can be packed onto the same area (Figure III-3b), resulting in a higher density. When solvent conditions improve, the polymer can further extend and form a layer that is both thicker and denser.

[xi] Presence of salt is expected to modify the hydrogen bonding and rearrangement of water molecules, which disfavors the expanded polymer coil. At sufficiently high concentrations, the effect may become so strong that polymer "salts out". A keyword associated with this is the so-called "cloud point" of PEG.[97,98]

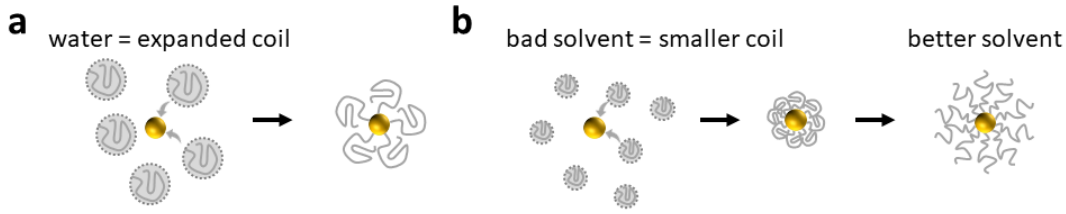

Figure III-3. Functionalization with PEG under different solvent conditions. (a) Sketch shows a gold particle and polymer coils in water. In a good solvent, the free polymer coil is well expanded, and the resulting packing on the particle is relatively low. (b) Sketch of a gold particle and polymer coils in a bad solvent. Compared to case shown in (a), the polymer can be packed tighter onto the particle when it is present as a smaller coil. After this initial packing step, the polymer can expand again, e.g. when the solvent conditions improve (sketch on the right).

In principle, this effect is expected similarly with both for sodium and potassium salts. However, since potassium ions are known to form crown ethers with PEG,[100] they may possibly favor a tighter polymer structuring and therefore a higher grafting density. Its effect on an already grafted polymer on a particle has also been previously shown in this group.[61]

Because of its simplicity and tunability, I chose this strategy for the functionalization.

3.2.2. The new vs old functionalization strategy

To find whether the state-of-the-art protocol can be improved by a modification with θ-solvent conditions, I conducted a study by performing the ligand exchange step with a growing fraction of salt and observing the trend. The method I chose for observation is the gel electrophoresis, because it can show trends such as a relative change of hydrodynamic radius. This is the case when a grafted polymer switches from a mushroom to a brush conformation and vice versa, and is seen in a change in mobility.[xii]

For the particle polymer composition, I used the polymer mixture with 10% amino-PEG (3000 g/mol) and 90% methoxy-PEG (2000 g/mol), respectively.[xiii] Additionally, to ensure that the observed mobility change is attributed to the hydrodynamic radius and not a charge effect, I repeated the experiment with particles functionalized with the neutral methoxy-PEG polymer only.

Figure III-4a shows one example of a salt titration to graft 10% amino-PEG functionalized particles, with the experiment being repeated at least three times for reproduction. Additional gel data is documented in the Appendix B. The figure shows a representative titration with Na_2SO_4, with a trend for slower mobility with higher salt concentrations. This suggests an increase in size and/or increase in positive charge

[xii] The Appendix B documents how changes in particle size and charge affect particle mobility in a gel electrophoresis experiment.

[xiii] The state-of-the-art protocol uses between 3-15% amino-PEG. 10% were chosen as a reasonable reference point.

coming from extra added, protonated amino groups. Both indicate that more polymer is packed onto the particle.

The control experiment with the neutral methoxy-PEG polymer shows that the increase of the particle size is a real contributing factor (Figure III-4b): Particles functionalized in the presence of higher salt content show a slower mobility, suggesting a bigger size. This means that salt promotes a change in polymer conformation.

Notably, a plateau in mobility change is reached at a salt concentration starting from 5-7 mM. This suggests that at this concentration, the polymer is maximally packed onto the particle.

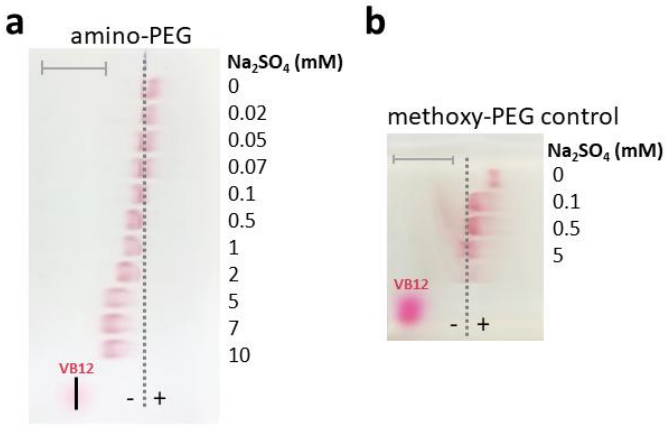

Figure III-4. The effect of salt on PEGylation. (a) Example of the effect of Na_2SO_4 on the gel mobilities of amino-particles, ranging from a concentration of salt from 0-10 mM in the resulting PEG solution. The PEGylation protocol is listed in the Appendix B. The reference, vitamin B12, is marked with a black line. It is used as a control and correction for the electroosmotic flow. Its mobility is used to correct the mobility data displayed in c). Scalebar: 1 cm. (b) Control experiment using uncharged methoxy-PEG. The sample mobility is reduced with increasing salt content, meaning that the increase in size is a real contributing factor.

The study shows that the salt functionalization successfully tunes the polymer conformation and thickness. This means that it can be used in the future to further improve the particle.

3.2.3. The cation type makes no difference in functionalization result

To find the optimal salt type and probe for the aforementioned sodium vs potassium effect, I conducted additional studies by switching Na_2SO_4 for K_2SO_4. Interestingly, the exchange of the cation for potassium does not appear to have an addional effect: Particle samples PEGylated with sodium or potassium show a similar trend in reduced mobility that stays within the margin of error (Figure III-5). This means that the effect of crown ether formation is either small or not meaningful enough to make a difference.

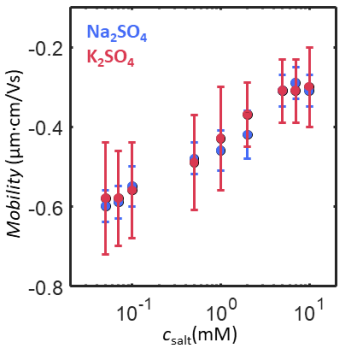

Figure III-5. Comparison of the effect of cation type on the mobilities of particles. Figure shows mobilities for amino-particles with increasing salt content during the PEGylation step, corrected for the electroosmotic flow. Data points with error bars are derived from three independently repeated experiments. Red dots represent K_2SO_4, blue dots Na_2SO_4.

I performed additional studies with chloride and phosphate salts, and saw a similar trend between potassium and sodium: The only difference is that a higher concentration is needed to reach the mobility plateau, which is natural because the sulfate salts have double the number of cations compared to the chlorides. Phosphate salts follow this trend, as is exemplarily shown in the Appendix B.

In conclusion, the observed lowered gel mobilities of particle samples suggest an increase in polymer density and thickness. This is a positive outcome, because a thicker density means better colloidal stability and less unspecific interactions. For the final functionalization protocol, I continued to work with K_2SO_4 salts at a final concentration 10x higher than the observed onset of a mobility plateau in the experiment illustrated in Figure III-4. The Appendix B documents the improved functionalization procedure.

In the next step, I moved on to further characterization of the polymer shell quality, and how it behaves under the experimental conditions of the plasmon ruler experiment.

3.3. Protein buffer affects low grafting densities, but not high grafting densities

One important aspect of the polymer shell is its behavior under experimental buffer conditions, as compared to the solution where the functionalization and characterization process takes place. This gives hints of the stability of the polymer shell thickness, and indirectly of the grafting density.

Because the gel electrophoresis method has limits in terms of ionic strength of the running buffer, I used dynamic scattering experiment (DLS) on selected samples to understand how differences in the functionalization affects the polymer shell stability under different ionic strength conditions.

As representative samples, I chose the amino-PEG functionalized particles introduced in the previous section. The first particle sample is made following the original protocol, I call it the "low grafted" sample. The second sample is made with the new protocol involving addition of salt and showing a slower mobility in the gel experiment, I call it the

"high grafted" sample. To test the polymer shell, I observe the value of their hydrodynamic radius under different ionic conditions: (1) water represents the state where the polymer is expected to be well solved and the polymer shell to be the thickest. (2) PBS represents the high ionic strength conditions where the assembly takes place. [xiv] A low grafted sample may show a collapse of the shell thickness due to the worse solvent conditions for the polymer. The last test is in (3) TBE 0.5x buffer, [xv] which is the agarose running gel buffer. The latter serves as a reference to make sure that conclusions drawn from the gel electrophoresis can be safely transferred to experimental conditions during assembly.

Figure III-6 summarizes the obtained data. Firstly, the DLS measurement confirms the trend seen in the gel electrophoresis: The particles size trend is bigger for the high grafted sample compared to the low grafted one across all solvents (a-b). Between the solvents, the low grafted sample shows a more dramatic trend. The particle size drops when the solvent is exchanged from water to either PBS or TBE, to a comparable extent. On the other hand, the high grafted sample shows no such behavior. This implies that the high grafted sample shell is more robust, presumably because the polymer is packed more densely and—for steric reasons—is more resistant to collapse (c).

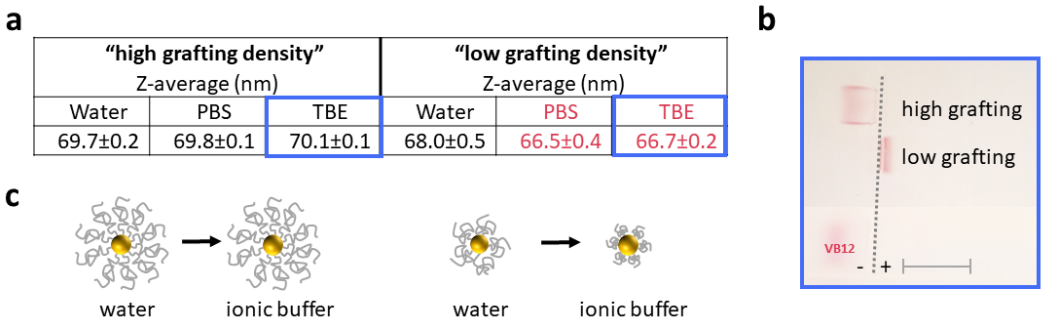

Figure III-6. Hydrodynamic diameter trend for low and high density grafted PEG particles in different solvents. (a) Z-average values from the DLS experiment in different solvents. The solvents have less effect on the hydrodynamic diameter when the grafting density is high. (b) Gel electrophoresis of the samples in (a). The "high grafted" sample shows a smaller mobility as compared to the "low grafted one". Scalebar: 1 cm. (c) Sketch suggesting an explanation for the effect of the solvent on the measured particle size.

To conclude, the study shows that the new protocol indeed leads to a thicker polymer shell. This polymer shell is also more resistant to collapse under experimental buffer conditions, presumably due to a switch to the favorable brush conformation. As shown in the previous chapter, this is expected to lead to better particle stability and less unwanted, nonspecific interactions. However, for a full understanding and certainty about

[xiv] 40 mM HEPES buffer: pH 6.7-7.4, 50-150 mM KCl, 10 mM Mg_2Cl, and 10 mM PBS buffer: pH 6.7-7.4, 137 mM NaCl, 2.7 mM KCl.

[xv] TBE 0.5x buffer, with a final concentration of of 0.05 M tris-borate and 1 mM EDTA.

the polymer conformation, a more thorough quantification of the shell thickness is necessary.

3.4. Polymer thickness is bigger than previously assumed, and depends on specific end groups

The theory chapter has provided a measure of minimal polymer layer thickness to ensure colloidal stability and a force-free state. Quantification of the polymer thickness ensures that this condition is fulfilled. At the same time, the knowledge about the thickness is necessary to gauge the final interparticle distance, which is critical for prediction of the plasmonic coupling strength. The polymer must not be too thin to prevent aggregation, and not too thick to avoid losing signal strength. Therefore, it is critical to quantify the polymer shell thickness under the final experimental conditions.

An additional complication arises when the polymer layer is made of a mixture of PEGs with different weights, such as shown in the previous section. Ideally, it is necessary to understand the contribution of each weight type, since the shorter PEG (2000 g/mol) is the main component responsible for particle stabilization, and the longer PEG (3000 g/mol) carries the linker groups for protein attachment. The longer polymer is therefore relevant for the interparticle distance.

To find out the connection between the specific polymer weight and the resulting expected polymer thickness, I conducted a DLS study with particles grafted with only one type of polymer. The polymers I tested were the two types used in the state-of-the-at dimer assembly (2000 g/mol methoxy-PEG and 3000 g/mol amino-PEG), as well as one longer methoxy-PEG (5000 g/mol) to have one more point of reference. 40 nm sized particles were used, with grafting details provided in the Appendix B.

Figure III-7 summarizes the results collected from three independently prepared particle samples. For reference and to gauge the polymer conformation, the theoretical estimations (for a mushroom vs brush conformation) are shown. Additionally, reference lines show the desired minimal polymer length to stabilize commonly used 40-60 nm sized particles. This allows comparison of the measured size with the desired values for optimal stability introduced in the theory.

The results show that the smaller 2000 g/mol methoxy-PEG is present in a mushroom conformation rather than brush, while the longer 5000 g/mol PEG is somewhere in between (Figure III-7a). Most importantly, the shorter PEG used in the state-of-the-art protocol falls below the desirable polymer thickness for sufficient colloidal stability, even for the smaller 40 nm particle size.

a

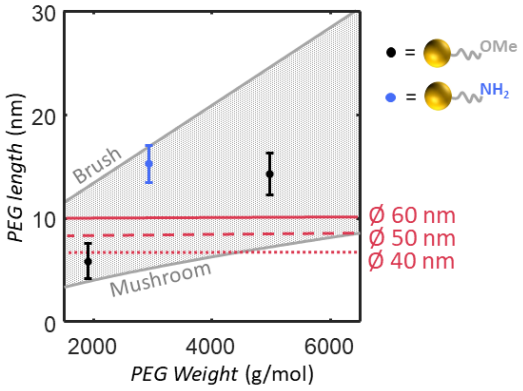

b

Polymer+Weight (g/mol)	Particle/TEM diameter (nm)	Polymer layer thickness *(nm)*
methoxy-PEG 2000	40.2±2.9	5.9±1.6
amino-PEG 3000		15.3±1.8
methoxy-PEG 5000		14.3±2.0

Figure III-7. DLS measurement results of different polymer grafted particles. (a) Measured brush length as compared to the theoretical expectation. Black points indicate 2000/5000 g/mol methoxy-PEG, blue dot is 3000 g/mol amino-PEG. The results are a mean of three repeatedly prepared samples. Red lines represent the minimal polymer layer thickness for 40-60 nm sized particles to ensure colloidal stability (see Theory 2.1.3.). (b) Data from (a), including the TEM (transmission electron microscopy) diameter of the particles, as well as the polymer thickness calculated from the Z-average values. The measurements were performed in the buffer used for Hsp90 measurements (HEPES 7.4, 50 mM KCl).

Another curious finding is that the 3000 g/mol amino-PEG sample (thickness: 15.3 nm) is bigger than the heavier 5000 g/mol methoxy-PEG (thickness: 14.3 nm). This may be due to charge repulsion of its NH_3^+ groups forcing a stretch.[xvi]

This small study has several important outcomes: Firstly, the polymer thickness is bigger than assumed when only using the Flory-radius for estimation. This is important, because this increases the average expected interparticle distance of the dimer, and weakens the measured intensity change between the "closed" and "open" state. Assuming the 15 nm polymer layer thickness for the amino-PEG, this would mean a dramatic increase of the interparticle distance by 20 nm (accounting for the difference to the previously assumed 5 nm)[51,52]. If that is true, then even in the case of a successfully assembled dimer, the dimerization would not be discernible by eye and the signal strength weak, depending on particle size.

This finding however must be treated with caution, because the polymer may shrink after further chemical modification. However, even if the 3000 g/mol PEG follows the trend of the uncharged methoxy-PEG, it would still be a few nanometers above the assumed 5 nm length.

[xvi] Considering the ionic strength of the buffer, the resulting Debye length is in the range of 1 nm. Therefore, there should be considerable charge shielding. Assuming an average grafting density of 0.5 chains/nm² and taking the measured polymer thickness of 15 nm into consideration, this means that 1 NH_3^+ group is present per roughly 6 nm². This is the case if all charged groups are present in the outer polymer shell, at a distance of 15 nm from the particle. The resulting average charged group distance would then be in the range of roughly 2.5 nm. Considering this, the resulting longer polymer length may be the result of charged end groups.

The second finding is that the main polymer component, the 2000 g/mol methoxy-PEG (making up 85-90% of the polymer shell in the state-of-the-art protocol), is present in a mushroom configuration. This implies less stabilization. And in fact, the guide in Figure III-7a shows that this length falls below the stability criterium, even for the smaller 40 nm particle. This implies that, even if the assembly succeeds, such particles could eventually stick together, if they happen to meet through random motion (e.g. Figure III-8). This would be a problematic outcome, since it would interrupt protein motion, as shown in the sketch by the two particles sticking.

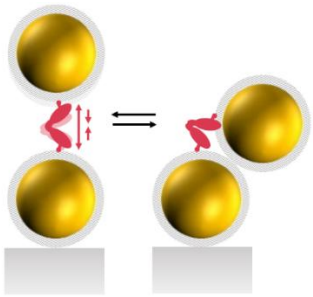

Figure III-8. Sketch of a fluctuating Hsp90 dimer. The dimer fluctuates until it may get stuck and, depending on the strength of the attraction, remain this way or unstick with thermal fluctuation.

In conclusion, this little study has revealed a discrepancy between the previous, theoretically expected polymer thicknesses and the actual measured values. With the current knowledge, the state-of-the-art assembly has a larger interparticle distance than anticipated. At the same time, the neutral and shorter methoxy-PEG polymer is not sufficiently thick for optimal stabilization. These two factors show that PEG brings insecurity into the assembly and measurement process due to the variety in conformation. Because both the colloidal stability and the interparticle distances are critical for the dimer measurement, it is not sufficient to work with theoretical estimations only when using PEG.

However, the role of the polymer is yet more complex, as the second part of this chapter will show.

4. Particle reactivity and the critical role of the second end group

As discussed in the theory, the reactivity of a particle is another critical factor for successful assembly. This is controlled by the number of available reactive sites in the polymer layer on the particle. To understand the role of the second end group modification in the assembly process, I studied literature and used my previous master thesis results as a basis for a deeper study, which I present here.

4.1. The role of the polymer's second end group

As stated previously, the polymer presents a complication. In the context of the reactive second end group, the issue lies in its random coil nature. This means that the end group

is not necessarily present in the outer shell where the assembly reaction can take place. Rather, literature shows that the distribution peak of the end group is located inside the polymer layer, in the example of a linear polystyrene.[101] This is further supported by experimental findings for PEG functionalized particles, e.g. Xia et al.[102] reporting that only 50% of amino polymer end groups were available for reaction in a given particle batch. Therefore, given the polymer's nature, it will be less reactive than theoretically possible, if only accounting for the total number of reactive end groups.

4.2. The state of the dimer assembly protocol

The state-of-the-art dimer assembly protocol works with a linear PEG polymer that is functionalized with a thiol to react with the gold and an amino group for assembly. It employs 3-15% amino-PEG, filling the rest with the neutral methoxy-PEG, as schematically represented in Figure III-9a. The original reason for this approach was to avoid a case where too many proteins attach to the first particle, because only one protein is wanted in between.[51] However, the reported low yields suggest that this approach is too extreme, and lowers the assembly efficiency. This is of no surprise, given the implications Xia et al.'s work.[102]

Taking into account the hints from the work of Xia et al., it is natural to assume that the assembly yield would instantly improve if the amino-functionalization of the second particle is maximized to 100%, as illustrated by comparison of the two cases in Figure III-9. However, as I show below, this leads to complications.

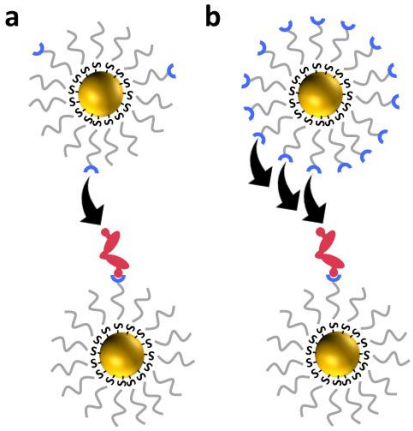

Figure III-9. Sketch of two viable assembly strategies. (a) Sketch represents the state-of-the-art assembly, with up to 15% amino groups present for the reaction. (b) Sketch showing one possible way to increase the assembly efficiency: The content of the amino groups on the second particle is increased to 100%, while the first particle is kept at a low amino-content fraction to avoid linking the two particles via multiple sites.

4.3. Tuning the reactivity of a particle reveals previously unaccounted for challenges

In my master thesis[103] I had attempted the strategy presented in Figure III-9, receiving unexpected results which are shown in Figure III-10. Part (a) and (b) show the state-of-the-art dimer assembly in the flow chamber: The assembly begins with deposition of the first particle (a), followed by the addition of the second (b). At first glance, even the naked

eye can see that the deposited first particles have changed color from green to orange, suggesting plasmon coupling between the particles. This effect happens almost instantaneously upon flushing in the second particle, which at first suggests good reactivity and assembly success.

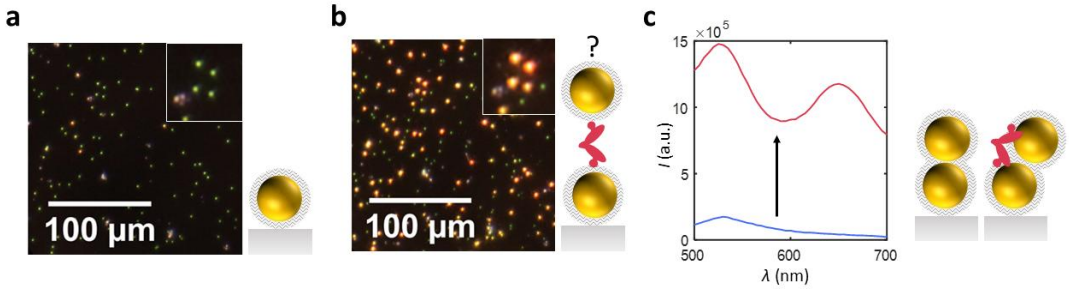

Figure III-10. Hsp90 dimer state-of-the-art assembly with 100% amino-PEG particles. (a) Real-color photograph of the first particle deposited in the flow chamber. (b) The second particle is added. Assembly happens in places where previously green particles appear orange. The inset shows a zoom in, with four previously green dots turning bright orange. (c) An example of a single-particle spectrum (blue), and the resulting spectrum after addition of the second particle (red). The unexpected, double peak may be a hint of two very closely stuck particles, as suggested by the sketch. From this result alone, it is not possible to tell whether the protein carries any role in this process, and whether the linking happened with and without the protein (see sketch). Data obtained during the time of the master thesis.[103]

However, the evaluation of dimer spectra shows unexpected double peaks instead of the simple red-shift and increase in scattering intensity (c). The observed color change is stronger and the assembly spectrum different from what is expected for the Hsp90 assembled dimer (see previous chapter). The double peak spectrum is also more indicative of an assembly with an interparticle gap close to the sub-nanometer range.[xvii] Although particle aggregates could also explain an unexpectedly strong scattering signal, this possibility is excluded. This is because of the color change occurring upon addition of a single particle, when observed by eye.

The master thesis ended with this observation, producing questions about the unexpected result. Theoretically, the sub-nanometer touching of the particles should have been prevented by the polymer layer and the protein in between. But this is not the case, as observed in the experiment. Oddly, this observation also does not fit with the DLS data on polymer thickness of an amino-PEG particle (see theory, part 1.3), which should have been big enough to prevent "touching" between the particles.

This discrepancy served as motivation for a deeper investigation of the connection between particle stability and specific reactive end groups. This serves for better understanding of the functionalization issues and helps to strategically improve the assembly protocol.

[xvii] The sub-nanometer range interparticle distance leads to additional effects aside from the plasmon coupling, where the plasmon can no longer be described with the model of classical electromagnetic theory.[104] The second, strongly red-shifted plasmon resonance of the formed construct belongs to the plasmon coupling peak. The peak in the monomer range could be attributed to the charge transfer plasmon mode.[104–106]

4.4. Amino-functionalized PEG particles—a record of issues

Observations show that amino-PEG functionalized particles show instability during characterization and handling in experimental buffers, which all appear to correlate with the amino group content. Here I list the total sum of observed issues, which I discuss and address in detail in the following section.

First of all, amino-PEG particles show aggregation when characterized by the means of gel electrophoresis. This instability increases with the growing amino-PEG fraction, as seen in the gradual broadening of the bands and eventual aggregation (Figure III-11a). This effect is also stronger when the grafting takes place in a solution containing salt, showing a total aggregation with as low as 20% of amino groups on the particles, as compared to the onset at 50% without the salt (Figure III-11b). Incidentally, 10% appears to be the turning point where the particles still show a clear band and therefore good stability. This corresponds with the previously used particles for the assembly.

Further, Figure III-11b shows a similar, time-dependent aggregation behavior with growing amino group content in the HEPES buffer. In part, this issue was also observed in the master thesis, where the 100% amino-PEG particles showed only short-term colloidal stability.

Lastly, particles containing amino-PEG are seen to stick to plastic walls during the cleaning process by means of centrifugation. This is noticeable as a colored film that sticks to the walls (Figure III-11c), as compared to a pellet forming at the bottom of the vessel.

At first glance, the sum of these findings does not appear logical. This is because amino groups are expected to add to stabilization through charge repulsion, and not the other way around.

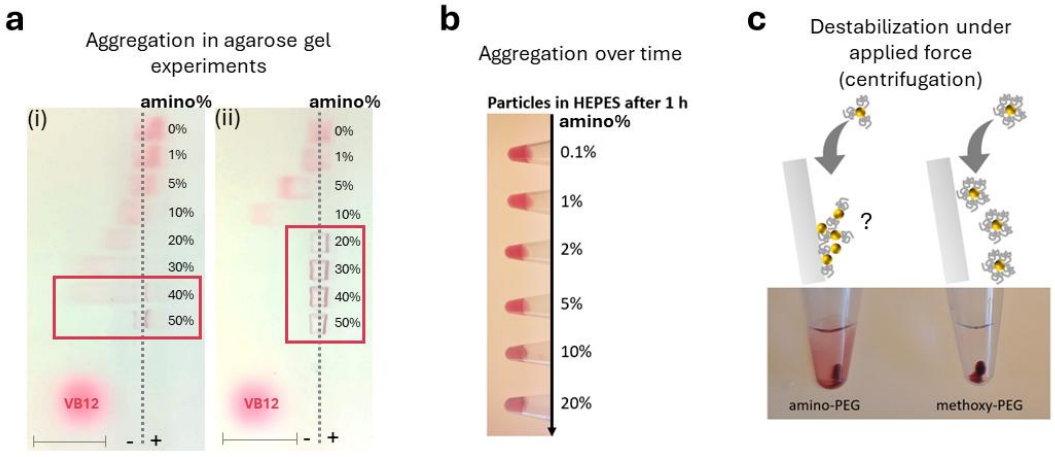

Figure III-11. Signs of issues with colloidal stability. (a) Gel electrophoresis image of particles with increasing amino-PEG content. The onset of total aggregation is marked with red squares. This effect is observed sooner in particle batches PEGylated with higher grafting density (ii) (PEGylated with salt), compared to low grafted particle batches (i). Scalebar: 1 cm. (b) Photographs of particles with different amino-PEG content after incubation in the buffer for 1 h, with noticeable discoloration starting after 10% amino-PEG. (10 mM HEPES buffer: pH 7.4, 150 mM KCl, 10 mM $MgCl_2$). (c) Photograph of amino-PEG functionalized particles forming "films" on walls of plastic tubes during centrifugation. On the right: A comparison of a methoxy-PEG particle batch forming a defined pellet.

As an additional point of observation, amino-PEG particles appear to show unspecific binding to the Hsp90 protein. This is seen by the difference in gel mobilities between amino-PEG particles and the same batch pre-incubated with the protein (Figure III-12). Interestingly, this does not occur with other two proteins chosen for control and comparison, bovine serum albumin (BSA) and streptavidin (SA). BSA and SA are both proteins involved in the assembly of the dimer. BSA can be used for better passivation of the flow cell, and SA is used to fix the first particle to a pre-passivated glass. Therefore, they too must not stick nonspecifically to particles.

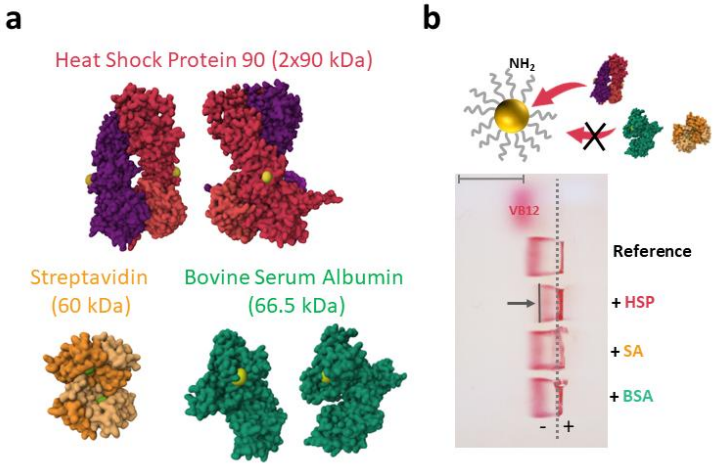

Figure III-12. Protein stickiness study. (a) Crystal structures of Hsp90 (PDB: 2CG9)[62], Streptavidin (PDB: 1MK5)[107] and BSA (PDB: 4F5S)[108]. Hsp90 is made up of two identical monomers, colored in red and violet, with the modified T285C cysteins marked with exaggerated, yellow spheres. Streptavidin is depicted with two biotins (green), marking the binding pockets. BSA is shown with the free cystein marked by an exaggerated, yellow sphere. (b) Of the three proteins, only Hsp90 shows nonspecific attachment to the particle sample. This sample wanders towards the anode (+). This is because Hsp90 carries a net negative charge in the TBE buffer (pH=8.5), given its isoelectric point of 4.9. The same effect would occur if the other proteins showed nonspecific attachment.

This finding is curious due to a relatively similar isoelectric point of Hsp90 (pI=4.9)[109] and BSA (pI=4.7-5)[110], suggesting the issue may not lie in attractive electrostatic interactions. Generally speaking, protein stickiness is a complex matter, where thermodynamics and the arrangement of water play an important role.[111] In this context, polymers such as PEG are usually applied to prevent non-specific attachment, with higher protein uptake hinting at issues with the polymer shell.[93] In this case, the observed interaction suggests that the PEG does not fulfill its intended passivating role in the case of the Hps90 protein. This is problematic, because a wrongly attached protein cannot form a proper construct.

The combined issues illustrate a deeper need for understanding the problem to ensure better control over the particle functionalization, which I address in the following sections.

4.5. Addressing the effect of amino-PEG functionalization on particle stability

In this section, I address the observed issues one by one, splitting them into results caused by artifacts of the measurement method, and real causes arising from interparticle interactions.

4.5.1. Aggregation in gel electrophoresis: An artifact of the measurement method

As previously shown, amino-PEG functionalized particles show band smearing and aggregation in gel pockets with growing amino group content. To understand if this problem arises from the sample or the method itself, a closer look at the agarose gel composition is necessary.

Commercial agarose contains impurities, one of which is agaropectin.[112,113] This impurity come with negatively charged sulfate groups, and freely movable counter ions.[xviii] This means that the agarose gel backbone has a negative charge, as sketched in Figure III-13a.

On the other hand, amino-PEG particles carry a pH-dependant positive charge. With an approximate pka of 9-11 for the amino-PEG,[94,102] the particle is expected to have still almost 100% protonated amino-groups in the buffer typically used in an agarose gel experiment (tris-borate-EDTA, TBE 0.5x, pH≈8.3-8.5). It can therefore happen that an attractive charge effect interferes with the particle movement. The more amino groups a particle carries, the more positive charge it has, and the higher may be the interaction with the gel matrix. This may cause band smearing and aggregation, as shown in the gel image in (b).

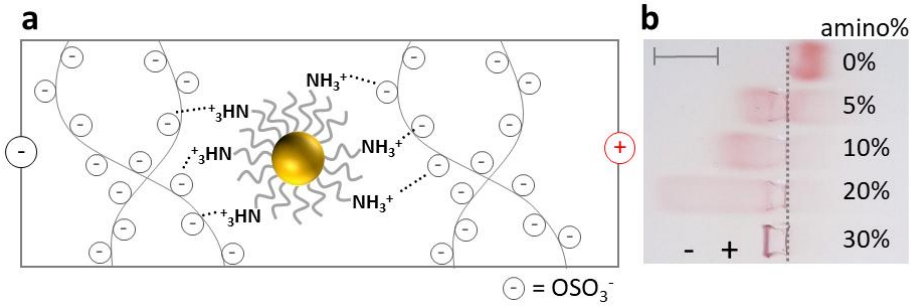

Figure III-13. Sketch of the possible origin of smearing in gel electrophoresis. (a) The sketch represents the gel chamber, with a positive and negative electrode. The agarose backbone carries fixed, negative sulfate ions. For better overview, positive counterions are omitted from this sketch. The positively charged amino-PEG particle may interact with this backbone, thus causing retardation of the particles in the gel matrix. (b). A gel image of amino-PEG particles with amino content between 0-30%. Particle bands show increasing smearing, and the 30% sample aggregates entirely in the pocket. Scalebar: 1 cm.

[xviii] Consequently, these counter ions are the origin of the observed electroosmotic flow, which is tracked by the vitamin B12 reference.

To test whether the protonation and positive charge truly causes an interference with the negative gel matrix, I tuned the pH of the standard electrophoresis buffer (TBE, 0.5x, pH≈8.3-8.6). For the pka of amino-PEG, I used a literature value as a reference (pka=9.6).[94] With this pka, the pH of the buffer needs to be at least around pH=11 to ensure that most amino groups are not protonated and therefore uncharged, as shown in the calculated protonation curve in Figure III-14a.

To account for the previously observed difference between functionalization strategies (grafting in water or in the presence of salt), I prepared two samples, each grafted only with amino-PEG. Both samples were then tested against the two running buffers, TBE pH=8.6 and pH=11. The result is shown in Figure III-14b: As previously observed, particles stop running in the TBE pH=8.6 buffer when reaching the gel pocket wall. On the other hand, particle samples show mobility in the more basic buffer, and the mobility slows in accordance with previously seen trend between the functionalization strategies (water vs in the presence of salt).

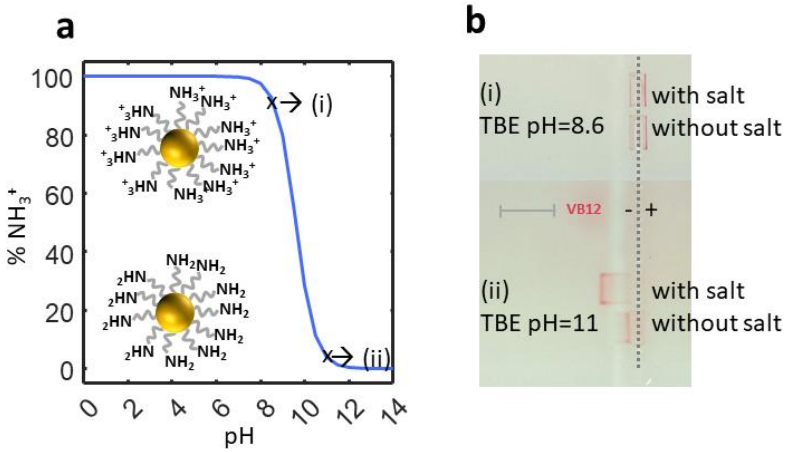

Figure III-14. Protonation of amino-PEG and its effect on gel mobility. (a) Protonation curve drawn for an amino-PEG with an assumed pka of 9.6.[94] Marked points show the protonation state at the given pH of the experimental TBE running buffer. (b, i) Particle samples PEGylated with and without salt (corresponding each to a high and low grafting density), shown to aggregate in the TBE pH=8.6 running buffer. (b, ii) The same particle samples run as thin, homogeneous bands in the higher pH buffer. The bands show the same trend previously observed for high and low grafted particles: the high grafted particle (with salt) shows a slower mobility, and therefore a bigger hydrodynamic size.

This simple test illustrates an easily underestimated problem of charge interactions that cause a misinterpretation of results. However, despite the particle samples now showing homogeneous and thin bands in the gel electrophoresis experiment, the aggregation behavior over time outside the gel matrix cannot be explained with this effect alone.

4.5.2. Instability in water vs buffer is complex

Further inspection is necessary to explain aggregation behavior outside the gel matrix. Previous experience with amino-PEG particles shows aggregation behavior in the experimental buffer. Considering the measured polymer layer thickness (ca. 15 nm), as well as the presence of charged amino groups, this finding is surprising. Even in a high ionic buffer, a layer of 15 nm is expected to sterically stabilize the particles, as predicted by theory.

However, the results suggest that the samples do not behave as expected. To get a better understanding and make conclusions where the real particle sample differs from the theoretical prediction, I conducted a study by (1) theoretically considering the expected particle behavior in a solution with a low and high ionic strength, and (2) comparing it to the experiment by observing its aggregation behavior. For the low ionic strength, I assumed ultrapure water. For the high ionic strength, I considered the PBS buffer.

As shown in the theory section, the ionic strength tunes the significance of electrostatic repulsion in colloidal stabilization. In theory, amino-PEG particles are expected to be well stabilized by electrostatic repulsion in ultrapure water due a significantly high Debye length of ≈1 µm (Figure III-15a). On the other hand, a solvent with higher ionic strength (e.g. PBS, with a Debye length of <1nm), is expected to shield the charges. As shown in the theory, the electrostatic stabilization becomes insignificant in this case. This can mean two things for a sample: first, if the polymer grafting density is high enough, then the entropic stabilization is sufficient to counteract the vdW attraction (b, i). In the case of a low grafting density, the polymer could collapse (as previously observed in the theory chapter, 1.2), and the sample aggregates. With the improved PEGylation protocol, the case (b, i) is expected to happen. Such a sample therefore should not aggregate neither in water nor in a buffer with high ionic strength.

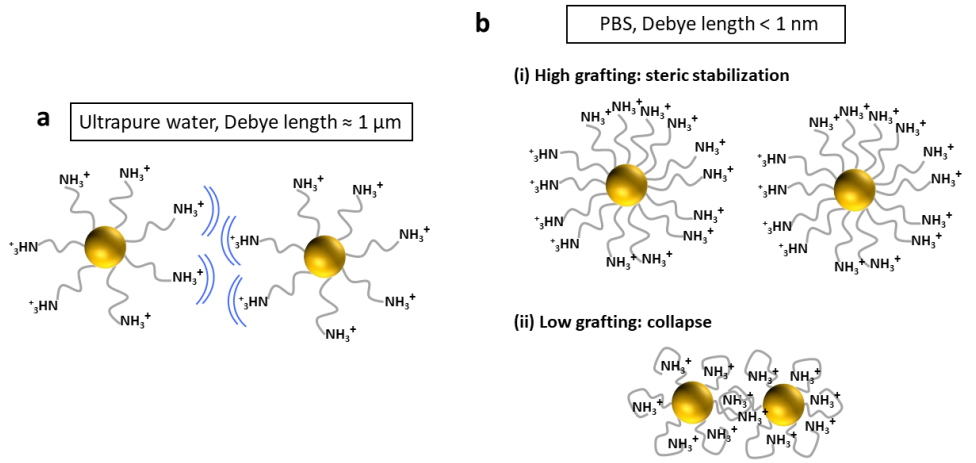

Figure III-15. Expected behavior of amino-PEG particles under different solvent conditions. (a) In ultrapure water, the particles should be sufficiently stabilized with electrostatic repulsion, arising from charged amino groups. (b) In the PBS buffer (pH=7.4), the Debye length shrinks to below 1 nm, and the charges are screened. High grafted particles (i) with a sufficiently thick polymer layer would still experience stabilization due to entropic repulsion of the polymer layer. Low grafted particles (ii) may collapse due to insufficient entropic repulsion.

To test this hypothesis, I observed particle behavior in a "good" solvent, ultrapure water, and a "worse" solvent, for which I chose PBS. Neutral methoxy-PEG particles were chosen as control and compared to two amino-PEG particle batches with different polymer lengths (2000 g/mol and 3000 g/mol, 45 and 68 repeating monomer units, respectively).

Curiously, the observed stability trend was opposite to prediction. While the neutral control particles containing only methoxy-PEG remained visibly stable (Figure III-16c), the amino-PEG particles instead show a broadening of their spectrum in water (a+b),

hinting at aggregation. On the other hand, no change occurs in the PBS buffer, which is the worse solvent for PEG.

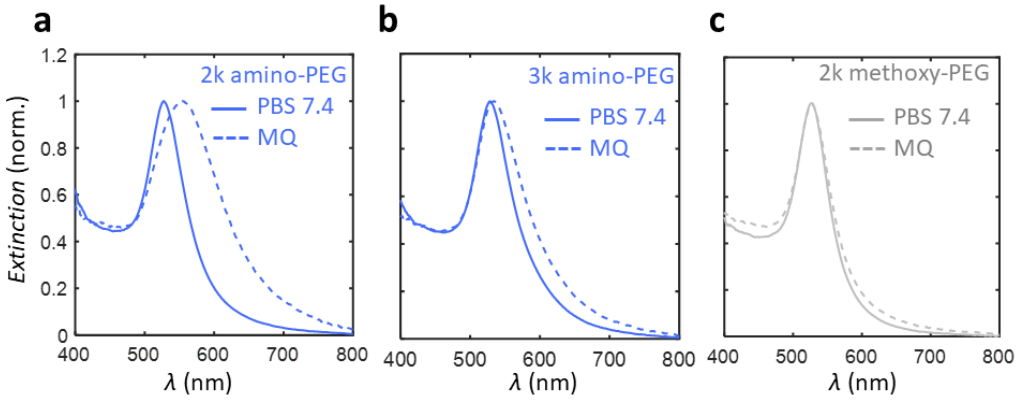

Figure III-16. Aggregation behavior as observed for differently PEGylated particle samples. (a) Particles functionalized with 2000 g/mol amino-PEG show aggregation in ultrapure water (also noted as milli-Q water=MQ), and stable behavior in PBS. (b) Particles functionalized with longer 3000 g/mol amino-PEG show less strong aggregation in ultrapure water. (c) A control sample of neutral methoxy-PEG (2000 g/mol) particles shows no aggregation in either solvent, suggesting the amino group plays a role in the aggregation process.

This behavior is unexpected, considering all factors speaking for better particle stabilization in low ionic strength environment. What is more curious is also the fact that longer amino-PEG is seemingly better at preventing aggregation than the shorter one.

A possible explanation for this behavior is sketched in Figure III-17. In a good solvent, the polymer is expected to be more stretched. Due to this stretching, there could be larger gaps in the layer, which would promote interaction of the amino-group with the more exposed gold surface. In a worse solvent such as PBS, the polymer would be more contracted, and the interaction thereby hindered. Possibly, depending on whether or not the ionic strength is enough to reduce interaction, this may explain why particles show better stability in PBS, but not so in the HEPES buffer with slightly lower salt content.[xix]

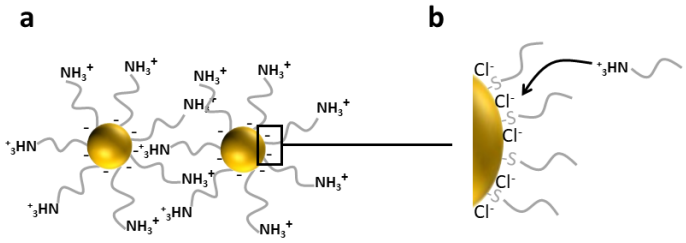

Figure III-17. Possible explanation for aggregation behavior in ultrapure water. (a) Sketch of interparticle interaction, wherein the positive amino group of one particle interacts with the gold surface of another. (b) This interaction may possibly be caused by adsorbed negative ions, e.g. chlorides left over from the previous stabilization with CTAC.

[xix] Refer to the Appendix B for buffer composition.

This explanation, however, raises the question: Why can the end groups reach the gold surface, when steric repulsion should stop their approach? However, even if the interaction is happening with other polymer chains and not specifically with the gold, this leads to the conclusion that the polymer layer retains significant gaps.

The logical next question is: Which physical or chemical effect causes these gaps in the first place, and is there a solution to this problem?

4.5.3. A summary of consequences

To summarize, amino-PEG functionalized particles show poor colloidal stability, and all experiments point to the fact that the amino group specifically causes the problem. The observed aggregation behavior suggests an interaction of the amino group from one particle with another particle. This interaction happens because of unexpectedly low polymer density. In Figure III-18, I summarize all logical consequences arising from the assumption that amino groups interact nonspecifically with other particles. For simplicity, the interaction is drawn to imply a connection to the gold surface, although it is also possible for the interaction to happen with another PEG instead.

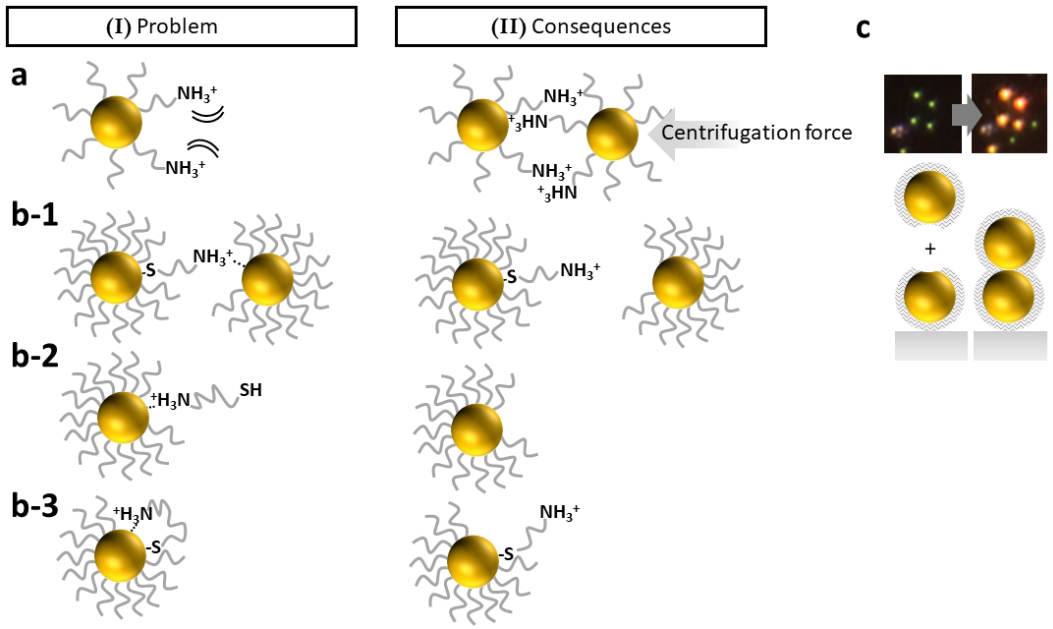

Figure III-18. Possible origin of observed problems with amino-PEG particles. (a) Charge repulsion: DLS measurements suggest that PEG chains may lay in a more stretched state (I), which may lower the polymer density and cause aggregation, e.g. under applied force, as is the case for particle cleaning via centrifugation (II). (b) If amino groups interact with the gold surface, they can also do this during the PEGylation step, bridging two or more particles (b-1). Similarly, the polymer could attach with the wrong end (b-2) or even attach with both ends to the same particle (b-3). The consequence of all three cases is that after depletion of excess polymer by cleaning, the particles are left with gaps in the polymer layer (II). (c) Gaps in the polymer layer may explain why in the previous experiments, unexpectedly strong plasmon coupling was observed after forming the dimer, as well as a lack of fluctuation expected of the Hsp90 protein.

As observed before, one of the cases leading to a lower polymer density may be charge repulsion (a). This is supported indirectly by the unexpectedly long polymer length

derived from the DLS measurement, as compared to the trend of the noncharged methoxy-PEGs.

However, this might not be the only cause for a lower polymer grafting density. Another possibility may be connected with the fact that amino groups also have a certain, non neglectable affinity to the gold surface that may cause interference in the functionalization process.[102] Following this logic, possible scenarios can happen during the functionalization step, leading to polymer adsorption with the "wrong" end during the PEGylation step (b1-3).

In summary, the insufficient grafting density—independent of its origin—appears a reasonable explanation for why after assembly, the particle dimers showed stronger than expected plasmon coupling (Figure III-18c). If there was any protein at all, then it is either stuck or not present to begin with. This also explains why the particles show formation of polymer films during centrifugation steps shown earlier.

This raises the question whether anything can be done to prevent the cases shown in Figure III-18a-b, such as possibly tuning the charged state of the end group, at least during the grafting step. However, as mentioned in theory, adsorption of species onto gold is a complicated process. Theoretically, gold is attractive to nucleophiles. This is how thiols react with the gold, forming a near covalent bond. Subsequently, a non-charged amino-PEG should still retain attraction on the basis of its nucleophilic state, leading again to cases in (b1-3).

All in all, amino groups appear to add complexity to the functionalization process and lower the quality of final grafted particle. This particle, as shown by assembly attempts leading to touching, small-gap dimers, is not sufficiently well stabilized by the polymer to reliably form protein dimers.

A logical question therefore is whether a change of end group could lead to better results, or if the PEG polymer as a whole is not a suitable strategy for assembly.

In the following section, I show that unwanted byproducts occur also with the negatively charged carboxy-PEG functionalized particle samples. This shows that a simple reaction with a bi-functional, linear PEG molecule may not be the best solution to receive a sufficiently thick and stable polymer layer.

5. Negatively charged carboxy-PEG shows additional complexity

Carboxy groups on PEG are one of many other alternative anchor points for subsequent, covalent attachment of particles to one another. A comparison of both can help determine if carboxy-PEG is a suitable alternative, and if similar problems arise in this case.

The difference between an amino and a carboxy functionalization is primarily the charge. In the range of physiological and neutral pH, both carboxy- and amino-PEG functionalized particles are be expected to be fully charged, with the particle being either positive or negative, respectively, as shown in Figure III-19a. This is because their

respective pka are pka(carboxy)=4.8,[94] pka(amino)= 9.6,[94] resulting in a charged state above 99% for each at pH=7.4, in accordance with the Henderson-Hasselbalch law.

Regardless of the charge type, this means that approximately similar charge repulsion is present in both cases as compared to the neutral example of methoxy-PEG, as sketched in (b). Therefore, if charge repulsion alone is the main responsible factor for particle instability in dispersion, it should also be seen with carboxy-PEG. If other factors also play a role (e.g. interaction with the gold surface as sketched in the previous section), then a behavior different from the amino-PEG is expected.

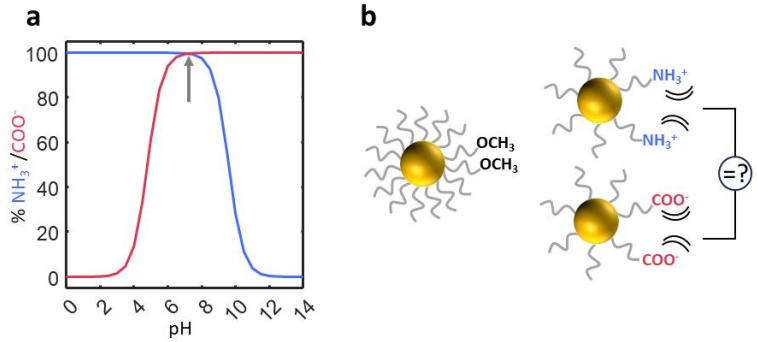

Figure III-19. The charged state of amino- and carboxy-PEG functionalized particles. (a) Protonation curves for amino- and carboxy-PEG respectively, with the physiological pH (where the assembly with the protein is done) marked with a gray arrow at pH=7.4. The approximate pkas of the amino and carboxy group on PEG are as reported in literature, e.g. pka(carboxy)=4.8,[94] pka(amino)= 9.6.[94]) At pH 7.4, the amino group with the respective pka of 9.6 is 99.4% protonated, meaning the particle is fully charged. Likewise, at pH 7.4, the carboxy group (pka=4.8)[94] is 99.7% deprotonated. (b) Sketches of methoxy-, amino- and carboxy-PEG functionalized particles. Methoxy-PEG particles are neutral, while amino- and carboxy-PEG functionalized particles carry a pH-dependent charge.

A repeat of the aggregation study in a low and high ionic strength environment show a difference in behavior. As seen in Figure III-20, amino-PEG particles display a broadening of the spectrum (indicating aggregation) in ultrapure water, but carboxy-PEG particles do not. Their spectrum remains the same also in the higher ionic strength medium (PBS). Therefore, if charge repulsion is causing the PEG layer to be less dense, then this effect does not affect the carboxy group to the extent that can be seen in an ensemble spectrum.

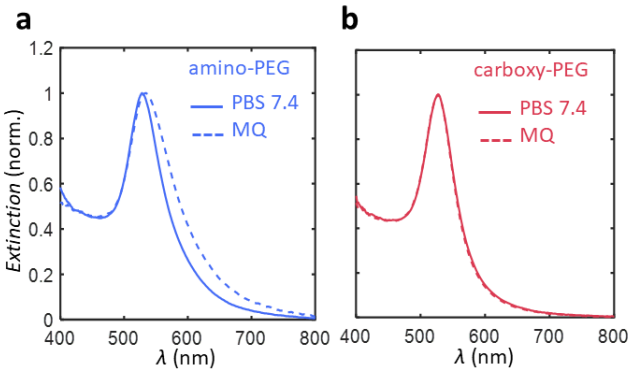

Figure III-20. Ionic-strength dependent colloidal behavior of amino/carboxy-PEG functionalized particles. (a) UV-Vis ensemble spectra of amino-PEG particles in ultrapure water (milliQ/MQ) and PBS 7.4. (b) Ensemble spectra of carboxy-PEG particles under the same conditions.

However, something different is seen when characterizing a carboxy-PEG particle batch in a gel electrophoresis. As shown in Figure III-21a (inset), additional bands appear to the left of the main band. Two extra bands can be seen, each with a slower mobility than the main band and fainter in color.[xx] When collected and characterized in TEM, the second band shows discrete dimer constructs. Following this trend, the third band belongs to trimers, although it was not specifically characterized due to a significantly lower yield.[xxi]

To understand their nature, the dimer constructs were further collected and imaged in the dark-field microscope as separate constructs. An example of this is shown in Figure III-21b, with a field of view displaying the constructs with visibly stronger intensity as compared to the control monomers (marked with arrows).

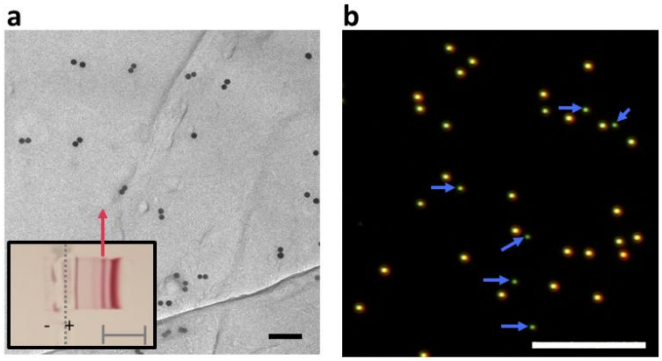

Figure III-21. "Carboxy-PEG" dimers and multimers. (a) TEM image of the isolated dimer band shown in inset. Most constructs seen are dimers, with some discrete single particles also appearing. Scalebar: 400 nm. Inset: Carboxy-PEG functionalized sample, separated in a gel electrophoresis experiment, with a visible multiband-structure hinting at discrete multimer constructs. Scalebar: 0.5 cm. (b) A dark-field, real-color photograph of the isolated dimer band. Blue arrows show a control group of single particles for reference. Scalebar: 50 μM.

Interestingly, the identified dimer constructs showed a time-dependent behavior. Figure III-22a shows the progressive images of a field of view, whereby constructs are observed over a period of 23 h. During this time, constructs change their color from yellow to orange, and this happens randomly to any given construct over a period of hours. This behavior was seen in all experiments[xxii] where the carboxy-PEG dimers were isolated and deposited in the flow chamber. The color change is indicative of the interparticle distance dropping, producing stronger plasmonic coupling. The color change

[xx] To observe the additional bands in the gel electrophoresis, a sufficiently high starting concentration is better. For a 20 μL gel pocket volume, I worked with a particle concentration in the range of 0.7-1 nM for visible results.

[xxi] In the next chapter related to the topic of assembly, I document the statistics and specifics of the dimer "yield" in the carboxy-PEG particle samples. Here I omit this information to focus on their nature instead.

[xxii] The experiment of carboxy-PEG dimers in the dark field was repeated more than three times, with equal behavior observed in all experiments.

is irreversible, suggesting that two such particles experience strong vdW attraction, as theoretically explained in the previous chapter.

Several possibilities could explain this behavior, as sketched in (b) and (c). In the first example, the dimer formation may be mediated by the carboxy group that connects two particles. In the second example, the interaction is based on some form of polymer entanglement. Both cases would mean that the starting distance between the particles is shorter, and the vdW attraction between the particles stronger. As such, this attraction may be the reason behind the eventual dimer collapse. At the same time, this collapse is not instantaneous, because there is still polymer present between the particles, albeit in a lesser amount than necessary for long-term stability.

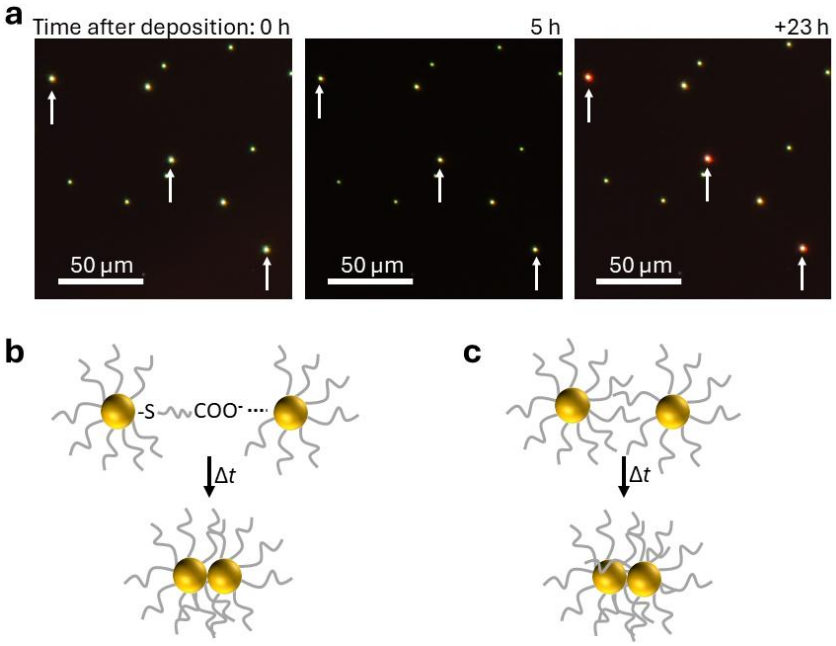

Figure III-22. Color change in isolated carboxy-PEG dimers. (a) Dark-field images of a field of view showing marked dimer constructs (white arrows). Images over time (right at the start of deposition=0 h, 5 h and then 23 h+) show a color change of the three marked constructs. (b) Sketch showing one particle connected to another through the carboxy group, and time-dependent dimer collapse due to an insufficient interparticle distance. (c) Sketch showing a polymer entangled dimer. The same logic applies as in (b).

Interestingly, this color change repeats the behavior seen during the amino-PEG mediated assembly, as described and shown in Figure III-10 and Figure III-18. This bears the question whether amino-PEG particles could also contain such nonspecific constructs. Unfortunately, the separation of the bands is favored in particle samples with high mobility. The amino-PEG particles used in this work have slower mobilities compared to carboxy-PEG ones. Due to this constraint, I could not determine the presence or absence of additional bands in these particle batches.

In summary, it appears that particles functionalized with PEG and certain end groups are prone to nonspecific interaction. This interaction is exemplarily shown as unexpected aggregation in a low ionic strength medium for amino-PEG particles, and the occurrence of nonspecifically formed multimer constructs for carboxy-PEG. The nature of this interaction may be complex, with possible causes being PEG-PEG entanglement, or an

effect of the specific end groups. This interaction makes the particle batches less stable and behave in unpredictable ways. This effect is unwanted for the protein dimer assembly, because it brings uncertainty into the assembly process and the subsequent measurement.

With this in mind, it is reasonable to consider alternatives to PEG.

6. A look beyond PEG modifications: Bad grafting density is also an issue for other functionalizations like DNA

Particle modifications based on the PEG polymer are not the only option for the plasmon ruler assembly. My predecessors had briefly used a particle modification based on single-stranded deoxyribonucleic acid (DNA). DNA-DNA hybridization is a common assembly strategy, and has been shown in the literature to successfully form different types of constructs.[59,114] However, the first tests in relation to the Hsp90 dimer assembly had reported a seemingly unspecific binding of the Hsp90 protein to the DNA-modified particles, leading my predecessors to discard this option.[51]

As I will show in the next chapter, the DNA modification strategy is superior in terms of reactivity compared to the state-of-the-art PEG. For this reason, I decided to re-investigate the reported nonspecific binding and its cause. On deeper insight, the reported interaction with negatively charged DNA is counter-intuitive, because the protein is also expected to carry a net-negative charge (see section 2.1). In addition, our collaborators from the group of Thorsten Hugel of the University Freiburg have anecdotally reported seeing no interference of DNA in their Hsp90 related FRET experiments.

As a first step, I reproduced the results of my predecessors[51] using the same DNA strands (see Appendix B-C for details). For this, I observed what happens when DNA particles are incubated with Hsp90 for a period of 30 min.[xxiii]

As seen in Figure III-23a, particles modified with single-stranded, thiol-capped DNA produce a shift in the gel electrophoresis band when incubated with the Hsp90 protein. This reduction of mobility is due to a larger size resulting from attached Hsp90. The protein itself carries no additional DNA modification, suggesting that the attachment is indeed nonspecific.

To have an additional reference point, I repeated this experiment by replacing the Hsp90 protein with BSA. Interestingly, a change of mobility is also seen with this sample (b), but it is reversed compared to the Hsp90. This may be because BSA is smaller, so the size effect is less dominant compared to the charge effect. Additionally, multiple bands

[xxiii] As shown in the theory chapter, 30 min is a reasonable time for assembly between particles. Therefore, if any interaction if to happen with the protein, it is certain to also happen on this time scale or faster. For better efficiency, the protein concentration is in the order of 100 μM, as compared to the nanomolar particle concentration.

are discernible after the monomer band, and the first band becomes sharper with the addition of the protein. The sharpness of the band suggests that the protein corona reduces the heterogeneity in the mobility behavior. This must be because the particles become more uniform in shape once the protein corona is added.

The multiple bands are an additional curious finding. However, the broadness (and therefore heterogeneity) of the original DNA particle band makes it impossible to judge whether they are present in the original sample, or added through the addition of the protein. In theory however, there should be no reason why BSA should bridge two or more particles. Therefore, it may be that the DNA particles have a low DNA coverage, similar to the carboxy-PEG case.

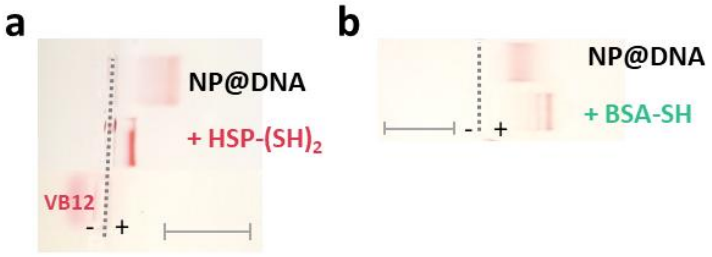

Figure III-23. Hsp90 and BSA attaching nonspecifically to DNA particles. (a) Gel electrophoresis image of a particle batch functionalized with thiol-capped DNA, and comparison with the same particle batch pre-incubated with Hsp90. Scalebar: 1 cm. (b) Incubation of DNA particles with BSA also shows a change in mobility. The band also appears sharper, and multiple bands are seen. Scalebar: 1 cm.

This gives a hint about the nature of the nonspecific interaction with the proteins. One crucial similarity between the two proteins is the presence of either one or two free cysteins (compare also Figure III-12a, protein structures).

To test if the cystein plays a key role in the observed protein corona formation, I repeated the experiment with a Hsp90 protein with blocked cysteins. For this, I pre-incubated the protein with the maleimide-based linker SMCC (reaction with thiols shown in Figure III-24a).

As shown in the gel image (b), the DNA particle sample with Hsp90 shows the previously seen, narrower band and additional bands. On the contrary, the sample with maleimide-blocked Hsp90 shows no such behavior. The band is broader, and no multiple bands are seen. This difference suggests that the protein corona formation is significantly mediated by the cystein, as sketched in (b, right).

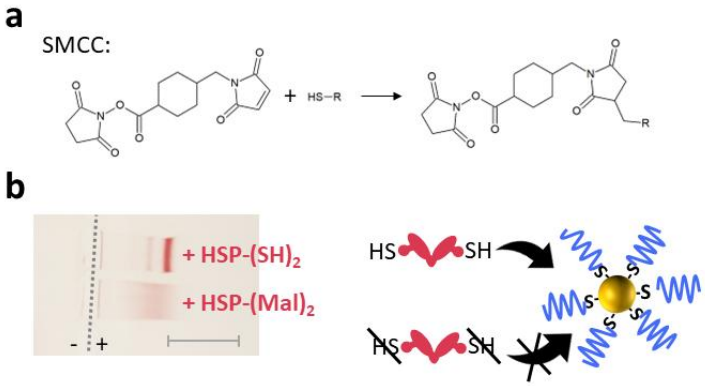

Figure III-24. Cystein-specific interaction with DNA-functionalized particles. (a) Reaction of succinimidyl 4-(N-maleimidomethyl)cyclohexane-1-carboxylate) (SMCC) with thiol (HS-R), and the resulting product. (b) Left: Image of a gel electrophoresis experiment, comparing DNA-functionalized particles pre-incubated with Hsp90 with two free cysteins and Hsp90 with maleimide-modified cysteins. Scalebar: 1 cm. Right: Sketch illustrates the difference observed in the gel experiment.

The findings point to the role of the cystein in the previously observed and unwanted protein corona formation. This means that the source of the interaction is not the DNA but rather the insufficiently covered particle surface. This is because the cystein has a thiol that attaches to the gold, similar to the principle of the thiol-PEG functionalization.

This means that the DNA strategy as an assembly principle is suitable for the assembly. However, it needs improvement to prevent unwanted attachment to the gold surface.

6.1.1. How to solve the insufficient grafting density problem?

An insufficient grafting density is a factor that must be addressed to ensure a repeatable and reliable assembly. The cause of low grafting can vary depending on chosen functionalization type. In the case polymers such as PEG, the issues may arise from the PEG itself, and/or from unintended competition of the functional groups for the gold surface. For DNA modifications, the problem may lie in charge repulsion between the negative DNA strands, as well as a possible competition for the gold surface.[xxiv]

Unwanted interactions appear complicated to suppress in straight-forward ways. In the case of amino-PEG, I had tried several strategies. In one attempt, I varied the pH during the modification from acidic to basic (pH=4-11). This tuned the overall particle charge, with an increasing fraction of the amino groups becoming deprotonated, and therefore uncharged. However, I noticed no improvement in particle stability. This may be because the deprotonated amino group also has a certain affinity for the gold surface.

[xxiv] In our protocols, the charge repulsion is gradually reduced by addition of NaCl to the functionalization mixture (see protocol for DNA functionalization in the Appendix B). However, this does not appear to deliver sufficient grafting density, as shown in the previous section.

I also made an attempt to work with sodium citrate stabilized particles instead of CTAC stabilized ones, in hopes that the adsorbed surfactant and salts may influence the undesired affinity of the amino group. This attempt also did not yield improvement.

It seems therefore that a straight-forward modification with a simple linear polymer strand is too unreliable to consider further. Coincidentally, the DNA modification strategy suffers from a similar issue: Despite the employed salt-aging process, it is not sufficiently densely packed to avoid nonspecific attachment.

Several strategies can be used to circumvent this issue: Either attempting to fill the gaps with additional neutral and small molecules after the first modification step (Figure III-25a), or "prime" the particle with a thin and dense base layer, before adding a second layer for the actual assembly (b). Like this, the particle surface is no longer available for unwanted attachment, even if the second layer, e.g. DNA, is not perfectly dense.

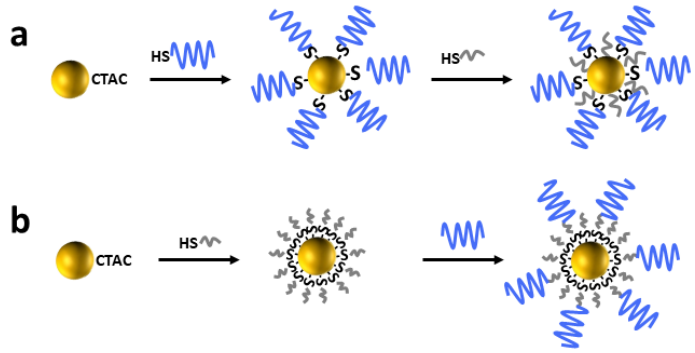

Figure III-25. Passivation strategies. (a) Sketch shows the functionalization steps. In a first step, a CTAC particle is modified with thiol-capped single-stranded DNA. In a second step, a small, thiol-capped molecule such as e.g. a short PEG is introduced to fill the gaps. (b) In the second strategy, the particle is passivated with a first, dense layer of small molecules. These molecules will serve as anchors for further modification, e.g. with DNA sketched in the second step.

To test which strategy is more promising for future investment, I have tested both with proof-of-concept experiments.

In a first test for strategy (a), I selected two small neutral PEG molecules, PEG_3 and PEG_6, modified with a thiol on one end and a methoxy group on the other (Figure III-26a). These PEGs are significantly smaller compared to the PEGs used in the PEG functionalization protocol (3-6 monomer units vs 45 units for the 2000 g/mol methoxy-PEG). As such, they could potentially fill gaps. However, a comparison of gel mobilities between control DNA particles and those additionally passivated with the small PEGs shows no significant difference. As seen in Figure III-26b, all samples still show a change of particle band mobility when the protein is added, signifying a formation of a protein corona.

Therefore, a small PEG is not suitable to fill the gaps with this strategy. The reason for this may be complex, such as the PEG not forming a sufficiently thick layer.

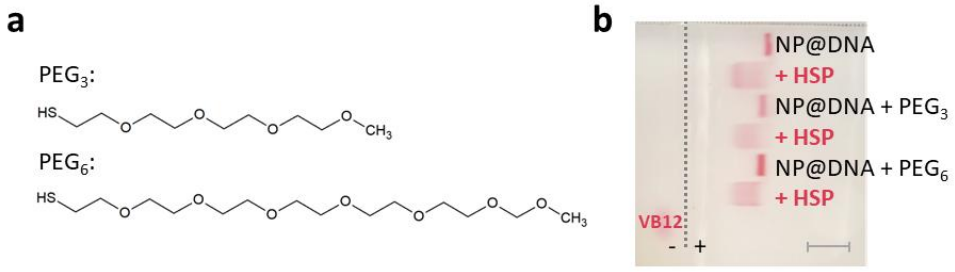

Figure III-26. Passivation by packing. (a) Structures of PEG_3 and PEG_6 used in the passivation protocol. (b) Gel electrophoresis of particle samples modified in a first step with DNA and in a second step with small PEGs. All samples show a change in mobility when incubated with the protein.

Therefore, I proceeded with the second strategy. For this, I covered the particles with a PEG polymer first and then added DNA on top. As a proof-of-concept, I used the 2000 and 3000 g/mol PEG. The resulting particles showed better dispersity, stability against aggregation in the assembly buffers (PBS, HEPES) and less sticking during centrifugation. This strategy is more efficient, which is due to a combination of gold surface coverage and the addition of extra space by the longer PEG.

For the assembly studies following in the next chapter, I continued using DNA particles with a layer of PEG below. This strategy is sufficient to improve particle stability. However, at the moment the interparticle distance is needlessly long due to the extra PEG layer, adding up to 12-30 extra nanometers. Considering a similar distance already added by the DNA itself, this makes for a non detectable plasmon coupling signal.

My proposal for the future is to reduce the distance by pre-passivating the gold with a shorter and more rigid molecule (e.g. short alkane chain). This type of functionalization has been shown to bring benefits of better passivation compared to PEG, as reported in literature, e.g. by Larson et al.[115] The DNA strand can then be covalently attached to this layer. This structure would ensure sufficient passivation of the gold surface against unwanted interactions.

7. Conclusion: Theory vs reality, and next steps

The insights gained in this chapter show that the particle functionalization is not as simple as previously theoretically assumed. In the case of the plasmon ruler assembly, the real polymer thickness is larger than expected, leading to a longer interparticle distance and a loss of signal. However, this is not the only complication. I observed lowered grafting densities of the polymer layer that lead to unwanted nonspecific interaction both between particles and a particle and the protein. These interactions occur when polymers with reactive end groups such as amino or carboxy are used. A similar effect is seen with DNA functionalization. To counteract this, I propose to passivate the particles in an additional step and present a suitable strategy.

In total, I show that characterization and quantification of particle functionalization is an indispensable step for controlled dimer assembly. However, it is not the only factor limiting assembly success, as I will demonstrate in the following chapter.

IV. Road Towards a More Effective and Reliable Assembly

A reliable assembly guarantees that dimer constructs form in a well-defined manner, which is crucial for data interpretation of protein motion.

Previous findings have shown some deficiencies, such as a too large interparticle distance and suspected lowered grafting density when particles are functionalized with a high fraction of amino-PEG (chapter 3). Coupled with knowledge gained from the theory chapter, this may explain why I and my predecessors could not measure a fluctuating plasmon coupling signal in single-particle dark-field experiments. However, even if the plasmon coupling is weak due to a large interparticle distance, the assembly itself should be seen: At the minimum, a construct of two particles in a diffraction limited spot produces double the measured scattering intensity. Nonetheless, my joint work with Bastian Flietel during my master thesis[103] showed no such results. Despite theoretically predicted reaction success (chapter 2), the assembly failed. This means that reality has additional factors that are not accounted for in the theory.

To find a smart strategy for future assembly optimization, I listed the remaining "unknowns" of the dimer assembly and addressed them experimentally. This allowed me to give each factor a weight and single out the highest contributing factor to assembly failure. The result of this work is a recommendation for a most optimal assembly strategy.

1. The "unknowns" of the dimer assembly

To find an optimal way to address the failing assembly, I structured the remaining unknowns. They fall into two types: (1) those that make assembly impossible for chemical reasons and (2) those that slow down the assembly, so that the realistic reaction time is longer than the theoretically assumed one (chapter 2, 30 min).

Figure IV-1a shows a sketch for the type (1). In this example, the protein loses its structure upon connection to the first particle. This scenario is known in literature in the context of protein interaction with a bare gold particle.[116] In theory, our particles should be sufficiently covered with the polymer to prevent this case, but the gaps highlighted in the previous chapter may reopen this possibility.

Figure IV-1b illustrates another case, where the protein attaches with both ends to the same particle. This is a real possibility due to the protein carrying the same functionalization on both ends. Upon reaction to the same particle, further reaction is excluded.

The remaining unknown of the second (2) type is more complex. Here, the assembly is perceived as unsuccessful because it is not given enough time to react. This happens

because the reaction does not happen upon the first hit, as assumed theoretically in chapter 2 (c). This can be for a number of reasons, such as the chosen linking groups possessing insufficient intrinsic chemical reactivity, or the groups themselves being additionally aligned in an unfavorable way in the polymer layer.

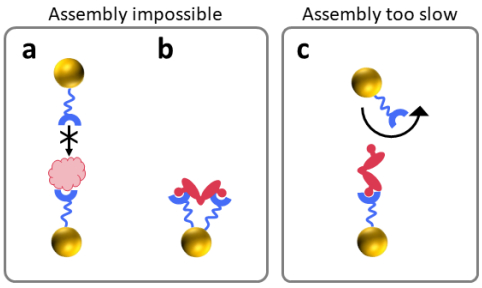

Figure IV-1. Questions that remain unanswered. (a) Possible protein denaturation may be in part responsible for the unreasonably low yield. (b) The same protein could attach with both linking sites to the same particle, becoming unavailable for the second particle attachment. (c) The reactive end groups on a particle don't cover the entire surface. Therefore, there may not be enough attachment points available to ensure reaction upon first hit. The more hits are necessary for success, the longer is the reaction time necessary to form the construct.

Realistically, all "unknowns" can be present at the same time, which complicates the matter. To address this problem, I designed a screening that considers the challenges presented in (a)-(c). The screening solves the presented problems for each case as follows:

(a) The protein is replaced by a more stable "dummy" molecule that cannot denature.
(b) An alternative assembly concept (as introduced in the following section) excludes the possibility of a both-sided reaction to the same particle.
(c) Reactivity is compared across a number of selected chemistries, revealing realistic reaction time trends and the best chemistry for future assembly.

Below, I introduce the screening concept in more detail and present the results. I then comment on what the results mean in regard to the questions (a)-(c). Experimental details follow in the section thereafter.

2. The screening concept

In this section I summarize the key ideas that went into the screening, addressing the complications presented in the section before.

Problem simplification. As previously stated, the protein and its state on the particle is a source of complexity. To remove this complication, I replaced the protein with bi-functional PEG polymer molecules that cannot denature upon contact with a particle.

Choosing an assembly experiment that favors efficiency. Optimizing an assembly concept requires screening across several variables. This leads to many experiments and repeats for reproduction purposes. Time and efficiency are therefore of critical essence: The assembly experiment must have an optimal tradeoff between information gained and time spent.

As introduced in the beginning of this work, there are numerous ways to perform an assembly experiment, each with its own strengths and drawbacks. Two ways previously used in this group are illustrated in Figure IV-2. The first illustration shows the sequential assembly on a surface, based on deposition of each assembly element one after another on a pre-passivated substrate (a). The second shows the concept of the batch synthesis (b), as mainly used in the work of Bastian Flietel.[52] Here, the assembly reaction happens in solution, with all reaction components present at the same time.

Sequential assembly offers better understanding through characterization of each single step during the assembly, however it may take several hours to receive results.[xxv] It also requires additional effort in terms of pre-passivation of the glass slide. Batch synthesis on the other hand is quick, and allows to test many iterations of the same experiment at the same time. Due to its high throughput, I chose the batch synthesis for the basis of my screening.

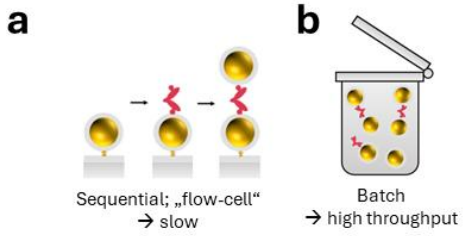

Figure IV-2. Sketch of two assembly concepts. (a) Sequential dimer assembly works by attaching every component in a separated step on a substrate. (b) In the batch dimer assembly, all components are mixed in a single step, resulting in a statistical distribution of products.

Excluding a both-side reaction to the same particle with a different assembly concept. The state-of-the-art assembly employs the simplest concept by connecting two same-type-particles (in terms of chemical groups), as illustrated in Figure IV-3a. I call it a "homo" assembly concept, referring to both particles having the same chemistry. This simplifies the synthesis and particle optimization. Additionally, a homo-dimer assembly is easier to characterize in a gel electrophoresis.[xxvi] However, the drawback of this method is the possibility of the protein (or dummy) reacting on both ends with the same particle, as previously introduced.

To test the significance of this problem, I use a different assembly concept that I call "hetero". As Figure IV-3b shows, the dimer construct is now made of two different-type particles. This complicates the protocol, requiring an optimization of two particle types instead of one. Additionally, the protein (or dummy) now requires additional modification

[xxv] As stated in the thesis of Bastian Flietel, the sequential assembly can take up to five hours.[52]

[xxvi] For details on characterization differences, refer to the Appendix B-C.

on the second site. In the case of the protein, the extra modification step also introduces statistical side products that complicate the reaction.[xxvii]

This constraint highlights why it is critical to understand the contribution of a possible two-side reaction to the same particle: While a hetero-type assembly may solve one complication, it introduces others. Therefore, my work tests both to answer the aforementioned questions and determine the simplest assembly strategy.

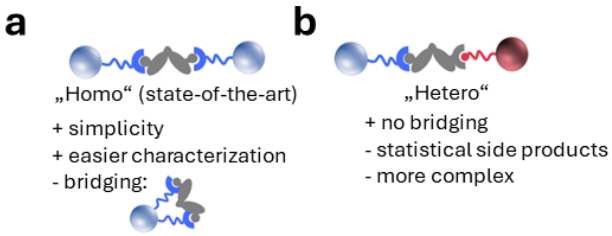

Figure IV-3. Homo and hetero assembly methods. (a) Homo assembly method uses two particles with the same type of chemistry. (b) Hetero assembly method features a different chemistry for each particle, preventing unwanted bridging of the protein over the same particle.

The optimal chemistry. The reactivity of a chemical linker is critical for a reaction that is already disfavored, e.g. by factors such as a slow diffusion coefficient of the 40-60 nm sized particles (compare chapter 2) and the availability and location of the functional groups in the polymer layer (see discussion chapter 3). The last point is further complicated by thermodynamic considerations: As Martinez-Veracoechea and Leunissen[117] highlight in their article on the topic of reaction between tethered systems, the entropic cost of a reaction between two tethered groups makes the reaction less favored as compared to the non-tethered one. For our assembly, this means that a small amine will react more readily with a maleimide as compared to a case when the same amine and maleimide are tethered to a PEG. To counteract these constraints, a highly reactive option for assembly is of essence.

The state-of-the-art chemistry in our group so far uses the free thiols on the protein and combines them with amino-PEG on the particles using maleimide chemistry.[49,52] This reaction is considered a “click-chemistry”, which among other things suggests an efficient reaction.[118] To ensure that the screened for chemistries have potential for improving the protocol, I selected other common chemistries on the basis of them being (1) commonly used in the field of the biochemistry and (2) known for efficiency, with the maleimide “click-chemistry” as the benchmark. Among these chemistries are: the EDC/NHS[xxviii]

[xxvii] For further modification, one batch of the protein dimer is reacted with group A and another batch with group B. Both are combined and re-mixed by applying temperature. This step cleaves the dimer and allows statistical recombination. The result is a statistical mix of dimers possessing the unwanted AA and BB modifications, together with the required AB for the hetero assembly.

[xxviii] 1-ethyl-3-(3-dimethylaminopropyl)carbodiimide/N-hydroxysuccinimide

coupling, the biotin-streptavidin association and DNA-DNA hybridization. Further details on each are provided in the respective experimental section.

The screening principle. To receive a maximum on information, I combined all of the above factors into a screening procedure, as sketched in Figure IV-4. As shown, I excluded the protein from the screening, and tested two different assembly concepts ("homo" and "hetero") to address the option of an undesired, two-sided reaction. At the same time, I combined the concepts with the above listed chemistries (i-iv). This allowed me to address the assembly unknowns and find the best, simplest and most reactive assembly concept for the dimer assembly.

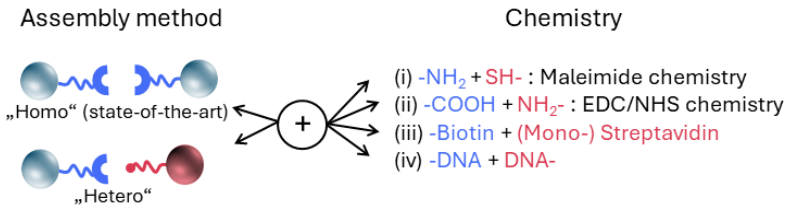

Figure IV-4. Principle of screening for the best assembly strategy.

In the following section, I present the key findings and highlight what they mean for the future of the assembly.

2.1. Screening reveals best assembly strategy and answers previous questions.

This section presents an overview over the screening results. After the summary, I show the most promising chemistry, the best assembly concept, and give answers to the assembly's unknows. To improve future decision making for assembly design, I also comment on why certain assembly strategies fail. Detailed experimental results are documented in the section thereafter.

Figure IV-5 summarizes the screening results. Using criteria listed in the experimental section (2.2), I separate the results into three categories of (1) assembly successful (green), (2) assembly successful but with complications (yellow) and (3) assembly failure (red).

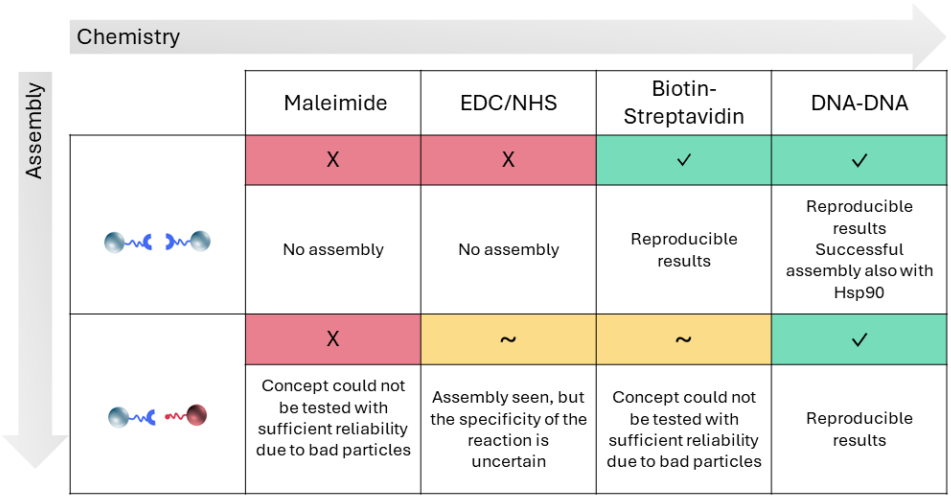

Figure IV-5. Overview assembly screening results. Red colors mark failed assembly, yellow stands for assembly that worked, but features complications, and green color shows reproducibly reliable assembly. Each chemistry contains comments highlighting key observations.

The picture shows heterogeneous results. On the topic of chemistry, the maleimide reaction used in the state-of-the-art protocol exhibits poor performance across both assembly strategies. This outcome further proves that the maleimide chemistry is not a suitable option for assembly. The EDC/NHS chemistry follows this trend. This is not surprising, considering that both reactions have a similar "click-chemistry" principle and reactivity (see experimental section 2.2 for details). On the other hand, both the biotin-streptavidin and DNA-DNA hybridization give reproducible results, proving the importance of a smart chemistry choice for particle assembly. Between these two choices, I see the advantage in the DNA-DNA for its flexibility in tuning the tether length, which is important for adjusting for the best interparticle distance.

In terms of assembly concept, the results prove the aforementioned complication of additional second particle optimization: For two of the chemistries (maleimide and biotin-streptavidin), the functionalization of the second particle could not be sufficiently improved for reliable test results. Additionally, the EDC/NHS variant showed assembly under conditions that introduced doubts to its chemical specificity (further details in 3.3). DNA-DNA alone delivered reproducible results, showing that it is the most robust option for future assembly.

Below I comment in greater detail on the key findings, including…

(1) the best chemistry for assembly,

(2) the resolution to the question of the two-sided attachment to the same particle,

(3) the best assembly concept,

(4) and the reasons why certain assembly strategies fail.

2.1.1. DNA-DNA hybridization is the best assembly option.

As highlighted, DNA-DNA hybridization shows the biggest promise for the future assembly strategy. It delivers reproducible results across both the homo- and hetero-type assembly, proving its versatility. In this section I list and summarize the important findings relevant for assembly, show where the DNA has its strong points compared to other chemistries, and comment on necessary optimization steps to ensure a reliable future assembly.

The first and most important pre-requisite for any strategy for dimer assembly is its compatibility with the protein buffers. My results show that DNA based assembly happens readily in the aforementioned buffers (PBS and HEPES), ensuring that this is a viable option for the protein dimer assembly. This is a positive insight, because DNA-DNA hybridization is sensitive to salts.[119] Among other factors, DNA requires some charge shielding to overcome its own charge repulsion. I show this importance in 3.5, where DNA functionalized particles do not assemble in a low ionic strength buffer, but do so in the PBS and HEPES buffers. With this, the most basic pre-requisite is met.

In terms of reactivity, the DNA-DNA hybridization shows the best effectivity across all tested systems, with the maximal effectivity achieved already at 10% reactive DNA fraction on a particle, for a reaction time of 30 min. Other systems either did not yet show signs of assembly or showed signs of unfinished assembly at this percentage of anchors and reaction time. This is beneficial for keeping the time between unfreezing of the protein and the measurement short.

An additional strong point is that DNA-based assembly is well suitable for both the batch and the sequential assembly. As mentioned previously, both assemblies have their strengths and drawbacks. In this context, the batch assembly is fast but contains a statistical mixture of constructs. This mixture benefits from further separation. One such method is the gel electrophoresis introduced in chapter 3. As I show in the experimental section (2.2) and in the Appendix C, the separation of constructs using gel electrophoresis is straight-forward when both particles have the same mobility. This is the case for DNA-based assemblies, with both particles carrying a similar negative charge. The situation is different other assemblies, such as the combination of the positive amino-PEG particles with negative carboxy-PEG ones (refer to 3.3 for examples). DNA-functionalization is superior in that regard.

In terms of particle design, I noticed that assembly happens more reliably with DNA particles that are additionally passivated with a PEG polymer layer under the DNA. This corresponds with my findings from chapter 3. The additional passivation improves stability in the experimental buffers and prevents nonspecific aggregation. At the moment, the passivating underlayer is not yet optimized for an interparticle distance suitable for a strong plasmon coupling signal. This should be addressed in future protocol modifications.

Finally, the biggest positive result to take away is assembly success with a DNA-modified Hsp90. This reaction formed successfully in the simple, homo-type assembly. This suggests that the protein is stiff enough not to attach with both ends onto the same

particle in a significant amount. This finding simplifies future particle improvement efforts, because only one particle type needs to me optimized for assembly.

For future improved protocols, this is the most promising starting point.

2.1.2. Attachment of a ligand with both sides to the same particle is not significant for proteins, e.g. streptavidin, Hsp90

An important question is whether the attachment of the protein with both sides to same particle may in part be the reason for failed or less effective assemblies. While this case cannot be entirely excluded, the results show that assembly happens in the cases where streptavidin and DNA-modified Hsp90 are the ligands connecting the particles. On the other hand, assembly does not happen with ligands such as bi-modified PEGs. Taking the reactivity trends into account, the assembly with bi-modified PEGs could have failed due to insufficient reactivity, rather than possible attachment of both ends to the same particle. Additionally, the random coil nature of a PEG may also lessen the availability of the second end group. Thus, it is not the best option for a dummy.

In total, possible non-availability of the second binding site is not the main factor in the assembly. This is the case for ligands such as Hsp90 and streptavidin. Their size and stiffness as compared to a polymer random coil must be the responsible factors.

2.1.3. Homo assembly strategy remains the best option.

When comparing the homo- and hetero-type assembly strategies, the screening results show that both strategies work. Between the two, the homo-type assembly is the easier option to realize. This is because this assembly type requires the optimization of one particle type only.

Additionally, its main strength is easier characterization in gel electrophoresis. This is because homo and hetero-type constructs behave differently in the gel electrophoresis. Due to both particles being identical, homo-type constructs can easily be identified and recovered from the gel, as shown later in the introduction to the methods in 2.2.2. This is not always as easy for hetero-type assembly, where the location of the dimer band is hard to predict. Therefore, homo assemblies offer the option of easier purification, which increases the dimer constructs available for measurement.

Another point is the protein modification. For the homo-type assembly, both reactive sites on the protein carry the same modification. For the hetero-type assembly, two different modifications are needed. As previously mentioned, such modification is typically done in a batch. This results in a statistical mixture of products and by-products. Due to statistics, some proteins will carry the wrong modification on one site. This lowers the assembly yield, due to 50% of constructs statistically carrying the wrong second modification site. This problem can be avoided by additional purification steps. However, they further complicate the procedure.

Thus far, the only drawback of the homo-type assembly is the danger of the protein attaching with both sides to the same particle. However, as said in section 2.1.2, this is not an issue.

For these reasons, I recommend homo-type assembly for future use.

2.1.4. A summary of reasons why certain assemblies fail

Lastly it is important to summarize reasons for assembly failures. The screening shows that the most critical factor is the particle reactivity.

To sum up the trends, the two tested "click-chemistry" type reactions, maleimide and EDC/NHS, showed no assembly. Biotin-streptavidin and DNA-DNA hybridization on the other hand delivered reproducible assembly.

One reason for this is because the biotin-streptavidin and DNA-based particles have a higher probability of reaction. For the first, this is because tetrameric streptavidin carries four reactive sites per one single protein. I show further proof of this in section 3.4, where monomeric streptavidin with one binding site does not promote assembly as compared to the tetramer. For DNA, I explain the higher reactivity because it is a strand that possesses a non-zero affinity along the entire length.

The second factor for assembly failure is an insufficient particle quality. This is an aspect that has been discussed in chapter 3. Low grafting density of the functionalization leads to less attachment points and more options for nonspecific interactions.

Furthermore, the screening shows that reaction time must not be underestimated when particle reactivity is low. While theory suggests that the assembly reaction—under given experimental conditions in the plasmon ruler experiment—is expected to be finished in under 30 min, this is not enough for maleimide and EDC/NHS mediated assemblies (compare experimental section in 3.3), and also not for biotin-streptavidin (3.4). Only the DNA-DNA hybridization assemblies have reached maximum assembly within the expected theoretical reaction time (3.5).

In total, all results point to the need for stable and well-defined particles, with a highly reactive functionalization. This is especially critical for assemblies where diffusion times and potential hits between the reactive partners are lower, e.g. for our 40-60 nm particles (see chapter 2), and where only one protein—and therefore only one reactive site—is available for reaction with a second particle to form a dimer.

2.2. Experimental Section

In this section I present a chronological documentation of results summarized in 2.1, Figure IV-5. Here I motivate the parameters used in the screening, and explain the criteria chosen to determine whether an assembly experiment is a success or failure. After that, I give a brief overview of the characterization methods used in this section. The

chronological documentation of the screening follows thereafter, with results sorted by chemistry and split by assembly type.

2.2.1. Screening parameters and criteria for success

As shown in the theoretical essentials (chapter 2) assembly success depends on factors such as interparticle forces and reaction kinetics. These conditions are experimentally represented by the ionic strength of the solvent, the particle and protein concentrations, as well as the reactivity of the chemistry used for the attachment. In addition, reactant ratio and assembly time are also variables that influence the results. Below, I summarize the key experimental constraints.

The **ionic strength** is fixed by the conditions imposed by the protein: A specific buffered medium is necessary to retain the protein in its natural state. In my work, I use the buffers HEPES and PBS, with the salt concentrations stated below:

HEPES buffer: 40 mM HEPES (2-[4-(2-hydroxyethyl)piperazin-1-yl]ethane-1-sulfonic acid), containing 10 mM $MgCl_2$ and either 50 mM or 150 mM KCl, at pH 7.4 or 6.7

PBS buffer: 10 mM PBS (phosphate buffered saline), 137 mM NaCl, 2.7 mM KCl, at pH 7.4 or 6.7.

The **reactant concentrations** are limited by the particles. Due to their considerable volume (65500 nm^3 for a 50 nm spherical particle, as compared to a small molecule such as a typical fluorescent dye, with a volume <1 nm^3 [120]), the particles can only be concentrated up to a certain degree. The working particle concentration for particles between sizes 40-60 nm is typically in the range of 1 nM. The protein stock is diluted accordingly.

The **reactivity** of a tested system is represented by the number of reactive and the chemistry type. For the purpose of better comparison, the percentage of reactive end groups on the default particle type is fixed at 10% as compared to nonreactive groups. This value stands representatively for the state-of-the-art particle. The fixed percentage allows a fair comparison of different chemistries in terms of their reactivity.

The **reaction time** is fixed to 30 min. The point of reference for this choice is the assembly protocol with the protein. This ensures that the time between protein defrosting, the subsequent assembly and the measurement is reasonably short, minimizing potential loss due to possible denaturation.

The remaining variable is the **ratio** of particles to the protein or ligand. Literature and previous work in this group[52,121] show that a batch synthesis gives the maximum dimer yield at a particle-to-ligand/protein ratio of 2:1. This is the theoretical ideal under perfect conditions. Therefore, to account for uncertainties, in the screening the ligand of choice is titrated around this ratio. As a side-effect, this also presents an additional qualitative reaction control: The titration of a ligand should lead to a saturation of the particle, following an increasing ligand concentration. If this trend is seen, the reaction of the ligand to the particle can be said to be well controlled.

In summary, any assembly reaction detected under the above specified conditions is considered successful.

2.2.2. A brief introduction to the methods

In the experimental section, I show assembly results in form of UV-Vis spectra and gel electrophoresis experiments. On the basis of this data, I decide whether the assembly is successful. To ensure that the reader can follow the results and reasoning, I use this section to briefly explain what a successful reaction looks like in the ideal case.

UV-Vis ensemble spectra allow to gauge reaction success through relative change of the spectrum. The change is caused by two factors, as shown in Figure IV-6a-b. Monomer dimerization changes the spectrum according to the strength of plasmon coupling, as previous described in the theory. The strength depends on the interparticle distance, and the closer the particles, the stronger the coupling and the more red-shifted is the resonance wavelength position. At a distance near 1 nm, the quantum tunneling effect leads to the appearance of a second peak. Figure IV-6a illustrates how this would look with an idealized sketch, where the entire sample is made of the dimers only. In reality, the solution contains a statistical mixture of monomers and constructs. The presence of dimers and higher constructs in this case can be seen as a shift of the resonance position and the broadening of the spectrum (characterized by the broadness at the full width half maximum, FWHM). Depending on the interparticle distance, a red-shifted shoulder can also appear.

A high presence of dimer and multimer constructs can also be discerned by eye. As shown in Figure IV-6b, a red solution containing monomers turns blue-violet upon reaction to higher constructs. This is because the constructs cause additional absorption and scattering in the red region, and the remaining transmitted color is perceived as blue-violet. Full aggregation of a sample causes loss of color. Due to growing size, the constructs no longer show plasmonic behavior, and settle down.

Thus, UV-Vis is a simple method to follow reaction time and presence of constructs.

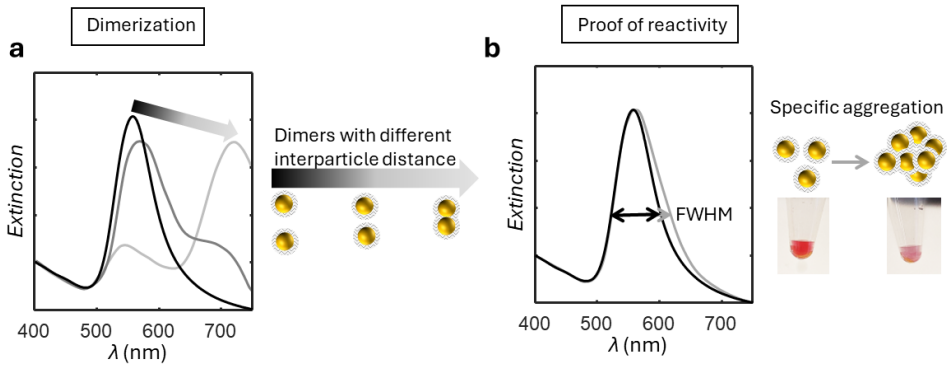

Figure IV-6. UV-Vis characterization method of successful assembly reaction. (a) Sketch of extinction spectra, under the assumption of the ideal case where all particles in the ensemble are forming dimers. In a real case, there would be a mix of products, and the formation of dimers seen as a growing shoulder of the monomer spectrum (black). The appearance of this shoulder is dependent, among other things, on the interparticle distance. (b) Formation of multimer constructs leads to a broadening of the FHWM (full width half maximum) of the spectrum. The extreme case can also be seen by eye, visible as a color change or complete loss of color at full aggregation.

The second method I use is the gel electrophoresis. Its strength lies in its high throughput, as well as specific identification of dimer constructs. Contrary to the UV-Vis, gel electrophoresis is not sensitive to specific interparticle distance, and can thus show presence of constructs even if their distance is too large for the plasmon coupling effect. This makes dimer detection more robust, but only in cases where particle mobility is high enough to separate the sample.

Figure IV-7 shows a sketch of the gel electrophoresis experiment. It displays what happens when a ligand (such as the Hsp90 protein) is added to a solution of reactive particles. In the simplest case of a homo-type assembly (a), the gel displays two effects: First, the addition of ligand causes a change of mobility of the monomer band. This is because the ligand leads to a change in size as well as charge. (a) shows how this would look like for a Hsp90 protein. The growing protein corona adds to the particle negative charge and moves the particle band to the anode.

Secondly, the formation of dimer and multimer constructs is seen as a "tail" behind the monomer band. These constructs have a slower mobility due to retardation caused by their size. This splits the constructs from the monomer band and makes them available for extraction and further study. The more of such constructs form, the less colored is the monomer band due to monomer particle loss.

Lastly, if higher order aggregates form, they remain in the pocket due to their size exceeding that of the gel mesh. In the sketch, they are shown as a violet rim around the pocket.

The gel image in Figure IV-7b illustrates how the sketched effects in (a) look in a real gel. The example shows a control sample and one incubated with a ligand. The ligand leads to a mobility change and formation of additional bands corresponding to the formed constructs.

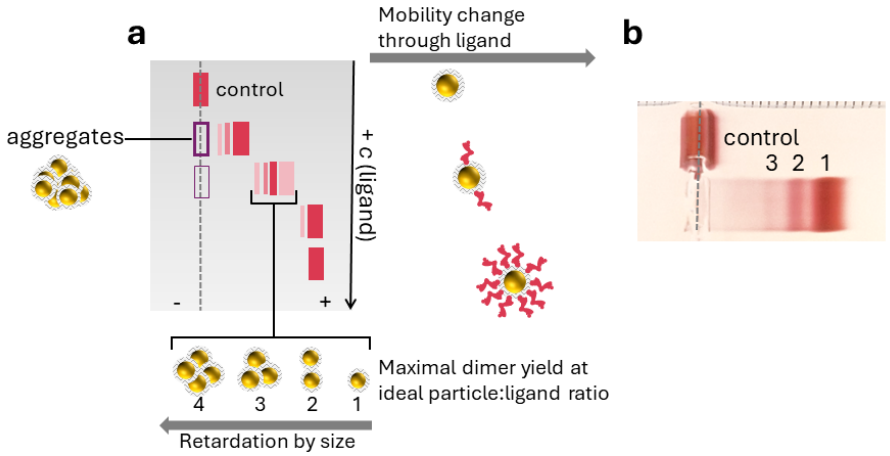

Figure IV-7. Sketch and example of a gel electrophoresis experiment, with details relevant for interpretation. (a) Sketch showcasing the combined effect of ligand saturation and construct formation. (b) Example of a gel electrophoresis image, with the control monomer band and the sample with marked multimer bands.

The case of a homo-type assembly, where all particles carry the same charge, is the simplest to characterize in the gel electrophoresis experiment. As shown later in the experimental section, the interpretation of hetero-type mixtures, containing differently charged particles, is more complex.

For this reason, I use both UV-Vis and gel electrophoresis in combination for a more complete picture of the assembly. In the Appendix C, I offer more insights and handling tips related to these two characterization methods.

3. Screening results

This section presents the screening results. It is structured chronologically, and documents the experimental findings by the chemistry type. Each section is further divided into the homo and hetero assembly.

3.1. The state-of-the-art: Maleimide reaction between amines and thiols

To serve as a reference point for the screening, the first step reproduces the state-of-the-art assembly protocol with the Hsp90 protein.

The protocol is a homo-type assembly. The maleimide chemistry is a click-type reaction, connecting amines with thiols. In a typical reaction protocol[122], the amine is first activated using the bifunctional crosslinker SMCC (succinimidyl 4-[N-maleimidomethyl]cyclohexane-1- carboxylate). The NHS (N-hydroxysuccinimid) ester side reacts selectively with primary amines at pH 7-9, and the maleimide side with thiols at pH 6.5-7.5. For this reason, the buffers in the state-of-the-art protocol are adjusted to 6.7 and 7.4, and exchanged for the respective reaction step to exclude unwanted side reactions. The crosslinker adds a total of 0.83 nm of extra length to the interparticle distance.[122] The thermofisher protocol states 30 min of reaction time at room temperature for both linker sides. Further reaction details are provided in the Appendix C.

In Figure IV-8 I show one screening example, containing results of the gel electrophoresis and the ensemble spectra. Here I incubated 10% amino-PEG particles with different ratios of particle-to-Hsp90 for 30 min, as sketched in (a). The ratios are between 1:0.5 and 1:5000. In accordance with previous results, the gel electrophoresis shows merely an adsorption of the protein to the activated particles (b), resulting in a mobility change. Compared to the control, there is no sign of further bands that could hint at formation of higher order constructs. Similarly, UV-Vis ensemble spectra of the samples show no difference between the reference particles and those incubated with the protein (c). This is further seen in the pictures of the samples (c, ii and iii), whereby the reference and the exemplarily picked sample with a ratio of 1:5000 show no difference in color.

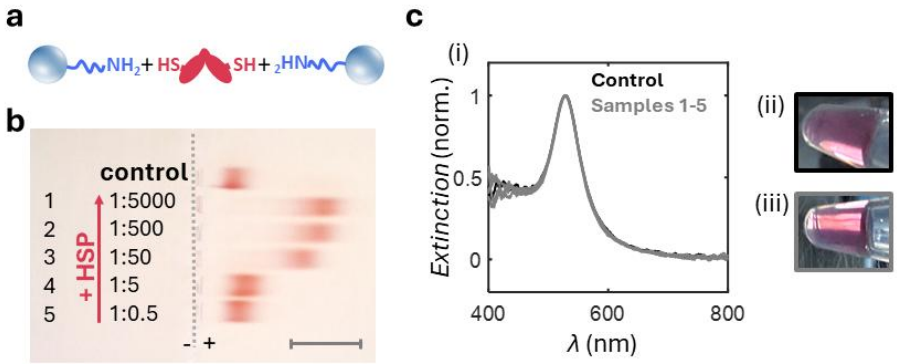

Figure IV-8. State-of-the-art maleimide reaction assembly with Hsp90, homo-type. (a) Assembly sketch: the Hsp90 protein is attached on two sides via maleimide chemistry to amino-PEG particles. (b) Agarose gel of a control sample of activated amino-PEG particles and a titration of the Hsp90 protein. The titration shows protein adsorption with higher protein ratio, but no signs of aggregation or multiple bands. Scalebar: 1 cm. (c) UV-Vis spectra show no signs of aggregation, suggesting no interparticle linking is happening within the time frame of 30 min (i). Photos of the reference (ii) and sample 1 (iii) for comparison, showing no aggregation or color change.

In total, the results reproduce and support previous assembly failures. The protein attaches to the first particle as according to the mobility change, but no reaction with a second particle is observed with the two characterization methods.

Such failures can arise from previously mentioned reasons such as unavailability of the second binding site, protein denaturation or insufficient reactivity. Notably, the diffusion coefficient of the free protein and a protein attached to a particle drops by roughly an order of magnitude (see chapter 2). This may additionally lower the successful hit-rate.

The following screening addresses these questions, starting by a simplification of the assembly by a replacement of Hsp90 with a robust non-protein dummy.

3.2. Maleimide reaction without the protein shows lack of assembly in both homo and hetero-type assembly.

To test if the protein is responsible for assembly failure, I replaced it with a linear and bi-functional PEG, as sketched in Figure IV-9a. For this I tested different sizes of PEGs between 2000, 3000 and 6000 g/mol, with respective hydrodynamic diameters between approximately 7-13 nm according to the Flory estimation.[97[p.382f]] This range is similar to the Hsp90 protein in its closed and open state, which makes the PEG a suitably sized substitute.

Here I present the results only for the shortest PEG (2000 g/mol). Across all tested PEGs, I saw the same trend, so I refer to the Appendix C for the other PEG lengths.

Figure IV-9b-d summarizes the results. In the gel, the particles show very slow mobility (b). This makes interpretation difficult. However, a similar trend to the previously presented Hsp90 experiment is seen: The mobility changes with higher concentrations of the dithiol-PEG linker, suggesting successful reaction with the first particle (b). The change is small and pushes the band more towards the anode. This is because the thiol is

present as a thiolate, adding a negative charge. However, no weakening of the band color is seen, meaning a lack of assembly.

This is further supported with ensemble spectra, the results identical to the Hsp90 experiment (c). No color change is observed across the titration with the dithiol-PEG (d). These results mean that the PEG attaches to the first particle, in agreement to the electrophoresis results, but do not form constructs with other particles. Notably, I observed no change in the UV-Vis spectra even on the following day after reaction start. This does not align with the theoretical assumption that the reaction should be finished after 30 min. The reactivity is therefore too low.

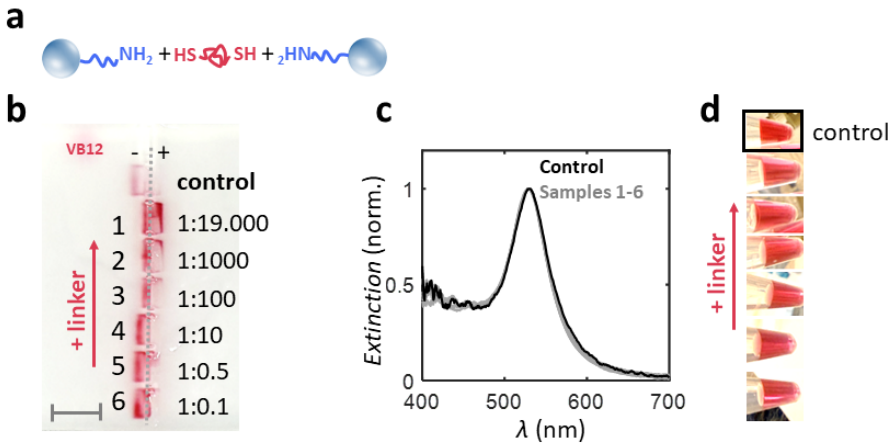

Figure IV-9. State-of-the-art maleimide reaction assembly with dithiol-PEG dummy linker, homo-type. (a) Assembly sketch: the dithiol-PEG is attached on two sides via maleimide chemistry to amino-PEG particles. (b) Agarose gel of a control sample of activated amino-PEG particles and a titration of the dithiol-PEG. The titration shows small migration change starting from 1:100 particle to ligand linker ratios, but no signs of aggregation or multiple bands. Scalebar: 1 cm. (c) UV-Vis ensemble spectra of samples from b, showing no change between the control sample and those with ligand. (d) Photographs of samples from b and c, showing no color change.

Overall, the experimental results show that even without the protein, the assembly fails. A dithiol-PEG has the same number of reactive end groups as the Hsp90. The similar trend of attachment to the first particle shows that the first attachment step happens similarly. Only the reaction to another particle is the problem. With this knowledge, the logical conclusion is that assembly fails because (1) the reaction chemistry is not efficient enough for particles with slower diffusion or (2) the second binding site is unavailable due to the ligand connecting to the first particle with both ends.

The first hypothesis is subject to test in the following sections. To test the remaining hypothesis of the unavailable binding site, I changed the assembly type to **hetero**, as previously introduced in 2. Figure IV-10a demonstrates the idea, where an animo-terminated particle is assembled with a thiol-terminated one. In this assembly type, the particles should react freely with each other, unless if point (1) plays a major role.

However, this test attempt did not succeed due to insufficient particle quality. In particular, my dithiol-capped particles displayed a strong tendency for self-aggregation,

even at high molar excess of the polymer during the PEGylation step.[xxix] I observed aggregation after washing steps, as demonstrated in Figure IV-10b.

Between the two tested PEG lengths, 2000 and 3000 g/mol, the aggregation is curiously stronger for the longer PEG. This may be due to differences in grafting density and polymer conformation, leading to different steric stabilization. I further noticed that this aggregation is reversible by sonication, but returns over time. This further supports the theory that particles are insufficiently stabilized by the PEG.

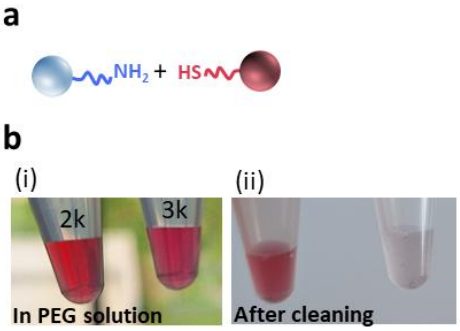

Figure IV-10. Problems with dithiol-functionalized particles. (a) Sketch of the original aim for the assembly. (b) Photographs of dithiol-PEG capped particle samples in PEG solution, for a 2000 and 3000 g/mol PEG, as well as photographs after cleaning steps by centrifugation. The longer PEG shows stronger aggregation by a depletion of color.

On the whole, the results suggest that functionalization with dithiol-PEG is not robust. In additional experiments, I attempted to circumvent this issue by starting with amino-PEG particles and modifying them into thiols with Traut's reagent[xxx], but the quality of these particles was also insufficient. The addition of the thiolation reagent led to aggregation.

The unsuccessful hetero-type assembly gives hints that particle functionalization and PEG end groups play a significant role, as already suggested in the previous chapter. In total, the strategy of using amino- and thiol-terminated PEG and coupling them with the maleimide chemistry is problematic and needs further optimization.

3.3. The EDC/NHS reaction: mixed results

The EDC/NHS coupling chemistry is used to couple proteins or other biomolecules.[123] In its principle, the EDC/NHS chemistry is similar to the previous reaction. A carboxy-terminated PEG is activated by a carbodiimide compound such as e.g. EDC (1-Ethyl-3-(3-dimethylaminopropyl)carbodiimide) and NHS (N-hydroxysuccinimide) reagents, turning into an NHS ester. This ester can be coupled to amines. One specialty of this

[xxix] The highest polymer concentration in use in a standard protocol is 10 mM PEG, roughly amounting to a x10^7 excess to the particle concentration.

[xxx] Traut's reagent: 2-iminothiolan, is used to modify primary amino-groups into thiols.[123]

reaction, compared to the maleimide one, is that it directly couples the carboxy and amino compounds. It is therefore called a "zero-space" link.[123] This makes it an attractive option for our assembly, because it saves interparticle space, which is important for plasmon coupling.

To test the performance of this chemistry, I functionalized particles with a carboxy-PEG instead of the amino-PEG. As previously said in chapter 3, carboxy-PEG particles have better stability, so I expected a more robust assembly. For the **homo-type assembly**, I used a diamino-PEG ligand (2000 g/mol) to replace the protein, as done similarly in 3.2. This is sketched in Figure IV-11a.

A first look at the titration of the linker to the activated carboxy particles shows a general trend of low mobility (b). The most difference is at the highest particle-to-linker ratio of 1:18.000, where the particle band is displaced towards the cathode (-). This is because of the positive amino-PEG attachment. Similar to the maleimide case, there are no signs of aggregation in the pockets and no additional bands.

At the same time, UV-Vis spectra show no difference between control and sample ensemble spectra (c, i). Additionally, there is no change even after overnight incubation: Samples retain their color even after 24 h+, as seen in (c, ii+iii)

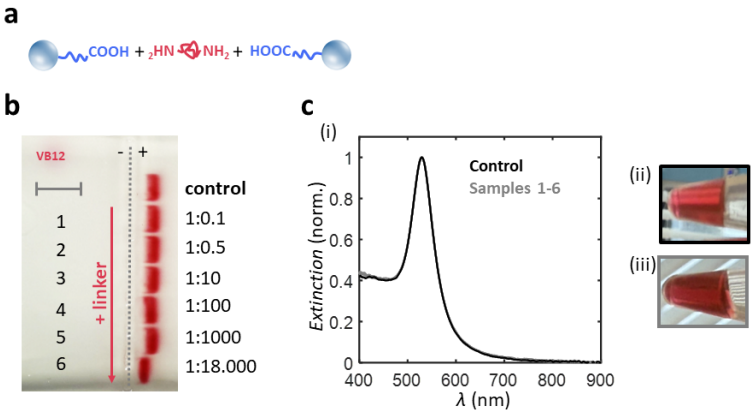

Figure IV-11. EDC/NHS reaction assembly with diamino-PEG dummy linker, homo-type. (a) Assembly sketch: the diamino-PEG is attached on two sides via NHS chemistry to activated carboxy-PEG particles. (b) Agarose gel of a control sample of activated carboxy-PEG particles and a titration of the diamino-PEG from a particle-to-ligand ratio of 1:01 to 1:18000. Scalebar: 1 cm. (c) UV-Vis ensemble spectra of samples from b, showing no change between the control sample and those with ligand. (d) Photographs of samples from b and c (control in black and sample 6 in grey) showing no color change after overnight incubation.

According to these observations, the maleimide and EDC/NHS chemistry are both equally ineffective in forming assemblies with the homo method. This is especially curious because carboxy particles have shown better stability compared to amino particles. This factor however does not appear to play a significant role in success.

To further test if this chemistry is viable when the particle is more reactive, I increased the fraction of carboxy-PEG end groups and repeated the titration. I expected that the increased reactive end groups would lead to assembly. However, I observed a complication instead of assembly which I explain as follows.

Figure IV-12a shows a gel image of a ligand titration to a sample of activated 75% carboxy-PEG particles, as done previously for the 10% carboxy-PEG particles. The gel shows an expected increase in particle band mobility to the anode in accordance with the increased negative charge from the carboxy groups. The mobility is slightly decreased when particles are activated successfully with EDC/NHS. Despite successful activation and a higher reactive end group fraction, the titration of the diamino ligand does not make a change.

At the same time, additional weakly colored bands are seen in both the original stock as well as in the activated particles. This observation is reproducible across several repeated experiments (see Appendix C for more examples). The second band can be isolated and observed in the TEM (b), revealing discrete dimer constructs. In chapter 3, I have reported on this finding more extensively. Here I remark that the presence of these nonspecific constructs in the monomer particle batch made no difference for the titration experiment. It is however curious that the nonspecific constructs are able to form during the functionalization step, but the ligand mediated assembly fails. This suggests that the nonspecific constructs are forming due to larger-scale interactions, as compared to a single-group reaction required for the specific assembly.

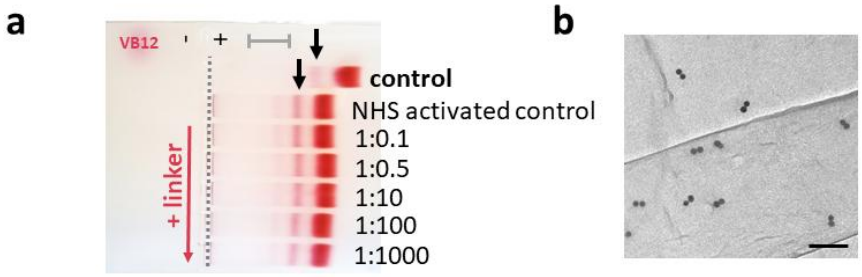

Figure IV-12. Multimer constructs appear in carboxy-PEG functionalized particle stock. (a) Gel electrophoresis image of 75% carboxy-PEG particles, EDC/NHS activated particles and the titration of the diamino-PEG. Arrows mark the dimer band present both in the control carboxy-PEG sample and the EDC/NHS activated samples. Scalebar: 1 cm. (b) TEM image of the isolated second band. Scalebar: 400 nm.

The key observation here is that increased particle reactivity does not increase success for the homo-type assembly. Similar to the maleimide chemistry, this could mean that either (1) the reactivity of this system is lower than expected, or (2) that the PEG linker cannot connect to the second particle, for example due to being connected with both ends to the first.

To test if the ligand is the weak point in this assembly type, I changed from the homo to **hetero-type** assembly, as sketched in Figure IV-13a.

For this, I mixed 10% amino-PEG particles with either 10% or 50% carboxy-PEG[xxxi] particles at equal volume ratios. Interestingly, I observed that simply mixing and

[xxxi] I continued using carboxy-PEG particles, knowing that they contain small amounts of nonspecific constructs. Because of their neglectable amount, they should not disturb the assembly.

incubating the two particle types does not lead to a change of the sample color (b). However, a one-time centrifugation of the mixed sample shows instant color change from red to violet. The change is less pronounced for the 10% carboxy sample, and strong for the 50% one. This is a positive outcome, because it aligns with the expectation of a higher reactivity leading to a higher aggregation rate. It is however curious that centrifugation is necessary to trigger aggregation. This suggests that the reaction is inefficient as a freely diffusing system, and needs forced close proximity between the particles to proceed. Most interestingly, further centrifugation steps made no difference.

The gel electrophoresis supports the above findings. As seen in (c), the 10% carboxy/amino-PEG particle mix separates into the monomers, with additional bands appearing in between. This example shows why interpretation of hetero-type assembly gels is more challenging: The dimer construct carries a mixed charge of the monomers and is additionally double the size. If the dimer is the only other construct present, then it can be discerned as the band approximately in the middle between the monomer bands. However, higher order constructs complicate this picture. My attempt to collect and assign the bands marked in (c) showed a heterogeneous result when imaged in TEM (d). Most constructs I found were monomers, with dimers also present.

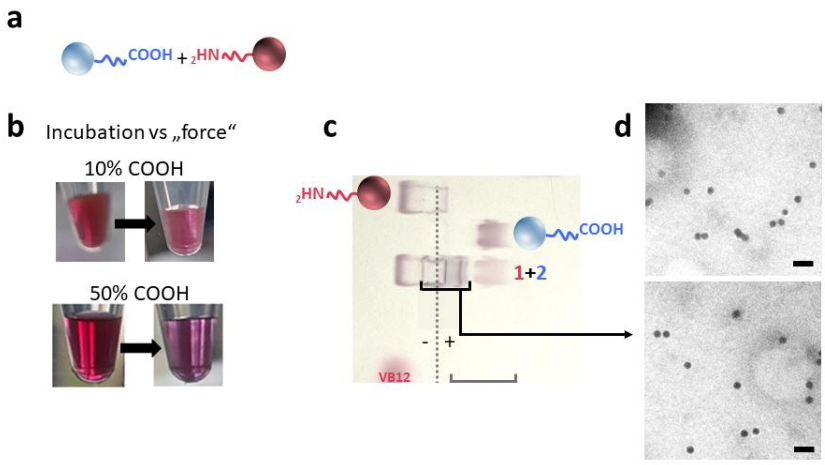

Figure IV-13. Hetero-type assembly of carboxy- and amino-PEG particles. (a) Sketch of hetero-type assembly: a carboxy-PEG particle is activated with EDC/NHS and coupled with an amino-particle. (b) For the 10% carboxy-PEG sample, centrifugation leads to slight loss of color. (c) Gel electrophoresis image of 10% carboxy- and 10% amino-PEG particle samples, as well as the assembly product after a 1:1 combination and centrifugation of the two. The assembled mixture splits into the respective monomers, as well as additional bands. Scalebar: 1 cm. (d) TEM images of the extracted constructs between the two monomer bands. Scalebar: 200 nm.

On the whole the hetero-type assembly is not suitable for batch synthesis due to difficulties in cleaning and gel band interpretation. However, generally it shows success under additional force. With this in mind, there is a possibility that the homo-type assembly may also work under additional force, such as the hetero-type.

I did not further pursue this question because the application of force is a risk factor for the future assembly with the protein. As such, the EDC/NHS chemistry is a possible option, but not an ideal one. Therefore, I do not recommend it for the Hsp90 dimer assembly.

3.4. Biotin-streptavidin assembles reliably

The biotin-streptavidin (SA) bond is well known in literature, and is in use in a variety of bioconjugate techniques, e.g. in immobilization of ligands[124] or even in force spectroscopy as by connecting beads in optical traps. Biotin is a relatively small molecule with a weight of only 244.3 g/mol.[125] Streptavidin is a ca 60 kDa protein[126] that can bind up to four biotin molecules. Their interaction is described with a dissociation constant of 10^{-15} M,[127] and is among the strongest non-covalent biological interactions.[xxxii] Their complex is robust against pH fluctuations as well as e.g. washing steps,[127] which is an important and critical point for dimer purification. This bond has been shown to work in particle self-assembly, e.g. by connecting rod-shaped particles into long strings.[131] In the following, I show that this chemical system also works reliably in the assembly of particles for our dimer experiment.

To compare the reactivity of the biotin-streptavidin chemistry against the others, I repeated the assembly and titration experiments as explained before (3.2-3.3). Figure IV-14a shows the **homo-type** assembly structure. Here, two biotin-PEG particles are connected with a streptavidin (SA).

Figure IV-14b illustrates the titration experiment in the gel. The samples display an expected reduced mobility in the process of saturation with streptavidin. This is because streptavidins contribute to the particle size. Contrary to the previous examples, saturation is not the only effect seen. Additional bands appear between ratios of particle-to-streptavidin of 1:10 and 1:1000. The band in 1:000 loses color due to aggregation. The sample 1:100 aggregates completely, as seen in the absence of a band and dark aggregated residue in the gel pocket. This aggregation is also noticeable in the color of the samples (c): The 1:100 sample is violet compared to others.

The difference between the 1:1000 and 1:100 samples is in the stronger saturation with streptavidin for the first. For the 1:1000 case, the streptavidins block free biotin anchors before those can react to other particles.

Ensemble spectra support these results, with 1:100 and 1:1000 samples showing significant broadening typical of aggregation (d). The broadening is strongest for the 1:100 sample, in accordance with the gel result. The yield of constructs in the 1:10 sample however is still too low to show significant broadening or resonance shift of the ensemble spectrum. This is also in part because of a large interparticle distance.

[xxxii] The exact biological function of the biotin-streptavidin interaction is not entirely understood. Streptavidin is found in *Streptomyces avidinii*, and is similar to its cousin avidin which is found in egg whites. In the case of the egg whites, the binding to the biotin is said to serve as an anti-microbial protection. Since biotin is an essential vitamin and critical for e.g. bacterial growth, its lack prevents bacterial growth in the egg white. Streptavidin is said to serve a similar role in competition between different bacterial species.[128–130]

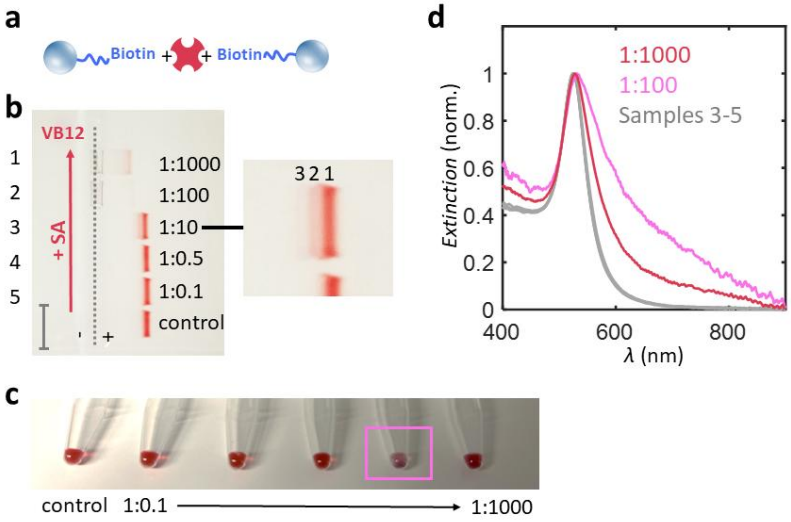

Figure IV-14. Key findings of the biotin-streptavidin homo-type assembly. (a) Sketch of the dimer assembly: two biotin-PEG functionalized particles are connected with a streptavidin (tetramer). (b) Agarose gel of a control sample of biotin-PEG particles and a titration of the streptavidin. Scalebar: 1 cm. (c) Photographs of samples from b, showing discoloration of the 1:100 sample (marked in pink). (d) UV-Vis ensemble spectra of samples from b.

Chemically, the reaction is successful as compared to the previous two. One important point is however that the reaction is not finished after 30 min, as the theory predicts. The samples 1:100 and 1:1000 decolorate further. Additionally, the theoretically best predicted ratio of particle to linker of 1:0.5 does not yet show signs of assembly, further suggesting that 30 min are not sufficient to reach equilibrium with the biotin-streptavidin assembly with our particles.

Nonetheless, several points speak for this chemistry as a good alternative to the maleimide and EDC/NHS:

(1) Firstly, this reaction shows assembly within the 30 min as compared to the other two, even if the reaction is not yet in equilibrium state.

(2) Secondly, the success of the homo-type assembly weakens the theory of our protein attaching with both ends to the same particle.

For the last point, I theorize that an unwanted two-end attachment is less probable for stiff and big proteins. For the streptavidin, this is because the first attachment orients the protein in such a way that the remaining binding sites show upwards and away from the first particle. Because Hsp90's linking sites are also located on the opposite sides, it can behave similar to streptavidin.

With this in mind, the biotin-streptavidin assembly is a good starting point for an improved Hsp90 plasmon ruler assembly. The current assembly however has a drawback, which is a large interparticle distance. Streptavidin adds approximately 5 nm to the interparticle distance,[132] and the PEG layers make up between 6-15 nm in total (see chapter 3). Hsp90 contributes 10.5 nm on average. If two streptavidins are used for both sides, this amounts to a minimal interparticle distance of 32.5-50.5 nm. This distance is too large for detecting protein motion via plasmon coupling. Even if the distance added by the polymer is optimized, streptavidin still adds 10 nm to the assembly.

The question now is: How can the working biotin-streptavidin chemistry be transferred to a viable assembly strategy? There are several possibilities, two of which I sketch as concepts in Figure IV-15.

The task is to shorten the interparticle distance. This can happen by removing or shortening components. One such way is to forego the PEG layer by attaching the streptavidin directly onto the particle (a). Another option is to use the smaller mono-streptavidin (b). With only about 15.5 kDa, this monomeric streptavidin is smaller (with a hydrodynamic diameter of approximately 3.3 nm).[132] Its affinity is typically weaker compared to the tetrameric streptavidin. But modified options exist, showing comparable bond strengths.[126] As such, it is a viable replacement.

Figure IV-15. Sketch of possible hetero-type assemblies. (a) A biotin-PEG functionalzed particle is coupled with a tetrameric streptavidin particle. (b) A biotin-PEG functionalized particle is coupled with a mono-streptavidin particle.

To test the usefulness of these strategies for the protein dimer assembly, I aimed to compare the two in proof-of-concept assembly experiments.

For strategy (a), I activated tetrameric streptavidin with a DTSSP reagent (3,3'-dithiobis(sulfosuccinimidyl propionate)), which reacts with primary amines on the protein and introduces a disulfide. In a following step, I attached the protein to a particle via the introduced disulfide. Protocols are listed in the Appendix C.

For strategy (b), I attached a mono-streptavidin via a His-tag to a DNA-NTA pre-functionalized particle.

I encountered complications with both strategies, which I list below.

Strategy (a) posed a challenge in the particle functionalization step (Figure IV-16a, reaction with DTSSP). I used protocols previously reported by our group, [51] and at first I could show successful reaction by characterization of the sample in the gel (b). As expected, the mobility of the citrate-capped particles is reduced by attachment of streptavidin. However, as the photo in (c) illustrates, the particles aggregate when left to stand in solution. Additionally, I observed aggregation during washing steps by centrifugation, which are important for following assembly steps.

Figure IV-16. Particle modification with tetrameric streptavidin. (a) Sketch of the attachment procedure of streptavidin (tetramer) via DTSSP to a gold particle. (b) Gel electrophoresis image of citrate-capped particles and the same batch incubated with DTSSP-activated streptavidin. Scalebar: 1 cm. (c) Photograph of a dark residue in a streptavidin particle sample.

Therefore, this functionalization protocol needs further improvement.

Contrary to this, strategy (b) showed no problems in the first particle functionalization step. As sketched in Figure IV-17a, the aim is to test how readily a mono-streptavidin particle assembles with a biotin one. As the gel image (b) shows, I could successfully attach the mono-streptavidin to DNA-NTA particles. The resulting band shows slower mobility due to increasing particle size.

To ensure that mono-streptavidin is reactive in principle, I additionally incubated it with biotin-PEG particles but without attaching it to a particle first. The gel image (b, right) shows successful reaction: The mobility of the biotin-PEG particles changes upon incubation with the mono-streptavidin.

However, the addition of the respective biotin and streptavidin particles to one another did not yield any visible change, despite the first two successful steps. The gels show no change apart from the monomer bands separating (c, i), and the individual samples retain their color, even when incubated for several hours and concentrated up to a dispersion of 8 nM (c, ii+iii).

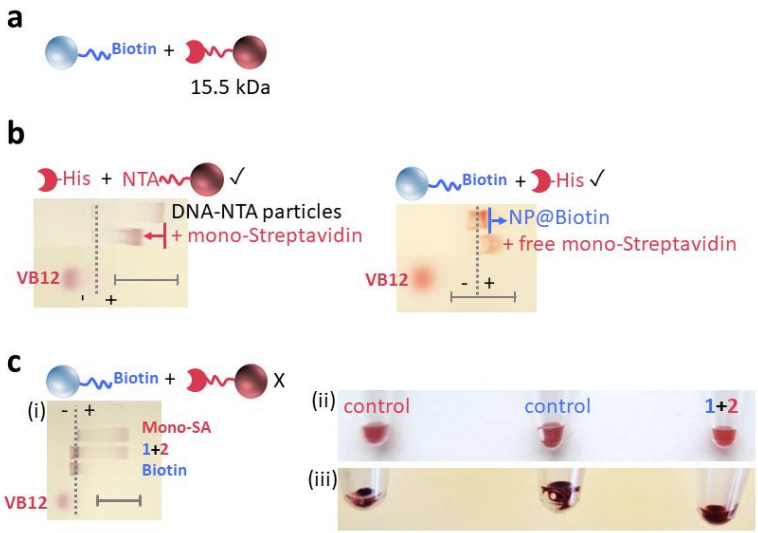

Figure IV-17. Mono-streptavidin assembly results. (a) Sketch of the assembly. (b) Gel of DNA-NTA particles and mono-streptavidin (left). Gel of biotin-PEG particles and the same batch reacted with mono-streptavidin. (right). Scalebars: 1 cm. (c) Gel of mono-streptavidin particles, biotin-particles and their mix (i). Scalebar: 1 cm. Mixed samples remain the same color (ii), and centrifugation and incubation in a pellet (at a particle concentration close to 8 nM) do not produce any visible reaction (iii).

These observations suggest that either mono-streptavidin is less reactive due to possessing only one reactive site for the biotin, or that it is geometrically aligned in such a way that it is no longer available for reaction. It is therefore not a viable option for the protein dimer assembly.

In summary, the reactivity of the biotin-streptavidin chemistry is superior to that of the maleimide and EDC/NHS. The homo-type assembly possesses the drawback of a large interparticle distance due to the size contribution of the streptavidin. Attempts to solve this challenge showed complications in the form of unstable particles. Additionally, mono-streptavidin is not as reactive as its tetramer. This has implications when compared to the maleimide and EDC/NHS chemistry, suggesting that streptavidin's advantages lie in its number of reactive sites. With this conclusion, the tetrameric streptavidin is the better option for assembly. However, streptavidin-functionalized particles require further optimization to ensure particle stability for a reliable assembly.

Compared to the streptavidin-based assembly, DNA-based particles offer more flexible tuning of interparticle distance and even better reactivity, as I show as follows.

3.5. DNA-DNA hybridization is the most robust assembly in both homo- and hetero-type assembly

In this section I introduce the DNA-based chemistry in greater detail to explain the advantages and constraints. This information is necessary to understand why I chose a certain assembly strategy. The aim of this introduction is also to serve as a reference for future optimizations of this protocol.

Assemblies based on DNA-DNA hybridization present the most flexible option of the introduced assembly strategies, as I explain as follows. This assembly method works through hybridization of any two complementary DNA strands. In literature, this assembly strategy is commonly known under the general title of "DNA origami".[133] It utilizes smart combination of base pairs, strand lengths and assembly geometries to form a variety of complex nano assemblies. There exist many reports of such assemblies, also featuring gold particles in various shapes. Most often, such assemblies are used in RAMAN-enhanced sensing applications.[134–136]

Despite their versatility, DNA hybridization has certain constraints. Stability of hybridized constructs depends on a number of factors, among them salt conditions for charge screening reasons, temperature, specific sequence, as well as the number of overlapping base pairs.[137,138] In particular, the dissociation rate of the hybridized strands is connected exponentially to the number of base pairs.[139] Nine overlapping base pairs are reported to have an average dwell time of 42 s.[139] Hour-long stability is reported starting from a minimum number of 12 overlapping base pairs, with the approximate threshold of 15 base pairs considered a safe overlap for long-term stability.[136,140]

I considered the contribution of the DNA to the interparticle distance first to estimate the suitability of this strategy for the protein dimer assembly. A double stranded 15 base

pair DNA has a length of 5.1 nm.[141][xxxiii] This is similar to the range of previously assumed polymer spacer length. However, if additional stabilizing molecules or a layer is added under the DNA (compare results in chapter 3), then the interparticle distance grows accordingly.

The DNA origami community offers a solution to this problem, which I document here for future reference. As sketched in Figure IV-18a, the single-stranded DNA is usually attached with its 5' end to the particle. This leads to a pairing in the "shear" type of geometry during assembly. The interparticle distance corresponds to the length of this double strand. However, if one DNA strand is instead attached with its 3' end to one particle, then a "zipper"-like hybridization geometry can be achieved (b).[143] This geometry can save interparticle space, but requires free lateral space along the particle surface.

For my proof-of-concept studies with DNA, I used the "shear" geometry shown in (a). For future protocols, such as when particles are pre-passivated, I recommend to move to strategy (b) to save interparticle distance.

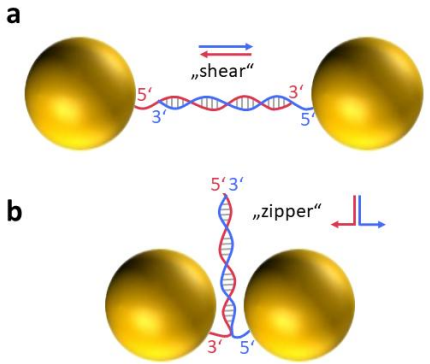

Figure IV-18. Illustration of two possible hybridization geometries. (a) "Shear" geometry: the DNA strands are both attached with their 5' ends to the respective particle. (b) "Zipper" geometry: one DNA strand is attached to the respective particle with its 3' end instead, forcing hybridization in a direction along the particle surface.

After selecting a suitable hybridization geometry, I needed reliable DNA sequences. For this reason, I used the DNA sequences from [40]. These sequences have been previously used successfully in optical trap experiments, which eliminates the danger of failure due to a nonideal sequence choice. In my experiments, I attached the DNA strands with a thiol to the particles,[135] in a similar way to the PEG protocol. All sequences are listed in respective figures and protocols are in the Appendix C.

To see if the DNA-based assembly can substitute the biotin-streptavidin one, I tested the assembly in the **homo-type** (Figure IV-19a). Because the biotin-streptavidin assembly showed no issues related to the two-sided attachment to the first particle, I used Hsp90

[xxxiii] Calculation for a double stranded DNA dublex goes according to: *length*=0.34 nm·*number of overlapping bases*. Note that this calculation is applicable to hybridized DNA, not for single stranded DNA. The single stranded DNA is longer. Additionally, both values are salt-dependent, so caution needs to be taken when estimating its length.[142]

directly instead of a dummy. For this, the Hsp90 (T285C) protein was functionalized on both cystein-modified sites with complementary DNA strands via maleimide coupling.[xxxiv]

The reproduced titration experiment (compare 3.4) shows results similar to the biotin-streptavidin assembly. Firstly, samples display a discoloration characteristic of aggregation (b). The peak of this discoloration is at the particle-to-protein ratio of 1:100.

In the gel characterization (c), titration of Hsp90 slows the particle mobility. This is because in this case, the size increase by the added protein outweighs the charge effect. Samples with a particle-to-protein ratio between 1:10 and 1:1000 show the strongest band discoloration. The biggest difference is a lack of the multiband structure characteristic of assembly. The reason for this is the heterogeneity of the DNA particle sample, seen in the broad band and smearing in the control band.

Ensemble spectra mirror this trend (d): The samples with the biggest discoloration, 1:100 and 1:1000, show a broadening of the FWHM indicative of aggregation.

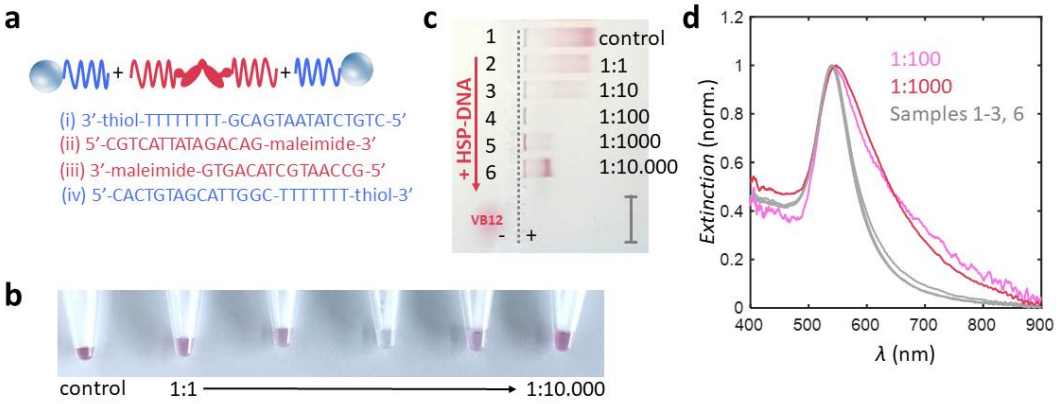

Figure IV-19. Homo-type assembly with DNA-modified Hsp90. (a) Assembly sketch: Particles are modified with thiol-capped DNA, and the Hsp90 is modified via maleimide chemistry with two identical, complementary strands. i-iv show respective color-coded DNA sequences.[40] (b) Photograph shows the control DNA particle sample, as well as samples containing particle-to-protein ratios ranging from 1:1 to 1:10.000. Similar to the biotin-streptavidin samples, the ratios 1:100 and 1:1000 show the strongest discoloration. (c) Gel electrophoresis image of particles in b. Image shows the control DNA particle sample and the titration of the DNA-Hsp90 with increasing particle-to-protein ratios. Scalebar: 1 cm. (d) UV-Vis ensemble spectra of samples from b.

The data shows that homo-assembly is possible with the DNA-modified Hsp90 protein. Unfortunately, further characterization is impossible due to the low particle quality. In particular, my DNA particles aggregated over time in the PBS and HEPES buffers used for assembly with the protein. I address and solve this problem in the second part of this screening.

To further test the flexibility of the DNA assembly and enable comparison with the previously introduced chemistries, I completed this screening with the **hetero-type**

[xxxiv] Protein and functionalization were kindly provided by the Hugel Group in University of Freiburg.

assembly. As a proof-of-concept, I did this study without the protein. Additionally, I addressed the particle stability problems by pre-passivating them as documented in chapter 3.

I first pre-passivated the particles with PEG. Then, for a fair comparison to the other chemistries but specifically the maleimide one (3.2), I tuned the number of DNA strands with the number of PEG anchors, setting it to 10%. The resulting assembly concept is illustrated in Figure IV-20a. The complementary particles are combined at a volume ratio of 1:1 and characterized after 30 min.

Figure IV-20b displays the characterization in the gel. Notably, the control bands of the monomer particles show a more defined shape, no smearing and no aggregation, meaning that the additional passivation step reduced particle heterogeneity and improved stability. The zoom in on the right shows multiple bands of the formed constructs.

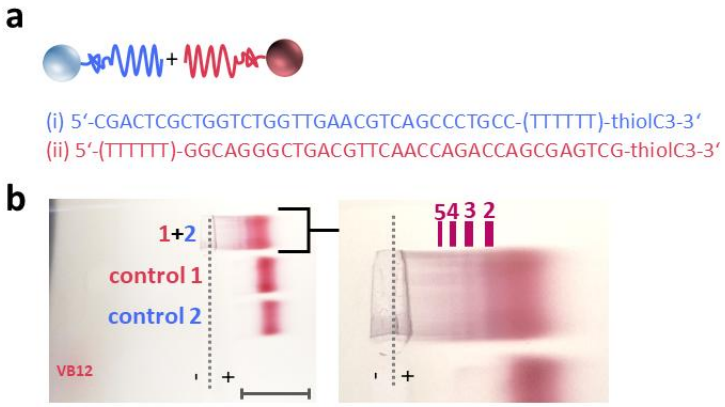

Figure IV-20. Hetero-type assembly, without Hsp90. (a) Sketch of the DNA-modified particles. The particles are pre-passivated with a methoxy-PEG and maleimide-PEG (2000 g/mol, 3000 g/mol). Thiol-capped DNA strands are attached via maleimide chemistry. In this example, the DNA is fixed at 10% via maleimide anchors. i-ii show the DNA sequences.[40] (b) Gel electrophoresis image of DNA particles (control 1 and control 2 are color coded according to sequences in i-ii), as well as the mixed sample. Closeup of the mixed sample (right) shows multiple bands beside the monomer band. Scalebar: 1 cm.

The results show that DNA-based assembly is flexible and successful regardless of assembly concept. Most importantly, it is more effective than the maleimide chemistry that serves as a basis for comparison.

Following this success, I decided to go one step further and explore the limit of the reaction efficiency as compared to the fraction of DNA strands on the particle. As previous successful tests with the EDC/NHS chemistry show (3.3), the assembly depends on the number of reactive sites. For the EDC/NHS case, the reaction was not yet at its optimum even at a fraction of 50% of end groups, as seen by the unreacted monomer bands separating in the gel.

For the comparison, I tuned the DNA fraction on a particle, resulting in samples with 1%-10%-50%-100% DNA.[xxxv] Similar to the first study, I mixed the complementary particles in equal volume and incubated them for 30 min. Figure IV-21a shows photographs of the study, with (i)-(iv) sequentially displaying the control monomer samples in the HEPES buffer and the mixed sample below. As a main observation, the particles retain their color in the HEPES buffer, signifying their stability even at higher ionic strengths. Secondly, no assembly is seen at lower ionic strength (ii, lowest sample). This underlines the importance of charge screening for assembly success. Lastly, the maximal discoloration happens already at 10% DNA, and increased DNA content does not improve this. Ensemble spectra of the mixed samples support this (b): All samples show broadening, with significant increase happening between 1 and 10%.

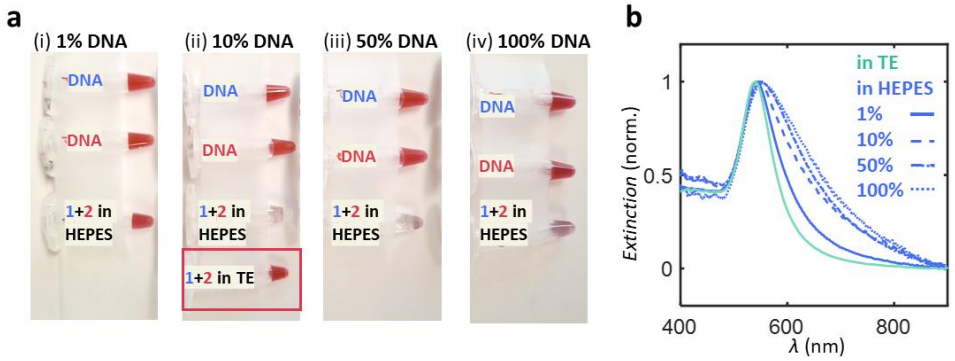

Figure IV-21. DNA-fraction dependent assembly speed. (a) Samples i-iv show control particles with complementary DNA strands (in red and blue), and a 1:1 mixed sample of both in HEPES buffer, after a waiting time of 30 min. To show the importance of salt for hybridization, a mixed sample with 10% DNA is shown in low-salt TE buffer (ii). (b) UV-Vis ensemble spectra of mixed samples from i-iv, with DNA% recorded in the legend.

The results of this study are helpful for future assembly design. Knowing that 10% of DNA anchors are already sufficient for maximal reactivity within the time frame of 30 min, study sets a reference point for future particle optimization.

Overall, both the homo and hetero-type assembly concepts show positive assembly results. The key points to success are well-passivated and optimally functionalized particles. This is especially important because more heterogeneous particles lead to smearing bands in the gel agarose experiments, and low stability in experimental buffers such as HEPES and PBS. In addition, DNA is an expensive component. It is therefore be better to use a cheaper polymer for passivation, and add only as much DNA as necessary for optimal reaction. For this, my study gives a useful reference point. In terms of assembly type, homo assembly is preferred due to simplicity, but hetero assembly works just as well. Both assembly methods are also suitable for both sequential synthesis in a flow cell and in batch. Constructs can be easily identified in gel electrophoresis due

[xxxv] Further, I improved the grafting protocol with the DNA. This is why in the following examples, the 10% DNA sample results in total aggregation that is not yet seen in the first study. The improved protocol is documented in the Appendix B.

to both particle types having the same charge and similar mobility. This makes this assembly strategy the most versatile and promising of all methods explored.

4. Summary and Conclusion

At the beginning of this chapter, I introduced three main theories why assembly fails. The screening addressed these theories, showing weaknesses in the assembly and providing guidance for an improved assembly protocol.

An important result is that the protein is not a source of failure. Previously theorized binding of the protein with both reactive ends to the same particle is also not the case, as demonstrated first with successful assembly with streptavidin and then with a DNA-modified Hsp90. On the other hand, the bottleneck that mainly decreases assembly success is the efficiency of the linkers connecting the two particles.

Upon giving answers to these theories, I found key aspects that improve the assembly process.

First, regarding best linkers for assembly, I found the biggest advantage in the DNA-DNA hybridization. These linkers are highly reactive, have tunable length as well as hybridization geometry. The last two points are important for the adjustment of the best interparticle distance for optimal plasmon coupling. For the reason of higher flexibility, I recommend this strategy over the comparably efficient biotin-streptavidin coupling.

In terms of assembly approach, the homo-type assembly approach is the best due to its simplicity. It requires the optimization of one particle type only. Additionally, the dimer constructs made in a batch synthesis can be easily identified in a gel electrophoresis experiment and separated for measurement. In this context, the batch synthesis method has the advantage of retrospective enrichment of the dimers in a sample. This way, more dimers can be simultaneously measured in a single experiment, improving the statistics. Looking beyond the current goals of the Hsp90 plasmon ruler project, the batch synthesis offers additional benefit of mixing and measuring different proteins at the same time in a single experiment.

Lastly, two additional steps are yet necessary to improve the current protocol's robustness. Here I leave a roadmap for these future steps, based on the findings of my proof-of-concept studies.

As the assembly study with the DNA-modified Hsp90 protein has shown, the DNA functionalization of the particles requires further improvement. In chapter 3, I have laid out the reasons and necessary steps. Briefly, an additional passivating layer below the DNA will ensure better stabilization, as shown in my last study where I employed PEG for this role. At present, the proof-of-concept layer is too thick and the interparticle distance too large for plasmon coupling. Additionally, chapter 3 has shown that PEG is not ideal due to the possibility of gaps in the polymer layer.

Therefore, a promising direction for the next-generation particle is an alkyl-type of underlayer. Literature shows that it offers more protection against unwanted (protein) adsorption, especially when compared to simple PEG layers.[144] The reason for this

appears to be an additional hydrophobic shielding effect that blocks the gold surface from potential nonspecific interaction, especially with molecules that contain thiols in form of cysteins.[115]

With these two steps, the future particle will fulfill the necessary requirements of passivation against nonspecific interactions, colloidal stability and reactivity.

V. PLASMON RULER MEASUREMENTS REQUIRE ASSEMBLY CONTROL

To understand the function of a protein it is important to study the behavior as fast as possible and on a long timescale. The intensity-based sensing developed in our group brings these advantages over several other single-molecule based methods. Our method is capable of measuring the protein at a resolution of 20 ms for 24 h, with a factor 4 of better signal-to-noise ratio compared to single-molecule FRET.[49]

The complication is that the measured signal requires additional (and often external) validation. This is especially the case for a batch-type assembly,[xxxvi] where no spectroscopical in-between characterization steps can guarantee that the measured signal originates from a properly assembled construct.

In the case of the Hsp90 assembled dimer, the validity of measured data has hitherto been guaranteed by comparison with available FRET data in terms of measured dwell times. However, FRET data is limited in time dimension, and the plasmon ruler's task and main motivation is to expand on its data and give a deeper insight into long-term protein behavior. When new dwell times or signal types are found with the plasmon ruler, they can no longer be verified with FRET. For this reason, it is especially critical to have control over the plasmon ruler assembly and assurance that newly discovered data can be traced back to the protein behavior.

In a previous work on the plasmon ruler by Bastial Flietel,[52] a new type of signal was discovered when measuring batch-synthesized Hsp90 plasmon rulers. This signal consisted of a multi-state pattern, as compared to the previously measured two-state pattern indicative of the protein's "open" and "closed" conformation. Similarly, the dwell times were in a comparable range with previously reported ones.[49] Using the established and previously tested control method of stopping the fluctuation signal of the protein by locking it to its closed state with adenylyl-imidodiphosphate (AMP-PNP),[49] the fluctuation signals stopped as expected, albeit not in all cases. Therefore, the nature of the novel fluctuating signals was not yet entirely clear. This topic remained of high interest for the project: If the signal originates from the protein, then this would be an interesting expansion on the previously known protein behavior. If the signal is an artifact, then this is still a positive outcome, because it helps improve the method and eliminate non-protein related data.

[xxxvi] As introduced in the first chapter.

In this chapter, I show the discovery of such patterns in PEG-functionalized samples in the absence of the protein. Here, the origin of these patterns is traced back to two key aspects: the weak interaction between the particles and the substrate in the presence of the buffer used for Hsp90 measurements, as well as the presence of nonspecifically assembled dimer (and possibly higher-order) constructs that are the culprit behind the protein-like fluctuation patterns in the time traces. Using control measurements, I show the importance of covalent attachment of the particles to the substrate, as well as the need for more control and characterization over the particle stock used for the protein dimer assembly.

1. PEG-functionalized particles without protein show similar, multi-state behavior in rare cases.

An important part of a well-controlled measurement is the preliminary characterization of the monomers. This serves as a reference for the typical additional measurement noise that is not related to the protein motion. Here I report how the characterization of the monomers led to the discovery of the protein-like traces in the original particle batch.

Similar to previously reported procedure,[49] particles are deposited onto a glass substrate previously washed with a 30% Hellmanex solution and then water, before switching to the measurement buffer (HEPES, pH=7.4). Thereafter time traces are taken. To conform with previous measurements,[52] the time traces have an exposure of 100 ms, and a duration of 30 min.

As expected, the measurements show single particle time traces with random noise σ[xxxvii] below 2% depending on the initial particle intensity I ($\sigma \sim I^{1/2}$), typical of PEGylated particles (Figure V-1a-b). Surprisingly however, in around 1% of traces across various measurements, discrete multi-step patterns are found (c-d), identical to previous measurements done with batch-assembled Hsp90 dimers.[52]

[xxxvii] σ is calculated using the standard deviation over the time trace.

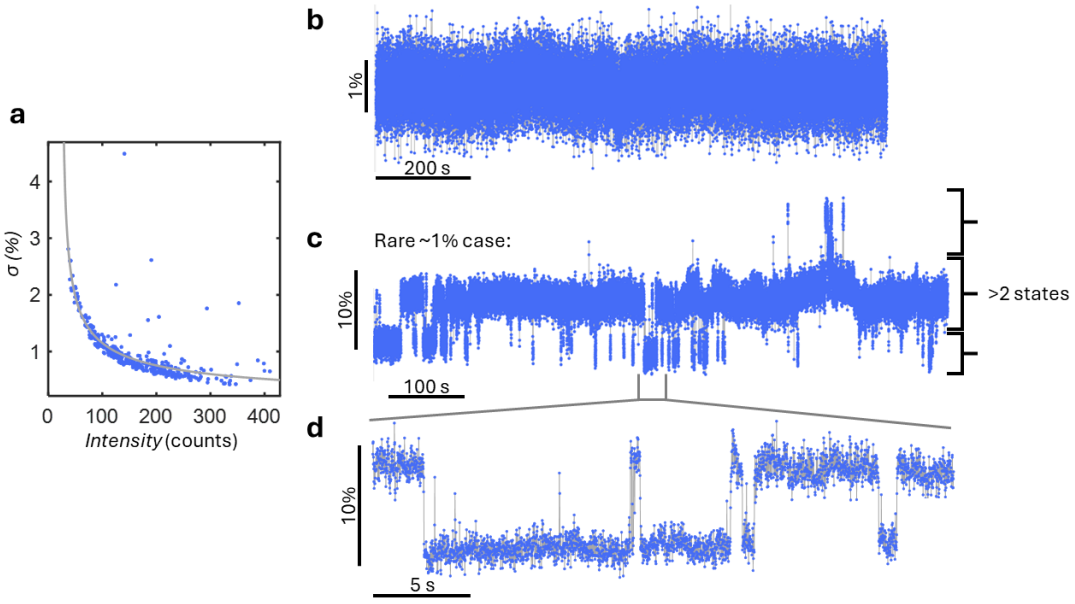

Figure V-1. Multi-state time traces found in monomer samples without protein. (a) Noise σ plot over intensity I of time traces of a total of 449 single particles. ($\sigma \sim I^{1/2}$) (b) A typical time trace of a single particle, corresponding to the statistical noise. The y-axis corresponds to relative intensity in %. (c) A time trace showing a step-wise three-state pattern, similar to previously reported and not understood multi-state time traces in Hsp90 batch-assembled dimers. (d) A closeup of the trace in c, showing the discrete step pattern with dwell times in the second's range.

Roughly, the observed time trace patterns can be distinguished by the fluctuation intensity as well as their pattern type. Figure V-2 shows two example time series for the different intensity cases. The trace in (a) shows multiple steps. When looked at separately, two steps marked in the figure show a fluctuation range of only 3-4%. On the other hand, the time trace example in (b) shows a range well above 10%. In addition, this time trace shows a bigger trend of varying fluctuation intensity.

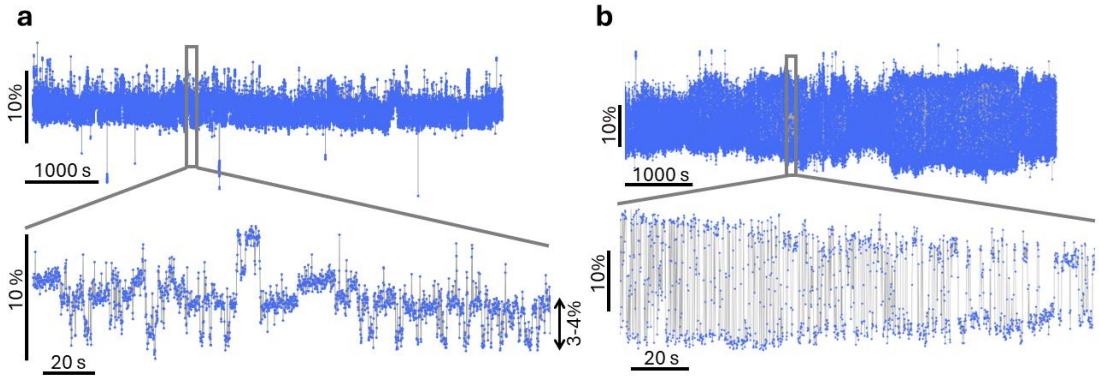

Figure V-2. Examples of the time trace fluctuation range. (a) Example of a time trace with intensity fluctuations in the range below 10%. (b) Example of a time trace with varying intensity range and above 10%.

The heterogeneous nature of data also shows in the types of recorded patterns (Figure V-3). Similar to previous work,[52] time traces with a distinct two-state pattern (similar to the ones expected of dimers with a dynamic protein) are found along with multi-state time traces, as well as more chaotic ones with intermediary distinct states. For some time

traces, the discrete step-pattern behavior can stop randomly or change without further experimental input.

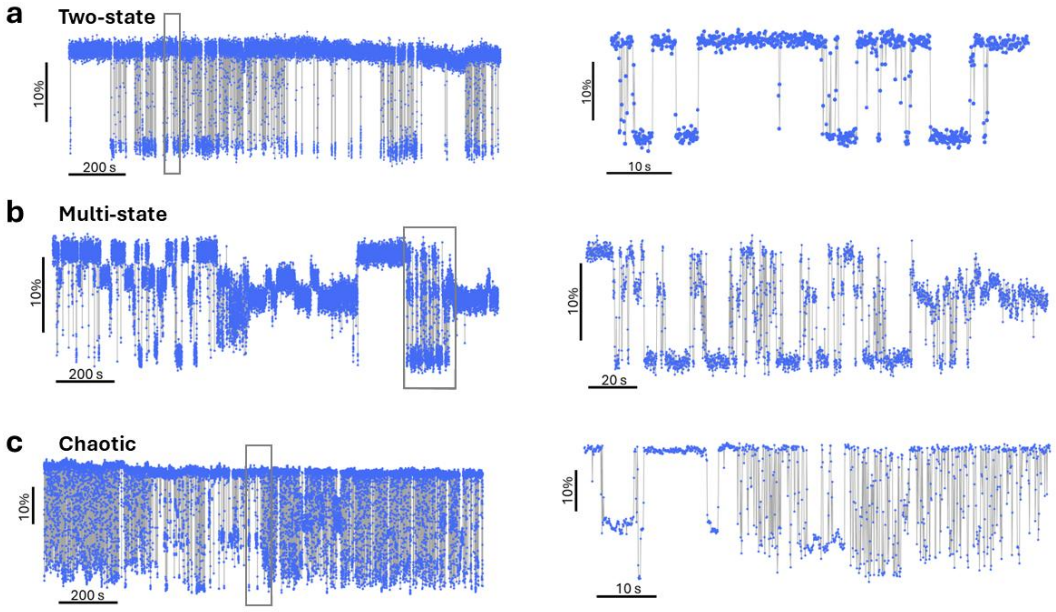

Figure V-3. Examples of time traces with a step-like pattern, with close-up (right). (a) A two-state time trace. (b) A multi-state time trace with at least four distinguishable states. (c) A time trace containing both regions with discrete steps and more chaotic patterns.

This discovery raises important questions about the nature of this data and when exactly it occurs. Understanding it is critical for the future of the plasmon ruler, because the occurrence of such artifact traces is as often as that of previously recorded protein time traces.[52] Their random fluctuation nature poses a challenge for distinction from protein related time traces, at least for methods that rely on e.g. locking the protein in one state and stopping the fluctuation.[xxxviii] Additionally, the seconds-range dwell times similar to the protein traces are a further reason to investigate their nature and/or eliminate them from the future measurements.

2. Theories

Understanding the source of fluctuations is key to eliminating their presence. Intensity based measurements are sensitive to various changes in the particle environment, such as plasmon coupling due to a close by particle or a variation in the local refractive index.[145] In our measurement configuration, the local refractive index around a particle is composed mainly by the substrate (glass), as well as the medium. The refractive index is affected by a number of factors, such as distance to the substrate, local fluctuations in ionic strength and the presence of contaminations. Any of these factors may be present

[xxxviii] Previously, this was done by incubating the plasmon rulers with adenylyl-imidodiphosphate (AMP-PNP) and therefore locking the protein in its closed state.[49]

at the same time in a given measurement. For discussion purposes, I separate these topics into three categories: the substrate, the contaminations and plasmonic coupling effects.

Figure V-4 illustrates possible scenarios arising from these interferences with the measurement. Below I briefly comment on each case.

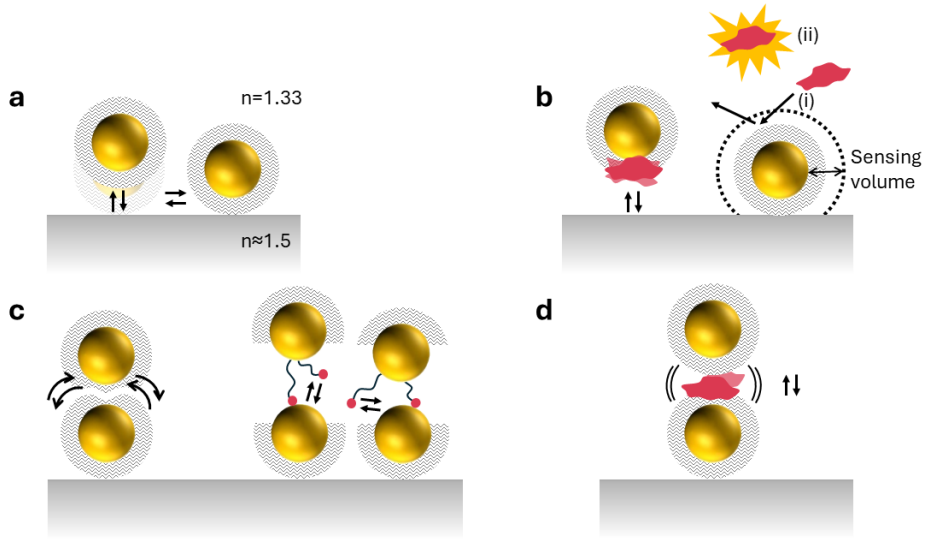

Figure V-4. Possible scenarios leading to artifact time traces in intensity-based particle measurement. (a) The substrate effect: Glass typically has a higher refractive index than the buffer (n=1.5 vs n=1.33). Thus, movement against the substrate can lead to a periodic change of the local refractive index. Additionally, it may happen that particles move to other spots on the substrate. Possible heterogeneity on the substrate itself (variation in roughness or charges) may then lead to a significant difference in environment. (b) Impurities either on the particle itself or in the sensing volume can lead to either unwanted particle movement on the substrate or local refractive index change by diffusion through the particle sensing volume (i). Additionally, an impurity can also contribute to the total collected light through its own scattering (ii). (c) Plasmonic effects: As shown in chapter 3 and 4, "impurities" in the form of nonspecifically coupled PEG-dimers (and higher order constructs) can be present in a particle sample. Such dimers could then move in different ways, causing changes in plasmonic coupling. In the left example, two such particles move due to PEG entanglement and heterogeneity of the polymer layer. In the right example, the end groups of one polymer chain interact with the other particle. Due to a relatively weak binding (e.g. as shown in chapter 3-4 for carboxy groups) and the natural polymer length heterogeneity, the polymer binding the particles may alternate, leading to a periodic change of interparticle distance. (d) In addition to cases shown in c, impurities may also nonspecifically connect two particles.

One possible origin is a **substrate effect** shown in cases a (and partially in b, left). The substrate effect arises from the difference in refractive index between the medium and substrate. The measurement buffer in the Hsp90 plasmon ruler experiment has a refractive index in the range between n=1.33-1.34, depending on the ionic strength of the buffer. The glass substrate has an approximate refractive index of n≈1.5.[xxxix] At the same time, the glass substrate itself may be heterogenic in nature, leading to differences in local roughness and charges present. As such, if thermal motion moves a particle in any given direction across or to and from the substrate, this leads to a change in the local refractive

[xxxix] As stated by supplier: VWR international for cover slip borosilicate glass.

index. A particle moving to and from a glass substrate can lead to a signal intensity change in the range of 1-2%, as previously shown by simulations in the work of Bastian Flietel.[52]

Another source may lay in **impurities**, as shown in (b, d). Impurities are a factor that is difficult to account for due to their unexpected nature. One possible way of an impurity affecting the measurement is by attachment to the original particle (Figure V-4b, left). This attachment can alter the interaction with the substrate, e.g. by changing the forces between the particle and substrate.[xl] This would make the particle more mobile, and also affected by refractive index changes, as shown in (a). On the other hand, impurities present in the buffer medium (as shown in b, on the right) can also affect the plasmonic signal. Depending on their chemical nature, the refractive index of impurities is generally higher than water, thus causing a local change.[xli] If such impurities are present in a certain amount, they may periodically enter the sensing volume of a particle and change the local refractive index. This effect however should be maximally in the range of the abovementioned 1-2% glass substrate effect, if not less.

An altogether different effect can happen when an impurity contributes through its own scattered light, as sketched (b). In this case, the intensity range for the signal is broad and unpredictable, depending on the size and scattering strength.

Lastly, **plasmonic coupling** effects may be responsible for the unexpected time trace signals. At first glance this is a counterintuitive statement, because particle batches are expected to contain isolated, single particles. This should especially be the case when conditions for colloidal stability (as described in chapter 2) are fulfilled. Nonetheless, results in chapters 3-4 have shown that even a batch of single particles may contain dimers and higher order constructs as "impurities". Assuming this case, different scenarios may arise and lead to step-like signals in the time traces, as shown in Figure V-4c-d. For simplicity, only dimer constructs illustrated, depicting different scenarios such as PEG-PEG entangled dimers, and those collected by polymer end groups (c), as well as some impurities (d). In the case of (c), the heterogenic nature of the polymer may be the factor responsible for the alternation of the interparticle distance. This could happen either because the polymer layer is uneven and has "dips", between which the particles may be rolling. It can also happen that physisorbed end groups (e.g. carboxy or amino, as discussed previously in chapter 3) on polymer chains with different lengths alternate in holding particle together against thermal motion. Further, some unaccounted-for contamination may also play a similar role by holding the particles together and possibly contributing to the motion (d).

[xl] Refer to chapter 2, theory and interparticle interactions.

[xli] This is assuming that the contaminations have a nature similar to either proteins or polymers. A possible contamination source for that are, for example, the plastic tubings and the polymer used to glue the flow chambers for the dark-field measurements. The refractive index of proteins and polymers lies in the range of n≈1.34-1.48 [146,147] as compared to water (n=1.33).

As previously suggested, none of these effects is guaranteed to be the only one present in a given measurement. Nonetheless, in the following section I attempt to address these theories with theoretical and experimental data to single out the most probable factor responsible for the artifact time traces.

3. Experiments hint at a combination of substrate and plasmonic coupling effect

To pinpoint the origin of the fluctuation signal, I address the theories by separately discussing the possible role of the substrate, impurities, as well as plasmonic coupling in the generation of the step-like time traces. As a preliminary summary: Several theoretical and experimental hints suggest that the substrate and the plasmonic coupling effect may be the dominant reasons for observed step-like time traces.

3.1. The substrate effect is complex

The substrate is a complex component. To understand its role, I use theoretical estimations and validate them, where possible, with experimental findings. This helps gain a picture of the substrate effect and estimate the proportion of its role.

3.1.1. The role of the vdW interaction

To estimate the role of the substrate, I focus first on the attractive interactions between the particle and the substrate. This is because the strength of the interactions under the given experimental conditions gives an estimate of the viability of particle movement after initial deposition onto the substrate.

On a bare glass substrate, **attractive van der Walls interaction** is responsible for keeping the particles stuck. I estimate its strength to understand if it is sufficient to prevent particle movement. The calculation is done in a similar way as in chapter 2 for two particle pairs, except that now the interaction is calculated for a spherical object and a plane. Assuming that the contribution of the vdW attraction of the surfactant is neglectable, the significant factor is the interaction between the gold sphere and the glass substrate at the respective distance.[xlii]

Therefore, I expect different vdW attraction depending on a presence or absence of functionalization, and its thickness. To show this trend, I estimated the attraction for different cases of functionalizations. In Figure V-5a, I show the estimations for vdW interaction as multiples of k_BT for cases of 50 nm sized particles with varying functionalization. The cases include a bare gold particle with an approximate gap to the substrate of 1 nm, a CTAC stabilized particle as it is present after particle synthesis, and

[xlii] Another neglected factor here is the electrostatic interaction. For this first estimation, I assume that the effect is neglectable due to sufficient charge screening in the protein buffer, as observed in the calculations done in chapter 2, theory.

then two cases of PEG functionalized particles with different thicknesses. The values for the thicknesses are taken from the measurements from chapter 3.

Expectedly, the vdW calculation for bare particles shows a strong attraction (k_BT=40), whereas PEGylated particles with a much larger distance between the gold and the substrate have an attraction that is close to the thermal energy range (k_BT=3-7). Therefore, they are comparably weakly attached, as far as vdW attraction is considered. Such particles are theoretically at the risk of moving or desorbing through thermal motion.

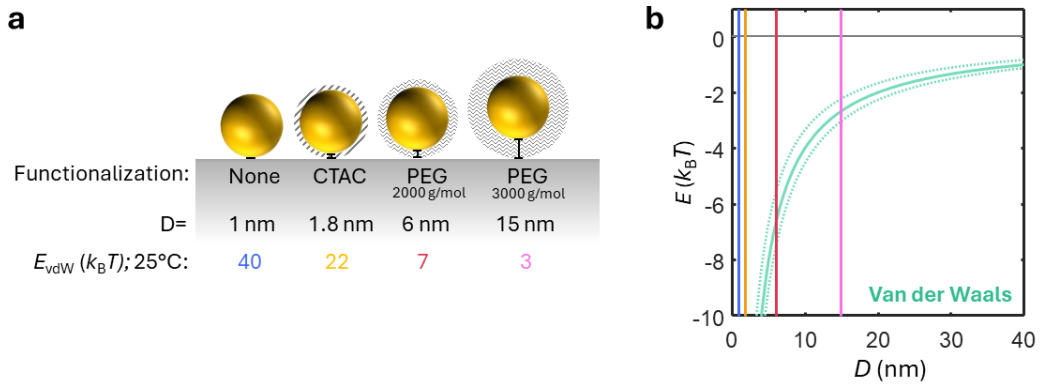

Figure V-5. Attractive vdW interaction between a particle and a glass substrate. (a) Sketch of particles with different surface functionalizations and respective distances D between the particle and the substrate. The PEG values are adapted from DLS measurements (chapter 3) and the CTAC value is from Meena et al.[148] (b) Van-der-Waals interaction calculated as multiples of k_BT according to a sphere-flat plane geometry with $\boldsymbol{E_{vdW} = -A_H R/(6D)}$,[97] with the Hamaker constant of gold/water/quartz 3.3-4.5·10^{-20} J.[149][xliii] The calculation with the average value (3.9·10^{-20} J) is indicated as the thick green line, with the calculation with the upper and lower values (3.3 and 4.5·10^{-20} J) displayed as a dashed line for comparison. Colored lines represent the cases from a.

In the dimer assembly, particles are typically functionalized with a mixture of 2000 g/mol and 3000 g/mol PEG. Therefore, the vdW attraction can be expected to lie in the range of several k_BT, and CTAC particles[xliv] should be firmly stuck to the substrate.

To test how this theory relates to reality, I deposited CTAC particles onto a glass substrate and measured their time traces in the HEPES buffer to mimic the original experimental conditions. One such typical measurement is shown in Figure V-6. Interestingly, the measurement shows a split of time traces into two populations: those that show a typical statistical noise trace, and those that show a "bumpier" and less expected traces (b).

[xliii] Refer to chapter 2, theory, for the calculation of the vdW interaction. A_H is the Hamaker constant, R the particle radius and D the distance to the substrate.

[xliv] CTAC: cetyl trimethyl ammonium chloride, a surfactant molecule used to stabilize gold particles during synthesis. See Appendix for synthesis protocol.

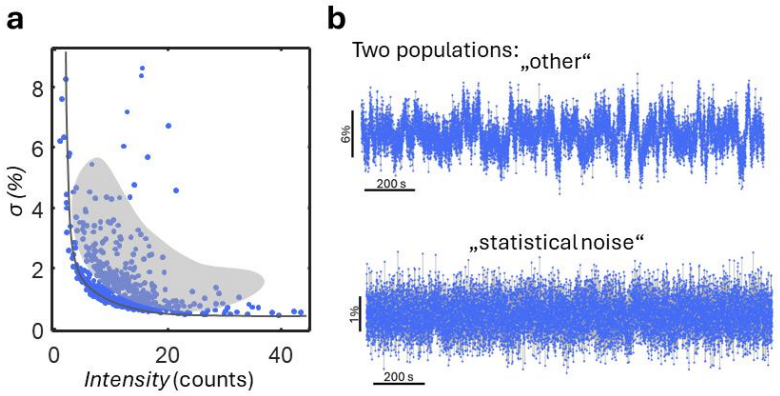

Figure V-6. Time traces of CTAC covered monomeric particles. (a) A noise plot over intensity for 700 measured particles, showing one population following the statistical noise. This is indicated by the guide-to-the eye drawn as a grey line. There is a noisier population beside it, indicated with the grey shaded area. (b) The recorded time series are split into two populations: one with an expected statistical noise pattern, and another with a noisier pattern.

Considering the small distance between the particles and the substrate, this suggests that more factors aside from the vdW interactions are responsible for particle instability. This is further supported by the evidence that particles typically require a salt solution (e.g. 1-2 M NaCl) to be deposited onto the substrate, suggesting the possible role of additional electrostatic interactions. With 50 mM KCl, the HEPES buffer may not have enough ionic strength to sufficiently screen the charges and reduce repulsion.

Consequently, the split between the statistically noisy and the non-statistically noisy population may be explained by the fact that CTAC is not evenly distributed over all particles, and is desorbing over time. Thus, some particles may be more prone to sticking compared to others. This result shows that consideration of vdW attraction alone is not enough to approximate the influence of the substrate.

3.1.2. The estimation of the total interaction is complex

As already shown in chapter 2, the estimation of the total interaction is complex. To give a more complete picture that can serve as a guideline for future persons working on a similar project, here I summarize additional factors to keep in mind, as well as anecdotical observations that require further consideration.

As a first note, the simplified vdW estimation approach neglects such factors as **surface roughness** (Figure V-7a) or the role of the **electrostatic attraction/repulsion** (b). The roughness reduces the attractive interaction between the partners, and electrostatic interaction can vary, depending on the medium and the electrostatic double layer that may potentially shield them.

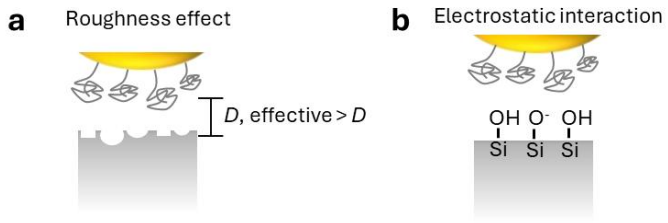

Figure V-7. Roughness effects and electrostatic interaction. (a) Two factors are responsible for the roughness: first that of the polymer layer on the particle, and second that of the glass substrate. (b) Generally, roughness leads to a larger effective distance between the particle and the substrate, and subsequently a lower vdW interaction. (d) Electrostatic repulsion may be an additional factor in possible repulsion or attraction of particles to the surface. In the case of a glass substrate, it may originate from deprotonated silanol groups.

As shown in Figure V-7a, the roughness effect is present in both the particle in the form of the polymer layer, as well as the substrate. Due to its small size and shape, the roughness of the particle is difficult to characterize as compared to a large flat surface. However, the polydispersity index (PDI) given by the manufacturer offers an idea of its length distribution. This is sketched in Figure V-8a+b, showing how a hypothetical, monodisperse polymer layer (a) naturally has a larger surface contact as compared to a polydisperse one (b) with a polydispersity index of 1.03, as given by the supplier's data sheet for our PEG polymers (PDI=1.03-1.04). Additionally, since the state-of-the-art protocol uses different weights and polymer types, the polymer layer on the resulting particle is even more uneven, as illustrated in (c). All of these factors reduce attractive interaction with the substrate and can explain the observed behavior in the time trace.

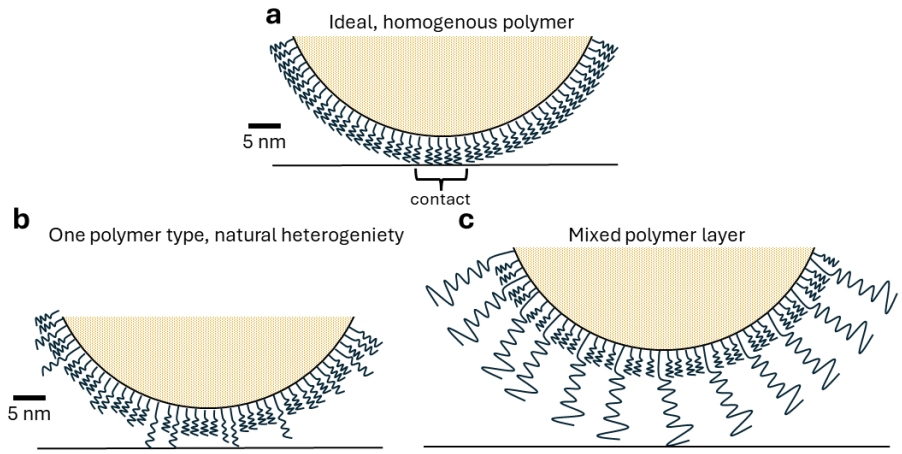

Figure V-8. To-scale sketches of different polymer cases. (a) Sketch of a particle on a substrate with the highest possible contact and shorted distance, due to a homogenous polymer layer. (b) Realistically, polymer layers do not consist of only one polymer length. Polymers have a distribution of chain length arising from the polymer process. For example, the PEG supplier Iris biotech gives a PDI of 1.03-1.04 in the data sheet for the methoxy and carboxy-PEGs in use in our protocols. (c) Sketch of a mixed polymer layer, where a 2000 g/mol methoxy-PEG polymer is mixed with a 3000 g/mol amino-PEG. For sizes, average DLS measurements from chapter 2 are taken for the sketch.

On the topic of substrate roughness, Chada et al.[150] report an average roughness of 19±9.6 Å for a borosilicate coverslip glass, as measured by atomic force microscopy (AFM). The roughness is reported to reduce significantly after etching with a KOH/ethanol solution to 1.7±0.3 Å.

This pre-treatment would expectedly increase vdW interaction of the substrate with a particle. At the same time, this effect goes along with electrostatic interaction (as sketched in Figure V-7b). This is because the base charges the glass by deprotonating the silanol groups, although other effects unrelated to the acid/base chemistry mechanism are also reported.[xlv]

In our experiments, we observe the influence of the above factors indirectly, as opposed to a more direct characterization with e.g. an AFM. One such way is to observe the stability of single particles is to measure a time trace, as shown above. Another way to visualize the substrate-particle interaction is to do a quantitative study of particle deposition. In this study, a fixed concentration of particles is added and incubated over a fixed time on a substrate. The unattached particles are flushed out. In this way, our group has previously characterized the passivation quality of substrates, e.g. as shown in the works of Laura Tueting[51] and Bastian Flietel.[52]

With the aim to understand how particle interaction differs specifically in the case of a bare glass substrate, our student Joscha Eisel[152] expanded this study during the time of my thesis. His findings help shed light on the complexity of deposition of particles on bare glass—a case where the novel time traces were first discovered by Bastian Flietel with his batch synthesis.[52]

In his master thesis,[152] Joscha Eisel has studied particle deposition on glass under different conditions. He compared the numbers of deposited particles: More particles signified higher attractive interactions, and less particles more repulsive interactions. His results show that a pre-treatment of the coverslip glass with a NaOH solution produces a significant effect and increases particle sticking. Thereby he compared non-treated coverslips with treated ones, and afterwards deposited CTAC particles, before switching to the HEPES measurement buffer for consistency with the plasmon ruler experiment. His data shows a deposition of only 28±18 particles on the untreated substrate, and 2233±1161 on the substrate pre-treated with NaOH. The treatment appears to introduce either additional charges and/or reduced roughness to the substrate.

Most curiously, he noticed that particle sticking also differs depending on the material used for substrate assembly in the in-lab manufacturing process. The substrate assembly process is described in detail in several previous works.[52,152] Briefly, a flow chamber is assembled by glueing two glass coverslips together. For this, either a pre-cut sheet of Parafilm® PM996 (made of a mixture of waxes and polyalkenes according to manufacturer datasheet, by Amcor), or a double-sided adhesive tape is used. The student noticed that coverslips with Parafilm® are affected by pre-treatment with NaOH, but

[xlv] One such example is the effect of "slide electrification".[151] The effect describes the charging of a water droplet when sliding across a substrate. In our experiment, something similar may happen when a flow chamber is first flooded with water at the start of a measurement. This effect shows that surface chemistry, especially in relation to glass, is a complex matter.

much less so when they are assembled with sticky tape. The latter case showed deposition of only 66±30 particles, a number comparable to the non-treated glass.[xlvi]

His results suggest several important points: First, that there is a possibility of the Parafilm® substrate evaporating and re-distributing on the substrate. And secondly, that treatment with NaOH makes a difference, although it is difficult to guess its nature since the exact composition of the waxes and polyalkenes is not known. The electrostatic charging of the bare glass therefore appears less significant than the unknown factor introduced by the Parafilm®.

To summarize, the particle-substrate interactions are weaker than necessary for firm attachment. Irregularities and possible contamination of the substrate can also cause additional noise in time traces in the predicted range of 1-2%.[52] However, they cannot explain the step-like patterns in the range of 10% and higher.

3.2. Big impurities are rare and isolated events

Impurities are another factor that may play a role in the generation of the nonstatistical noise time traces. The topic of impurities is a broad one, as the term "impurity" suggests. For the purpose of this work, I separate the impurities into two categories: those present on a particle and those present in the solution. The first is category difficult to account for since it requires the characterization of the particle and possible impurities in chemicals involved in the grafting process. Because of this, I focus on the second category instead.

Generally, impurities in the solution are avoided by filtration of the buffer. This process however does not include possible dirt that may be present anywhere in the experimental setup. However, such dirt is not expected to be present in high concentrations, and should be flushed out during the flushing steps at the beginning of the experiment. This leaves one last possibility: since particles were shown to have a weak binding to the substrate, they can become a form of "impurity" that disturbs the measurement.

Here I demonstrate how such particles may affect the measured time trace. For this example, I show a dark-field measurement of CTAC stabilized particles in the presence of freely diffusing other particles.

Figure V-9a depicts a field-of-view of a dark-field image with particles deposited onto the substrate, seen as fixed dots. At the same time, freely diffusing particles are seen as faint and enlarged shadows in the background. Examples traces in (b) show how these unattached particles affect the measured time trace: For the duration of the diffusion time through the measured area, the signal increases. The resulting rapid increase and fall of intensity in the time trace is also an isolated event. This is because the diffusor is moving away by statistical, Brownian motion. In this particular measurement, the signal increase

[xlvi] The possible difference may lie in the pre-treatment process. In the case of Parafilm®, heat (several seconds at 90-120°C on a heat plate, applied evenly across the coverslip) is used to promote adhesion. This is not the case for the double-sided tape. Temperature may play a role by altering the surface, e.g. by evaporating the polymer and depositing it elsewhere on the glass.

is in the range of 10%. It is important to note that here, the signal increases because the scattered light of the diffusor is collected in addition to the measured particle. Depending on such factors as the scattering strength of the diffusor and the distance from the focus, the collected total intensity can be less or more than what is displayed in (b).

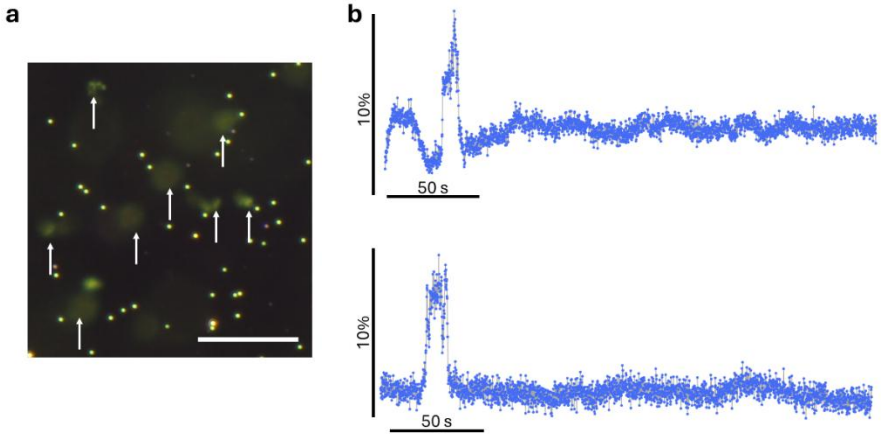

Figure V-9. Effects of freely diffusing particles on a time trace. (a) Dark-field real color image of deposited particles and some freely diffusing ones (marked with white arrows). Scalebar: 50 μm. (b) Two example time traces of a measurement with freely diffusing particles.

Overall, this example shows that an impurity or in this case a freely diffusing particle can affect the measured time series if it reaches the area where the light of a particle is collected for the time trace. The intensity change caused by this event can be in the range expected for events related to the plasmon coupling. However, diffusion events are rare and isolated. Because they are propelled by Brownian motion, they do not yield a discrete step-like intensity change pattern. As such I exclude them from the possible explanations of the protein-like time traces.

3.3. Plasmonic coupling is a significant factor

The third theory attempting to explain the step-like patterns in time traces is the presence of plasmonic coupling. Here I show experimental evidence suggesting that this is one of the major contributing factors.

As previously mentioned, this theory assumes that nonspecifically assembled constructs (e.g. dimers or higher order assemblies) are present in the particle batches. To prove if such nonspecific constructs indeed cause the characteristic multi-step patterns, I used the previously discovered carboxy-PEG samples containing nonspecifically attached, higher order constructs (see chapter 4). From this mixture, I collected the dimers[xlvii] using gel electrophoresis as a cleaning method and characterized it in a single-particle dark-field experiment. I first characterized the construct type distribution (Figure V-10a) by differentiating remaining monomers from dimers by the means of a

[xlvii] The collection method is based on extraction of the particles from the gel. As seen in the statistics, this is not a clean method, leading to a collection of monomers and dimers together. The main cause may be due to crowding and retardation effects in the gel. Additionally, the dimers may also separate with time.

polarization measurement. This separation is done on the basis of the geometry-dependent plasmon resonance. Briefly, the measurement separates spherical constructs that show no polarization dependance in their scattering intensity from non-spherical ones. Egg-shaped and rod-shaped particles are an example, as is the particle dimer. The latter examples show a polarization-dependent scattering intensity that differentiates them from ideal spheres.

This measurement shows a splitting of the construct population into two groups (b). I used the minimum between these two populations as a reasonable threshold to split the monomers from the dimers. From a total of 362 observed constructs, 37% are assigned as dimers (b).[xlviii]

I then recorded time traces of these constructs to compare the statistical occurrence of the step-like time trace patterns to the 1% observed in the PEG particles at the beginning of this chapter. In the dimer-rich measurement, 14% of constructs showed a characteristic step-like fluctuation. The sample fluctuation statistics are shown in Figure V-10c. In an independently repeated experiment with a new batch of constructs, a similar percentage of fluctuating traces (14%, 44 out of 315 measured time traces) was seen.

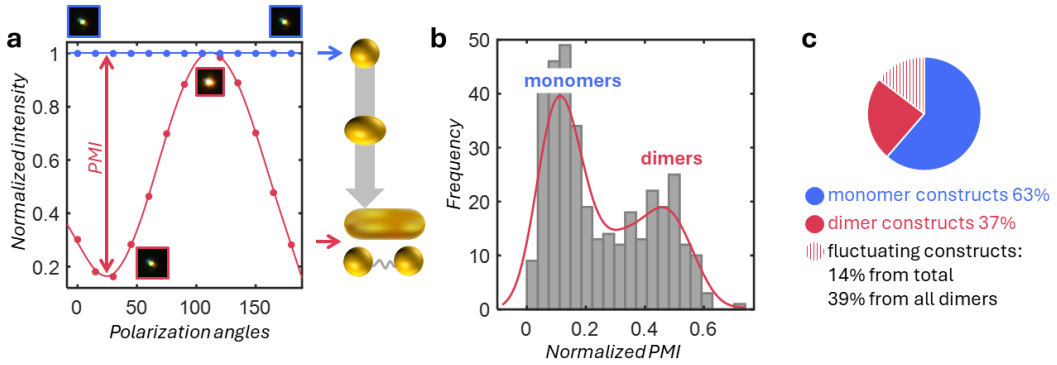

Figure V-10. Identification and statistics of a dimer-rich sample. (a) Identification of particle type by the polarization modulation index (PMI). The plasmon scattered light of an ideally spherical particle is independent of the polarization angle. A non-isotropic shape, such as an egg or a rod (and similarly a coupled particle dimer) shows a dependance due to its geometry-dependent plasmon resonance. The depth between the maximum and minimum of the normalized intensity is called the polarization modulation index (PMI). (b) A distribution of PMIs in a sample. The groups (monomers and dimers) are separated by the fit (red), with the minimum taken as a threshold value. (c) Statistics of a dimer-rich sample, with highlighted amount of fluctuating time traces.

The previously recorded time trace types (two-state, multi-state and chaotic) could also be found in these measurements. Examples are shown in Figure V-11, displaying a two-state pattern that is similar to an expected protein time trace, a multiple state time trace and a more chaotic one.

[xlviii] This is an approximate number, because the polarization measurement cannot differentiate between less spherical single particles and dimers. However, since there are two clear populations seen in the distribution, this is seen as a reasonable approximation.

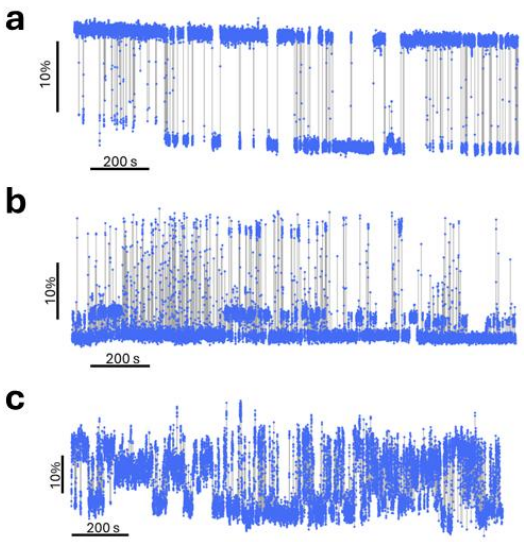

Figure V-11. Time trace examples as measured in the dimer-rich sample. (a) A two-state time trace. (b) a multiple state time trace. (b) A time trace with a more chaotic pattern and variable intensity fluctuation.

Due to the reproducible increase in fluctuating, step-like traces in the dimer-rich sample, the nonspecifically formed dimers are a key contributing factor to the observed patterns.

Two remaining questions are how particles connected only by a polymer can produce (1) a signal range starting from 2-10% and higher and (2) how the discrete step-like patterns come to be.

The intensity range goes back to the interparticle distance, as shown in chapter 2. It depends on many factors, such as the position of the LED and polymer dynamics. Thus, many assumptions are necessary to relate the measured intensity in this experiment to theory. Deriving information on the assembly (e.g. the specific interparticle distance and the distance change) is therefore complicated.

From the group's experience with intensity measurements and previous experiments with PEG dimers[61] and Hsp90 linked dimers[49], we know that the signal amplitude is expected in the range of 10% for such assemblies. The signal intensity variation comes from the heterogeneity of the particle sizes in a sample and the heterogeneity of the polymer's length (compare Figure V-8).

The patterns observed additionally support a variation in how the constructs are moving. Out of all time trace patterns, chaotic ones are the easiest to explain. In this case, particles must be loosely attached and fluctuate similar to a Brownian motion. Two-step time trace patterns suggest a motion between two specific interparticle distances, and multiple-step patterns mean more. Figure V-4 shows different possibilities, assuming that in these cases particles may be connected in a polymer layer constellation that promotes directional movement. The random nature of the polymer supports this theory, explaining why not all time traces look the same.

4. Conclusion

In conclusion, theoretical and experimental data show that particle-substrate interactions and unwanted nonspecific constructs in the particle batches are responsible for the artifact time traces.

Weak particle-to-glass attachment occurs under the buffer conditions used for the plasmon ruler experiment. Additionally, variations in the pre-treatment of the bare glass show that the unprotected substrate is liable to charging effects. This introduces a potential source of variation in sticking strength and noise to the time traces. For future measurements it is better to work with pre-passivated substrate with covalently attached particles for overall better control over attachment and suppression of nonstatistical noise.

Additionally, control measurements reveal that PEG-functionalized particles contain unwanted, nonspecifically attached dimers and higher order constructs. These dimers are are responsible for time traces with chaotic and discrete step-like patterns. The exact mechanistical origin of these time traces is not understood. However, the PEG functionalization must play a role in it. To avoid artifacts in future measurements, it is reasonable to avoid PEG functionalization, where such nonspecific constructs are found. All together, the observations show that it is safer to go for a more rigid and homogenous particle functionalization, for example with defined thiol-alkanes and DNA attachments, as suggested in the previous chapter.

VI. CONCLUSION

Plasmon rulers are a helpful tool in the portfolio of single-molecule studies. In a proof-concept study, our group has previously shown that protein motion can be recorded over an unprecedented time frame of 24 h, with an improved signal-to-noise ratio as compared to a single-molecule FRET experiment.[49] To improve this method's robustness and yield, I investigated the plasmon ruler dimer assembly, found the key challenges and addressed them in this work.

(1) Hsp90 plasmon ruler assembly is theoretically possible under the experimental state-of-the-art conditions.

In **chapter 2**, I provided a theoretical study to understand the physical constraints of the dimer assembly. I did this to provide trends to serve as a guide, and to review if the state-of-the-art assembly protocol fulfills the necessary criteria. I observed the factors signal strength, colloidal stability, the state of interparticle interactions and assembly kinetics.

For the signal strength, I used MNPBEM simulations to predict signal trends depending on particle size and interparticle distance. The simulations predicted a growing signal for bigger particle sizes. For the state-of-the-art dimer, I showed that the measurement of the protein motion is possible with the previous, theoretically assumed interparticle distance of 18-23 nm.

Although bigger particles are preferable, I observed in the next part that growing van der Waals attraction between the particles limits the upper particle size to up to 50-55 nm. At this distance, the plasmon coupling signal and colloidal stability are reasonably balanced under the functionalization conditions given in the dimer assembly protocol. The requirement for this is a sufficient steric stabilization by an appropriate particle functionalization thickness.

Lastly, I revised the assembly kinetics and found that assembly reaction is expected to happen on a second-to-minute time scale, despite the lower diffusion of the 50-55 nm particles in solution. Because the diffusion and reaction conditions in the assembly experiment are fixed, the factor that governs the assembly time within this theoretical observation is the reactivity of the particles.

Thus, I concluded that the dimer assembly should happen successfully. However, because the state-of-the-art dimer assembly fails, there must be a discrepancy between theoretical assumptions and reality, which I investigated in the following chapters.

(2) Discrepancies between theoretical assumptions and reality lead to complications for assembly.

To understand why the state-of-the-art dimer assembly does not give the necessary yield despite the theory, I revised the theoretical assumptions such as the interparticle distance and colloidal stability in **chapter 3**. For this, I compared the previous theoretical assumptions with experimental data. I measured the polymer functionalization thickness and studied its stability under experimental conditions.

This uncovered discrepancies between previous assumptions and reality: First, the measured polymer length for the amino-PEG used for coupling was bigger than theoretically assumed for the state-of-the-art polymer, leading to a larger interparticle distance and a lower expected plasmon coupling. Second, the measured layer thickness of the methoxy-PEG used as a main component for colloidal stability is smaller than desired according to the calculations in chapter 2. Third, I uncovered a complication arising from the use of polymers with non-neutral end groups. These end groups lowered the colloidal stability of particles when their fraction exceeded a critical number, which I attributed to the lowered grafting density of the functionalization. This supplementary knowledge served as a basis to further explore alternatives to the current functionalization protocol.

To improve the current protocol and overcome the stability problem, I addressed the grafting density challenge. With alternatives in mind, I did this both for the current PEG-based strategy and a DNA-based strategy. For PEG, I showed that thickening of the polymer layer is possible but insufficient to solve the problem arising from the reactive end group. For DNA, I uncovered that grafting density is similarly a challenge, and proposed one strategy to overcome it. This improved assembly results, which I documented in chapter 4.

In summary, my investigation in this chapter showed that theoretical assumptions are not sufficient to reliably ensure sufficient plasmon coupling and colloidal stability, and that the polymer functionalization is a critical factor playing a central role in the dimer assembly.

(3) Reactivity is the main factor responsible for successful assembly.

The assembly is a complex structure, and is made of more than just the particles. To determine the key component responsible for assembly success or failure, I observed factors such as: (1) The role of the protein, (2) the theory of the protein being blocked due to a both-end reaction to the same particle and (3) the assembly failing due to a low chemical reactivity.

In **chapter 4**, I developed an assembly screening procedure that allowed me to test these theories. The result of the screening proved irrelevance of points (1) and (2) and highlighted the important role of the chemical reactivity. This was a key result that helped narrow down the optimization efforts to particle quality and reactivity.

I found that DNA-DNA hybridization surpasses the previously used maleimide chemistry. An additional strong point is the flexibility introduced by the DNA in terms

of the tunable strand length and resulting interparticle distance, as well as homogeneity of a DNA functionalization as compared to PEG. Focusing on this functionalization and taking the results from chapter 3 in to view, I showed that improvement in particle quality through additional passivation increases assembly success for the DNA-based method. The particles displayed better stability in protein buffers and dimer constructs formed in a batch synthesis could be discerned in a gel electrophoresis method for further studies.

With this I provided a guide for a faster and more robust assembly. Additionally, I showed that better particle quality improves characterization and helps to successfully separate and enrich the dimerized sample. All of the above points are important for better control and statistics in the plasmon ruler measurement.

(4) Characterization of the unknown signal as an artifact highlights the importance of substrate passivation and particle quality.

In the last chapter, I expanded the knowledge on the previously observed, novel time-traces in the work of Bastian Flietel.[52] Originally, the multi-state time traces were discovered during his batch synthesis of Hsp90 dimers. As I continued his work, I performed complementary control measurements. In this context, I found similar time traces in control measurements without the protein, suggesting their artifact nature. Upon further study, I could narrow down the sources of the artifacts. The first source is the weak binding of the particles to the bare glass substrate as used in the batch synthesis protocol. The second source is the occurrence of nonspecifically attached dimers and higher order constructs. With my experiments I showed that these constructs are responsible for the occurrence of the curious multi-state and other time traces that resemble the protein motion. As a result, I recommended to use a passivated substrate and to attach particles covalently for noise reduction. Additionally, I suggested to use a non-PEG based functionalization to avoid the nonspecific constructs occurring in these particle batches. Following both suggestions, the future plasmon ruler measurements will be more robust and reproducible.

A summary of contributions to the plasmon ruler method:

To summarize, my work contributed to the understanding of key assembly features that require attention for a controlled assembly and reliable measurement. Before my work, there existed many theories regarding assembly failure and improvement. Many strategies could potentially address the hitherto unknown problems, requiring effort that may or may not yield results. I found a direction in this sea of possibilities. With the recommendations and knowledge gained, the plasmon assembly gains robustness and yield. These key points will help the single-molecule community by increasing the long-term protein dynamic data, reveal heterogeneity in protein populations and expand the experimental possibilities with multiplexed measurements. In particular, this will help expand our knowledge on the topics of ergodicity and memory effects,[1] both of which require long-term single-protein study.

VII. BIBLIOGRAPHY

(1) Vollmar, L.; Bebon, R.; Schimpf, J.; Flietel, B.; Celiksoy, S.; Sönnichsen, C.; Godec, A.; Hugel, T. Model-Free Inference of Memory in Conformational Dynamics of a Multi-Domain Protein. *J. Phys. Math. Theor.* **2024**, *57* (36), 365001. https://doi.org/10.1088/1751-8121/ad6d1e.

(2) Bauer, C. On the Respiratory Function of Haemoglobin. In *Reviews of Physiology, Biochemistry and Pharmacology, Volume 70*; Reviews of Physiology, Biochemistry and Pharmacology; Springer-Verlag: Berlin/Heidelberg, 1974; Vol. 70, pp 1–31. https://doi.org/10.1007/BFb0034292.

(3) Morris, R.; Black, K. A.; Stollar, E. J. Uncovering Protein Function: From Classification to Complexes. *Essays Biochem.* **2022**, *66* (3), 255–285. https://doi.org/10.1042/EBC20200108.

(4) Nelson, D. L.; Cox, M. M.; Lehninger, A. L. *Lehninger Biochemie*, 4., vollständig überarbeitete und erweiterte Auflage, Übersetzung der 5. amerikanischen Auflage, korrigierter Nachdruck.; Häcker, B., Held, A., Jarosch, B., Maxam, G., Schön, C., Zellerhoff, N., Translators; Springer-Lehrbuch; Springer: Berlin Heidelberg, 2011.

(5) Jeyaraj, G.; Rajendran, A. K.; Sathishkumar, K.; Almutairi, B. O.; Vadivelu, A.; Chokkakula, S.; Tu, Y.; Xie, W. High-Resolution Protein Modeling through Cryo-EM and AI: Current Trends and Future Perspectives – a Review. *Front. Mol. Biosci.* **2025**, *12*, 1688455. https://doi.org/10.3389/fmolb.2025.1688455.

(6) Borman, S. Cryo-Electron Microscopy Innovators Win 2017 Nobel Prize in Chemistry. *c&en* **2017**.

(7) Chien, C.-T.; Maduke, M.; Chiu, W. Single-Particle Cryogenic Electron Microscopy Structure Determination for Membrane Proteins. *Curr. Opin. Struct. Biol.* **2025**, *92*, 103047. https://doi.org/10.1016/j.sbi.2025.103047.

(8) Korukottu, J.; Bayrhuber, M.; Montaville, P.; Vijayan, V.; Jung, Y.; Becker, S.; Zweckstetter, M. Fast High-Resolution Protein Structure Determination by Using Unassigned NMR Data. *Angew. Chem. Int. Ed.* **2007**, *46* (7), 1176–1179. https://doi.org/10.1002/anie.200603213.

(9) Jumper, J.; Evans, R.; Pritzel, A.; Green, T.; Figurnov, M.; Ronneberger, O.; Tunyasuvunakool, K.; Bates, R.; Žídek, A.; Potapenko, A.; Bridgland, A.; Meyer, C.; Kohl, S. A. A.; Ballard, A. J.; Cowie, A.; Romera-Paredes, B.; Nikolov, S.; Jain, R.; Adler, J.; Back, T.; Petersen, S.; Reiman, D.; Clancy, E.; Zielinski, M.; Steinegger, M.; Pacholska, M.; Berghammer, T.; Bodenstein, S.; Silver, D.; Vinyals, O.; Senior, A. W.; Kavukcuoglu, K.; Kohli, P.; Hassabis, D. Highly Accurate Protein Structure Prediction with AlphaFold. *Nature* **2021**, *596* (7873), 583–589. https://doi.org/10.1038/s41586-021-03819-2.

(10) Gremer, L.; Schölzel, D.; Schenk, C.; Reinartz, E.; Labahn, J.; Ravelli, R. B. G.; Tusche, M.; Lopez-Iglesias, C.; Hoyer, W.; Heise, H.; Willbold, D.; Schröder, G. F. Fibril Structure of Amyloid-β(1–42) by Cryo–Electron Microscopy. *Science* **2017**, *358* (6359), 116–119. https://doi.org/10.1126/science.aao2825.

(11) Ostrem, J. M.; Peters, U.; Sos, M. L.; Wells, J. A.; Shokat, K. M. K-Ras(G12C) Inhibitors Allosterically Control GTP Affinity and Effector Interactions. *Nature* **2013**, *503* (7477), 548–551. https://doi.org/10.1038/nature12796.

(12) Henzler-Wildman, K.; Kern, D. Dynamic Personalities of Proteins. *Nature* **2007**, *450* (7172), 964–972. https://doi.org/10.1038/nature06522.

(13) Englander, S. W. Hydrogen Exchange and Mass Spectrometry: A Historical Perspective. *J. Am. Soc. Mass Spectrom.* **2006**, *17* (11), 1481–1489. https://doi.org/10.1016/j.jasms.2006.06.006.

(14) Bai, Y. Protein Folding Pathways Studied by Pulsed- and Native-State Hydrogen Exchange. *Chem. Rev.* **2006**, *106* (5), 1757–1768. https://doi.org/10.1021/cr040432i.

(15) Mittermaier, A.; Kay, L. E. New Tools Provide New Insights in NMR Studies of Protein Dynamics. *Science* **2006**, *312* (5771), 224–228. https://doi.org/10.1126/science.1124964.

(16) Kikhney, A. G.; Svergun, D. I. A Practical Guide to Small Angle X-ray Scattering (SAXS) of Flexible and Intrinsically Disordered Proteins. *FEBS Lett.* **2015**, *589* (19PartA), 2570–2577. https://doi.org/10.1016/j.febslet.2015.08.027.

(17) Mazal, H.; Haran, G. Single-Molecule FRET Methods to Study the Dynamics of Proteins at Work. *Curr. Opin. Biomed. Eng.* **2019**, *12*, 8–17. https://doi.org/10.1016/j.cobme.2019.08.007.

(18) Hu, C.; Yang, J.; Qi, Z.; Wu, H.; Wang, B.; Zou, F.; Mei, H.; Liu, J.; Wang, W.; Liu, Q. Heat Shock Proteins: Biological Functions, Pathological Roles, and Therapeutic Opportunities. *MedComm* **2022**, *3* (3), e161. https://doi.org/10.1002/mco2.161.

(19) Basu, R.; Fletcher, S. Protein Structural Dynamics in Covalent Drug Design: Insights from Irreversible and Reversible Covalent Inhibitors. *RSC Chem. Biol.* **2026**, *7* (3), 376–399. https://doi.org/10.1039/D5CB00230C.

(20) Wayne, N.; Bolon, D. N. Dimerization of Hsp90 Is Required for in Vivo Function. *J. Biol. Chem.* **2007**, *282* (48), 35386–35395. https://doi.org/10.1074/jbc.M703844200.

(21) Shukla, M.; Narayan, M. Proteostasis and Its Role in Disease Development. *Cell Biochem. Biophys.* **2024**, *83* (2), 1725–1741. https://doi.org/10.1007/s12013-024-01581-6.

(22) Weikl, T.; Muschler, P.; Richter, K.; Veit, T.; Reinstein, J.; Buchner, J. C-Terminal Regions of Hsp90 Are Important for Trapping the Nucleotide during the ATPase Cycle 1 1Edited by R. Huber. *J. Mol. Biol.* **2000**, *303* (4), 583–592. https://doi.org/10.1006/jmbi.2000.4157.

(23) Verma, S.; Goyal, S.; Jamal, S.; Singh, A.; Grover, A. Hsp90: Friends, Clients and Natural Foes. *Biochimie* **2016**, *127*, 227–240. https://doi.org/10.1016/j.biochi.2016.05.018.

(24) Welch, W. J.; Feramisco, J. R. Purification of the Major Mammalian Heat Shock Proteins. *J. Biol. Chem.* **1982**, *257* (24), 14949–14959. https://doi.org/10.1016/S0021-9258(18)33376-3.

(25) Silbermann, L.-M.; Vermeer, B.; Schmid, S.; Tych, K. The Known Unknowns of the Hsp90 Chaperone. *eLife* **2024**, *13*, e102666. https://doi.org/10.7554/eLife.102666.

(26) Vollmar, L.; Schimpf, J.; Hermann, B.; Hugel, T. Cochaperones Convey the Energy of ATP Hydrolysis for Directional Action of Hsp90. *Nat. Commun.* **2024**, *15* (1), 569. https://doi.org/10.1038/s41467-024-44847-6.

(27) Krukenberg, K. A.; Street, T. O.; Lavery, L. A.; Agard, D. A. Conformational Dynamics of the Molecular Chaperone Hsp90. *Q. Rev. Biophys.* **2011**, *44* (2), 229–255. https://doi.org/10.1017/S0033583510000314.

(28) Krukenberg, K. A.; Förster, F.; Rice, L. M.; Sali, A.; Agard, D. A. Multiple Conformations of E. Coli Hsp90 in Solution: Insights into the Conformational Dynamics of Hsp90. *Structure* **2008**, *16* (5), 755–765. https://doi.org/10.1016/j.str.2008.01.021.

(29) Zhang, W.; Hirshberg, M.; McLaughlin, S. H.; Lazar, G. A.; Grossmann, J. G.; Nielsen, P. R.; Sobott, F.; Robinson, C. V.; Jackson, S. E.; Laue, E. D. Biochemical and Structural Studies of the Interaction of Cdc37 with Hsp90. *J. Mol. Biol.* **2004**, *340* (4), 891–907. https://doi.org/10.1016/j.jmb.2004.05.007.

(30) Didenko, T.; Duarte, A. M. S.; Karagöz, G. E.; Rüdiger, S. G. D. Hsp90 Structure and Function Studied by NMR Spectroscopy. *Biochim. Biophys. Acta BBA - Mol. Cell Res.* **2012**, *1823* (3), 636–647. https://doi.org/10.1016/j.bbamcr.2011.11.009.

(31) Zhao, D.; Liu, S.; Gao, Y. Single-Molecule Manipulation and Detection. *Acta Biochim. Biophys. Sin.* **2018**, *50* (3), 231–237. https://doi.org/10.1093/abbs/gmx146.

(32) Schmid, S.; Dekker, C. Nanopores -- a Versatile Tool to Study Protein Dynamics. arXiv 2020. https://doi.org/10.48550/ARXIV.2010.07399.

(33) Helms, V. *Principles of Computational Cell Biology: From Protein Complexes to Cellular Networks*; Wiley-VCH: Weinheim, 2008.

(34) Stryer, L. Fluorescence Energy Transfer as a Spectroscopic Ruler. *Annu. Rev. Biochem.* **1978**, *47* (1), 819–846. https://doi.org/10.1146/annurev.bi.47.070178.004131.

(35) Schmid, S.; Götz, M.; Hugel, T. Effects of Inhibitors on Hsp90's Conformational Dynamics, Cochaperone and Client Interactions. *ChemPhysChem* **2018**, *19* (14), 1716–1721. https://doi.org/10.1002/cphc.201800342.

(36) Ha, T. Single-Molecule Fluorescence Resonance Energy Transfer. *Methods* **2001**, *25* (1), 78–86. https://doi.org/10.1006/meth.2001.1217.

(37) Roy, R.; Hohng, S.; Ha, T. A Practical Guide to Single-Molecule FRET. *Nat. Methods* **2008**, *5* (6), 507–516. https://doi.org/10.1038/nmeth.1208.

(38) Neuman, K. C.; Nagy, A. Single-Molecule Force Spectroscopy: Optical Tweezers, Magnetic Tweezers and Atomic Force Microscopy. *Nat. Methods* **2008**, *5* (6), 491–505. https://doi.org/10.1038/nmeth.1218.

(39) Jahn, M.; Tych, K.; Girstmair, H.; Steinmaßl, M.; Hugel, T.; Buchner, J.; Rief, M. Folding and Domain Interactions of Three Orthologs of Hsp90 Studied by Single-Molecule Force Spectroscopy. *Structure* **2018**, *26* (1), 96-105.e4. https://doi.org/10.1016/j.str.2017.11.023.

(40) Jahn, M.; Buchner, J.; Hugel, T.; Rief, M. Folding and Assembly of the Large Molecular Machine Hsp90 Studied in Single-Molecule Experiments. *Proc. Natl. Acad. Sci.* **2016**, *113* (5), 1232–1237. https://doi.org/10.1073/pnas.1518827113.

(41) Silbermann, L.; Fottner, M.; Van Der Meulen, R.; Migdad, N.; Lang, K.; Tych, K. One-pot Dual Protein Labeling for Simultaneous Mechanical and Fluorescent Readouts in Optical Tweezers. *Protein Sci.* **2025**, *34* (4), e70098. https://doi.org/10.1002/pro.70098.

(42) Schmid, S.; Dekker, C. The NEOtrap – En Route with a New Single-Molecule Technique. *iScience* **2021**, *24* (10), 103007. https://doi.org/10.1016/j.isci.2021.103007.

(43) Huang, G.; Willems, K.; Soskine, M.; Wloka, C.; Maglia, G. Electro-Osmotic Capture and Ionic Discrimination of Peptide and Protein Biomarkers with FraC Nanopores. *Nat. Commun.* **2017**, *8* (1), 935. https://doi.org/10.1038/s41467-017-01006-4.

(44) Si, W.; Aksimentiev, A. Nanopore Sensing of Protein Folding. *ACS Nano* **2017**, *11* (7), 7091–7100. https://doi.org/10.1021/acsnano.7b02718.

(45) Wen, C.; Bertosin, E.; Shi, X.; Dekker, C.; Schmid, S. Orientation-Locked DNA Origami for Stable Trapping of Small Proteins in the Nanopore Electro-Osmotic Trap. *Nano Lett.* **2023**, *23* (3), 788–794. https://doi.org/10.1021/acs.nanolett.2c03569.

(46) Kopatz, I.; Zalk, R.; Levi-Kalisman, Y.; Zlotkin-Rivkin, E.; Frank, G. A.; Kler, S. Packaging of DNA Origami in Viral Capsids. *Nanoscale* **2019**, *11* (21), 10160–10166. https://doi.org/10.1039/C8NR10113B.

(47) Tang, L.; Yi, L.; Jiang, T.; Ren, R.; Paulose Nadappuram, B.; Zhang, B.; Wu, J.; Liu, X.; Lindsay, S.; Edel, J. B.; Ivanov, A. P. Measuring Conductance Switching in Single Proteins Using Quantum Tunneling. *Sci. Adv.* **2022**, *8* (20), eabm8149. https://doi.org/10.1126/sciadv.abm8149.

(48) Wang, Y.; Zhou, Y.; Qi, L.; Wang, Y.; Sun, L.; Cai, M.; Fan, Q.; Zhang, L. Visualizing Single-Molecule Protein Conformational Transitions and Free Energy Landscape. *Anal. Chem.* **2024**, *96* (29), 12006–12011. https://doi.org/10.1021/acs.analchem.4c01970.

(49) Ye, W.; Götz, M.; Celiksoy, S.; Tüting, L.; Ratzke, C.; Prasad, J.; Ricken, J.; Wegner, S. V.; Ahijado-Guzmán, R.; Hugel, T.; Sönnichsen, C. Conformational Dynamics of a Single Protein Monitored for 24 h at Video Rate. *Nano Lett.* **2018**, *18* (10), 6633–6637. https://doi.org/10.1021/acs.nanolett.8b03342.

(50) Ali, M. M. U.; Roe, S. M.; Prodromou, C.; Pearl, L. H. Crystal Structure of an Hsp90-Sba1 Closed Chaperone Complex: 2cg9, 2006. https://doi.org/10.2210/pdb2cg9/pdb.

(51) Tueting, L. Molecular Dynamics Investigated by Plasmon Rulers, Mainz: Johannes-Gutenberg University, 2017.

(52) Flietel, B. E. M. Advances in Plasmon Ruler Assembly Reveal Complex Dynamics Between Conformational States of Hsp90, Mainz: Johannes-Gutenberg University, 2024.

(53) Mie, G. Beiträge Zur Optik Trüber Medien, Speziell Kolloidaler Metallösungen. *Ann. Phys.* **1908**, *330* (3), 377–445. https://doi.org/10.1002/andp.19083300302.

(54) Bohren, C. F.; Huffman, D. R. *Absorption and Scattering of Light by Small Particles*; A Wiley-Interscience publication; Wiley-CH Verlag GmbH & Co KGaA: New York, 2004. https://doi.org/10.1002/9783527618156.

(55) Nolting, W. *Grundkurs Theoretische Physik 3: Elektrodynamik*, 10. Aufl. 2013.; Springer-Lehrbuch; Springer Berlin Heidelberg: Berlin, Heidelberg, 2013. https://doi.org/10.1007/978-3-642-37905-5.

(56) Saha, K.; Agasti, S. S.; Kim, C.; Li, X.; Rotello, V. M. Gold Nanoparticles in Chemical and Biological Sensing. *Chem. Rev.* **2012**, *112* (5), 2739–2779. https://doi.org/10.1021/cr2001178.

(57) Wei, Q.-H.; Su, K.-H.; Durant, S.; Zhang, X. Plasmon Resonance of Finite One-Dimensional Au Nanoparticle Chains. *Nano Lett.* **2004**, *4* (6), 1067–1071. https://doi.org/10.1021/nl049604h.

(58) Kreibig, U.; Vollmer, M. *Optical Properties of Metal Clusters*; Toennies, J. P., Gonser, U., Osgood, R. M., Panish, M. B., Sakaki, H., Lotsch, H. K. V., Series Eds.; Springer Series in Materials Science; Springer Berlin Heidelberg: Berlin, Heidelberg, 1995; Vol. 25. https://doi.org/10.1007/978-3-662-09109-8.

(59) Sönnichsen, C.; Reinhard, B. M.; Liphardt, J.; Alivisatos, A. P. A Molecular Ruler Based on Plasmon Coupling of Single Gold and Silver Nanoparticles. *Nat. Biotechnol.* **2005**, *23* (6), 741–745. https://doi.org/10.1038/nbt1100.

(60) Jain, P. K.; Huang, W.; El-Sayed, M. A. On the Universal Scaling Behavior of the Distance Decay of Plasmon Coupling in Metal Nanoparticle Pairs: A Plasmon Ruler Equation. *Nano Lett.* **2007**, *7* (7), 2080–2088. https://doi.org/10.1021/nl071008a.

(61) Tüting, L.; Ye, W.; Settanni, G.; Schmid, F.; Wolf, B. A.; Ahijado-Guzmán, R.; Sönnichsen, C. Potassium Triggers a Reversible Specific Stiffness Transition of Polyethylene Glycol. *J. Phys. Chem. C* **2017**, *121* (40), 22396–22402. https://doi.org/10.1021/acs.jpcc.7b08987.

(62) Ali, M. M. U.; Roe, S. M.; Vaughan, C. K.; Meyer, P.; Panaretou, B.; Piper, P. W.; Prodromou, C.; Pearl, L. H. Crystal Structure of an Hsp90–Nucleotide–P23/Sba1 Closed Chaperone Complex. *Nature* **2006**, *440* (7087), 1013–1017. https://doi.org/10.1038/nature04716.

(63) Hellenkamp, B.; Wortmann, P.; Kandzia, F.; Zacharias, M.; Hugel, T. Multidomain Structure and Correlated Dynamics Determined by Self-Consistent FRET Networks. *Nat. Methods* **2017**, *14* (2), 174–180. https://doi.org/10.1038/nmeth.4081.

(64) Hohenester, U.; Trügler, A. MNPBEM – A Matlab Toolbox for the Simulation of Plasmonic Nanoparticles. *Comput. Phys. Commun.* **2012**, *183* (2), 370–381. https://doi.org/10.1016/j.cpc.2011.09.009.

(65) Celiksoy, S. Single Line IMaging Method (SLIM) for Biochemical Applications, Mainz: Johannes Gutenberg University, 2021.

(66) Wiese, G. R.; Healy, T. W. Effect of Particle Size on Colloid Stability. *Trans. Faraday Soc.* **1970**, *66*, 490. https://doi.org/10.1039/tf9706600490.

(67) Atkins, P. W.; De Paula, J. *Atkins' Physical Chemistry*, 9th ed.; Oxford University Press: Oxford ; New York, 2010.

(68) Wijenayaka, L. A.; Ivanov, M. R.; Cheatum, C. M.; Haes, A. J. Improved Parametrization for Extended Derjaguin, Landau, Verwey, and Overbeek Predictions of Functionalized Gold Nanosphere Stability. *J. Phys. Chem. C* **2015**, *119* (18), 10064–10075. https://doi.org/10.1021/acs.jpcc.5b00483.

(69) Verwey, E. J. W. Theory of the Stability of Lyophobic Colloids. *J. Phys. Colloid Chem.* **1947**, *51* (3), 631–636. https://doi.org/10.1021/j150453a001.

(70) *Intermolecular and Surface Forces*, 3rd ed.; Israelachvili, J. N., Ed.; Academic Press: Burlington, MA, 2011.

(71) Hsu, J.-P.; Liu, B.-T. Effect of Particle Size on Critical Coagulation Concentration. *J. Colloid Interface Sci.* **1998**, *198* (1), 186–189. https://doi.org/10.1006/jcis.1997.5275.

(72) Bishop, K. J. M.; Wilmer, C. E.; Soh, S.; Grzybowski, B. A. Nanoscale Forces and Their Uses in Self-Assembly. *Small* **2009**, *5* (14), 1600–1630. https://doi.org/10.1002/smll.200900358.

(73) Zámbó, D.; Radnóczi, G. Z.; Deák, A. Preparation of Compact Nanoparticle Clusters from Polyethylene Glycol-Coated Gold Nanoparticles by Fine-Tuning Colloidal Interactions. *Langmuir* **2015**, *31* (9), 2662–2668. https://doi.org/10.1021/la504600j.

(74) Biggs, S.; Mulvaney, P. Measurement of the Forces between Gold Surfaces in Water by Atomic Force Microscopy. *J. Chem. Phys.* **1994**, *100* (11), 8501–8505. https://doi.org/10.1063/1.466748.

(75) Li, Z.; Ruiz, V. G.; Kanduč, M.; Dzubiella, J. Ion-Specific Adsorption on Bare Gold (Au) Nanoparticles in Aqueous Solutions: Double-Layer Structure and Surface Potentials. *Langmuir* **2020**, *36* (45), 13457–13468. https://doi.org/10.1021/acs.langmuir.0c02097.

(76) Fujita, T.; Guan, P.; McKenna, K.; Lang, X.; Hirata, A.; Zhang, L.; Tokunaga, T.; Arai, S.; Yamamoto, Y.; Tanaka, N.; Ishikawa, Y.; Asao, N.; Yamamoto, Y.; Erlebacher, J.; Chen, M. Atomic Origins of the High Catalytic Activity of Nanoporous Gold. *Nat. Mater.* **2012**, *11* (9), 775–780. https://doi.org/10.1038/nmat3391.

(77) Li, X.; Ågren, H. Molecular Dynamics Simulations Using a Capacitance–Polarizability Force Field. *J. Phys. Chem. C* **2015**, *119* (33), 19430–19437. https://doi.org/10.1021/acs.jpcc.5b04347.

(78) Fatehah, M. O.; Aziz, H. A.; Stoll, S. Nanoparticle Properties, Behavior, Fate in Aquatic Systems and Characterization Methods. *J. Colloid Sci. Biotechnol.* **2014**, *3* (2), 111–140. https://doi.org/10.1166/jcsb.2014.1090.

(79) Wuithschick, M.; Birnbaum, A.; Witte, S.; Sztucki, M.; Vainio, U.; Pinna, N.; Rademann, K.; Emmerling, F.; Kraehnert, R.; Polte, J. Turkevich in New Robes: Key Questions Answered for the Most Common Gold Nanoparticle Synthesis. *ACS Nano* **2015**, *9* (7), 7052–7071. https://doi.org/10.1021/acsnano.5b01579.

(80) Kang, H.; Buchman, J. T.; Rodriguez, R. S.; Ring, H. L.; He, J.; Bantz, K. C.; Haynes, C. L. Stabilization of Silver and Gold Nanoparticles: Preservation and Improvement of Plasmonic Functionalities. *Chem. Rev.* **2019**, *119* (1), 664–699. https://doi.org/10.1021/acs.chemrev.8b00341.

(81) Lohse, S. E.; Murphy, C. J. The Quest for Shape Control: A History of Gold Nanorod Synthesis. *Chem. Mater.* **2013**, *25* (8), 1250–1261. https://doi.org/10.1021/cm303708p.

(82) Otsuka, H.; Nagasaki, Y.; Kataoka, K. PEGylated Nanoparticles for Biological and Pharmaceutical Applications. *Adv. Drug Deliv. Rev.* **2003**, *55* (3), 403–419. https://doi.org/10.1016/S0169-409X(02)00226-0.

(83) Hanauer, M.; Pierrat, S.; Zins, I.; Lotz, A.; Sönnichsen, C. Separation of Nanoparticles by Gel Electrophoresis According to Size and Shape. *Nano Lett.* **2007**, *7* (9), 2881–2885. https://doi.org/10.1021/nl071615y.

(84) Nicholas, A. R.; Scott, M. J.; Kennedy, N. I.; Jones, M. N. E¡ect of Grafted Polyethylene Glycol (PEG) on the Size, Encapsulation E¤ciency and Permeability of Vesicles. *Biochim. Biophys. Acta.*

(85) Jeppesen, C.; Wong, J. Y.; Kuhl, T. L.; Israelachvili, J. N.; Mullah, N.; Zalipsky, S.; Marques, C. M. Impact of Polymer Tether Length on Multiple Ligand-Receptor Bond Formation. *Science* **2001**, *293* (5529), 465–468. https://doi.org/10.1126/science.293.5529.465.

(86) Li, M.; Jiang, S.; Simon, J.; Paßlick, D.; Frey, M.-L.; Wagner, M.; Mailänder, V.; Crespy, D.; Landfester, K. Brush Conformation of Polyethylene Glycol Determines the Stealth Effect of Nanocarriers in the Low Protein Adsorption Regime. *Nano Lett.* **2021**, *21* (4), 1591–1598. https://doi.org/10.1021/acs.nanolett.0c03756.

(87) Popov, P.; Steinkerchner, L.; Mann, E. K. Molecular Dynamics Study of Rhodamine 6G Diffusion at n -Decane–Water Interfaces. *Phys. Rev. E* **2015**, *91* (5), 053308. https://doi.org/10.1103/PhysRevE.91.053308.

(88) Lepvrier, E.; Nigen, M.; Moullintraffort, L.; Chat, S.; Allegro, D.; Barbier, P.; Thomas, D.; Nazabal, A.; Garnier, C. Hsp90 Oligomerization Process: How Can P23 Drive the Chaperone Machineries? *Biochim. Biophys. Acta BBA - Proteins Proteomics* **2015**, *1854* (10), 1412–1424. https://doi.org/10.1016/j.bbapap.2015.07.003.

(89) Flietel, B. E. M. am Fachbereich Chemie, Pharmazie und Geowissenschaften der Johannes Gutenberg-Universität in Mainz.

(90) Grebenkov, D. S.; Metzler, R.; Oshanin, G. Strong Defocusing of Molecular Reaction Times Results from an Interplay of Geometry and Reaction Control. *Commun. Chem.* **2018**, *1* (1), 96. https://doi.org/10.1038/s42004-018-0096-x.

(91) Shi, X.; Perry, H. L.; Wilton-Ely, J. D. E. T. Strategies for the Functionalisation of Gold Nanorods to Reduce Toxicity and Aid Clinical Translation. *Nanotheranostics* **2021**, *5* (2), 155–165. https://doi.org/10.7150/ntno.56432.

(92) Xue, Y.; Liu, S.; An, Z.; Li, J.-X.; Zhang, N.-N.; Wang, C.-Y.; Wang, X.; Sun, T.; Liu, K. θ-Solvent-Mediated Double-Shell Polyethylene Glycol Brushes on Nanoparticles for Improved Stealth Properties and Delivery Efficiency. *J. Phys. Chem. Lett.* **2021**, *12* (22), 5363–5370. https://doi.org/10.1021/acs.jpclett.1c01291.

(93) Walkey, C. D.; Olsen, J. B.; Guo, H.; Emili, A.; Chan, W. C. W. Nanoparticle Size and Surface Chemistry Determine Serum Protein Adsorption and Macrophage Uptake. *J. Am. Chem. Soc.* **2012**, *134* (4), 2139–2147. https://doi.org/10.1021/ja2084338.

(94) Toro-Mendoza, J.; Maio, L.; Gallego, M.; Otto, F.; Schulz, F.; Parak, W. J.; Sanchez-Cano, C.; Coluzza, I. Bioinspired Polyethylene Glycol Coatings for Reduced Nanoparticle–Protein Interactions. *ACS Nano* **2023**, *17* (2), 955–965. https://doi.org/10.1021/acsnano.2c05682.

(95) Retout, M.; Brunetti, E.; Valkenier, H.; Bruylants, G. Limits of Thiol Chemistry Revealed by Quantitative Analysis of Mixed Layers of Thiolated-PEG Ligands Grafted onto Gold Nanoparticles. *J. Colloid Interface Sci.* **2019**, *557*, 807–815. https://doi.org/10.1016/j.jcis.2019.09.047.

(96) Wang, R.; Wei, Q.; Sheng, W.; Yu, B.; Zhou, F.; Li, B. Driving Polymer Brushes from Synthesis to Functioning. *Angew. Chem. Int. Ed.* **2023**, *62* (27), e202219312. https://doi.org/10.1002/anie.202219312.

(97) *Intermolecular and Surface Forces*, 3rd ed.; Israelachvili, J. N., Ed.; Academic Press: Burlington, MA, 2011.

(98) Park, S. R.; Hauver, J.; Zhang, Y.; Revyakin, A.; Coleman, R. A.; Tjian, R.; Chu, S.; Pertsinidis, A. A Single-Molecule Surface-Based Platform to Detect the Assembly and Function of the Human RNA Polymerase II Transcription Machinery. *Structure* **2020**, *28* (12), 1337-1343.e4. https://doi.org/10.1016/j.str.2020.07.009.

(99) Ortiz, R.; Olsen, S.; Thormann, E. Salt-Induced Control of the Grafting Density in Poly(Ethylene Glycol) Brush Layers by a Grafting-to Approach. *Langmuir* **2018**, *34* (15), 4455–4464. https://doi.org/10.1021/acs.langmuir.8b00030.

(100) Terashima, T.; Kawabe, M.; Miyabara, Y.; Yoda, H.; Sawamoto, M. Polymeric Pseudo-Crown Ether for Cation Recognition via Cation Template-Assisted Cyclopolymerization. *Nat. Commun.* **2013**, *4* (1), 2321. https://doi.org/10.1038/ncomms3321.

(101) Spiliopoulos, N.; Koutsioubas, A. G.; Anastassopoulos, D. L.; Vradis, A. A.; Toprakcioglu, C.; Menelle, A.; Mountrichas, G.; Pispas, S. Neutron Reflectivity Study of Free-End Distribution in Polymer Brushes. *Macromolecules* **2009**, *42* (16), 6209–6214. https://doi.org/10.1021/ma900971k.

(102) Xia, X.; Yang, M.; Wang, Y.; Zheng, Y.; Li, Q.; Chen, J.; Xia, Y. Quantifying the Coverage Density of Poly(Ethylene Glycol) Chains on the Surface of Gold Nanostructures. *ACS Nano* **2012**, *6* (1), 512–522. https://doi.org/10.1021/nn2038516.

(103) Kuzmina, A. Optimierung Des Hsp90-Plasmon Rulers, 2021.

(104) Esteban, R.; Borisov, A. G.; Nordlander, P.; Aizpurua, J. Bridging Quantum and Classical Plasmonics with a Quantum-Corrected Model. *Nat. Commun.* **2012**, *3* (1), 825. https://doi.org/10.1038/ncomms1806.

(105) Lermusiaux, L.; Bidault, S. Temperature-Dependent Plasmonic Responses from Gold Nanoparticle Dimers Linked by Double-Stranded DNA. *Langmuir* **2018**, *34* (49), 14946–14953. https://doi.org/10.1021/acs.langmuir.8b00133.

(106) Cha, H.; Yoon, J. H.; Yoon, S. Probing Quantum Plasmon Coupling Using Gold Nanoparticle Dimers with Tunable Interparticle Distances Down to the Subnanometer Range. *ACS Nano* **2014**, *8* (8), 8554–8563. https://doi.org/10.1021/nn5032438.

(107) Hyre, D. E.; Le Trong, I.; Merritt, E. A.; Eccleston, J. F.; Green, N. M.; Stenkamp, R. E.; Stayton, P. S. Cooperative Hydrogen Bond Interactions in the Streptavidin–Biotin System. *Protein Sci.* **2006**, *15* (3), 459–467. https://doi.org/10.1110/ps.051970306.

(108) Bujacz, A. Structures of Bovine, Equine and Leporine Serum Albumin. *Acta Crystallogr. D Biol. Crystallogr.* **2012**, *68* (10), 1278–1289. https://doi.org/10.1107/S0907444912027047.

(109) Sun, D.; Wei, L.; Yi, R.; Hong, Y.; Wang, Y.; Dong, W.; Jiang, F.; Nie, Q.; Ouyang, X. Identification and Characterization of Heat Shock Protein 90 in Cyclina Sinensis and Its Function under Thermal and Vibrio Parahaemolyticus Infection. *Gene Rep.* **2025**, *40*, 102303. https://doi.org/10.1016/j.genrep.2025.102303.

(110) Regev, O.; Khalfin, R.; Zussman, E.; Cohen, Y. About the Albumin Structure in Solution and Related Electro-Spinnability Issues. *Int. J. Biol. Macromol.* **2010**, *47* (2), 261–265. https://doi.org/10.1016/j.ijbiomac.2010.04.012.

(111) Moyano, D. F.; Ray, M.; Rotello, V. M. Nanoparticle–Protein Interactions: Water Is the Key. *MRS Bull.* **2014**, *39* (12), 1069–1073. https://doi.org/10.1557/mrs.2014.255.

(112) Tako, M.; Teruya, T.; Tamaki, Y.; Uechi, K.; Konishi, T. Molecular Origin for Strong Agarose Gels: Multi-Stranded Hydrogen Bonding.

(113) Zhang, C.; An, D.; Xiao, Q.; Chen, F.-Q.; Zhang, Y.-H.; Weng, H.-F.; Xiao, A.-F. Convenient Agarose Preparation with Hydrogen Peroxide and Desulfation Process Analysis. *Mar. Drugs* **2021**, *19* (6), 297. https://doi.org/10.3390/md19060297.

(114) Li, K.; Liu, Y.; Lou, B.; Tan, Y.; Chen, L.; Liu, Z. DNA-Directed Assembly of Nanomaterials and Their Biomedical Applications. *Int. J. Biol. Macromol.* **2023**, *245*, 125551. https://doi.org/10.1016/j.ijbiomac.2023.125551.

(115) Larson, T. A.; Joshi, P. P.; Sokolov, K. Preventing Protein Adsorption and Macrophage Uptake of Gold Nanoparticles *via* a Hydrophobic Shield. *ACS Nano* **2012**, *6* (10), 9182–9190. https://doi.org/10.1021/nn3035155.

(116) Woods, K. E.; Perera, Y. R.; Davidson, M. B.; Wilks, C. A.; Yadav, D. K.; Fitzkee, N. C. Understanding Protein Structure Deformation on the Surface of Gold Nanoparticles of Varying Size. *J. Phys. Chem. C* **2016**, *120* (49), 27944–27953. https://doi.org/10.1021/acs.jpcc.6b08089.

(117) Martinez-Veracoechea, F. J.; Leunissen, M. E. The Entropic Impact of Tethering, Multivalency and Dynamic Recruitment in Systems with Specific Binding Groups. *Soft Matter* **2013**, *9* (12), 3213. https://doi.org/10.1039/c3sm27766f.

(118) Northrop, B. H.; Frayne, S. H.; Choudhary, U. Thiol–Maleimide "Click" Chemistry: Evaluating the Influence of Solvent, Initiator, and Thiol on the Reaction Mechanism, Kinetics, and Selectivity. *Polym. Chem.* **2015**, *6* (18), 3415–3430. https://doi.org/10.1039/C5PY00168D.

(119) Fuchs, J.; Fiche, J.-B.; Buhot, A.; Calemczuk, R.; Livache, T. Salt Concentration Effects on Equilibrium Melting Curves from DNA Microarrays. *Biophys. J.* **2010**, *99* (6), 1886–1895. https://doi.org/10.1016/j.bpj.2010.07.002.

(120) Chenyakin, Y.; Ullmann, D. A.; Evoy, E.; Renbaum-Wolff, L.; Kamal, S.; Bertram, A. K. Diffusion Coefficients of Organic Molecules in Sucrose–Water Solutions and Comparison with Stokes–Einstein Predictions. *Atmospheric Chem. Phys.* **2017**, *17* (3), 2423–2435. https://doi.org/10.5194/acp-17-2423-2017.

(121) Esashika, K.; Saiki, T. DNA Hybridization Assay Using Gold Nanoparticles and Electrophoresis Separation Provides 1 pM Sensitivity. *Bioconjug. Chem.* **2018**, *29* (1), 182–189. https://doi.org/10.1021/acs.bioconjchem.7b00682.

(122) thermoscientific. SMCC and Sulfo-SMCC User Guide, 2022. https://assets.thermofisher.com/TFS-Assets/LSG/manuals/MAN0011295_SMCC_SulfoSMCC_UG.pdf (accessed 2025-08-11).

(123) Hermanson, G. T. *Bioconjugate Techniques*, 3d edition.; Academic Press: Amsterdam, 2013.

(124) Hermanson, G. T. Immobilization of Ligands on Chromatography Supports. In *Bioconjugate Techniques*; Elsevier, 2013; pp 589–740. https://doi.org/10.1016/B978-0-12-382239-0.00015-7.

(125) National Institute of Standards and Technology. *Biotin*. NIST Chemistry WebBook. https://webbook.nist.gov/cgi/inchi/InChI=1S/C10H16N2O3S/c13-8(14)4-2-1-3-7-9-6(5-16-7)11-10(15)12-9/h6-7,9H,1-5H2,(H,13,14)(H2,11,12,15).

(126) Kroetsch, A.; Chin, B.; Nguyen, V.; Gao, J.; Park, S. Functional Expression of Monomeric Streptavidin and Fusion Proteins in Escherichia Coli: Applications in Flow Cytometry and ELISA. *Appl. Microbiol. Biotechnol.* **2018**, *102* (23), 10079–10089. https://doi.org/10.1007/s00253-018-9377-7.

(127) Diamandis, E. P.; Christopoulos, T. K. The Biotin-(Strept)Avidin System: Principles and Applications in Biotechnology. *Clin. Chem.* **1991**, *37* (5), 625–636. https://doi.org/10.1093/clinchem/37.5.625.

(128) Krkavcová, E.; Kreisinger, J.; Hyánková, L.; Hyršl, P.; Javůrková, V. The Hidden Function of Egg White Antimicrobials: Egg Weight-Dependent Effects of Avidin on Avian Embryo Survival and Hatchling Phenotype. *Biol. Open* **2018**, bio.031518. https://doi.org/10.1242/bio.031518.

(129) Kurosawa, S.; Mo, J.; Diao, X.; Xie, F.; Wang, T.; Zhao, H.; Wu, D.; Müller, R.; Fu, C. Streptavidins Play a Multifunctional Role within a Biotin-Pathway Antibiotic Network Encoded in a Biosynthetic Supercluster. Microbiology November 11, 2025. https://doi.org/10.1101/2025.11.10.687665.

(130) Laitinen, O. H.; Kuusela, T. P.; Kukkurainen, S.; Nurminen, A.; Sinkkonen, A.; Hytönen, V. P. Bacterial Avidins Are a Widely Distributed Protein Family in

Actinobacteria, Proteobacteria and Bacteroidetes. *BMC Ecol. Evol.* **2021**, *21* (1), 53. https://doi.org/10.1186/s12862-021-01784-y.

(131) Kincanon, M.; Murphy, C. J. Nanoparticle Size Influences the Self-Assembly of Gold Nanorods Using Flexible Streptavidin–Biotin Linkages. *ACS Nano* **2023**, *17* (23), 24090–24103. https://doi.org/10.1021/acsnano.3c09096.

(132) Erickson, H. P. Size and Shape of Protein Molecules at the Nanometer Level Determined by Sedimentation, Gel Filtration, and Electron Microscopy. *Biol. Proced. Online* **2009**, *11* (1), 32–51. https://doi.org/10.1007/s12575-009-9008-x.

(133) Rothemund, P. W. K. Folding DNA to Create Nanoscale Shapes and Patterns. *Nature* **2006**, *440* (7082), 297–302. https://doi.org/10.1038/nature04586.

(134) Dass, M.; Gür, F. N.; Kołątaj, K.; Urban, M. J.; Liedl, T. DNA Origami-Enabled Plasmonic Sensing. *J. Phys. Chem. C* **2021**, *125* (11), 5969–5981. https://doi.org/10.1021/acs.jpcc.0c11238.

(135) Hartl, C.; Frank, K.; Amenitsch, H.; Fischer, S.; Liedl, T.; Nickel, B. Position Accuracy of Gold Nanoparticles on DNA Origami Structures Studied with Small-Angle X-Ray Scattering. *Nano Lett.* **2018**, *18* (4), 2609–2615. https://doi.org/10.1021/acs.nanolett.8b00412.

(136) Mirkin, C. A.; Letsinger, R. L.; Mucic, R. C.; Storhoff, J. J. A DNA-Based Method for Rationally Assembling Nanoparticles into Macroscopic Materials. *Nature* **1996**, *382* (6592), 607–609. https://doi.org/10.1038/382607a0.

(137) Ouldridge, T. E.; Šulc, P.; Romano, F.; Doye, J. P. K.; Louis, A. A. DNA Hybridization Kinetics: Zippering, Internal Displacement and Sequence Dependence. *Nucleic Acids Res.* **2013**, *41* (19), 8886–8895. https://doi.org/10.1093/nar/gkt687.

(138) Morrison, L. E.; Stols, L. M. Sensitive Fluorescence-Based Thermodynamic and Kinetic Measurements of DNA Hybridization in Solution. *Biochemistry* **1993**, *32* (12), 3095–3104. https://doi.org/10.1021/bi00063a022.

(139) Dupuis, N. F.; Holmstrom, E. D.; Nesbitt, D. J. Single-Molecule Kinetics Reveal Cation-Promoted DNA Duplex Formation Through Ordering of Single-Stranded Helices. *Biophys. J.* **2013**, *105* (3), 756–766. https://doi.org/10.1016/j.bpj.2013.05.061.

(140) Owczarzy, R.; Moreira, B. G.; You, Y.; Behlke, M. A.; Walder, J. A. Predicting Stability of DNA Duplexes in Solutions Containing Magnesium and Monovalent Cations. *Biochemistry* **2008**, *47* (19), 5336–5353. https://doi.org/10.1021/bi702363u.

(141) Saenger, W. *Principles of Nucleic Acid Structure*; Springer Advanced Texts in Chemistry; Springer New York: New York, NY, 1984. https://doi.org/10.1007/978-1-4612-5190-3.

(142) Tinland, B.; Pluen, A.; Sturm, J.; Weill, G. Persistence Length of Single-Stranded DNA. *Macromolecules* **1997**, *30* (19), 5763–5765. https://doi.org/10.1021/ma970381+.

(143) Vietz, C.; Lalkens, B.; Acuna, G. P.; Tinnefeld, P. Functionalizing Large Nanoparticles for Small Gaps in Dimer Nanoantennas. *New J. Phys.* **2016**, *18* (4), 045012. https://doi.org/10.1088/1367-2630/18/4/045012.

(144) Maus, L.; Dick, O.; Bading, H.; Spatz, J. P.; Fiammengo, R. Conjugation of Peptides to the Passivation Shell of Gold Nanoparticles for Targeting of Cell-Surface Receptors. *ACS Nano* **2010**, *4* (11), 6617–6628. https://doi.org/10.1021/nn101867w.

(145) Celiksoy, S.; Ye, W.; Wandner, K.; Kaefer, K.; Sönnichsen, C. Intensity-Based Single Particle Plasmon Sensing. *Nano Lett.* **2021**, *21* (5), 2053–2058. https://doi.org/10.1021/acs.nanolett.0c04702.

(146) Vörös, J. The Density and Refractive Index of Adsorbing Protein Layers. *Biophys. J.* **2004**, *87* (1), 553–561. https://doi.org/10.1529/biophysj.103.030072.

(147) De Sá Costa, B.; Garcia-Rojas, E. E.; Coimbra, J. S. D. R.; Teixeira, J. A.; Telis-Romero, J. Density, Refractive Index, Apparent Specific Volume, and Electrical Conductivity of Aqueous Solutions of Poly(Ethylene Glycol) 1500 at Different Temperatures. *J. Chem. Eng. Data* **2014**, *59* (2), 339–345. https://doi.org/10.1021/je400802t.

(148) Meena, S. K.; Celiksoy, S.; Schäfer, P.; Henkel, A.; Sönnichsen, C.; Sulpizi, M. The Role of Halide Ions in the Anisotropic Growth of Gold Nanoparticles: A Microscopic, Atomistic Perspective. *Phys. Chem. Chem. Phys.* **2016**, *18* (19), 13246–13254. https://doi.org/10.1039/C6CP01076H.

(149) *Soft Colloids*; Lyklema, H., Ed.; Fundamentals of interface and colloid science; Elsevier Academic Press: Amsterdam London, 2005.

(150) Chada, N.; Sigdel, K. P.; Gari, R. R. S.; Matin, T. R.; Randall, L. L.; King, G. M. Glass Is a Viable Substrate for Precision Force Microscopy of Membrane Proteins. *Sci. Rep.* **2015**, *5* (1), 12550. https://doi.org/10.1038/srep12550.

(151) Leibauer, B.; Pop-Georgievski, O.; Sosa, M. D.; Dong, Y.; Tremel, W.; Butt, H.-J.; Steffen, W. How Surface and Substrate Chemistry Affect Slide Electrification. *J. Am. Chem. Soc.* **2024**, *146* (14), 10073–10083. https://doi.org/10.1021/jacs.4c01015.

(152) Eisel, J. Nichtkovalente Passivierungsstrategie von Glasoberflächen für die Einzelpartikelspektroskopie. Masterarbeit, Johannes Gutenberg University Mainz, Mainz, 2024.

(153) Aboudzadeh, M. A.; Iturrospe, A.; Arbe, A.; Grzelczak, M.; Barroso-Bujans, F. Cyclic Polyethylene Glycol as Nanoparticle Surface Ligand. *ACS Macro Lett.* **2020**, *9* (11), 1604–1610. https://doi.org/10.1021/acsmacrolett.0c00730.

(154) Lee, J.; Nakouzi, E.; Heo, J.; Legg, B. A.; Schenter, G. K.; Li, D.; Park, C.; Ma, H.; Chun, J. Effects of Particle Shape and Surface Roughness on van Der Waals Interactions and Coupling to Dynamics in Nanocrystals. *J. Colloid Interface Sci.* **2023**, *652*, 1974–1983. https://doi.org/10.1016/j.jcis.2023.08.160.

(155) Hanauer, M.; Pierrat, S.; Zins, I.; Lotz, A.; Sönnichsen, C. Separation of Nanoparticles by Gel Electrophoresis According to Size and Shape. *Nano Lett.* **2007**, *7* (9), 2881–2885. https://doi.org/10.1021/nl071615y.

(156) Nyborg, J. K.; Peersen, O. B. That Zincing Feeling: The Effects of EDTA on the Behaviour of Zinc-Binding Transcriptional Regulators. *Biochem. J.* **2004**, *381* (3), e3. https://doi.org/10.1042/BJ20041096.

(157) Sanderson, B. A.; Araki, N.; Lilley, J. L.; Guerrero, G.; Lewis, L. K. Modification of Gel Architecture and TBE/TAE Buffer Composition to Minimize Heating during Agarose Gel Electrophoresis. *Anal. Biochem.* **2014**, *454*, 44–52. https://doi.org/10.1016/j.ab.2014.03.003.

(158) Burns, J. A.; Butler, J. C.; Moran, J.; Whitesides, G. M. Selective Reduction of Disulfides by Tris(2-Carboxyethyl)Phosphine. *J. Org. Chem.* **1991**, *56* (8), 2648–2650. https://doi.org/10.1021/jo00008a014.

Appendix

A. Appendix: Theoretical Essentials

1. Plasmon Coupling: The Simulation.

The simulations were performed using the MNPBEM toolbox (version 2017).[64] In this toolbox, a particle is approximated as an object made out of discrete elements. One important variable that determines the final resolution of this shape is the number of vertices. The more vertices are used for approximation, the closer does the object resemble an ideal sphere. For each face resulting from this approximation, the toolbox solves the Maxwell equations. The simulation therefore becomes more accurate with higher numbers of vertices. At the same time, the scattering cross section takes longer to calculate.

1.1. The balance between vertices number, accuracy and previously obtained data.

The toolbox provides fixed values for the numbers of vertices to choose from. Previously in this group, the value of 625 vertices has been used to simulate spectra. To get a feeling for the quality of the simulated data obtained with this number of vertices, a particle dimer simulation was performed for two particle sizes of 30 and 60 nm at a minimal relevant distance of 8 nm. This represents the absolute minimal interparticle distance, given by the Hsp90 protein size in its closed state. The smaller the interparticle distance is, the higher is the required resolution. It is therefore important to test the simulation at the smallest relevant interparticle distance.

This test was done for a number of vertices ranging from 144 to 1444. The following figures show the progression of simulated spectra for a dimer for 30 and 60 nm particles. The progress of the resonance wavelength and maximal scattering cross section is fitted with an exponential function, and its limit is taken as the "true" value. For all three particle sizes, the values produced by a simulation using the number of vertices=625 lie in the range of 1% deviation from this "true" value. The plots in (d) show that the chosen number of vertices has a different variation from the "true" value, with the result being closer for the smaller 30 nm particle dimer. The value for the bigger 60 nm dimer pair still fits the criterium, but is already at the edge.

Within the scope of this work, this deviation from the "true" value is accepted as sufficient. To keep the simulation results comparable to previous works in our group, the number of vertices was fixed at 625 for all simulated data.

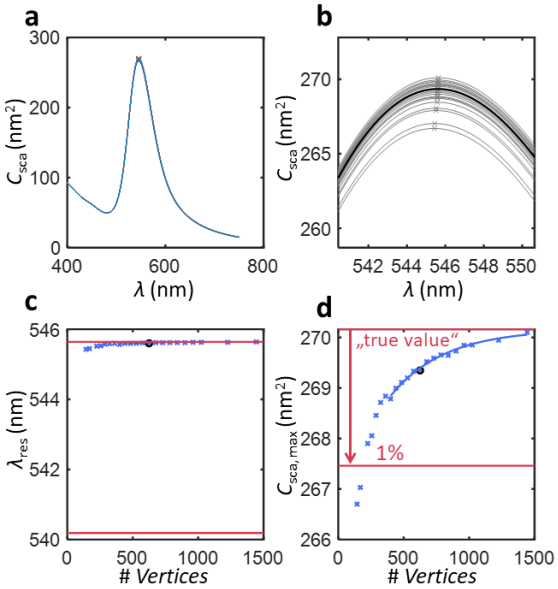

Figure A-1. Simulated particle dimer scattering cross sections for a 30 nm particle dimer at a distance of 8 nm. (a) All simulated spectra ranging from 144-1444 number of vertices. (b) A closeup of (a), with the simulated cross section at the number of vertices=625 marked in black. The resonance position is marked with crosses. (c) Resonance positions form a-b) recorded from each spectrum obtained at a different number of vertices. Red line marks a deviation of 1% from the "true" value. The value at number of vertices=625 is marked with a black circle. (d) The maximal scattering cross section from a-b), with a fit (blue line) to obtain the "true" maximal value. Red lines mark this value, as well as the lower boundary at a 1% deviation from it. The scattering cross section obtained at a number of vertices=625 is marked with a black circle. Data obtained with bemsolver.

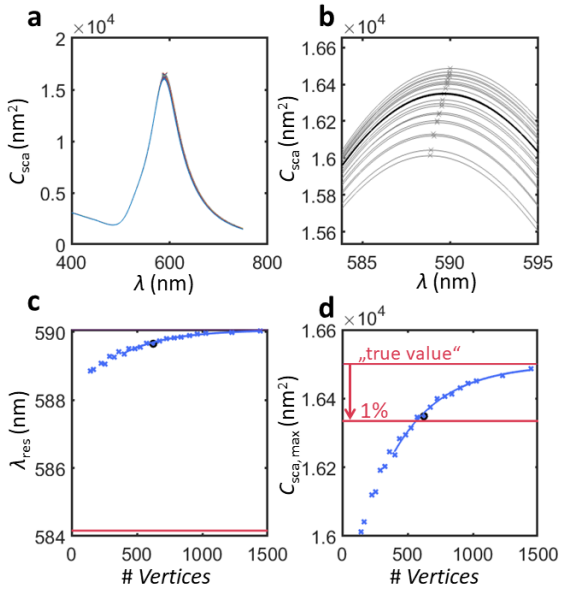

Figure A-2. Simulated particle dimer scattering cross sections for a 60 nm particle dimer at a distance of 8 nm. (a) All simulated spectra ranging from 144-1444 number of vertices. (b) A closeup of (a), with the simulated cross section at the number of vertices=625 marked in black. The resonance position is marked with crosses. (c) Resonance positions form a-b) recorded from each spectrum obtained at a different number of vertices. Red line marks a deviation of 1% from the "true" value. The value at number of

vertices=625 is marked with a black circle. (d) The maximal scattering cross section from a-b), with a fit (blue line) to obtain the "true" maximal value. Red lines mark this value, as well as the lower boundary at a 1% deviation from it. The scattering cross section obtained at a number of vertices=625 is marked with a black circle. Data obtained with bemsolver.

1.2. Conditions for the simulation of particle dimers.

Simulations were done for single particles and particle pairs that mimicked the dimer (Figure A-3). For the medium, n=1.33 was chosen, corresponding to the experimentally determined refractive index of the HEPES buffer (50 mM KCl). The light is falling at an angle of 30°, mimicking the dark-field illumination produced by the Zeiss ultracondenser. This angle was assumed with the NA of the condenser (1.2-1.4), using the average value of 1.3 and the relationship $NA = n \cdot sin\alpha$. The polarization was chosen in the x/z direction for the excitation of the coupled plasmon mod

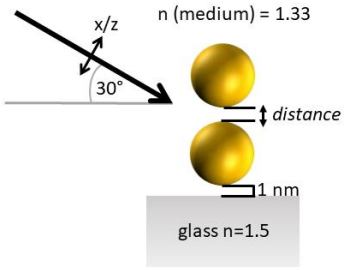

Figure A-3. Sketch of a simulated dimer. The dimer is standing on glass (grey shaded area), and the interparticle distance is varied by moving the top particle in the z-direction. Black arrow indicates the light, which is falling at an angle of 30°. The refractive index of the medium is 1.33, corresponding to the measured value for the protein buffer (HEPES 7.4, 50 mM KCl).

The simulation has to describe the experiment without relying too much on (often not well known) experimental conditions. For this reason, the particles were simulated without the extra polymer layer on top of the particles, but with the glass substrate. The effect of the glass substrate is of special note, and is recorded in the following section.

1.3. Resolution and fit.

Each spectrum was simulated in steps of 1 nm for the interparticle distance. The resulting data was first fitted with a double Lorentz function. This is shown Figure A-4. In a first approximation, this fit is sufficient at describing the data.

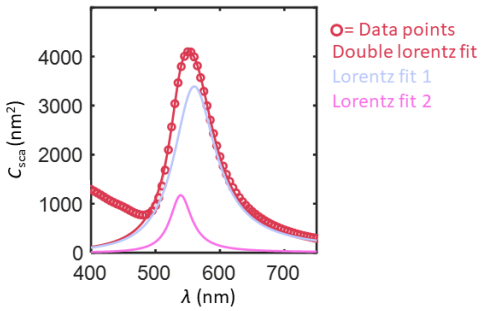

Figure A-4. Simulated scattering cross section data for a 50 nm dimer at a distance of 23 nm. Circles represent the simulated data points, the red line the double Lorentz fit and the other two lines (blue+pink) show the two Lorentz fits.

However, we noticed that this fit produced artifacts in the data evaluation step. This is because the fit does not describe the data as well, with the error depending on the form of the spectrum. This was especially critical for extraction of intensity data on the right-side shoulder of the spectrum.

To avoid discrepancies in further data analysis, the data was instead interpolated with a spline function. Figure A-5 shows this using the example of a 50 nm particle dimer. The fit was used to extract the resonance position as well as the scattering values at given wavelengths.

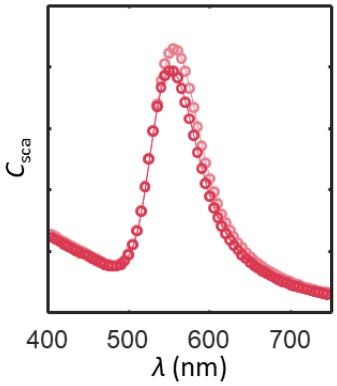

Figure A-5. Example spectra with highlighted individual data points and the spline function. The spectra depict a 50 nm particle dimer at a distance of 18 (red) and 23 (pale red), representing the state-of-the-art protein dimer. The line represents the interpolation with a spline.

1.4. Practical hints for simulation with the MNPBEM toolbox: the role of the solvers and discrepancies in certain simulated cases

This section contains practical notes for simulating different cases with the toolbox, especially regarding the "solvers".

The toolbox has various algorithms to solve the Maxwell equations for each boundary element face. The procedure used to implement a specific algorithm is named "solver".[64] The toolbox provides a standard call for the solver (called "bemsolver"). The various options determine which solver algorithm (from a range of possible algorithms) will be used. For the user, it is not obvious which algorithm the toolbox selects. This depends

on parameters, e.g. whether a single particle or a dimer is simulated, and whether there is a substrate present. Alternatively, user can call the solver with a specific algorithm. There are two possibilities for the user: to choose "bemret" or "bemretlayer".

During the processing of simulations, we have noticed discrepancies when using "bemsolver". This is because this solver picks different algorithms depending on starting simulation parameters (e.g. particle type and substrate). This decision cannot be influenced by the user. The resulting discrepancies affected specific simulation cases, which I report on in the following section for future reference.

The final simulated data used for the extraction of sensitivity were all produced using the solver "bemretlayer". For the case where no additional layer is present (when particles are simulated in a free state without a substrate), the input for the refractive index was set to $n_1=n_2$. This setting helped to avoid discrepancies shown in the following sections.

1.1.1. Use of bemsolver leads to illogical discrepancies between monomer and dimer spectrum without substrate.

Here I document a discrepancy found when the bemsolver was used to simulate and quantitatively compare monomer and dimer spectra. This problem is illustrated in Figure A-6, for a 30 nm and a bigger 50 nm particle (pair). An unexpected crossing point happens between the spectra in the right shoulder of the spectrum. From this point and up to higher wavelengths, the dimer spectrum scattering cross section is counterintuitively lower than that of the monomer. The effect is also stronger for the smaller particle.

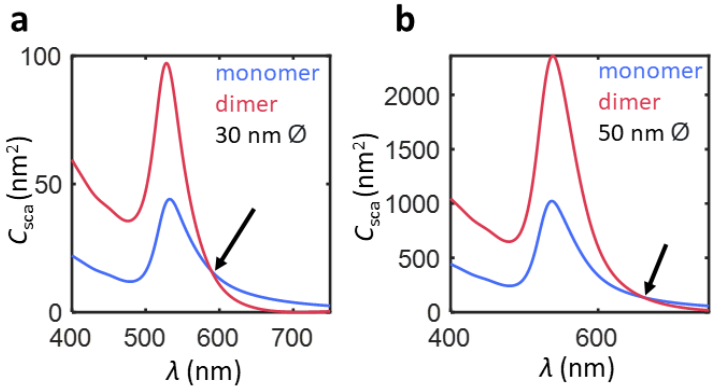

Figure A-6. Monomer and dimer spectra produced by the bemsolver. (a) Simulated monomer and dimer spectrum of a 30 nm particle (pair) at a distance of 20 nm. (b) Simulated monomer and dimer spectrum of a 50 nm particle (pair) at a distance of 20 nm. Both cases show a crossing point between the dimer and monomer spectrum (marked with black arrow), which cannot be explained by physical reasons.

1.1.2. The use of bemret solver corrects this discrepancy.

As shown in Figure A-7, the phenomenon of crossing spectra disappears when the bemret solver is used instead. It is therefore recommended to use the bemret solver when making quantitative comparisons between monomer and dimer spectra.

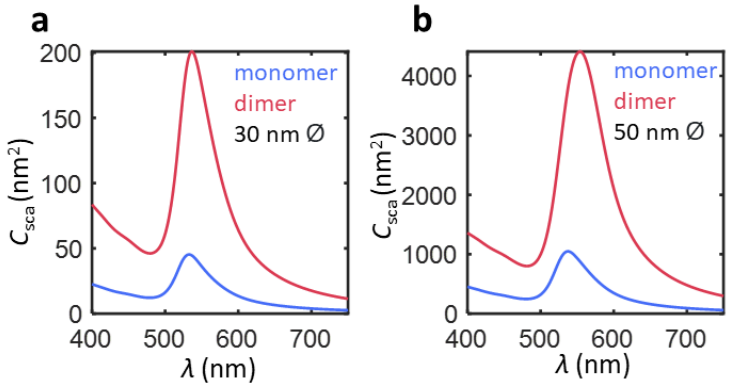

Figure A-7. Monomer and dimer spectra produced by the bemret solver. (a) Simulated monomer and dimer spectrum of a 30 nm particle (pair) at a distance of 20 nm. (b) Simulated monomer and dimer spectrum of a 50 nm particle (pair) at a distance of 20 nm. Both cases show a crossing point between the dimer and monomer spectrum (marked with black arrow), which cannot be explained by physical reasons.

The team's understanding of this situation is that in the case of bemsolver, the script operates differently for the cases of monomer and dimer, and that certain options are chosen by the toolbox without specific user input. These out-of-screen options lead to different quantitative outcomes for each case.

1.1.3. To compare data with and without a substrate, use "bemretlayer"

Through testing, it was found that the toolbox's most robust option is the "bemret with layer". This option led to consistent and quantitatively comparable spectra both with and without a substrate. When no substrate was used, the refractive index of the layers was set to n_1=n_2 in the options. Figure A-8a-d shows that the use of this option leads to consistent results for both cases with and without a substrate. No issues as seen with the use of bemsolver are observed.

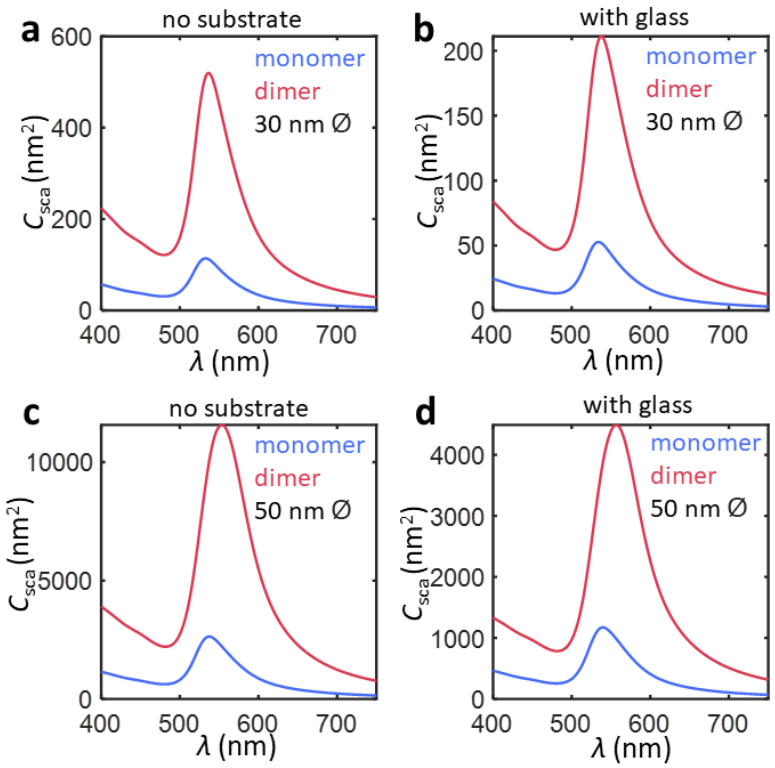

Figure A-8. Spectra obtained for monomers and dimers under different conditions, with the bemret with layer solver. (a)-(b) 30 nm monomer and dimer spectra at a distance of 20 nm, simulated for the case without a substrate and with glass. (c)-(d) 50 nm monomer and dimer spectra at a distance of 20 nm, simulated for the case without a substrate and with glass.

The figures with and without substrate show an important difference: simulated spectra without a substrate show higher intensities than those with glass. In the next part, I show how this affects the sensitivity, and why the effect of the substrate should ideally be accounted for.

1.5. Simulation is good for trend prediction, but not for determination of absolute values.

Overall, it is important to note that the simulation is not meant to predict exact experimental data. One reason for this is the difficulty in representing actual realistic experimental conditions in the simulation. A lot of factors such as the exact influence of the additional polymer layer on the particle, as well as on the glass substrate, are simply not known. Notably, the influence of a present or absent substrate near the dimer is of particular importance for intensity-based predictions. Figure A-9 shows is by comparing calculated sensitivities of simulated dimers at a fixed distance (20.5 nm, representing the average state-of-the-art dimer assembly interparticle distance). Figure (a) shows that simulated sensitivities for dimers on a glass substrate and without it are in good agreement with each other. This however is not the case for sensitivity related to intensity. There is a constant offset, with data with the glass substrate showing a higher sensitivity.

At present, the exact origin of this is not yet explored. There may be a complex (and not purely physical) reason for this, for example because of an interplay between the spectrum…

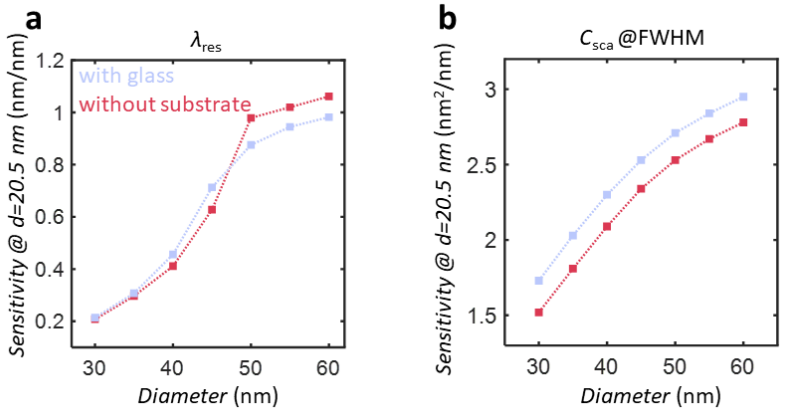

Figure A-9. Sensitivity comparison with and without a substrate, at an interparticle distance of 20.5 nm for particle dimers between 30-60 nm in diameter. (a) Resonance wavelength sensitivity. (c) Relative intensity sensitivity at the FWHM.

1.6. Compilation of simulated data, with and without substrate.

Below I append simulation data obtained without substrate, which was not shown in the main part.

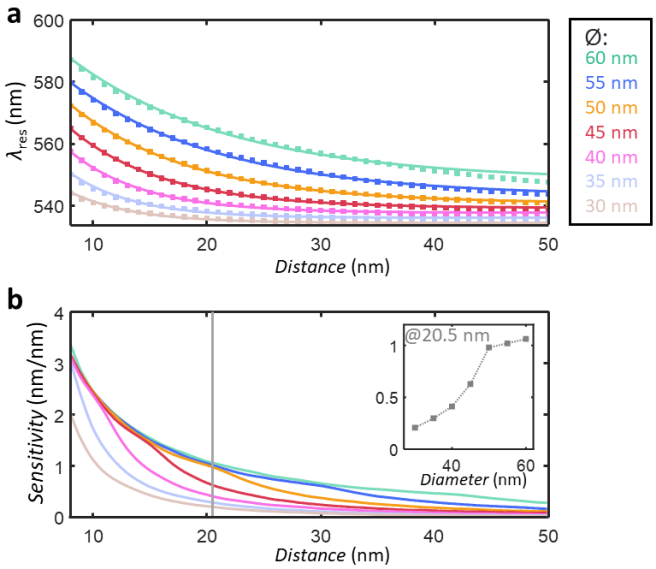

Figure A-10. Predicted resonance wavelength shift, without substrate. (a) Resonance position is plotted against the interparticle distance for dimer pairs varying from 30 to 60 nm in particle diameter. Individual squares show simulated data, connected by a guide to the eye. Grey lines mark the interparticle distance resulting from the "open" and "closed" protein conformation in the state-of-the-art Hsp90 dimer. (b) Sensitivity determined from data in (a), derived by numerical differentiation of the plot in a). Grey line at 20.5 nm marks the average interparticle distance between the "closed" and "open" conformation of the Hsp90 protein in the state-of-the-art assembly. Inset: Sensitivity value trend at the interparticle distance of 20.5 nm, for particle diameters between 30-60 nm.

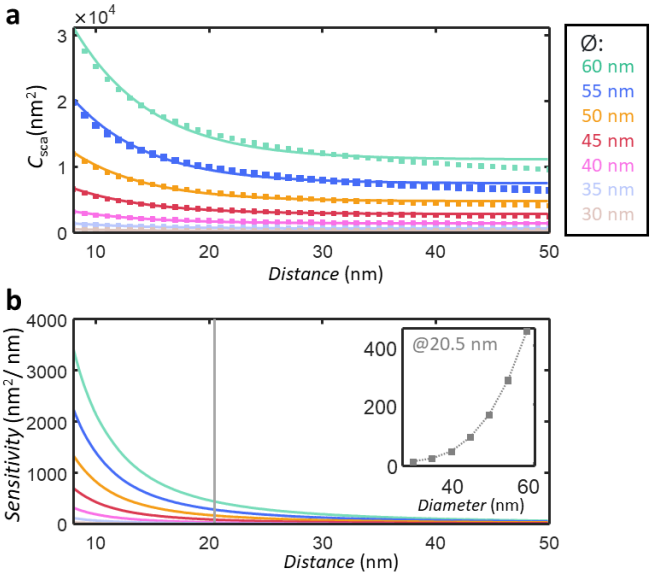

Figure A-11. Predicted scattering cross section change at the FWHM. (a) Scattering cross section plotted against the interparticle distance for dimer pairs varying from 30 to 60 nm in particle diameter. Individual squares show simulated data, connected by a guide to the eye. Grey line marks the average interparticle distance resulting from the "open" and "closed" protein conformation in the state-of-the-art Hsp90 dimer. (b) Sensitivity determined from data in (a), determined by numerical differentiation of the plot in a). Inset: Sensitivity value trend at the interparticle distance of 20.5 nm, for particle diameters between 30-60 nm.

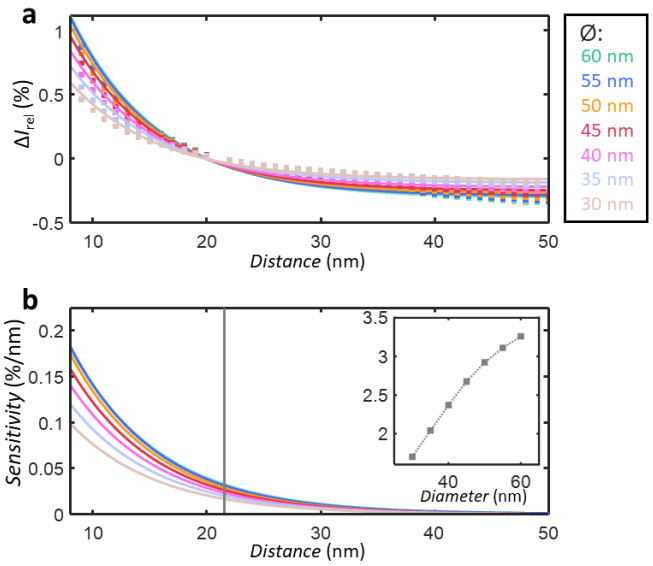

Figure A-12. Relative intensity change at the FWHM. (a) Scattering cross section plotted against the interparticle distance for dimer pairs varying from 30 to 60 nm in particle diameter. Individual squares show simulated data, connected by a guide to the eye. Grey line marks the average interparticle distance resulting from the "open" and "closed" protein conformation in the state-of-the-art Hsp90 dimer. (b) Sensitivity determined from data in (a), determined by numerical differentiation of the plot in a). Inset: Sensitivity value trend at the interparticle distance of 20.5 nm, for particle diameters between 30-60 nm.

1.7. Fit data for plots shown in the main section.

Following two tables show fit data for plots in Figure II-6 and Figure II-8 for reproduction purposes. Data shown belongs to the simulated series in the presence of a glass substrate. *D* stands for the interparticle distance.

a With glass

λ_{res}/nm = a·exp(-D/b)+off			
Particle Ø (nm)	**a**	***b***	**off**
30	46.2947	5.4398	535.5452
35	60.6943	5.8140	537.2595
40	64.9266	7.0216	539.0901
45	64.2976	8.9926	541.0073
50	63.3487	11.3808	543.4843
55	64.1786	12.6729	548.1302
60	67.0188	12.8425	554.1190

b With glass

I@FWHM/nm² = a·exp(-D/b)+off			
Particle Ø (nm)	**a**	***b***	**off**
30	301.2581	7.0614	101.3003
35	946.3947	6.8994	252.5962
40	2466.7	6.7821	543.2341
45	5384.9	6.6908	1019.9
50	10002	6.6853	1721.0
55	16495	6.8196	2720.4
60	24728	7.0740	4074.2

Figure A-13. Fit data for plots shown in the main section. (a) Exponential fit data for resonance wavelength dependance on the edge-to-edge dimer distance D, with substrate. (b) Exponential fit data for absolute intensity dependance on the dimer distance, with substrate.

a Without substrate

λ_{res}/nm = a·exp(-D/b)+off			
Particle Ø (nm)	**a**	***b***	**off**
30	42.1123	5.5795	534.3895
35	59.1002	5.6890	535.9280
40	66.7133	6.6026	537.5797
45	67.6816	8.2765	539.2168
50	66.8002	10.7302	540.7864
55	66.9449	13.3511	543.0673
60	69.0715	14.2522	4.8464

b Witout substrate

I@FWHM/nm² = a·exp(-D/b)+off			
Particle Ø (nm)	**a**	***b***	**off**
30	711.8348	6.6305	259.0250
35	2256.8	6.5951	655.5923
40	5983.2	6.5679	1436.9
45	13460	6.5322	2762.9
50	25627	6.5029	4698.7
55	42892	6.5965	7442.6
60	64909	6.8021	11156

Figure A-14. Fit data for plots without substrate. (a) Exponential fit data for resonance wavelength dependance on the edge-to-edge dimer distance D, without substrate. (b) Exponential fit data for absolute intensity change dependance on the dimer distance, without substrate.

The following two tables show fit data for the relative intensity exponential fits.

a Without substrate

ΔI_{rel}@FWHM/% = a·exp(-D/b)+off			
Particle Ø (nm)	**a**	***b***	**off**
30	3.4778	0.1530	-0.2164
35	2.6045	7.6329	-0.1943
40	3.0495	7.5993	-0.2244
45	3.4508	7.5903	-0.2521
50	3.7890	7.5690	-0.2745
55	3.9615	7.6433	-0.2931
60	3.9291	7.8862	-0.3108

b With glass

ΔI_{rel}@FWHM/% = a·exp(-D/b)+off			
Particle Ø (nm)	**a**	***b***	**off**
30	3.5177	0.1629	-0.2551
35	2.6834	8.2986	-0.2427
40	3.1678	8.0798	-0.2696
45	3.5963	7.9431	-0.2938
50	3.9138	7.8764	-0.3131
55	4.0156	8.0126	-0.3321
60	3.9306	8.3244	-0.3510

Figure A-15. Relative intensity with and without substrate. (a)-(b) Exponential fit data for relative intensity change dependance on the dimer distance, without and with substrate.

2. The interaction potential.

The following section summarizes all supplementary material related to the calculation of the interaction potential.

2.1. The contribution of the polymer layer to the vdW interaction is complicated.

Calculating the vdW attraction for a spherical gold particle is simple, because the average radius of the particle is known and the particle itself is uniform in terms of material. However, literature offers mixed treatments of the polymer layer on top, which theoretically should be expected to also contribute to the attractive vdW interaction. Assumptions are made, for example about the polymer density and volume fractions, as well as how the interaction is calculated in the first place.

For example, Zámbó et al.[73] have shown that for two gold particles covered by PEG, the vdW attraction becomes significant only at separations below 1-2 nm between the PEG layers, and for PEG volume fractions of 0.3-0.5 or higher. Their assumption is mainly based on volume fractions of PEG. On the other hand, Aboudzadeh et al.[153] have attempted a more complex model that accounts for additional interactions, such as that of the PEG layer with the gold.

To get a feeling for the range of attraction caused by PEG, I compared the vdW attraction between two 50 nm gold spheres with that caused by a 4 nm polymer layer on each. For the Hamaker constants, I used $2.5 \cdot 10^{-19}$ J for the gold/water/gold and $3.7 \cdot 10^{-20}$ J for the PEG/water/PEG system[153]. I approximated the polymer shell as having a thickness of 4 nm, for a 2000 g/mol PEG with 45 repeating units.

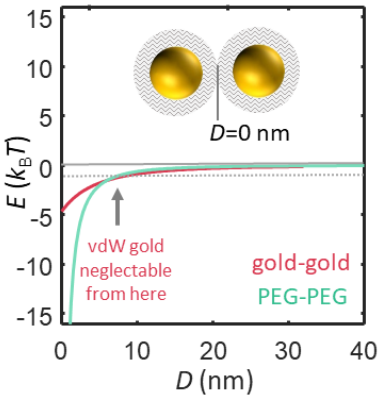

Figure A-16. Sketch of vdW interactions for two 50 nm gold spheres covered by a PEG polymer layer. The vdW interaction potential of the gold spheres is shown with an offset that equals the polymer layers. The starting distance D begins where the polymer layers touch. Arrow shows the distance where the contribution of the gold-gold interaction (red) becomes negligible due to the polymer spacer. Green line shows the calculated PEG-PEG vdW interaction. According to this example, the interaction falls below the thermal energy (1 k_BT) at a distance as long as about 6 nm. The attraction becomes stronger at lower separation, suggesting that the particles should aggregate.

The sketch showcases the following: The polymer serves as a spacer that separates the gold particles until their vdW attraction becomes negligible. For better visualization of the vdW potential location, I show an example where the polymer layer is not yet thick enough to separate the gold spheres sufficiently: Ideally, the potential of the gold spheres would be around -1 $k_B T$ at the distance D=0 nm. Here, it is still at about -5 $k_B T$. This means the particles still experience each other's attraction at a distance larger than their polymer shell.)

However, a second, more important point becomes apparent: the vdW attraction of the polymer shells grows rapidly at a distance of several nanometers between the polymer layers. The particles should therefore stick before the steric and entropic repulsion has the chance to stabilize them. More on this follows in the next section.

2.2. The "true" starting point of the vdW interaction between polymer layers is not known.

The previous, right estimation shows that the vdW interaction of the polymer layer exists and is not negligible. The following problem arises: according to the model, the vdW interaction becomes, per definition, infinitely strong at a distance of several nanometers. At the same time, the entropic and steric repulsion begin only when the polymer shells begin to overlap. Mathematically, this would suggest that particles should stick to each other, because there is a strong attraction present that is not cancelled out by repulsion. However, experimental evidence shows that this is not so. Particles covered by a sufficiently thick PEG layer do not stick to each other in solution.

This observation hints at an issue in the model in use. There is, for example, one factor that is presently not included: This is the fact that the vdW interaction is also dependent on the surface roughness, which is entirely neglected.[154] Figure A-17 illustrates the difference between the simplified model and the more realistic case of a "rough" polymer shell. It shows how the "effective" interparticle distance grows with roughness. This influences the starting point of the vdW interaction.

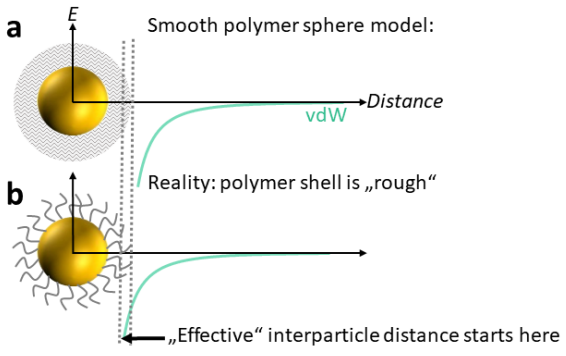

Figure A-17. Sketch of the effect of surface roughness on the vdW interaction. (a) In the simple model, the polymer layer is approximated as a smooth shell, with a vdW interaction starting distance at the edge of this shell. (b) In reality, polymer shells are not smooth. This means that the realistic, "effective" interparticle distance is bigger.

This complicates the calculation, because the effective interparticle distance would depend on factors such as polymer density and length. As Lee et al.[154] show, it is well possible to make assumptions and calculate values. However, since the experimental evidence shows that the polymer shells do not aggregate due to their own vdW attraction, it is sufficient, for the questions treated in this thesis, to simply acknowledge this fact. The polymer fulfills its primary role as a spacer that makes the vdW interaction of gold particles negligible.

2.3. Calculation of the Coulomb potential for two spherical gold particles.

Following formula is derived for two particles at a variable distance *D* with a radius *r* and a Debye length κ^{-1}.

$$E_{\text{Coulomb}}(D) = \left(\frac{r^2}{2r}\right) Ze^{\kappa D} \tag{A.1}$$

Z is the interaction constant, and is calculated as follows:

$$Z = 64\pi\varepsilon_0\varepsilon\left(\frac{k_B T}{e}\right)^2 \tanh^2\left(\frac{ze\Psi_o}{4k_B T}\right) \tag{A.2}$$

The formula includes the permittivity of the vacuum, ε_0=8.854·10^{-12} F/m, the dielectric constant of the medium ε (water in this case, with ε=80 at 20°C), elemental charge e, valence of ions z, the concentration of the electrolyte c_∞ and the surface potential Ψ_o.

The surface potential is determined using the surface charge density σ. The surface charge density is derived from the experimentally measurable ζ-potential of the particle sample.

The interaction constant is calculated using is the surface potential of the particle Ψ_o. Ψ_o is determined from the surface charge density σ, which is derived from the experimentally measurable ζ-potential of a particle sample.

$$\Psi_o = \frac{2k_B T}{ze}\sinh^{-1}\left[\frac{\sigma}{(8RT\varepsilon_0\varepsilon c_\infty)^{1/2}}\right] \tag{A.3}$$

$$\sigma = \frac{\varepsilon_0\varepsilon k_B T}{ze}\kappa\left[2\sinh\left(\frac{\zeta ze}{2k_B T}\right) + \frac{4}{\kappa r}\tanh\left(\frac{\zeta ze}{4k_B T}\right)\right] \tag{A.4}$$

($k_B T$=4.11·10^{-21} J ; R=8.314 J/(K·mol))

1.1.4. The relevance of the particle size to the calculation of the electrostatic repulsion is neglectable.

Since the particle radius is a variable that also plays a role in the total calculation, I varied it for the sake of a complete picture Figure A-18 shows that its contribution to the electrostatic potential is neglectable compared to the contribution to the vdW attraction.

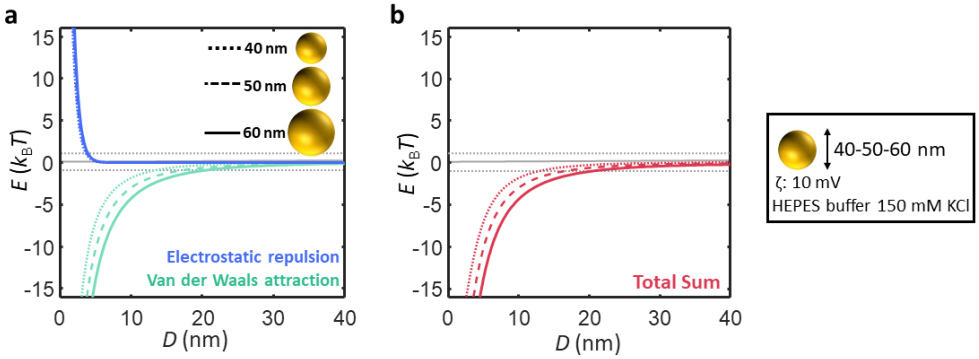

Figure A-18. Particle size leads to no significant difference at high salt conditions. (a) Electrostatic repulsion calculated for a 40-50-60 nm pair of particles, with a hypothetical ζ-potential of 10 mV in the 150 mM KCl buffer (blue lines). Respective vdW potential is shown in green. (b) The total sum of both potentials.

1.1.5. The starting distance for the vdW potential is different from that of the electrostatic potential.

One problem that arises when weighing the vdW attraction against electrostatic repulsion is the starting distance. This problem is known in literature[70(p.330)], and is sometimes referred to as the issue of the definition of the "plane of origin". For simplicity, this thesis assumes that the starting point for both the vdW and electrostatic potentials is the same. This is however not true in reality. An additional complication is that I calculate the potentials while foregoing the polymer layer to keep the calculation simple. The only exception is when the steric repulsion produced by the polymer layer is taken into account.

For the case of the high salt protein buffer, this problem can be safely neglected, as the contribution of the electrostatic repulsion is small enough. However, when considering other buffers or assembly conditions, this issue should be taken into account.

To get a feeling for the error caused by the neglection of the polymer, I did the calculation of the electrostatic potential for a 50 nm particle with a ζ-potential=10 mV, with and without the polymer taken into account for the starting distance. I chose the high salt HEPES buffer with 150 mM KCl. Unsurprisingly, the potential curves in Figure A-19 show barely any difference between the two under the conditions of the strong ionic buffer.

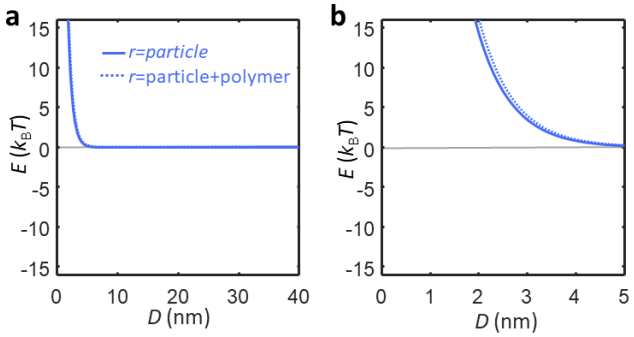

Figure A-19. Electrostatic potential for a 50 nm particle. (a) Potential shown with and without taking the polymer layer into account. (b) A closeup of the potential curve in (a).

3. Assembly kinetics: How to calculate the average interparticle distance.

To convert a concentration c into the average center-to-center interparticle distance, we first need to calculate the number of particles per cubic meter, N:

$$N = \frac{cN_A}{10^{-3}} \ [\mathbf{particles/m^3}] \quad \text{A.5}$$

c: concentration
N_A: Avogadro number ($6.022 \cdot 10^{23}$ particles/mol)
Factor 10^{-3}: conversion factor from L to m^3

Next, we assume that the cubic space is filled up filled with particles at the same distance to all their neighbors. The center-to-center distance r_0 is found by taking the cube root of the number of particles per cubic meter, N:

$$r_0 = \sqrt[3]{N} \quad \text{A.6}$$

Figure A-20 illustrates the distance dependance for a concentration range from 0.1 nM to 1 mM. Note that for particles specifically, the center-to-center distance should be corrected to edge-to-edge distance by adding the particle radius to the average distance.

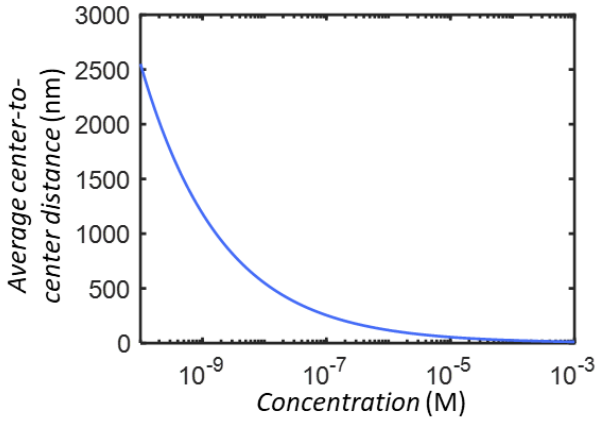

Figure A-20. Conversion of concentration to average distance.

B. Appendix: Particle Functionalization

1. Chemicals

Nanoparticles
50-60 nm CTAC particles were made according to protocol listed below.
40 and 60 nm citrate capped particles were purchased from sigma aldrich: 40 nm (OD=1, c=0.12 nM, 741981-100ML, #MCKM0274), 60 nm (OD=1, c=0.03 nM, 742015-100ML, #MCKQ7314).

PEGs
Following PEGs were purchased from Iris Biotech: methoxy-PEG-thiol 2000 g/mol, 5000 g/mol; amino-PEG-thiol, 3000 g/mol; dithiol-PEG-thiol, 2000 g/mol, dithiol-PEG-thiol, 3000 g/mol, dithiol-PEG-thiol, 6000 g/mol; carboxy-PEG-thiol, 3000 g/mol amino-PEG-thiol, 2000 g/mol; methoxy-PEG_4-thiol; methoxy-PEG_6-thiol; diamino-PEG-thiol, 2000 g/mol, 3000 g/mol were purchased from sigma aldrich.
biotin-PEG-thiol, 2000 g/mol was purchased from Biopharma PEG Scientific Inc.

DNA
DNA was purchased from biomers.net.
cgactcgctggtctggttgaacgtcagccctgcc(tttttt); 3': Thiol C3 (internal codename: DNA3long)
ggcagggctgacgttcaaccagaccagcgagtcg(tttttt); 3': Thiol C3 (internal codename: DNA4long)
ctgtctataatgacg(tttttt); 3': Thiol C3 (internal codename: DNA1short)

Other
Deionized water (>18 MΩ), from a Millipore Q-Pod.
CTAC (hexadecyltrimethylammonium chloride) >98%, sigma aldrich
Tween20 (polyoxyethylenesorbitan monolaurate), sigma aldrich
DMSO (dimethylsilfoxide) 99.7%, Acros Chemicals
SMCC (Succinimidyl 4-(N-maleimidomethyl)cyclohexane-1-carboxylate), thermo scientific
TCEP (tris(2-carboxyethyl)phosphine), Merck
$HAuCl_4$, sigmal aldrich
L(+) ascorbic acid, AppliChem
$NaBH_4$ >99%, sigma aldrich
NaOH 1N, Roth
BSA, >98%, sigmaaldrich

Streptavidin from Streptomyces avidinii
Mono-Streptavidin
NaCl, >99.5% Fisher Scientific
KCl, >99%, sigmaaldrich
$MgCl_2$, 98%, sigmaaldrich
Na_2SO_4, >99%, sigmaaldrich
K_2SO_4, >99%, sigmaaldrich

Hsp90 protein

Hsp90 protein was kindly provided by the group of Thorsten Hugel, University of Freiburg. The full exprimation and purification protocol is listed in reference.[49]

2. Particle synthesis, 50-65 nm spheres.

This synthesis typically gives particles between 50-65 nm, with exceptions sometimes giving larger sizes. Synthesis is performed as in references.[51,61]

At the start, all glassware is cleaned with aqua regia (HCl 37%, 60 mL + HNO_3 65% 20 mL, mix carefully!). Glassware is then cleaned with milliQ water for synthesis and dried overnight.

Prepare chemicals:

$HAuCl_4$ 50 mM
CTAC 100 mM
CTAC 25 mM $NaBH_4$ 20 mM, then dilute 1:10 (100 μL dulited in 900 μL ice-cold milliQ water)
Ascorbic acid 100 mM, 1 mL

Step 1, seeds: Prepare a 20 mL glas vial with a teflon stirring bar. Add 1 mL 100 mM CTAC under stirring, then add 10 μL $HAuCl_4$. Solution turns light yellow. Quickly and under vigorous stirring add 40 μL $NaBH_4$. Solution turns light brown. Turn off the stirring and leave at rest for 5 min. Then add 9 mL 100 mM CTAC.

Step 2, 10 nm seeds: Put in 5 mL 25 mM CTAC a 20 mL glass vial. Ass 450 μL of seeds prepared in step 1 and stir. Under stirring, add 20 μL ascorbic acid. Then under vigorous stirring add 25 μL $HAuCl_4$. Leave at rest for 10 min at room temperature. Measure UV-Vis ensemble spectrum. The resonance peak should be around 520 nm.

Growth: Prepare a 200 mL glass beaker. Put in 100 mL 25 mM CTAC and 250 μL seeds from step 2. Stir. Add 400 μL ascorbic acid under vigorous stirring. Then, under vigorous stirring, add 500 μL 0.05 $HAuCl_4$. Leave solution at rest for 1 h at room temperature. (The longer you wait, the bigger will the particles become.) Measure UV-Vis spectrum. The resonance peak should be around 552 nm.

Oxidative etching: To the growth solution, add 100 μL NaClO solution under vigorous stirring. Stir for 30 s. After 5 min add 20 μL $HAuCl_4$. Leave to rest at 30°C for 45 min. UV-Vis resonance peak should be around 533 nm.

Cleaning: Particle solution is split in three tubes and centrifuged at 10230 rcf for 15 min. The supernatant is removed and replaced with 30 mL 25 mM CTAC. This step is repeated 2 times. After last cleaning step, the particles are filled up to 30 mL with 25 mM CTAC.

Characterization in TEM: 500 μL of the original particle solution are centrifuged for 4 min. The supernatant is removed and replaced with 100 μL milliQ water. This step is repeated. 10 μL of this solution are dropped onto a TEM grid and dried overnight.

Following figure shows example images of particles obtained with this method.

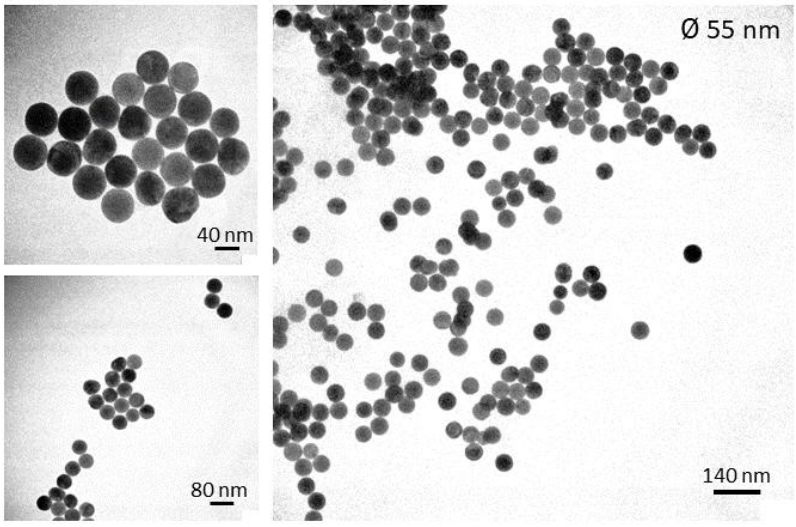

Figure B-1. TEM images of a sample of 55.0±2.7 nm particles. The values are obtained from a total of 132 particles.

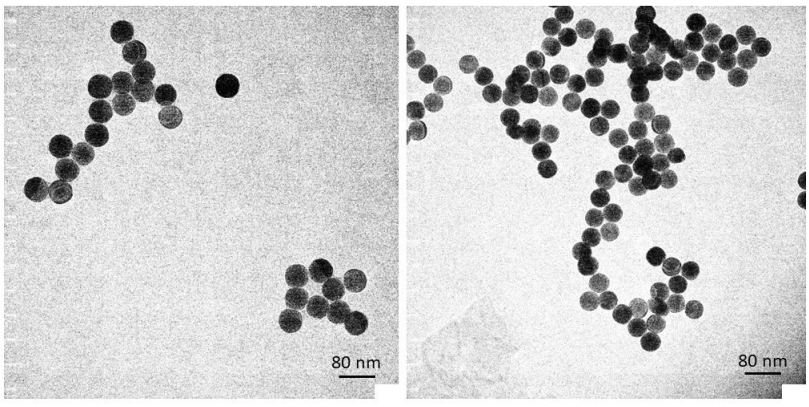

Figure B-2. TEM images of a sample of 54.4±2.3 nm particles. The values are obtained from a total of 250 particles.

3. Particle functionalization with PEG

The commonly used particle stocks have particles ranging between 50-60 nm in diameter, at a concentration between c=0.08-0.15 nM.

300 μL of original particle stick is diluted with 700 μL milliQ water and centrifuged at 10230 rcf for 8 min. The supernatant is removed and the pellet left. 200 μM thiol-capped PEG solutions with respective end groups are prepared. The PEG solutions are mixed at corresponding ratios, e.g. 5 μL amino-PEG (3000 g/mol) with 45 μL methoxy-PEG (2000 g/mol) for a 10% amino-PEG particle batch. Next the PEG solution is diluted either with 50 μL milliQ water (for functionalization without salt) or with 100 mM potassium sulfate or sodium sulfate. The final solution contains 100 μM PEG and 50 mM salt. Into this mixture, the nanoparticle pellet is dropped and quickly mixed. Ultrasound until particles are redispersed. The solution is left to stand overnight, typically for at least 12 h. Next day, the particles are cleaned by centrifugation. For this, the batch is centrifuged at 10230 rcf for 3 min. The supernatant should be clear. The supernatant is removed at the particles centrifuged 5x in 100 μL 50 mM salt solution with addition of 10 μL 2% Tween20. Particles can also be washed in PBS.

4. Particle functionalization with DNA

For sigma aldrich 40/60 nm OD=1 citrate capped particles: 30 μL 100 μM thiol-capped DNA is mixed with 5 μL TCEP (100 mM in 0.3 M NaOH), the mixture incubated for 5 min at room temperature. 10 μL of this mixture are added to 400 μL citrate capped particles and mixed. Then 0.4 μL 10% SDS is added. The particle solution is stored at -80°C for at least 10 min, two times.

DNA particles are washed by centrifugation 5 x in TE buffer (pH=8) + 20 μL 1% Tween20. After the last step, particles are redispersed in HEPES buffer.

For CTAC particles: 300 μL particles form original stock are mixed with 700 μL milliQ water and centrifuged at 10230 rcp for 5-8 min. Pellet is redispersed in DNA solution: 30 μL 100 μM thiol-capped DNA in TE buffer (pH=8) + 5 μL TCEP (100 mM), then incubated for 5 min at room temperature. Afterwards 30 μL 1% SDS are added. The mixture is incubated for 1 h at room temperature, then 2 μL 2M NaCl are added 5x at intervals of 10 min.

DNA functionalization of pre-PEGylated particles: For pre-covered DNA particles, CTAC particles are first functionalized with amino- and methoxy-PEG according to the general protocol above. After cleaning, particles are transferred to PBS or HEPES buffer pH=6.7. per 100 μL particle solution, 30 μL thiol-capped DNA (100 μM in TE buffer pH=8) is added. Incubation at room temperature overnight. Cleaning according to the PEG functionalization protocol, 5x at 10230 rcf, 3-5 min, either in TE or HEPES/PBS buffer. Long-term storage preferably in TE buffer.

Two-step passivation with PEG_3 and PEG_6: DNA particles are washed according to protocol. PEG_3 or PEG_6 is dissolved in water at a concentration of 10 mM. To a pellet

of DNA particles from 100 µL of original solution, 100 µL of this PEG solution are added. Incubation overnight, and subsequent washing like in the first step.

Incubation of particles with proteins (Hsp90, BSA, SA) for test of nonspecific sticking behavior: A 100 µM solution of protein is prepared in HEPES buffer. As an exception, streptavidin is dissolved in PBS 7.4 (due to original stock being in PBS 7.4). This solution is added to a pellet of particles. Per 10 µL particle volume, c(particles)≈0.15-1 nM, an equal volume of the protein is added and incubated at room temperature for 30 min.

5. Methods

This section describes the methods used in the thesis.

5.1. UV-Vis ensemble spectra

Ensemble spectra were done with the USB2000 Fiber Optic Spectrometer by OceanOptics.

5.2. Agarose gel electrophoresis

Agarose gel electrophoresis was done with a Bio-Rad PowerPac Basic Power Supply, in Mini-Sub GT cells. Gels were cast in a typical gel range was 0.7-1%. For this, agarose (for routine use) by sigma-alrich was used (batch #078K0140, A9539-250G). Agarose was suspended in 0.5x TBE buffer. (Rotiphorese TBE-buffer 10x: 1 M Tris-Borat, 20 mM EDTA; pH 8,3.) The suspension is heated in a microwave until all agarose is dissolved. Then it is cast immediately, with a 8-well comb, giving approximately 20 µL pockets. Gel requires at least 60 min to harden. After hardening, gel is removed and placed into the measurement cell. 0.5x TBE buffer is used as a running buffer. Buffer typically has a pH 8.3-8.5. For a pH=11 buffer, NaOH is added until the required pH is reached. Gel is run at 150 V, typically between 10-30 min. Vitamin B12 is used as a reference.

When sample contains the Hsp90 protein or DNA, the gel chamber is pre-cooled in an ice bath, and cooled further during the electrophoresis. This is because the gel gets hot during electrophoresis, and electrophoresis times above 30 min can heat the gel up to 40°C and more, which can cause protein dimer dissociation or split the hybridized DNA.

5.3. Microscope setup

Most measurements were done using modified Zeiss dark-field microscopes. For real-color images, a halogen lamp (HAL100 by Zeiss) and a white light LED (LED Nano, LEJ) were used interchangeably. Spectral images were taken with a Thorlabs VariSpec Kurios VB1. For single-wavelength detection, the 625 nm LED was used (M625L4, by Thorlabs). Measurements were done with a 40x objective (plan-apochromat) with a NA=1.3 from Zeiss. For the dark-field illumination, an ultracondenser by Zeiss was used (1.2/1.4). For measurement, a Hamamatsu Orca flash 4.0 CMOS camera was employed.

6. Supplementary gel electrophoresis images

This part lists supplementary gel electrophoresis images to complement the data shown in the main part. Figure B-3 and Figure B-4 show the gel images were processed for the particle mobility plot and comparison. The evaluation was done as described in source [155].

#	Na_2SO_4/ mM
1	0
2	0.02
3	0.05
4	0.07
5	0.1
6	0.5
7	1
8	2
9	5
10	7
11	10

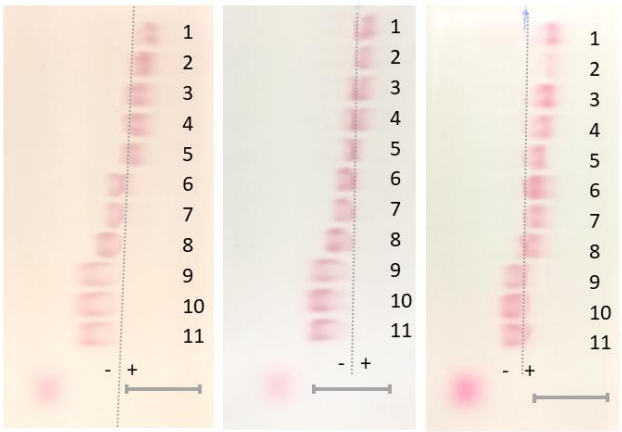

Figure B-3. Gel electrophoresis images of 10% amino-PEG particles. Table shows the respective salt content used during functionalization with PEG. The gels are from three independently performed functionalizations. Scalebar: 1 cm.

#	K_2SO_4/ mM
1	0
2	0.02
3	0.05
4	0.07
5	0.1
6	0.5
7	1
8	2
9	5
10	7
11	10

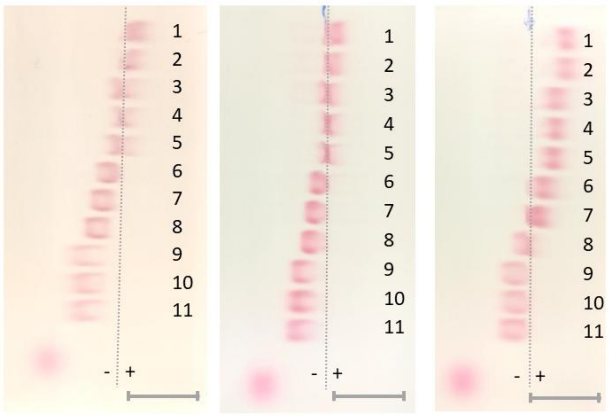

Figure B-4. Gel electrophoresis images of 10% amino-PEG particles. Table shows the respective salt content used during functionalization with PEG. The gels are from three independently performed functionalizations. Scalebar: 1 cm.

Figure B-5 additionally shows how a variation of anion type and consequently the cation concentration influences the mobility behavior. At the same salt concentration, K_3PO_4 has a higher ionic strength as compared to KCl, and the mobility plateau is reached earlier in comparison. Most interestingly, K_3PO_4 seems to have a reverse effect starting from a concentration of 5 mM: After reaching the maximally slow mobility, the next bands have increasing mobility. This may be either because too high salt concentrations have a negative impact, such as salting out and reducing the polymer content. It could also be because the phosphate somehow plays an additional role, perhaps by interacting

with the gold surface. Due to this unexpected effect, I do not recommend using phosphate salts.

#	c(salt)/ mM
1	0
2	0.02
3	0.05
4	0.07
5	0.1
6	0.5
7	1
8	2
9	5
10	7
11	10

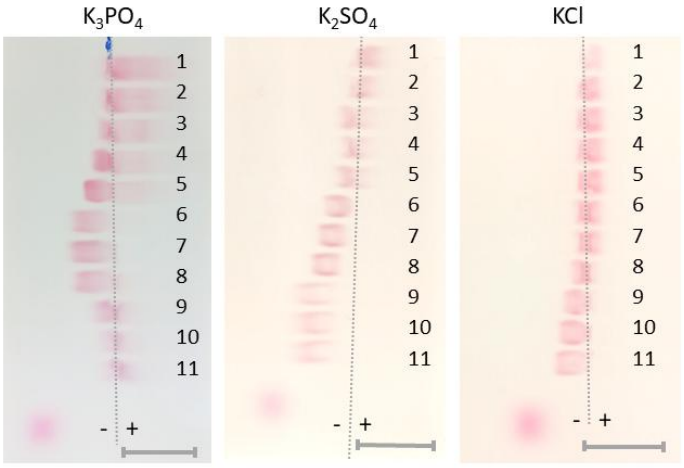

Figure B-5. Gel electrophoresis images of 10% amino-PEG particles functionalized in the presence of different salts. The anion type and cation content are varied, between KCl, K_2SO_4 and K_3PO_4 (from right to left). Table shows the salt content.

6.1. A word of caution for interpretation of gel electrophoresis results

In this section I document some findings that may be of interest and importance when performing functionalization steps containing additional small molecules.

As follows, I anecdotally report on interference caused by small molecules present in many protocols that involve proteins or the handling of free thiols. The molecules in question are ethylene diamine tetra acetic acid (EDTA) and Tris(2-carboxyethyl)phosphin-hydrochloride (TCEP), which coincidentally share structural similarities with sodium citrate (Figure B-6c). EDTA is found in many functionalization protocols, as well as gel running buffers.[156,157] Its role is to bind divalent ions that can negatively impact certain molecules and reactions. TCEP is a common reagent for splitting disulfide bridges to prepare a reactive thiol group for further attachment to either gold or other chemistries.[158] In our work, it is used to cleave potential disulfide bonds in Hsp90 protein stocks. Similarly, in another type of assembly strategy, it is also used to prepare thiol-DNA for attachment to particles.

While working with these molecules, I have observed two major issues: First, when using with positively charged amino-particles, a presence of EDTA can unexpectedly cause aggregation. This may be because EDTA bridges over the particles, since it has several negatively charged groups. Second, that the reagent TCEP can easily replace CTAC, and that the characterization of its mobility in a gel electrophoresis experiment makes it look exactly the same as DNA, when the latter is the target of attachment (Figure B-6b).

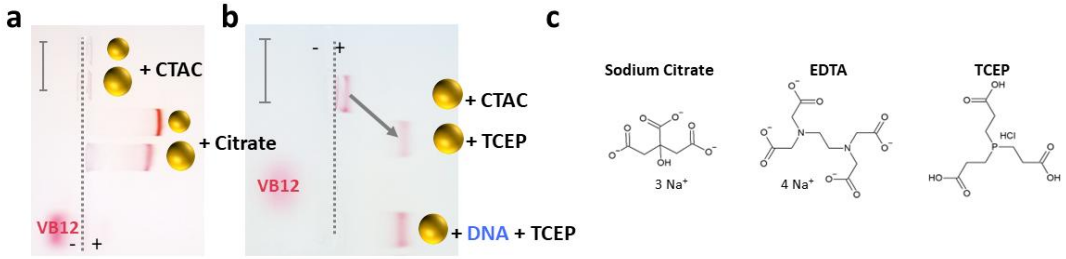

Figure B-6. Behavior of particles in the presence of physisorbed molecules. (a) Gel electrophoresis image showing two aggregated CTAC-stabilized 40 and 60 nm particles, and two running bands of citrate-stabilized 40 and 60 nm particles. The bigger particle batch shows a smaller mobility due to its relative size. (b) Gel electrophoresis image of a CTAC particle which was incubated with TCEP to show that not only does TCEP replace CTAC due to higher affinity, it also stays firmly attached even when run in the gel. Additionally, TCEP-functionalized particles show the exact same mobility as particles incubated with a mixture of both. The gel can therefore not guarantee that attachment of DNA was sufficiently successful. Scalebar: 1 cm. (c) Structures of sodium citrate, EDTA and TCEP.

For modification steps, these observations mean that special caution needs to be taken when such molecules are present in the protocol. In the case of TCEP and EDTA, my recommendation would be to avoid using them or to use desalting columns to remove them from stock.

C. Appendix: Assembly

1. Characterization methods: tips and trick, limits and strengths.

Identification of assembly success requires a combination of several methods, because not every method works well for every single case. Here I summarize which methods work best in which case, and when they fail due to limitations. This is important to know, because a lack of "positive assembly" result using a certain method does not necessarily mean that no assembly happened.

1.1. Agarose gel electrophoresis

Out of all easily available methods, the gel electrophoresis is the one method with the best throughput. However, as shown in the main part, it can fail with particles that have excessive positive charge, requiring tuning of running buffer pH. This can become complicated, because the straight-forward tuning of the pH also alters the ionic strength of the buffer, which influences the electrophoresis process. Ideally, it is best to avoid excessively positively charged samples.

The separation of dimers and higher constructs generally happens due to increasing construct retention in the gel. Whether or not separation is easily seen depends on the dimer type. For example, a dimer consisting of two same-charged negative particles has double the size and double the charge, and so the charge-per-area value remains the same. The separation therefore is governed by retardation in the gel matrix. This process is straight-forward for same-charge constructs, but may be more difficult to predict for different-charge dimer constructs, as seen in the case of carboxy-amino hetero-type dimers.

I have observed better separation for negatively charged particles with high mobilities, such as carboxy or DNA-functionalized ones. Better separation is seen for carboxy end group content starting from about 50%. Generally, 30 min of running time in a 0.5-0.7% agarose buffer at 150 V in a 0.5x TBE buffer is enough to see band separation for carboxy-PEG samples. A similar trend is seen in DNA samples. The difference between a low and high mobility sample is shown in Figure C-1a.

Another key aspect, shown in Figure C-1b, is the sample heterogeneity. As the gel image shows, the separation between the monomer band and the dimer band can be as low as the width of a heterogeneously functionalized monomer band. This is problematic, because a broad monomer band can hide higher order constructs. Heterogeneity of a sample is often the result of insufficient and uneven particle functionalization. In this case, the functionalization needs improvement. However, often times a good sample shows a broad band due to pocket overload, which causes a retention of the sample. To

avoid this issue, the sample should be diluted until it runs as a slim band. This of course can be counter-productive to detection of low amounts of multimer constructs. As an in-between solution, I recommend not diluting the sample too much and running it for longer than 30 min. In terms of detectable dimer-to-monomer ratio, I found the threshold to be around 10%, depending on the stock concentration. Lower ratios may be difficult to detect with this method.

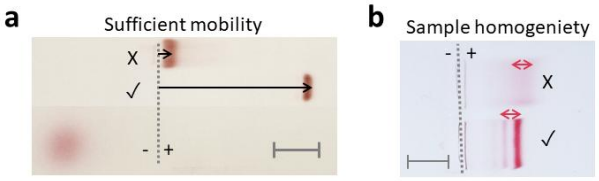

Figure C-1. Examples of gel electrophoresis results. (a) Gel electrophoresis image of two samples with a low and high mobility. Low mobility is undesired for a clean separation of higher order constructs from the monomer band. This typically happens to samples where the particle size and charge cancel out each other in such a way that the resulting mobility is near zero. Scalebar: 0.5 cm. (b) An example of a heterogeneous sample band and a more homogeneous one. Arrows show how the width of the heterogeneous monomer sample can be as large as the separation between monomer and dimer bands. Scalebar: 0.5 cm.

One important thing to note is that gel electrophoresis can be used not only for construct separation but also for purification. This is all the more important when the original stock has unwanted non-specifically connected constructs.

1.2. TEM: Better for characterization of repeatedly cleaned dimer samples

Transmission electron microscopy (TEM) is a method that can directly visualize construct types. It is best used however on already pre-cleaned and isolated construct samples, rather than construct sample mixtures. This is because there are always drying effects than can "emulate" the presence of higher order constructs where there are none. This effect can be somewhat reduced, for example, by diluting the sample, or applying tricks such as charging the sample grid prior to the deposition of the sample.

I applied this method mainly for characterization of the additional bands in the gel electrophoresis experiment to prove the presence of dimers in the samples. While doing so, I noticed that even seemingly "clean" dimer bands in an agarose experiment can still contain significant amounts of monomers, as seen in TEM (Figure C-2b, 1 cleaning step). This happens due to crowding effects in the gel, and the relatively small separation between the bands. As a solution, I found that extracting the dimer band and separating it repeatedly in a gel helps reduce the monomer fraction (Figure C-2b, 2 cleaning steps), so that over 80% of identifiable constructs in the TEM image can be attributed to dimers.

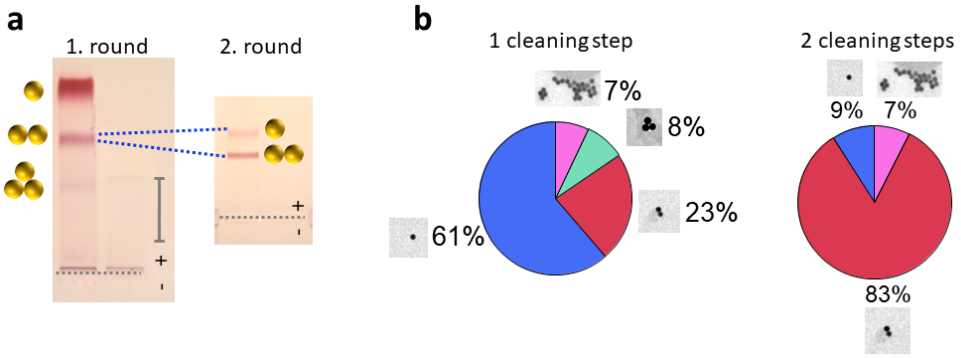

Figure C-2. Comparison of construct identification in TEM. A sample with a one-time agarose gel cleaning step and subsequent isolation of the dimer band still shows a significant number of monomers of around 60%. On the other hand, a repeated cleaning of the isolated dimer gel band shows only 9% remaining monomers. Images and colors show the respective constructs, with the pink color signifying aggregated particle groups that could not be identified due to drying effects.

1.3. UV-Vis: Ensemble reliability depends on assembly distance and dimer concentration

Using ensemble spectra for characterization of higher order constructs can be tricky, as already mentioned in the main part. Here I show one example from my assembly experiments. As shown in Figure C-3, the carboxy-PEG particle mixture containing mostly monomers and below 20% dimers (gauged by band intensity in the agarose gel) shows barely any difference to the simple monomer particle spectrum. On the other hand, there is a slight resonance wavelength shift of 3 nm when measuring the isolated dimer band, which contains around 80% of identifiable dimer constructs according to TEM. (This is of course not the absolute number of constructs, and the true number of dimers may be lower, due to the presence of unidentifiable aggregated particle groups.) The small resonance shift is because the constructs have a relatively large interparticle distance, and the plasmonic coupling effect being relatively weak.

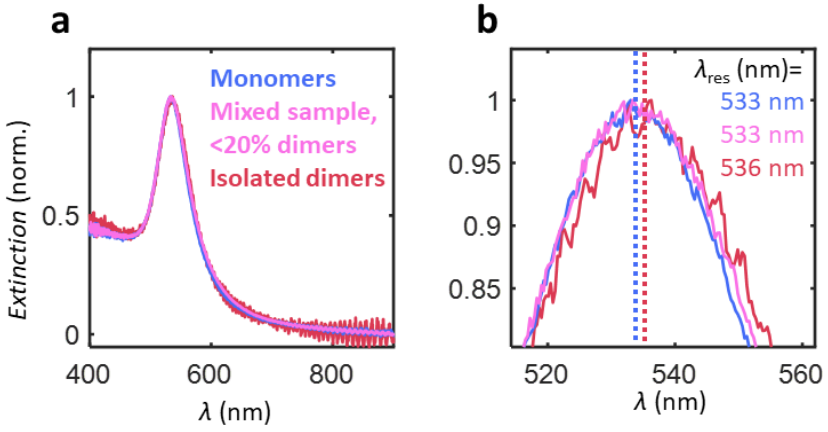

Figure C-3. UV-Vis detection of dimer presence in a sample. (a) Extinction spectrum of a monomer sample, a mixed sample with dimers and small amounts of higher order constructs, and a spectrum of a dimer band that was isolated from an agarose gel. (b) Closeup of the extinction spectrum shown in a.

The previous sections presented the methods of agarose gel electrophoresis, TEM and UV-Vis ensemble spectra. One method not yet mentioned is the construct identification by **single-particle dark field spectroscopy**. This method was not chosen for the screening of assembly strategies due to being less high-throughput than the gel electrophoresis, and also because it is highly dependent on specific interparticle distance. Presuming that the interparticle distance is too large, the difference between a monomer and a dimer construct becomes too small to see by eye. Technically, even with no plasmonic coupling present, such a dimer should exhibit a two times higher intensity compared to a monomer. However, particle samples are already heterogeneous. Therefore, for better control it is best to perform the dimerization with before and after measurements in the dark field, which again lengthens the experimental time and reduces the number of experiments.

Another possibility is also to change the system, for example by adding certain salts as potassium that are known to complex PEG and therefore reduce the interparticle distance.[61] This method however also requires time, and is better suited for further characterization, rather than simple identification of dimer presence.

1.4. Identification of assembly success, a summary

I find that all methods taken together serve sufficiently well to give a hint of a successful reaction. Not every method works equally well, depending on particle charge and size and interparticle distance, which is why a combination of methods is necessary for a clearer picture. Since the goal of this work was to primarily find the best system for quick and efficient assembly, the identification of dimers specifically was not a main objective. This simplified the task by defining reaction success by presence or absence of reaction-specific aggregation. Compared to dimer constructs, which may be difficult to isolate and separate from the sample mixture, specific aggregation can be quickly seen even by eye in the form of a discoloration of the sample mixture. Figure C-4 presents a summary of the methods, with the special emphasis on the aggregation as a must-have indicator of success.

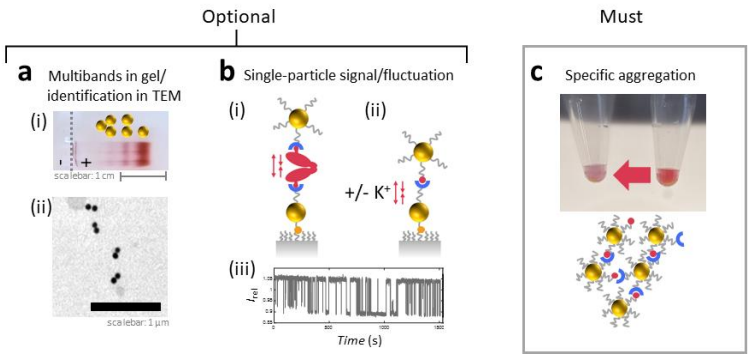

Figure C-4. Different methods for identifying assembly success. (a-i) Identification via separation of reaction mixture in a gel electrophoresis experiment. (a-ii) Confirmation of gel electrophoresis experiment by TEM. The example shows an extracted second band, which contains discrete dimer constructs. (b-i, ii) Single-particle experiments are low-throughput, but they can serve to give more information on the constructs, such as the presence of a fluctuating signal in the case of a protein coupled dimer confirming the presence of the protein between the particles. In the case of a non-protein coupled PEG-

functionalized particle dimer, a reversible change in PEG size by addition of salts such as potassium can confirm the presence of successfully formed constructs. (b-iii) An example of a fluctuation signal of a dimer construct. (c) The best criterium for assembly success is chemistry-specific aggregation of the sample.

I refer to this strategy as "backwards tuning". Upon selecting a reliable chemistry that gives the fastest specific aggregation, the number of reactive anchors and linker molecules can be reduced and tuned to a ratio with the statistically expected highest dimer yield.

2. Assembly protocols

This section lists the assembly protocols used in this thesis.

2.1. Maleimide coupling

Particle activation. Amino-PEG functionalized particles are cleaned by centrifuging 5x at 10.230 rcf for 3-8 min, depending on the volume. Per 100 μL of solution, 10 μL 2v% Tween20 is added before centrifugation. The supernatant is replaced with equal volume of PBS 7.4. Before activation, the particle sample is left as a pellet.

SMCC is stored at -20°C in water-free DMSO at a concentration of 20 mg/mL (=60 mM). An aliquot of this solution is taken out and diluted in RT milliQ water to a final concentration of 0.6 mM (typically 1 μL of the original solution is quickly added to 99 μL of PBS 7.4 or HEPES 7.4 buffer, and then vortexed). SMCC has a low solubility in water, and cold buffers especially should be avoided during this step. The diluted solution is quickly added to the particle pellet. Due to the high excess of SMCC compared to the particles (x2.400.000), minor differences in particle concentration and reactive PEG end groups are neglected in this protocol. Per 100 μL of an approx. 0.1-0.25 nM particle solution, 50 μL of a 0.6 mM SMCC solution are added, vortexed and left to react for about 2 h. In gel experiments, I have observed that a minimum of 1-1.5 h are necessary until the gel bands no longer show a change in mobility. Particles are then cleaned in PBS 6.7 or HEPES 6.7, 5x at 10.230 rcf for 3-8 min. Per 100 μL of solution, 10 μL 2v% Tween20 is added before centrifugation.

Particle storage. I observed that maleimide particles stored in PBS 6.7 at RT remain active towards thiol-capped molecules for weeks. Nonetheless, activated particles were typically stored as aliquots in a -80°C freezer.

Homo-type assembly. The linker (dithiol-PEG, 2000g/mol, 3000 g/mol, 6000 g/mol) is prepared at a necessary concentration according to the particle-to-ligand ratio. The particle solution is mixed with the ligand solution at a volume ratio of 1:1 (typically in the range of e.g. 20 μL+20 μL). The concentrations are adjusted accordingly. For better characterization in the gel electrophoresis, particle concentration should not be below 0.5 nM in the sample.

It is important that mixing happens uniformly and fast. For this, one solution is placed at the bottom of an eppi tube, and another in the inside of the cap. Then the eppi is closed

and shook so that the particle droplet combines with the ligand droplet. The mixture is then left to stand for 30 min/overnight at room temperature. Thereafter the mixture is immediately characterized in gel electrophoresis, and a UV-Vis spectrum is recorded.

Hetero-type assembly. Particles are functionalized with respective ratios of methoxy-PEG (2000 g/mol) and either amino-PEG (3000 g/mol) or dithiol-PEG (2000 g/mol, 3000 g/mol). 10% amino-PEG is used for the first particle, and 100% dithiol-PEG for the second. After activation with SMCC and subsequent cleaning, particles were mixed at a volume ratio of 1:1 and characterized.

2.2. EDC/NHS coupling

Particle activation. After cleaning by centrifugation, 100 μL of carboxy-PEG particles (c≈0.5 to 0.25 nM) are left as a pellet in the eppi. Prepare EDC and NHS solutions in MES (2-morpholin-4-ylethanesulfonic acid) buffer (pH=4.5; 0.1 M): Dissolve 1.55 mg EDC per 100 μL buffer, and 1,15 mg NHS per 100 μL buffer. This gives a 100 mM solution. Per 100 μL original particle solution, add first 50 μL of the EDC solution, vortex and mix well, then add 50 μL NHS solution, mix. Minimal incubation time is 30 min for a complete reaction, according to gel electrophoresis controls. Thereafter particles are washed in PBS 7.4. Per 100 μL buffer add 10 μL 2% Tween20. Centrifugation is at 10230 rcf, 3-8 min depending on particle size and volume. The remaining protocol is exactly as the one for the maleimide chemistry. The diamino-PEG linker (2000 g/mol, 3000 g/mol) is dissolved and the particle and linker solutions are added at a volume ratio of 1:1. The mixture is left to rest at room temperature, and thereafter characterized.

2.3. Biotin-streptavidin.

Homo-assembly. For assembly, 10% biotin-PEG particles are made according to the general protocol. Particles are cleaned by centrifuging 5x at 10.230 rcf for 3-8 min, depending on the volume. Per 100 μL of solution, 10 μL 2v% Tween20 is added before centrifugation. I observed no difference between cleaning in PBS or potassium sulfate (50 mM) or water. In the final step, the supernatant is replaced with equal volume of PBS 7.4. Streptavidin (tetramer) is stored at -20°C as a 5 or 1 mg/mL solution in PBS 7.4. a 1 mg/mL solution corresponds to approximately 16.6 μM, assuming a molar mass of 60 kDa. Similar to the other homo-assembly protocols, this solution is diluted accordingly. The particle and protein solutions are mixed at a volume ratio of 1:1 and left to react at room temperature for 30 min or overnight. The mixture is then characterized accordingly.

Hetero-assembly. This section compiles the protocols for all hetero-assembly related reactions.

Functionalization of mono-streptavidin particles. The mono-streptavidin (SAvPhire-Streptavidin from sigmaaldrich) is attached to particles via His-tag. For this, particles are first functionalized with DNA-NTA, incubated with Ni^{2+} and then with mono-streptavidin.

Synthesis of DNA-NTA: DNA (5'-SH-TTTTTTTTTTTT-NH_2-3', from Biomers.net GmbH) is diluted in TE buffer (c=500 μM) and stored at -20°C. i-NTA (Isothiocyanobenzyl-nitrilotriacetic acid) is diluted in DMSO (100 mg/mL) at stored at -20°C. 69 μL of the 100 mg/mL NTA solution is added to 207 μL of 500 μM DNA. The solutino gets turbid and yellowish. The solution is then incubated for 3-5 h at room temperature on the orbital shaker. After incubation the sample is dialyzed (10 mM Tris-HCl pH 8) at room temperature, the buffer is exchanged 3x and the last dialysis step is overnight. A Micro Float-A-Lyzer MWCO 500-1000 Da is used for dialysis. Next day, 30 μL aliquots are prepared and stored at -20°C.

Particle functionalization with DNA-NTA: 300 μL (25 mM CTAC) particles (c≈0.1-0.25 nM) are mixed with 700 μL milliQ water and centrifuged at 10230 rcf for 8 min. The supernatant is removed. 5 μL 100 mM TCEP (dissolved in 0.3 M NaOH) is added to 30 μL DNA-NTA and incubated for 30 min at room temperature. This solution is then added to the particle pellet. After 10 min 30 μL 1% SDS is added. The sample is then incubated for 1 h, then 2 μL 2M NaCl are added, and this step repeated 3 more times. Thereafter the sample is incubated at room temperature on the orbital shaker overnight.

Functionalization with the mono-streptavidin: 15 μL NTA-particles are incubated with 70 μL milliQ water, 5 μL 2% Tween20 and 15 μL 2 mM Ni^{2+} for 10 min at room temperature. The particles are then centrifuged at 10230 rcf for 3 min. The pellet is resispended in 5 μL miliQ water. To this solution, 95 μL of 50 nM His-tag mono-stepravidin is added. 50 nM streptavidin is sufficient to cover the particles, there is no improvement when going up to 5 μM, according to a characterization in gel electrophoresis. I have observed that 10 min were already enough for a complete reaction, but 30 min are chosen for the standard procedure. Due to aggregation during centrifugation, particles are cleaned via dialysis in PBS 7.4 instead. Mono-streptavidin particles may need extra SDS to remain redispersed. DNA-particle coverage may need further improvement.

Hetero-assembly. For assembly, 10% biotin-PEG particles are mixed with an equal ratio of mono-streptavidin particles and left to react for 30 min at room temperature. The particles are thereafter characterized.

Functionalization of tetramer streptavidin particles with DTSSP. 50 μL of a 1 mg/mL streptavidin solution in PBS 7.4 is incubated for 30 min at room temperature with 50 μM 0.3 mM DTSSP (3,3´-Dithiobis(sulfosuccinimidylpropionate)) in PBS. Remaining DTSSP is removed with a Zeba Spin Desalting Column MWCO 7K (Pierce). 500 μL of 40 nm citrate capped particles from BBI are centrifuged at 10230 rcf for 5 min. Add the streptavidin solution and incubate at room temperature overnight. I noticed no difference between incubation at room temperature and 4°C in the gel electrophoresis experiments. However, the resulting particles showed aggregation during centrifugation cleaning steps. Removal of excess streptavidin is therefore difficult.

2.4. DNA assembly

Functionalization: Protocol see particle functionalization.

The assembly protocol follows the same procedure as the previous ones. In the homo-type assembly, particles and the protein are diluted accordingly, mixed and left to react for 30 min or overnight. In the hetero-type assembly, complementary particles are mixed at a volume ratio of 1:1 and left to react similar to the homo-type assembly.

3. Supplementary experimental figures

This section contains figures showing reproduction experiments and supplementary experiments that the main section refers to.

3.1. Maleimide chemistry with varying linker sizes

This part shows additional experiments for the maleimide reaction related assembly. Several dithiol-PEG length between 2000 g/mol and 6000 g/mol were tested additionally as viable linkers for amino-PEG functionalized homo-type assembly. As Figure C-5 shows, no significant change was seen after addition of the linker molecules at the ratios where for other systems such as biotin-streptavidin, assembly was seen.

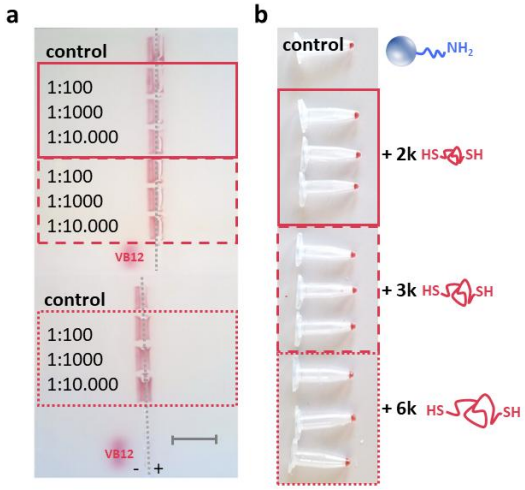

Figure C-5. Gel electrophoresis image of homo-type assembly with different dithiol-PEGs. (a) Gel images of maleimide-activated amino-PEG functionalized particle samples, incubated over 48 h. The particle-to-linker ratios are shown beside the sample band. The samples don't show significant change compared to the control. Scalebar: 1 cm. (b) Respective samples from a, showing no sign of aggregation.

3.2. Multiple bands in carboxy-PEG functionalized samples

Here I show additional figures depicting how the multiple bands in the PEG functionalized samples look like. Figure C-6 a-b shows repeated experiments. The appearance of the additional bands is seen when switching to other particle batches and seems reproducible. Figure d also displays that longer gel running times may be needed to reveal the multi-band structure of the sample. Curiously, the multi-band structure

appears also when the ratio between methoxy-PEG and carboxy-PEG is tuned (c), suggesting that the interaction may not be dependent on the carboxy-group content.

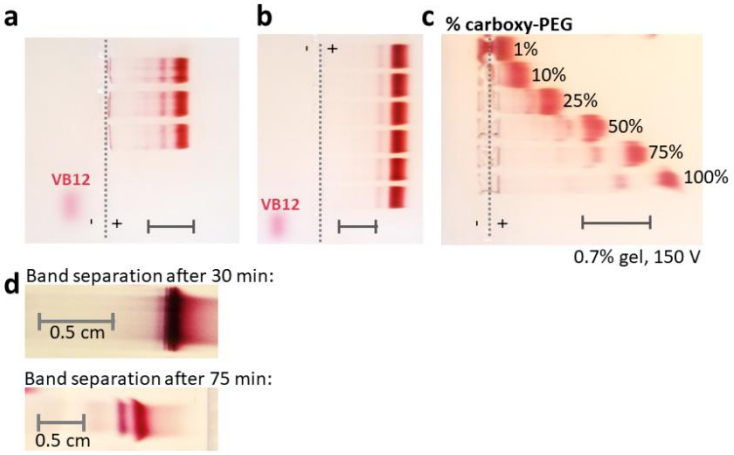

Figure C-6. Supplementary gel images for carboxy-PEG multimer constructs. (a-b) Gel images of repeatedly functionalized carboxy-PEG particles with 75% carboxy-PEG (3000 g/mol) and 25% methoxy-PEG (2000 g/mol). (c) Multiple bands appear visibly starting from 25% carboxy-PEG. Scalebar: 1 cm. (d) Gel requires at least 30 min of running time in a 0.7% agarose gel at 150 V to reveal other bands. The structure is better to discern after 75 min of running time.

Following figures show typical TEM images recorded of the second band, showing that it indeed contains dimers. In a majority of cases, the dimers show no gap, suggesting that the particles "snap" together during the drying process. A more sophisticated sample preparation may be necessary to reveal the true gap size, since the particle dimers evidently do not start out with a near zero gap when in solution, as shown in dark-field experiments in the next chapter.

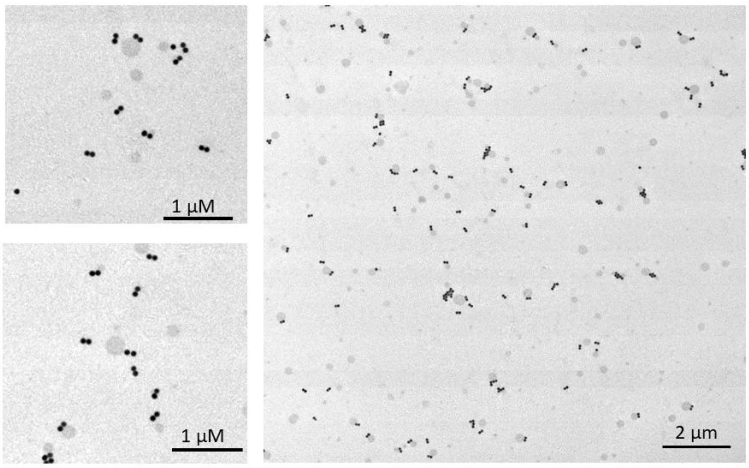

Figure C-7. TEM images of dimer constructs from carboxy-PEG particles.

The following figure shows complementary information on hetero-type assembly experiments with the EDC/NHS chemistry type. No reaction could be observed when incubating mixtures of particles with varying ratios of end groups (a). On the other hand, centrifugation of said mixtures or freezing at -80°C reproducibly yielded results (b).

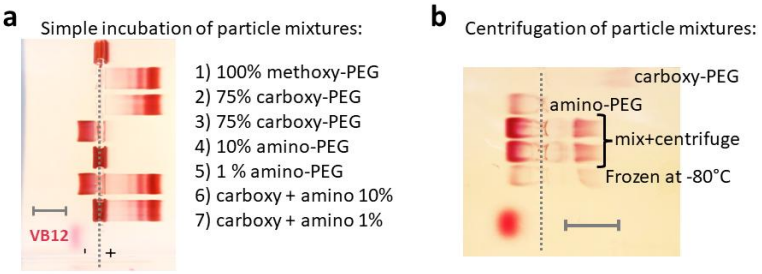

Figure C-8. Supplementary gel images for hetero-type EDC/NHS assembly. (a) Gel image of carboxy- and amino-PEG particles and their mixtures. Upon simple incubation (30 min), the samples separate into respective monomer bands, with no hint of assembly or aggregation. (b) Gel images of centrifuged reactive particle mixtures show appearance of new bands approximately in between the monomer bands. Freezing the sample mixture also appears to weaken the band color. This may happen due to aggregation, suggesting that freezing also leads to reaction due to forced particle proximity.

Interestingly, these samples show a variety of gaps between the particles, as compared to the consistent zero-gap seen in several TEM recordings of the carboxy-PEG samples. Due to the small statistics and unreliable band identification and isolation however, it is difficult to say whether the sample dried under better conditions. Qualitatively, I observed that the gaps in the hetero-type samples can in some cases be larger than the typical PEG lengths. This may be a hint that the attachment between the particles is not covalent but rather adsorbed. Since this assembly type is less effective than the biotin-streptavidin and DNA-DNA one, I did not further pursue the question of dimer formation in this hetero-type constellation.

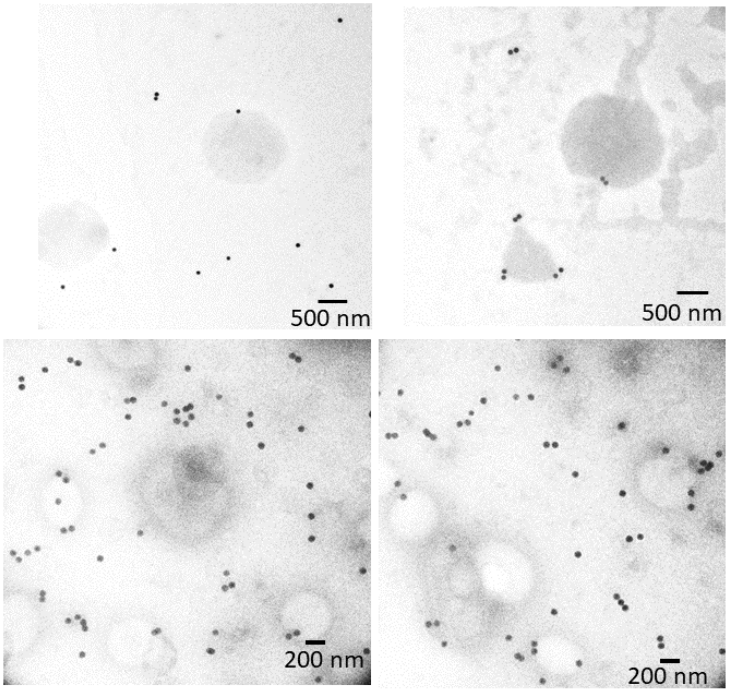

Figure C-9. TEM images from hetero-type assembled constructs. The images show a heterogeneous sample, with many monomers and dimers with a variety of interparticle gaps.

3.3. Biotin-streptavidin chemistry

The biotin-streptavidin assembly is reproducibly successful. Figure C-10 shows another such gel image and the typical discoloration of the sample when streptavidin is added to the particle solution.

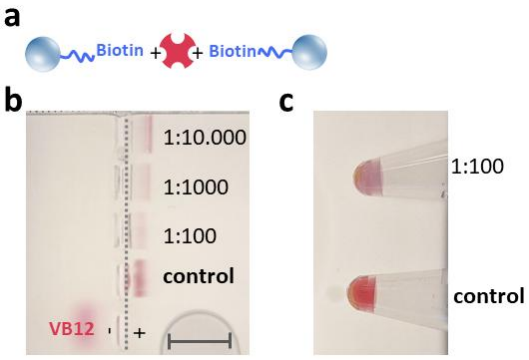

Figure C-10. Reproduction of biotin-streptavidin homo-type assembly. (a) Assembly sketch. (b) Gel electrophoresis image of samples with different particle-to-streptavidin ratios, and a control. (c) After 30 min, the 1:100 sample shows discoloration, hinting at aggregation caused by streptavidin.

D. Copyright and Permissions

License Details

This Agreement between Alena Kuzmina ("You") and Elsevier ("Elsevier") consists of your license details and the terms and conditions provided by Elsevier and Copyright Clearance Center.

Print Copy

License Number	6247661396361
License date	Apr 14, 2026
Licensed Content Publisher	Elsevier
Licensed Content Publication	Biochimie
Licensed Content Title	Hsp90: Friends, clients and natural foes
Licensed Content Author	Sharad Verma,Sukriti Goyal,Salma Jamal,Aditi Singh,Abhinav Grover
Licensed Content Date	Aug 1, 2016
Licensed Content Volume	127
Licensed Content Issue	n/a
Licensed Content Pages	14
Type of Use	reuse in a thesis/dissertation
Portion	figures/tables/illustrations
Number of figures/tables/illustrations	1
Format	both print and electronic
Are you the author of this Elsevier article?	No
Will you be translating?	No
Title of new work	Challenges in the Functionalization of Nanoparticles for Plasmon Ruler-Based Single-Protein Studies
Institution name	Johannes Gutenberg University Mainz
Expected presentation date	Apr 2026
Portions	Figure 1
The Requesting Person / Organization to Appear on the License	Alena Kuzmina
Requestor Location	Alena Kuzmina Duesbergweg 10-14 Mainz Am Rhein, 55128 Germany
Order reference number	7
Total	**0.00 EUR**

License Details

This Agreement between Alena Kuzmina ("You") and John Wiley and Sons ("John Wiley and Sons") consists of your license details and the terms and conditions provided by John Wiley and Sons and Copyright Clearance Center.

Print Copy

License Number	6247641510934
License date	Apr 14, 2026
Licensed Content Publisher	John Wiley and Sons
Licensed Content Publication	ChemPhysChem
Licensed Content Title	Effects of Inhibitors on Hsp90's Conformational Dynamics, Cochaperone and Client Interactions
Licensed Content Author	Sonja Schmid, Markus Götz, Thorsten Hugel
Licensed Content Date	May 25, 2018
Licensed Content Volume	19
Licensed Content Issue	14
Licensed Content Pages	6
Type of Use	Dissertation/Thesis
Requestor type	University/Academic
Format	Print and electronic
Portion	Figure/table
Number of figures/tables	1
Will you be translating?	No
Title of new work	Challenges in the Functionalization of Nanoparticles for Plasmon Ruler-Based Single-Protein Studies
Institution name	Johannes Gutenberg University Mainz
Expected presentation date	Apr 2026
Portions	Figure 1, part A
The Requesting Person / Organization to Appear on the License	Alena Kuzmina
Requestor Location	Alena Kuzmina Duesbergweg 10-14 Mainz Am Rhein, 55128 Germany
Order reference number	4
Total	**0.00 EUR**

License Details

This Agreement between Alena Kuzmina ("You") and Elsevier ("Elsevier") consists of your license details and the terms and conditions provided by Elsevier and Copyright Clearance Center.

Print Copy

License Number	6247650121828
License date	Apr 14, 2026
Licensed Content Publisher	Elsevier
Licensed Content Publication	Structure
Licensed Content Title	Folding and Domain Interactions of Three Orthologs of Hsp90 Studied by Single-Molecule Force Spectroscopy
Licensed Content Author	Markus Jahn,Katarzyna Tych,Hannah Girstmair,Maximilian Steinmaßl,Thorsten Hugel,Johannes Buchner,Matthias Rief
Licensed Content Date	Jan 2, 2018
Licensed Content Volume	26
Licensed Content Issue	1
Licensed Content Pages	14
Type of Use	reuse in a thesis/dissertation
Portion	figures/tables/illustrations
Number of figures/tables/illustrations	1
Format	both print and electronic
Are you the author of this Elsevier article?	No
Will you be translating?	No
Title of new work	Challenges in the Functionalization of Nanoparticles for Plasmon Ruler-Based Single-Protein Studies
Institution name	Johannes Gutenberg University Mainz
Expected presentation date	Apr 2026
Portions	Figure in graphical abstract
The Requesting Person / Organization to Appear on the License	Alena Kuzmina
Requestor Location	Alena Kuzmina Am Gonsenheimer Spieß 10 Mainz Am Rhein, 55122 Germany
Order reference number	6
Total	**0.00 EUR**

Order Date	14-Apr-2026	**Type of Use**	Republish in a thesis/dissertation
Order License ID	1719386-1	**Publisher**	RSC Pub
ISSN	2040-3372	**Portion**	Image/photo/illustration

LICENSED CONTENT

Publication Title	Nanoscale	**Publication Type**	e-Journal
Article Title	Packaging of DNA origami in viral capsids.	**Start Page**	10160
Author / Editor	Royal Society of Chemistry (Great Britain), National Center for Nanoscience and Technology.	**End Page**	10166
		Issue	21
Date	01/01/2009	**Volume**	11
Language	English	**URL**	http://www.rsc.org/Publishing/Journals/N...
Country	United Kingdom of Great Britain and Northern Ireland		
Rightsholder	Royal Society of Chemistry		

REQUEST DETAILS

Portion Type	Image/photo/illustration	**Distribution**	Worldwide
Number of Images / Photos / Illustrations	1	**Translation**	Original language of publication
Format (select all that apply)	Print, Electronic	**Copies for the Disabled?**	No
Who Will Republish the Content?	Not-for-profit entity	**Minor Editing Privileges?**	Yes
Duration of Use	Life of current edition	**Incidental Promotional Use?**	No
Lifetime Unit Quantity	Up to 499	**Currency**	EUR
Rights Requested	Main product		

NEW WORK DETAILS

Title	Challenges in the Functionalization of Nanoparticles for Plasmon Ruler-Based Single-Protein Studies	**Institution Name**	Johannes Gutenberg University Mainz
		Expected Presentation Date	2026-04-19
Instructor Name	Carsten Sönnichsen		

ADDITIONAL DETAILS

Order Reference Number	7	**The Requesting Person / Organization to Appear on the License**	Alena Kuzmina

REQUESTED CONTENT DETAILS

Title, Description or Numeric Reference of the Portion(s)	Figure 2, image second row	**Title of the Article / Chapter the Portion Is From**	Packaging of DNA origami in viral capsids.
Editor of Portion(s)	Frank, Gabriel A.; Kler, Stanislav; Kopatz, Idit; Levi-Kalisman, Yael; Zalk, Ran; Zlotkin-Rivkin, Efrat	**Author of Portion(s)**	Frank, Gabriel A.; Kler, Stanislav; Kopatz, Idit; Levi-Kalisman, Yael; Zalk, Ran; Zlotkin-Rivkin, Efrat
Volume / Edition	11	**Issue, if Republishing an Article From a Serial**	21
Page or Page Range of Portion	10160-10166	**Publication Date of Portion**	2026-04-20